Computational modelling of pollution dispersion in the near wake of a vehicle

by

Kathryn Richards, B.Eng (Hons)

Thesis submitted to the University of Nottingham for the degree of Doctor of Philosophy

August 2002

Abstract

The feasibility of using CFD to model the dispersion of pollutant in the near wake of a model vehicle was investigated through a series of experimental and computational studies. The near wake structure of the MIRA 33% scale reference vehicle (fastback) was measured using Particle Image Velocimetry (PIV), and hotwire anemometry and the dispersion of a tracer measured using Flame Ionisation Detectors (FIDs). The experimental data not only provided insight into the dispersion character of the model vehicles' near wake but more importantly produced data for the validation of the numerical simulations of the measured near wake and dispersion fields. The numerical simulations of the near wake flow field were conducted using the CFD code STAR-CD with the standard, RNG, Chen and non-linear (quadratic) k-ε models in combination with Upwind (UD), Linear Upwind (LUD) and the Monotone Advection and Reconstruction (MARS) differencing schemes. Validation showed the predicted flow field to be in good agreement with the measured flow field. Using the numerical flow field predictions as a foundation the dispersion of a passive gaseous pollutant was simulated by modelling the dispersion of scalar quantity released into the computational domain using a fluid injection technique. The numerical predictions of both mean velocity and concentration fields were validated against the experimental data using various statistical validation techniques. Several short investigations into the influence of vehicle speed and exhaust mass flow rate were also conducted to further assess the applicability and use of the technique in investigating dispersion in the near wake of a vehicle. Relative successes in both the velocity field and dispersion simulations were demonstrated in making predictions of the mean velocity and concentration fields. However there is clearly the need for more development and in particular the application of time-dependent techniques for the underlying velocity solutions in order that peaks in mean concentration resulting from build-up due to unsteadiness in the flow field are fully captured. Nevertheless the study demonstrated the potential for the use of STAR-CD to investigate and understand in more detail the dispersion of pollution close behind a road vehicle and possibly assess the concentration levels, at the road side of different pollutants released.

Table of Contents

Page No

Chapter 4: Experimental Study 1 – Near wake velocity measurements

Chapter 5: Experimental Study 2 – Measurement of tracer gas concentration within the near wake of a model vehicle

Chapter 6: Computational Study 1: Simulation of the near wake flow field of a model vehicle

Appendices

List of figures

List of Tables

Principle notation

b	Half the width of the model base
c	Instantaneous concentration
$\overline{c}$	Mean concentration
f	Frequency
$F_{\overline{\varpi}_p}$	The factor difference between the predicted values of $\overline{\varpi}_p$
FID	Flame Ionisation detector
H	The overall height of the model from the ground
n	Number of samples
ppm	Parts per million
S	Strouhal Number
$\overline{u}_{HW}$	Mean streamwise velocity measured using Hot-wire anemometry
$\overline{u}_{PIV}$	Mean streamwise velocity measured using PIV
$\overline{v}_{HW}$	Mean vertical velocity measured using Hot-wire anemometry
$\overline{v}_{PIV}$	Mean vertical velocity measured using PIV
$\overline{w}_{HW}$	Mean cross-stream velocity measured using Hot-wire anemometry
$\overline{w}_{PIV}$	Mean cross-stream velocity measured using PIV
U_∞	Free stream velocity (m/s)
(x,y,z)	Co-ordinate system for mean velocity components $\overline{u}$, $\overline{v}$, and $\overline{w}$ respectively
x/l	Non-dimensional distance downstream of the model base
z	Cross-stream distance from the model centreline
z/b	Non-dimensional distance from the model centreline
α	Base slant angle
σ	Standard deviation
$\overline{\varpi}_p$	Mean proportion of propane to air
$\overline{\varpi}_{p_{max}}$	Maximum mean measured proportion of propane to air
$\overline{\varpi}_{p_{Lmax}}$	Local maximum mean proportion of propane to air
ξ_x	Streamwise vorticity

Published papers

The following are papers published as a result of this research,

Richards, K. A., Wright, N. G., Baker, C. J. and Baxendale, A. J. (2000), *'Computational modelling of pollution dispersion in the near wake of vehicles'*, Proceedings of CWE2000 Conference, Birmingham, UK.

Richards, K. A., Wright, N. G., Baker, C. J. and Baxendale, A. J. (2000), *'Computational modelling of pollution dispersion in the near wake of a vehicle'*, Proceedings of MIRA International Vehicle Aerodynamics Conference, Rugby, UK.

Acknowledgements

There are many people I would like to acknowledge for their contribution and support throughout this research project. Firstly I would like to offer thanks to the University of Nottingham, School of Civil Engineering and the Motor Industry Research Association (MIRA) for giving me the opportunity to carry out the research and for the financial support over the duration of the project. I am grateful to Anthony Baxendale and Geoff Callow for all their support and encouragement, and to Wayne Lee for his expertise in mesh construction.

My sincere thanks go to my principal supervisor Dr. Nigel Wright for all his unfailing efforts throughout the project. His influence and assurance have given me so much confidence. The monumental task of proof reading fell to his lot and he did not fail me. I am forever in his debt. Additional thanks go to Prof. Christopher Baker for his inspirational contributions and constructive comments during proof reading and will be remembered always for his immense enthusiasm for spectral methods.

I would also like to thank Michael Brown, Robert Palin, Richard Cook, David Arthur and David Wain of MIRA and Peter Jones and Robert Jaryzewski of Dantec for their invaluable contributions during the experimental program. An additional thanks to Dr. Andrew Quinn who not only played a vital role during the experimental program but whose knowledge and proof reading skills were very much appreciated. I would like also to acknowledge the contributions made by the support staff at Computational Dynamics and in particular Stephen Ferguson and Fred Mendonca for their patients and perseverance.

On a more personal note my heartfelt thanks must go to Matthew Ryan for his invaluable assistance and advice during the project. Thank you for being a good friend, for all the kindness you have shown me and for just listening when times were hard. Last but no means least I would like to thank my family for all their love and support through my years of study. Their kind words of encouragement have made what at times seemed an insurmountable task seem possible. My final thought goes to someone who gave me so much love and more. Thank you.

Chapter 1: Introduction

The state of our environment due to air pollution has become of increasing concern in terms of adverse health effects. In 1995 there were an estimated 600 million vehicles in use world-wide, 480 million of which were passenger vehicles (United Nations, 1999). Suggestions that a 50% increase in the prevalence of childhood asthma in the past 30 years is the result of environmental factors such as air pollution come from the increased emissions of nitrogen and volatile organic compounds from road vehicles over the same period (COMEAP, 1995a). In addition to carbon monoxide, nitrogen oxides and so-called 'air toxics' i.e benzene, 1,3 butadiene and formaldehyde, road vehicles have also significantly increased the levels of particle pollution, or particulates. In 1996 25% of emitted particles in the UK came from road vehicles with up to 80% recorded in London (QUARG, 1996). The risks from increasing levels of air pollution to healthy individuals are still unclear but risks to the elderly or those with pre-existing respiratory conditions such as asthma are considered more severe i.e. small changes in ventilatory function to increases in deaths among the elderly and chronically sick (COMEAP, 1998).

Particles emitted from both diesel and gasoline engines are approximately 0.05μm - 1μm in diameter and it is believed that road traffic is responsible for 4.1% of particles <2.5μm [1.1] in urban areas (Greenwood *et al*, 1996; Rickeard *et al*, 1996). These fine particles remain airborne for many days and are easily inhaled penetrating deep within the lungs and have thus become of growing concern to health. Both the character and composition of particles vary with respect to their source and airborne time therefore it is unclear whether effects on health are related to certain components or non-specific effects of inhaled particles (COMEAP, 1995b; USEPA, 1996, Verhoeff *et al*, 1996). It is these more localised effects that are difficult to quantify and a detailed understanding of the effects of air pollution on human health is an ongoing quest of government and health organisations. The following work does not endeavour to provide this detailed understanding but to demonstrates a modelling technique that could be used in the quest for this understanding.

[1.1] Particles of <2.5μm diameter, are collectively known as $PM_{2.5}$

The **aim** of the project was to investigate the feasibility of using commercially available numerical software to model and understand the dispersion of pollution in the near wake of a model vehicle. The numerical technique applied allowed the dispersion of a gaseous pollutant within the near wake of a model vehicle to be simulated without the need for limiting assumptions made in previous dispersion models (Eskridge *et al,* 1979*;* Eskridge and Hunt*,* 1979*;* Eskridge and Rao*,* 1983*,* 1986; Hider 1998). The overall **objective** was to demonstrate an alternative, accessible technique to modelling dispersion behind a road vehicle that could be easily implemented, does not use limiting assumptions of previous methods and could be used to understand in more detail the dispersion character in the near wake of a model vehicle. The project aim and objective were realised through a series of experimental and computational studies figure 1.1.

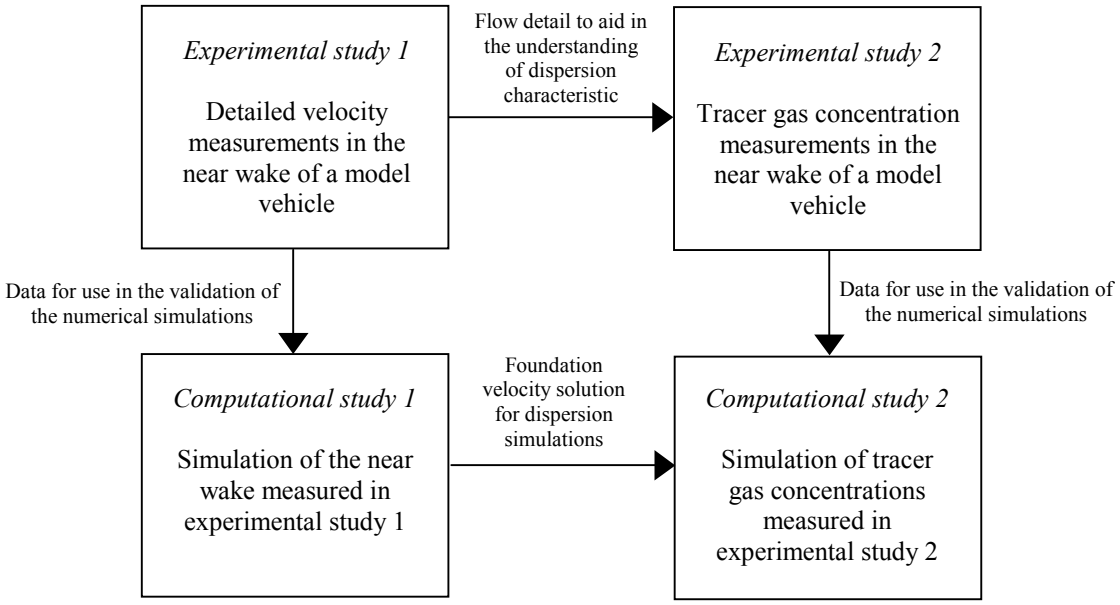

Figure 1.1 – Overall project strategy

It is imperative to recognise the importance of the individual stages in the study that were necessary to achieve the overall project aim, refer to figure 1.1. It was for this reason that care was taken in detailing and assessing each stage of the study in order to determine its relative success before continuing to the next stage.

The experimental studies were conducted essentially to provide data for the validation of the numerical simulations but also provided insight into the near wake and dispersion character of the model vehicle considered.

The application of CFD for such dispersion modelling was new therefore the study was an initial investigation into the application concentrating on obtaining an agreeable solution as opposed to the development of a tuned dispersion model. As a feasibility study the technique was demonstrated using simple examples with no changes to modelling parameters in both determining the scalar and underlying velocity fields. Modelling techniques where the only basic parameters need be defined potentially make the technique accessible to relatively inexperienced users.

Only the dispersion of a gaseous pollutant was considered in the study because the small particles also emitted by vehicles of a size that may be considered to behave like a gas.

The primary characteristics of the near wake of a road vehicle including both time-averaged and time-dependent flows are introduced in chapter 2 with a brief discussion on previous vehicle wake dispersion modelling techniques making their limiting assumptions in relation to the current modelling technique applied (section 2.4 and 2.5). Chapter 3 introduces the basic principles and methods used in the numerical technique applied i.e. Computational Fluid Dynamics (CFD). The principles of numerical discretisation, differencing schemes applied and descriptions of each turbulence model used are given in sections 3.3 and 3.4 respectively.

The experimental studies conducted to obtained data for the validation are discussed in chapters 4 and 5, chapter 4 detailing velocity measurements using hot-wire anemometry and Particle Image Velocimetry (PIV) and chapter 5 concentration measurements using a flame ionisation detector (FID). The results from two flow visualisation studies conducted to obtain additional information into the characteristics of the velocity fields are also discussed. Spectral methods were used to analyse the unsteady characteristics of the near wake and dispersion field from the measured data (section 5.6).

The numerical simulations of the measured velocity and dispersion fields using STAR-CD are detailed in chapter 6 and 7 respectively. The performances of different turbulence models, differencing schemes used in the prediction of the near wake flow field are assessed (sections 6.3, 6.4 and 6.5) with comprehensive validation using the techniques described in section 3.5. The "best" solution was put forward as the foundation for the dispersion simulations. The effectiveness of the technique used to simulate the dispersion field was assessed by comparing numerical results with measured data and applying the rigorous validation techniques described in section 3.5. The applicability of the method was also assessed through examining the influence of vehicle speed, exhaust mass flow rate on the numerical results (section 7.3). The passive technique of particle tracking was used to visualise the trajectory of mass-less particles demonstrating another way of visualising a predicted velocity and dispersion field. This technique was not used to model the particle pollution but visualise the path of a mass-less particle using the existing velocity field to gain further insight into the dispersion character within the near wake recirculation region. Additional insight into the dispersion character of the recirculation region was also obtained showing the influence pollutant release point on the subsequent dispersion, in this case the trajectory of a mass-less particle.

Chapter 8 sets out the main findings and conclusions of the study detailed in chapters 4-7. The overall achievements of the project are also discussed commenting on the success in meeting the stated project aim and objective. Recommendations for further work are made.

Chapter 2: The near wake of a road vehicle

2.1 Introduction

The primary aim of this chapter is to introduce the reader to the key elements in the formation of the near wake flow behind a road vehicle, information which later aids in the discussion of results from both the experimental and numerical studies. Both time-dependent and time-averaged near wake flow characteristics are discussed, section 2.2.1 and 2.2.2 respectively. There is a brief discussion on previous vehicle wake dispersion modelling techniques making clear their limiting assumptions in relation to the current modelling technique applied (section 2.4). It was not within the scope of the current project to make any changes to the theories discussed.

2.2 The wake

Consider a simple vehicle-like shape moving through undisturbed air figure 2.1. The velocity far ahead of the body U_∞, is undisturbed. As the body moves forward through the air the flow separates from the blunted rear end resulting in a velocity deficit behind the body that extends many body lengths downstream.

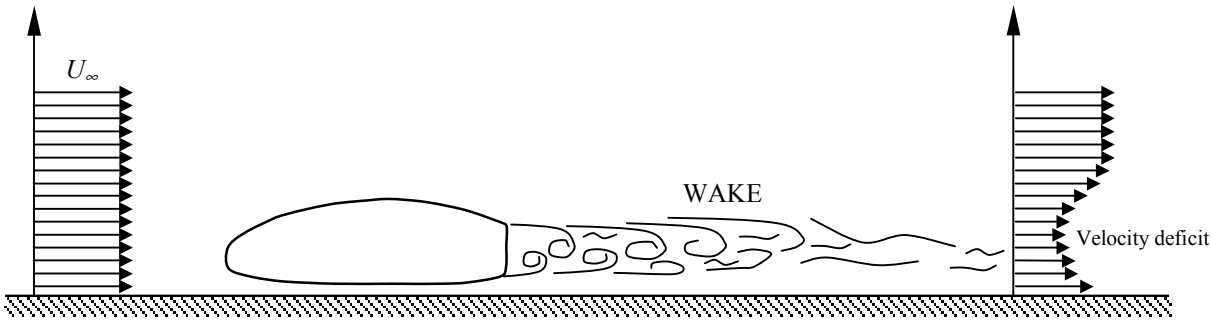

Figure 2.1 – The wake of a simple vehicle-like shape (Katz, 1995)

This region of flow separation is more commonly known as the **wake**. The wake may generally be divided into two distinct regions: the near wake and the far wake. The near wake is the region of separation closest behind the body and for a road vehicle is characterised by both a region of recirculation and the formation of a pair

of streamwise longitudinal vortices. The far wake is an area of general turbulence downstream of the near wake, which has no discernable flow structure. Figure 2.2 shows clearly the definition of these two regions.

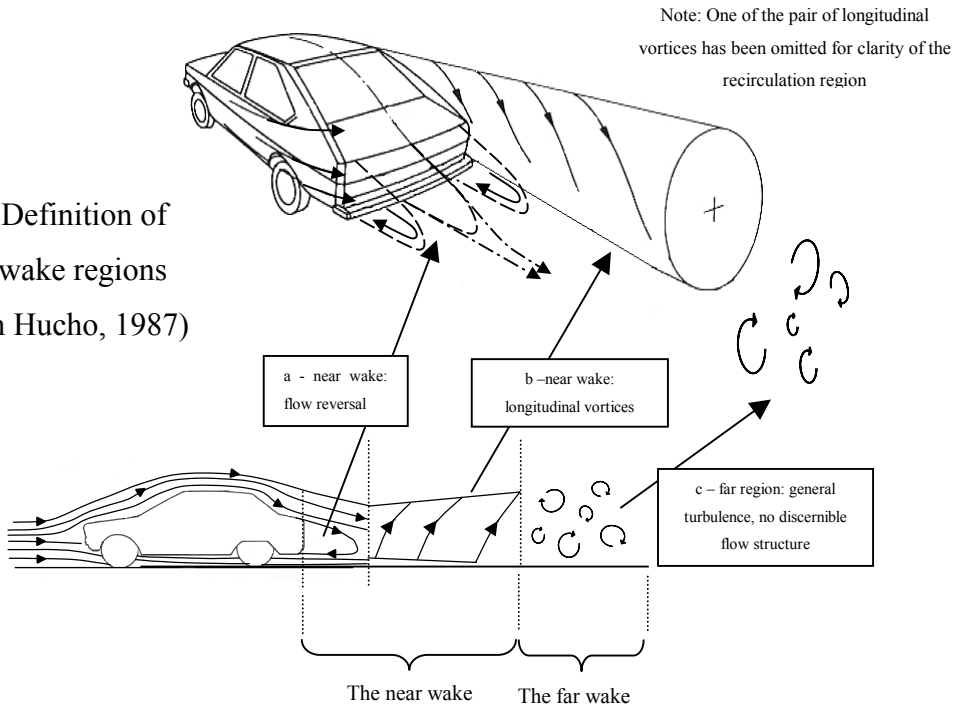

Figure 2.2 – Definition of near and far wake regions (Adapted from Hucho, 1987)

The main focus of the current study is the dispersion of a pollutant within the near wake of a road vehicle therefore the following sections focus on the formation and character of the near wake only. Both the time-averaged and time-dependent characteristics are considered.

While the flow field around a road vehicle is predominantly streamlined upstream of the wake flow, regions of local disturbance do occur as a result of features such as wing mirrors, a sunroof and underbody roughness. The model vehicle used in the current study was a simplified shape free of all appendages with a smooth underside therefore the following section only focuses on the main features of the near wake flow field. For more detailed discussions on road vehicle aerodynamics refer to Hucho (1998). In addition no wind was assumed i.e. the vehicle has the same velocity with respect to the ground as it does with respect to the air.

2.2.1 The near wake; time-averaged flow characteristics

Figure 2.3 shows a schematic of the near wake flow of a simplified vehicle shape (Ahmed *et al*, 1984).

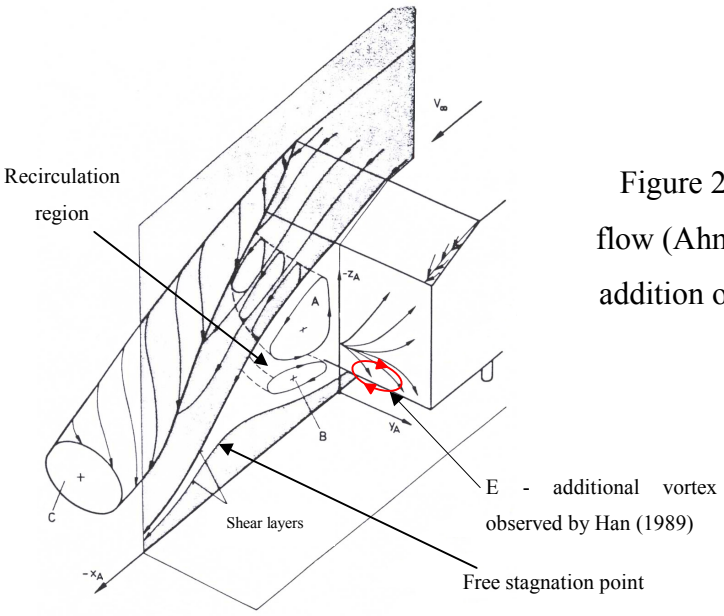

Figure 2.3 –Schematic of wake flow (Ahmed *et al*, 1984), with the addition of the vortex observed by Han (1989).

Separation occurs at the blunt edges of the body to form a recirculation region that is bounded by shear layers, figure 2.3. These shear layers grow downstream from the point of separation and are drawn together aft the recirculation region at a point known as the free stagnation point. The location of the time-averaged free stagnation point is given by the local minimum of the non-dimensionalised local mean velocity $\overline{u}/U_\infty$ where $\overline{u}$ is the local mean streamwise velocity and U_∞ is the free stream velocity (Duell and George, 1999). An important feature of the near wake is the near wake recirculation length, which is defined as the distance between the base of the body and the mean location of the free stagnation point.

The recirculation region is characterised by two small inner vortices, A and B in figure 2.3, which form as the inner part of shear layers roll-up from the upper and lower edges of the vehicle base. While Ahmed *et al* (1984) could show no clear indication of whether these flow regions ended on the body base the bound legs of these vortices were seen to be approximately parallel to the base surface, the trailing leg of the upper vortex A being aligned with the onset flow and merging with vortex

C coming from the base slant edge. The shear layer separating at the side edges of the base was observed to split with part of the flow being drawn upwards into vortex A and C, and the rest flowing downwards into vortex B, indicated by streamlines on the base in figure 2.3. Another study by Han (1989) showed the presence of another recirculating flow region E, which is generated from the left and right edges of the flat vertical base. These might be induced by the cross flow at the base that was observed by Ahmed and his colleagues due to the separation of the shear layer at the edges of the base.

The relative size of the two inner vortices is dependent on the geometry of the vehicle upstream of the blunt base edge (Howell, 1975; Morel, 1978,1980; Ahmed and Baurmet, 1979; Ahmed, 1981,1983; Ahmed *et al,* 1984). There are essentially three different vehicle configurations; the squareback, the fastback and the notchback. These geometries differ primarily in the angle of the slanted rear window (to be known as rear base slant angle) with the squareback essentially a fastback with a zero angle of base slant and the notchback a fastback with a boot lid. The sketches presented in figure 2.4 show the difference between these configurations.

Squareback Fastback Notchback

Figure 2.4 – The three basic vehicle geometries
(taken from Ahmed and Baumert, 1979)

Figure 2.5 shows the influence of the rear end geometry i.e. the rear base slant angle α, on the flow structure within the near wake recirculation region. The model vehicle used in the current was a fastback type with rear base slant angle of 23°.

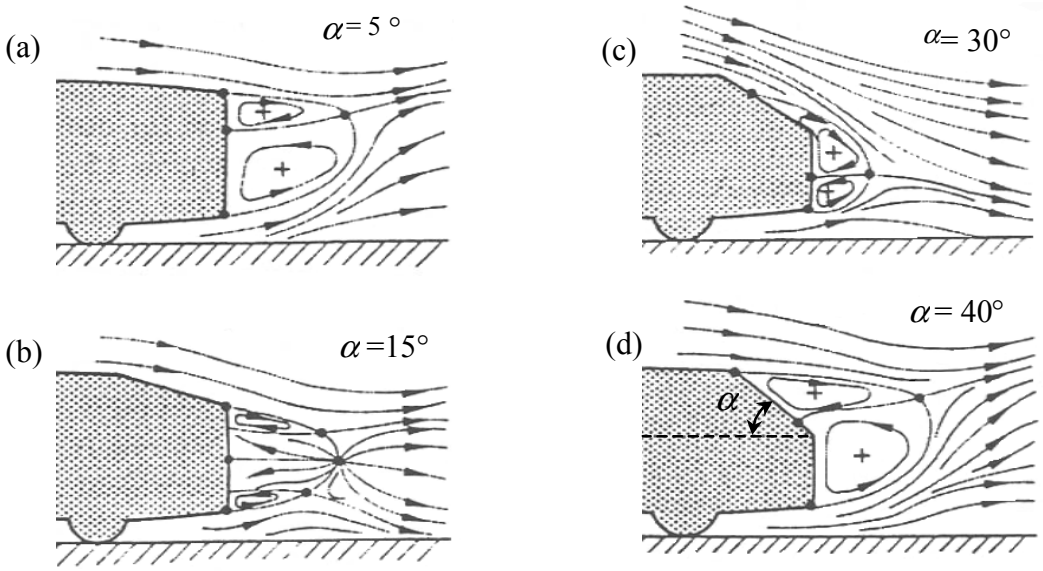

Figure 2.5 - Streamline flow pattern in the wake centreline for different base slant angles, α observed using flow visualisation (Ahmed, 1983)

The other important feature of the near wake flow of a road vehicle is the formation of a pair of streamwise longitudinal vortices, figure 2.2. These vortices form when air is forced to flow, at an angle, around a slanted blunt edge. A static pressure difference exists between the underside and the roof of a vehicle, which induces a cross-flow on the underside resulting in an upward flow around the lower edges and along both sides of the vehicle. Towards the rear of the road vehicle this air is forced to flow around blunt edges known as C-pillars, causing the air to rolling up into cone-shape streamwise vortices figure 2.6a.

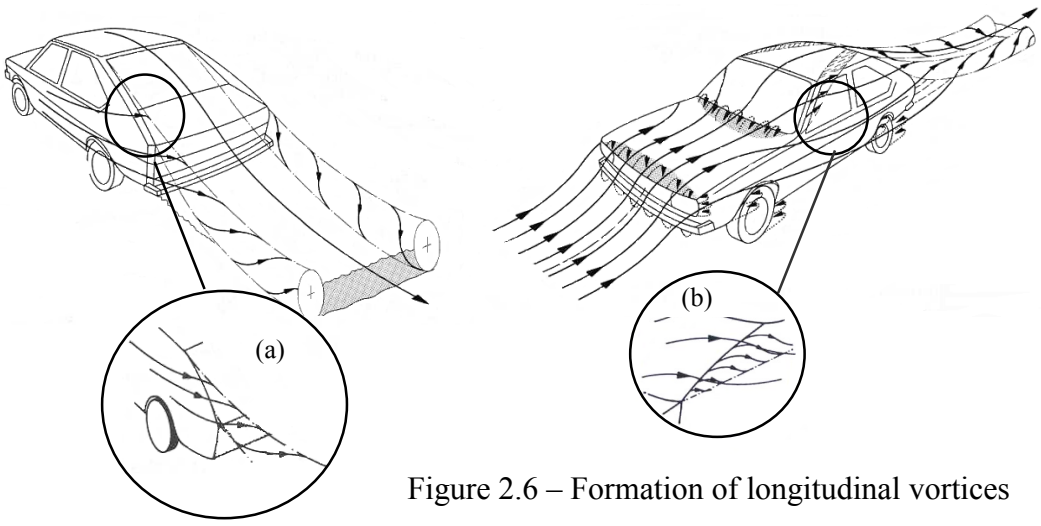

Figure 2.6 – Formation of longitudinal vortices (adapted from Scibor-Rylski, 1984)

These vortices grow in size with distance downstream but eventually decay to general turbulence in the far wake and are easily observed when leaves and dust are picked up by a passing vehicle and swirled along the road behind it. A contribution to these vortices also comes from further upstream where flow around the edges of the windscreen, the A-pillars, result in the formation of two additional but a smaller longitudinal vortex, figure 2.6b. The size and strength of these additional vortices are influenced by the angle of the windscreen.

The initial development of the longitudinal vortices is complicated by the presence of the recirculation region. But in general the size and strength of the vortex pair are dependent on the angle of the slanted rear window i.e. the rear base slant angle α and the aerodynamic pressure difference between the upper and lower surfaces of the vehicle. Also the size and strength of the internal vortices are dependent on α therefore the existence of these two flow structures are both dependent on the value of α and as Ahmed and his colleagues observed the two flows are highly dependent on each other (Morel, 1978, 1980, Ahmed *et al*, 1983). Referring to figure 2.3 the strength of the inner vortex A is dependent on the strength of vortex C but the strength of vortex B is also influenced by vortex A and so is also indirectly influenced by the longitudinal vortex C. For road vehicle with little or no base slant i.e. a squareback a region recirculation is the dominant feature because there are no slanted edges around which a longitudinal vortex may form. But as the angle of base slant increases longitudinal vortices begin to develop and the two flow structures coexist (figure 2.5 c-d). The developing vortex pair becomes stronger as the base slant angle increases and become dominant over the two vortices within the recirculation region. The longitudinal vortices are most influential between the angles of 10 and 30° (Morel, 1978). The model used in the current study α = 23° and so it would be expected to see a near wake structure similar to that illustrated for the 30° angle of base slant figure 2.5c, with longitudinal vortices developing from the base slant edge.

2.2.2 The near wake: time-dependent flow characteristics

Three basic vehicle geometries were defined in figure 2.4; the squareback, fastback and the notchback. While the vehicle geometry used in the current study was a fastback the time-dependent characteristics of both the fastback and squareback are discussed. The unsteady wake characteristics of a fastback and squareback vehicle are significantly different and therefore the following discussion is aimed at helping the reader understand the basic principles of the unsteady characteristics of vehicle wakes.

The time-dependent near wake of a squareback geometry is characterised by shedding from both sides of the base with periodic fluctuations in the wake recirculation length, a behaviour also observed behind axisymmetric bluff bodies such as spheres and discs (Howell, 1975; Fuchs *et al*, 1979; Berger *et al*, 1990; Duell and George, 1992,1999). Duell and George (1992,1999) showed that for a simple squareback shape vortices were shed from the separation point into the shear layer enclosing the recirculation region, figure 2.7a.

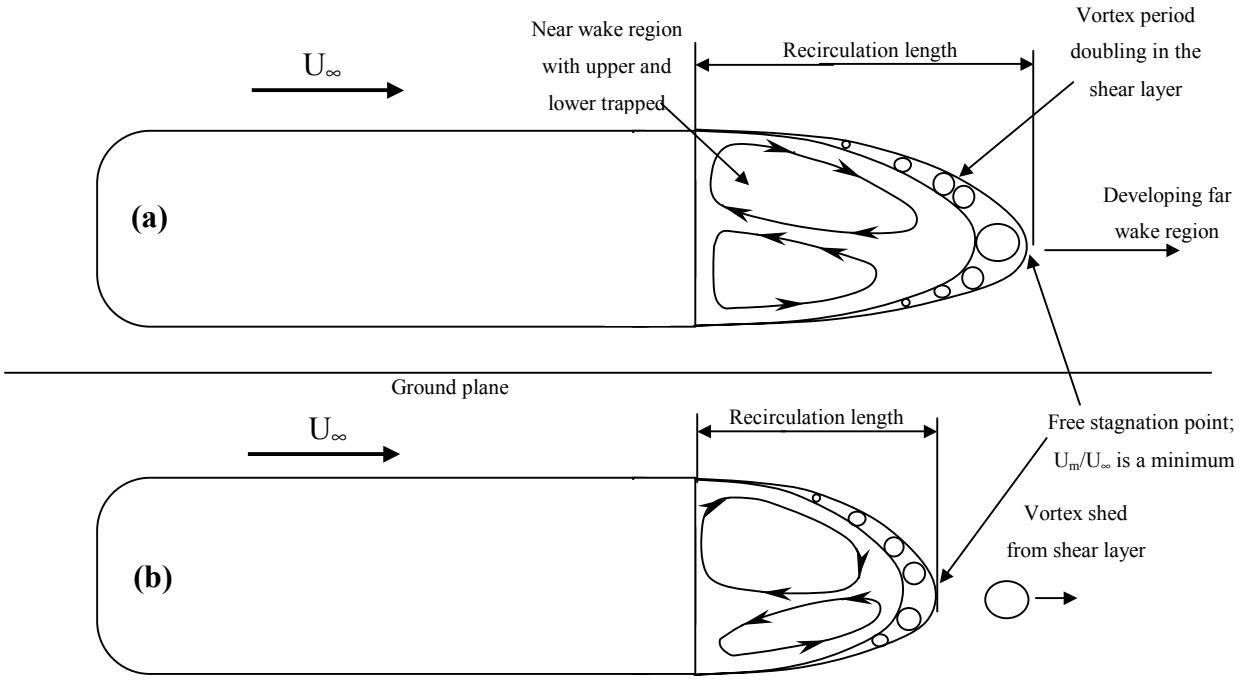

Figure 2.7 –Schematic of mean near wake recirculation region at two successive times. The growth of eddies in the shear layer and eventual vortex shedding, resulting in the free stagnation point moving (Duell and George, 1999).

The amount of fluid within the recirculation region increases as fluid is entrained and vortices are shed. Eventually the region becomes unstable, at which point a vortex is shed from the free stagnation point, figure 2.7b. Vortex shedding from the free stagnation point causes it to moves closer to the body thus reducing the size of the near wake. The frequency at which this shedding occurs is defined as the 'pumping frequency' and may be used to determine the unsteadiness of the recirculation region. The characteristic frequency of vortex shedding or pumping frequency was measured at 0.069**S**. Refer forward to section 5.5.1 and equation 5.8 for definition of Strouhal number.

Figure 2.4 shows that the fundamental difference between the squareback geometry and the fastback geometries is the slanted rear surface. The slanted rear surface results in a faster approach flow to rear of the vehicle and thus different time-dependent flow characteristics. The longitudinal vortices that emanate from these slanted surfaces (figure 2.6) effectively eliminate shedding from the sides of the vehicle (Morel, 1978,1980; Xia and Bearman, 1983). The vortex shedding frequency from an axisymmetric body continuously tends to increase as the rear end geometry changed from a squareback to fastback i.e. a shedding frequency of 0.28**S** for a base slant angle of 10° to 0.36**S** for an angle of 40° (Xia and Bearman, 1983). The flow field tends towards more general unsteadiness at larger base slant angles. Sims-Williams *et al*, 2001 showed the near wake flow structures of both a real and idealised fastback to be less coherent and less periodic than the vortex shedding or cavity resonance of a squareback configuration with a more general unsteadiness at low frequencies.

2.3 The influence of the ground

In a study of vehicle flows the simulation of the flow close to the ground is important as the viscosity of air plays an important role in the character of the flow. As a vehicle moves through the air the boundary layer[2.1] which forms on the underside of the vehicle tends to thicken with distance along the underside depending on ground

[2.1] Viscous effects govern the flow field close to the surface of a solid body. Air near to the surface is slowed and air in contact with the surface has zero velocity i.e. no-slip condition. This retarded layer is known as a boundary layer.

clearance, Z_h, figure 2.8 (Scibor-Rylski, 1984; Hucho, 1998). Depending on the ground clearance Z_h, the boundary layer may reach the ground at some point along the underside. If this occurs then the mass of air aft this point is forced to travel with the vehicle sliding along the ground resulting in the formation of a secondary boundary layer. The flow along the underside of the vehicle becomes complex and highly turbulent.

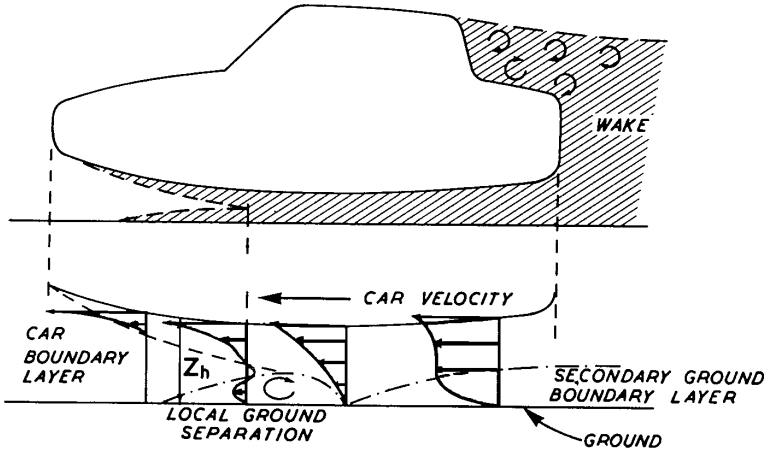

Figure 2.8 – Airflow pattern underneath a vehicle (Scibor-Rylski, 1984).

Ideally a moving floor should be used to correctly simulate the relative motion between the road and a vehicle however a stationary floor is still more often used for reasons of availability and convenience. An inherent disadvantage of this however is the unwanted build-up of the boundary layer along the stationary wind tunnel floor, which can interfere with a developing wake flow field and its measurement. A moving floor potentially draws air underneath the vehicle, which keeps the air moving discouraging boundary layer growth. The effects of using a moving ground depends on the underbody geometry, and can significantly alter the structure of the wake flow Bearman *et al* (1988) and Lajos and Hegel (1996). However Bearman *et al* (1988) also showed that for an idealised vehicle shape with a smooth flat underside there was little change in the near wake character using either a moving or fixed ground at a ground clearance of 13% vehicle height. The current study uses the same combination of a model vehicle with a smooth flat underside and a stationary floor with a ground clearance of 14% vehicle height. While the results presented by Bearman *et al* (1988) inspire confidence for the current study the inherent disadvantage of a stationary floor must not be ignored and considered where appropriate.

2.4 The limits of existing vehicle wake and dispersion modelling techniques

The most well known and documented vehicle wake theory is that of Eskridge and Hunt (1979). Based on the on a perturbation analysis of the equations of motion the theory describes the velocity field far downstream of a single vehicle moving through still air. Using the assumptions of constant vehicle velocity, flat terrain and no wind, expressions were developed for the velocity deficit far downwind of a vehicle i.e. the far wake, figure 2.2. Figure 2.9 shows a schematic of the basic modelling approach.

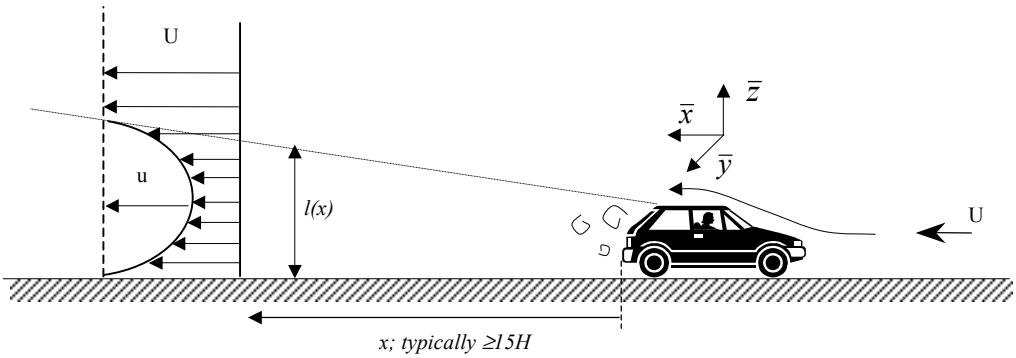

Figure 2.9 – Schematic showing model approach and co-ordinate systems
(note the co-ordinate directions denoted here are different from those used in the current study, figure 4.4)

The solution for the far wake velocity u is independent of the velocity distribution around the vehicle and determined by the distance downstream of the vehicle and the value of the couple C acting on the vehicle (Hunt, 1971). After detailed mathematical analysis[2.2] Eskridge and Hunt (1979) arrived at a solution for the far wake velocity u for $x \geq 15H$ where H is vehicle height. A more recent study by Hider (1998) saw the derivation of the same expression using a different method, the solution for u expressed as (Hider, 1998),

[2.2] It is not within the scope of this project to include the complete derivation of this theory. Full derivations maybe found in Eskridge and Hunt (1979) and Hider (1998).

$$\text{Downwake velocity} = u = \left[\frac{U^2\Lambda_1^2 C}{2\gamma^3(8\pi)^{5/2}}\right]^{1/4} x^{-3/4}\zeta \exp\left[\frac{-(\zeta^2+\eta^2)}{8}\right] \quad (2.2)$$

The couple C acting on the vehicle is used to determine the strength of the wake as opposed to the wake induced drag (Hunt, 1971). ζ and η are the scaled co-ordinates perpendicular to the downstream direction and expressed as *z/l(x)* and *y/l(x)* respectively and Λ_1 is a constant determined during the analysis. γ is a constant of the order of magnitude of von Kármán constant κ and was introduced into the analysis through the definition of eddy diffusivity coefficient, ν_T. The eddy diffusivity coefficient is used to describe the effect of turbulence and is assumed to be constant across the far wake. It is expressed as a function of the complete wake length *l(x)* and velocity *u*,

$$\nu_T(x) = \gamma l(x) u_{max}(x) \quad (2.3)$$

where u_{max} is the maximum value of u in the far wake at any distance x. Further expressions for the crosswake and vertical velocity v and w respectively were developed by Hider (1998) but are not detailed here. Hider (1998) also made further developments to the theory to include the effects of a crosswind and of a viscous sub-layer close to the ground. Nevertheless the underlying theory, originally developed by Eskridge and Hunt (1979) describes the mean velocity and its unsteady contributions as $\bar{\mathbf{u}} = [U+u, v, w]$, several vehicle heights downstream i.e. $x \geq 15H$. For an average size road vehicle $x \geq 15H$ is a significant distance and most certainly outside the near wake region discussed in the previous section therefore the theory of Eskridge and Hunt (1979) and subsequent developments by Hider (1998) only describe the velocity field far downstream. While the overall velocity deficit caused by the near wake is included in the deficit defined at $x \geq 15H$ the theory does not allow for detailed modelling of the near wake region and ignores any interaction between the longitudinal vortices and the drag induced wake. The computational techniques employed in the current study endeavour to bridge the gap left by the these theories in that it enables the simulation of the complete wake flow i.e. both the recirculation region and longitudinal vortices can be modelled in detail.

The same limitations are found in the modelling of vehicle emissions. They are wide ranging models available many of which, APARC-1A, CALINE3 and HIWAY-2 to name just a few, treat the emissions from a road vehicle as a line source and use a Gaussian approach to describe the dispersion of emissions (Dabberdt, 1973; Benson, 1979; Rao and Keene, 1980; Namdeo, 1995). This approach essentially approximates the growth of a puff or section of plume using a Gaussian function, figure 2.10.

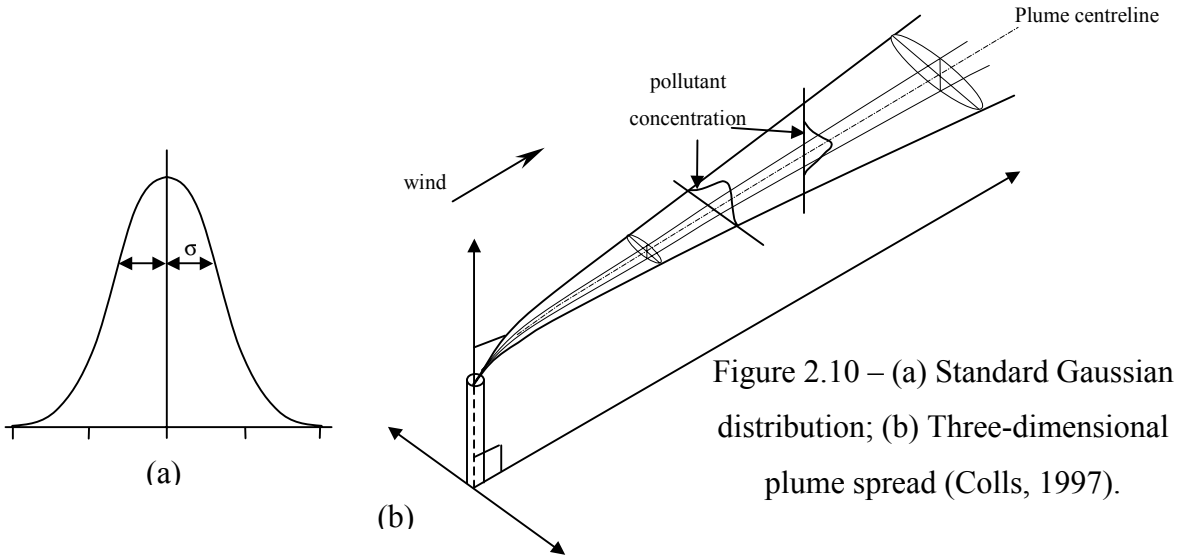

Figure 2.10 – (a) Standard Gaussian distribution; (b) Three-dimensional plume spread (Colls, 1997).

The effective source is regarded as the roadway itself and available traffic and meteorological data is used in the prediction of concentration profiles within the vicinity of these road networks. The effects of vehicle induced turbulence are generally considered through modified vertical and horizontal dispersion curves.

Dispersion models, which include a description of the vehicle wake flow, are less common and are primarily based on the wake descriptions developed by Eskridge and Hunt (1979), (Eskridge *et al*, 1979; Eskridge and Rao, 1983, 1986; Baker, 1996; Hargreaves and Baker, 1997; Hider 1998). The well known ROADWAY model uses surface similarity theory[2.3] and the wake theory of Eskridge and Hunt (1979) to determine the atmospheric structure along a roadway due to the presence of vehicles

[2.3] Similarity theory assumes the vertical spread near the source is mathematically similar to the spread of pollutant further downstream

(Eskridge *et al*, 1979; Eskridge and Rao, 1983, 1986). A conservation of species, or advection-diffusion equation is solved using finite difference approximations to obtain the concentration field along the roadway for a multi-vehicle situation. The model is essentially used to predict vertical and lateral concentrations emitted from many vehicles at any instance along a roadway.

While subsequent studies lead to further improvements of the ROADWAY (Eskridge and Rao , 1983, 1986; Eskridge and Thompson, 1982) its basis was still with the wake theory of Eskridge and Hunt (1979) describing the foundation wake flow field in terms of a velocity deficit at $x \geq 15H$. Hider (1998) conducted a similar but more detailed study using a three dimensional form of the advection–diffusion equation to model the spread of pollutant in the wake in all directions. In her work Hider uses the developed theory to make predictions of pollutant dispersal at distances closer to the vehicle i.e. $\geq 5H$. However as with the ROADWAY model the work of Hider (1998) has its foundations with the wake theory of Eskridge and Hunt (1979) and does not enable the study of the dispersion field close behind a vehicle under the direct influence of the recirculation region i.e. at $x < 2H$. Hider (1998) also looked at the mathematical modelling of particle pollution in the wake of a vehicle but as only the dispersion of a gaseous pollutant was considered in the current study details of this study are not included but may be found in Hider (1998).

The computational techniques applied to model both the near wake velocity and dispersion field enabled the dispersion of a gaseous pollutant within the complete near wake flow field to be modelled without the limiting assumption described above i.e. assuming a velocity deficit at $x \geq 15H$. The influence of both the recirculation region and longitudinal vortices on the dispersion close behind a model vehicle may be captured in detail. The dispersion models based on the wake theory of Eskridge and Hunt (1979) introduce the pollutant uniformly at the beginning of the far wake at a concentration less than source in order to generally account for any upstream dispersion as a result of the near wake. The current technique allows the pollutant to be injected at a realistic location i.e. to one side at the base of the vehicle.

Chapter 3: Basic principles of computational fluid dynamics

3.1 Introduction

The aim of this chapter is to put forward the basic principles and methods employed in computational software used in this study, namely STAR-CD V3.05. A more in-depth look at the fundamentals of computational fluid dynamics (CFD) may be found in Abbott and Basco (1989), and Versteeg and Malalasekera (1996). A description of each turbulence model used in the study is given based on the definitions within STAR-CD V3.05. The techniques used in modelling the dispersion of gaseous pollution are discussed later in Chapter 7. The chapter also includes details of the techniques used in the validation of the numerical simulations against the experimental data (section 3.5).

3.2 The equations governing fluid motion

The foundations of CFD lie with the basic equations of fluid flow. These equations must be solved in their entirety in order to obtain a full solution for the flow problem being analysed. The fundamental equations of motion for a fluid are derived from the conservation laws of physics and are based on the conservation of mass and momentum. For a laminar incompressible fluid these equations are expressed as, using tensor notation (Wilcox, 1994),

$$\frac{\partial u_i}{\partial x_i} = 0 \tag{3.1}$$

$$\rho \frac{\partial u_i}{\partial t} + \rho u_j \frac{\partial u_i}{\partial x_j} = -\frac{\partial p}{\partial x_i} + \frac{\partial}{\partial x_j}\left[\mu\left(\frac{\partial u_i}{\partial x_j} + \frac{\partial u_j}{\partial x_i}\right)\right] \tag{3.2}$$

where i = 1,2,and 3 corresponding to the x, y and z-directions respectively and p is pressure, μ is fluid viscosity and ρ is fluid density.

Equation (3.1) and (3.2) are the instantaneous continuity and Navier-Stokes equations respectively but may only used to solve for simple flows. To solve for turbulent flows the effects of turbulence must be included. The most common approach, and that employed in the current study is the use of time-averages of the Navier-Stokes equations, often referred to as Reynolds averaged Navier-Stokes equations (RANS). Only the basic principles of this approach are to be discussed, for more detail refer to Abbott and Basco (1989), Wilcox (1994) and Versteeg and Malalasekera (1996).

From equation (3.2) it is assumed that each instantaneous variable may be expressed as the sum of its mean, X and fluctuating, x' components i.e. for u

$$u = U + u' \tag{3.3}$$

Substituting equations (3.5) into (3.3) and integrating over time the time-averaged continuity and Navier-Stokes equations are obtained (Wilcox, 1994),

$$\rho \frac{\partial U_i}{\partial t} + \rho U_j \frac{\partial U_i}{\partial x_j} = -\frac{\partial P}{\partial x_i} + \frac{\partial}{\partial x_i}\left[\mu\left(\frac{\partial U_i}{\partial x_j} + \frac{\partial U_j}{\partial x_i}\right) - \overline{\rho u_j' u_i'}\right] \tag{3.4}$$

$$\frac{\partial U_i}{\partial x_i} = 0 \tag{3.5}$$

This process introduces new terms into the Navier-stokes equations, known as Reynolds stresses, which constitute the convective momentum transfer due to velocity fluctuations. These additional expressions cause problems when solving for turbulent flows in that the disparity in number of unknowns and number of equations makes the direct solution of any turbulent flow problem impossible using this formulation. Modelling the turbulence and expressing the unknown variable in terms of known variables such that the number of unknowns is reduced to the number of equations solves the "closure problem". The modelling of turbulence in discussed in section 3.4.

These governing equations of fluid motion cannot be solved directly therefore a technique known as numerical discretisation is employed to find an approximate solution.

3.3 Numerical discretisation

Three of the major numerical discretisation techniques are the finite difference, finite element and finite volume methods. The technique employed by STAR-CD V3.05, is the finite volume method and the only discussed here. For detail of additional techniques refer to Versteeg and Malalasekera, (1995), Computational Dynamics (1998a) and (Shaw, 1992). The finite volume method is the best established of differencing schemes and involves several stages;

1. The solution domain is sub-divided into a finite number of control volumes.
2. The fluid flow governing equations are formally integrated over each finite control volume in the solution domain.
3. Finite difference type approximations representing flow processes such as convection, diffusion and sources are substituted for the terms in the integrated governing equations. The integrated governing equations are thus transformed into a system of algebraic equations.
4. The system of algebraic equations is solved using iterative methods.

Step 3 uses differencing schemes to obtain expressions for the transported variables at the control volume faces and convective and diffusive fluxes across its boundaries.

3.3.1 Differencing schemes

The differencing schemes described here are only those used in the current study. Consider the one-dimensional control volume (CV) with flow variable ϕ where P is a node at the centre of the CV and W and E are the nodes to the West and East of P respectively. The sides of the CV are identified by w and e, the west side and east side CV faces respectively.

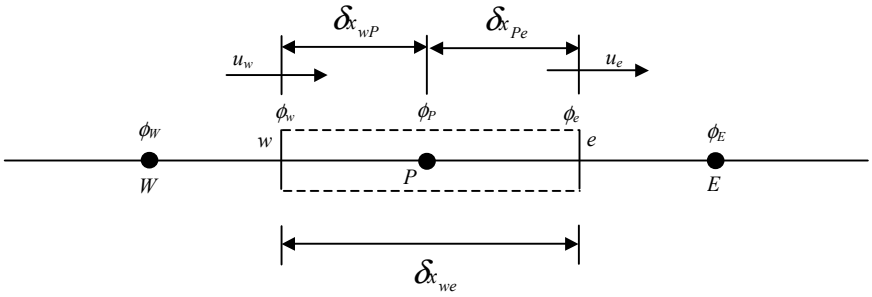

Figure 3.1 – One dimensional control volume around node *P*
(adapted from Versteeg and Malalasekera, 1995),

If the number of cells or CVs within a computational domain were infinitely large irrespective of the differencing method, in theory, it would be possible to obtain numerical results that are almost synonymous with the 'exact' solution. However in practical calculations only a finite number are used resulting in numerical results that are only physically realistic when a differencing scheme has certain fundamental properties: conservativeness, boundedness and transportiveness (Versteeg and Malalasekera, 1995). A differencing scheme is conservative when it obeys all the conservation laws of physics ensuring the conservation of the fluid property ϕ locally for each individual CV and globally for the computational domain. Boundedness is achieved when the solution to a flow problem is bounded by the maximum and minimum boundary values of the flow variables. Physically non-negative quantities such as density and turbulent kinetic energy must always be positive. Differencing schemes that do not possess boundedness produce unbounded solutions resulting in numerical instabilities i.e. under- and over-shoots. To possess transportiveness a differencing scheme must allow for changes in the relative strength of convection and diffusion adjusting the bias towards the upstream (*W*) and downstream (*E*) nodes as appropriate refer to figure 3.1.

3.3.1.1 Upwind differencing (UD)

Upwind differencing (UD) is a first order accurate scheme i.e. terms of second order and higher of the Taylor series expansion are truncated (Versteeg and Malalasekera, 1995). The terms omitted are known as the truncation error or discretisation error i.e. errors due to neglecting these terms. However this is also seen as a measure of

accuracy of the approximation and is why first order accurate schemes are less accurate than second or third order accurate schemes.

The UD scheme takes account of flow direction (transportiveness) and is suited to strongly convected flows. With reference to figure 3.1 the value of ϕ at the east face of the control volume or upwind of P may be expressed as

$$\phi_e = \begin{cases} \phi_E & \text{if } u_e < 0 \\ \phi_P & \text{if } u_e > 0 \end{cases} \tag{3.6}$$

Upwind differencing produces generally stable solutions that are expected to obey their physical bounds i.e. boundedness. However such schemes sometimes give rise to the smearing of gradients commonly known as numerical diffusion i.e. sharp peaks or rapid variations in flow variables are smoothed out.

3.3.1.2 Linear upwind differencing (LUD)

The linear upwind differencing scheme (LUD) is a second order accurate scheme specific to STAR-CD V3.05, based on the scheme of Wilkes and Thompson (1983). Details of the scheme are therefore limited. However using Wilkes and Thompson (1983) a finite difference approximation for the gradient of ϕ at a point in terms of two of its upwind neighbours is expressed as

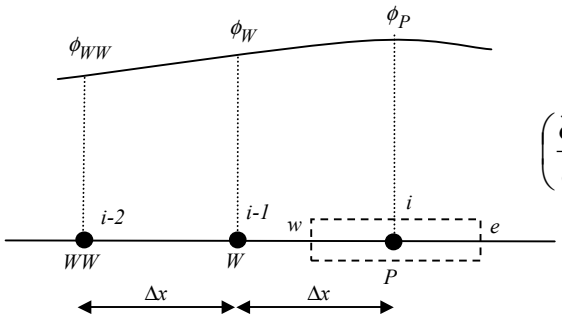

$$\left(\frac{\partial \phi}{\partial x}\right)_p \cong \frac{3}{2}\Delta x\phi_P - 2\Delta x\phi_W + \frac{1}{2}\phi_{WW} \tag{3.7}$$

The LUD scheme generally produces less numerical diffusion than the UD scheme through preserving steep gradients but as a result causes some numerical instability and on occasion unbounded solutions. In addition the LUD scheme may be blended

with the UD scheme to suppress numerical instabilities. A user specified blending factor $\gamma$is applied to the convective terms (Computational Dynamics, 1998a),

$$C_j^{BD} = \gamma C_j^{LUD} + (1-\gamma) C^{UD}_j \tag{3.8}$$

3.3.1.3 Monotone advection and reconstruction scheme (MARS)

The Monotone Advection and Reconstruction Scheme (MARS) is unique to STAR-CD V3.05 therefore detail of the scheme is very limited but it is defined as a multi-dimensional second order accurate scheme that operates in two separate steps, reconstruction and advection (Computational Dynamics, 1998a). In order to describe the principles behind the scheme other literature was consulted (Van Leer, 1977; Zalesak, 1979; Shyy, 1994).

The reconstruction stage of the MARS scheme combines the properties of TVD (total variation diminishing) and monotone schemes. Applying a purely monotonic condition (first order accurate) would lead to a loss in accuracy as sharp gradients are suppressed i.e. numerical diffusion, but using higher order schemes would result in spurious oscillations and unbounded solutions. A compromise is therefore found by combining the strong condition of monotonicity with a weaker condition that says the '*total variation'* of the numerical scheme is bounded i.e. TVD scheme requires that the total variation of the numerical scheme should not increase with time. This allows schemes with higher order of accuracy to be designed to achieve better accuracy than that achieved by monotone schemes alone while at the same time allowing for a stable solution (Shyy, 1994).

The advection stage may be likened to a technique known as Flux Corrected Transport (FCT) (Boris and Book, 1973). It essentially 'constructs' the transportive flux point by point (non-linearly) as a weighted average of flux computed by both a low and high order scheme. The weighting is done in such a way to ensure the higher order flux is used to the greatest extent possible without introducing numerical instability. For MARS this weighting is achieved by altering the 'compression level' value between 0 and 1. A higher compression level gives a

better resolution but increases computational effort. In comparison to UD, CD and LUD the MARS scheme offers the least sensitivity to mesh structure and skewness.

3.3.2 Solution Algorithm

The different solution algorithms available within STAR-CD V3.05 are PISO, SIMPISO and SIMPLE (Computational Dynamics, 1998a). The SIMPLE (Semi-Implicit Method for Pressure-Linked Equations) method, developed by Patankar and Spalding (1972), was employed for the current study and essentially solves algebraic equation sets by iterative means and is a guess and correct procedure. The stages of SIMPLE are shown in figure 3.2. For more detailed refer to Versteeg and Malalasekera (1995) and Computational Dynamics (1998a).

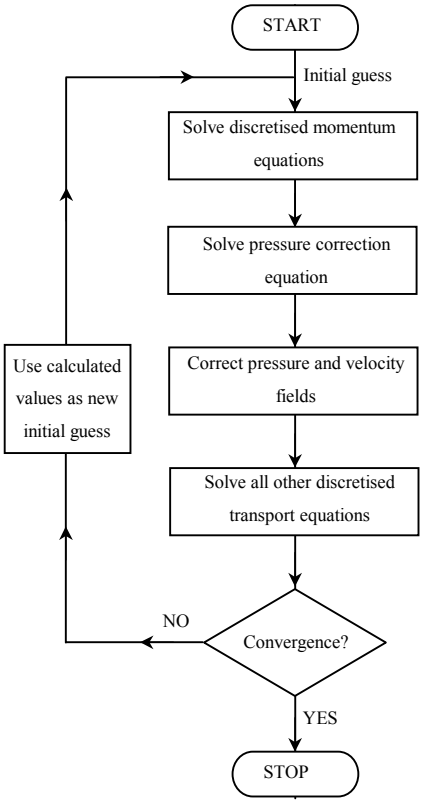

Figure 3.2 – Fundamental stages in the SIMPLE algorithm (source Versteeg and Malalasekera, 1995).

Convergence is achieved when the solution at the *k*th iteration is equal to the discretised solution. If convergence is not achieved the predicted velocities and pressure are returned as an initial guess and the process starts again. STAR-CD V3.05 uses the normalised absolute residual sum R_ϕ^k to monitor overall solution progress where (Computational Dynamics, 1998a),

$$R_\phi^k \equiv \frac{\sum \left| r_\phi^k \right|}{M_\phi} \qquad \text{(summed over all grid cells)} \qquad (3.9)$$

M_ϕ is a normalisation factor evaluated internally and r_ϕ is the residual of flow variable ϕ, at a particular grid location, at iteration k and is the imbalance in the finite volume transport equations arising from an incomplete solution. R_ϕ^k is used to terminate the solution when an accepted level of convergence is achieved i.e. R_ϕ^k falls below a user prescribed value λ typically of the order 10^{-3}.

Instabilities in a solution are observed when residuals fluctuate continually or begin to rapidly increase causing the solution to diverge. To avoid numerical instability an under-relaxation is introduced in the form of a weighted mean. If the iteration number is k the solution of variable ϕ at k, ϕ^k is taken as the weighted mean of the previous value ϕ^{k-1} and the (provisional) current one ϕ^{k*} where α_ϕ is the under-relaxation factor (Computational Dynamics, 1998a),

$$\phi^k = \alpha_\phi \phi^{k*} + (1-\alpha_\phi)\phi^{k-1} \qquad (0 \le \alpha_\phi \le 1) \qquad (3.10)$$

3.4 Modelling turbulence

The following section describes the basic principles of the turbulence models used in the current study and are defined based on the definitions within STAR-CD V3.05 (Computational Dynamics, 1998a).

Most turbulence models, including those to be described rely on the presumption that there exists an analogy between the action of Reynolds stresses and viscous stresses on the mean flow. Proposed by Boussinesq in 1877, the Boussinesq assumption is commonly used to relate the Reynolds stresses, τ_{ij} to the mean strains through the turbulent or eddy viscosity μ_t. Within STAR-CD V3.05 the turbulent Reynolds stresses and scalar fluxes are linked to the ensemble average flow properties through the same assumption expressed as (Computational Dynamics, 1998a),

$$-\overline{\rho u_i' u_j'} = 2\mu_t s_{ij} - \frac{2}{3}\left(\mu_t \frac{\partial u_k}{\partial x_k} + \rho k\right)\delta_{ij} \tag{3.11}$$

The turbulent kinetic energy k is defined as $k \equiv \frac{1}{2}\overline{u_i' u_i'}$, s_{ij} is the rate of strain tensor and δ_{ij} is the Kronecker delta which equals 1 if $i = j$ and 0 if $i \neq j$. ρ is the fluid density. The turbulence length scale ℓ, k and ε the turbulent dissipation are related by (Computational Dynamics, 1998a),

$$\ell = C_\mu^{3/4} \frac{k^{3/2}}{\varepsilon} \tag{3.12}$$

where C_μ is an empirical coefficient. The turbulent viscosity μ_t is related to k and ε through (Computational Dynamics, 1998a),

$$\mu_t = f_\mu \frac{C_\mu \rho k^2}{\varepsilon} \tag{3.13}$$

f_μ is a coefficient. The turbulence models used in this study are all variants of the two-equation standard k-ε model, which solve two transport equations for the turbulence quantities k and ε, in order to obtain closure and find a solution to the flow problem. The variants used were the non-linear (quadratic) k-ε model (Launder and Spalding, 1974; Rodi, 1979), the RNG k-ε model (Yakhot *et al*, 1992) and Chen's k-ε model (Chen and Kim, 1987). The standard k-ε model was used as a benchmark for the other three models used. For more detail discussion on the principles of turbulence modelling refer to Wilcox (1994) and Versteeg and Malalasekera (1995).

3.4.1 The standard k-ε model

The standard k-ε model, developed by Launder and Spalding (1974) is one of the most widely used of turbulence models. For fully turbulent compressible or

incompressible isothermal flows the model equations for the turbulent kinetic energy and the turbulent dissipation rate are (Computational Dynamics, 1998a):

Turbulent kinetic energy;

$$\frac{1}{\sqrt{g}}\frac{\partial}{\partial t}\left(\sqrt{g}\,\rho k\right)+\frac{\partial}{\partial x_j}\left(\rho\tilde{u}_j\,k-\frac{\mu_{eff}}{\sigma_k}\frac{\partial k}{\partial x_j}\right)=\mu_t\left(2s_{ij}\frac{\partial u_i}{\partial x_j}+P_B\right)-\rho\varepsilon-\frac{2}{3}\left(\mu_t\frac{\partial u_i}{\partial x_i}+\rho k\right)\frac{\partial u_i}{\partial x_i} \tag{3.14}$$

μ_{eff} is the effective viscosity, $\tilde{u}_j$ is the relative velocity between the fluid, u_j and local (moving) co-ordinate frame with velocity u_{cj}. $\sqrt{g}$ is the determinant of metric tensor. The third term on the right-hand side represents amplification and attenuation due to compressibility effects. P_B is the turbulence generation due to buoyancy forces. The flow field under consideration in this study was isothermal and incompressible therefore effects due to buoyancy and compressibility were not included.

Turbulence dissipation rate;

$$\frac{1}{\sqrt{g}}\frac{\partial}{\partial t}\left(\sqrt{g}\,\rho\varepsilon\right)+\frac{\partial}{\partial x_j}\left(\rho\tilde{u}_j\,\varepsilon-\frac{\mu_{eff}}{\sigma_\varepsilon}\frac{\partial\varepsilon}{\partial x_j}\right)=\frac{\varepsilon}{k}\left[\left(C_{\varepsilon1}2s_{ij}\frac{\partial u_i}{\partial x_j}+C_{\varepsilon3}P_B\right)-\frac{2}{3}\left(\mu_t\frac{\partial u_i}{\partial x_i}+\rho k\right)\frac{\partial u_i}{\partial x_i}\right]$$
$$-C_{\varepsilon2}\,\rho\frac{\varepsilon^2}{k}+C_{\varepsilon4}\,\rho\varepsilon\frac{\partial u_i}{\partial x_i} \tag{3.15}$$

The empirical coefficients σ_ε, σ_k, are the Prandtl numbers which relate the diffusivities of k and ε to the eddy viscosity μ_t. The value of these coefficients and C_μ, $C_{\varepsilon1}$, $C_{\varepsilon2}$, $C_{\varepsilon3}$, and $C_{\varepsilon4}$ are given in Table A1-1, Appendix 1. It is assumed, in equation (3.14) that the production and destruction terms are proportional to the equivalent production and destruction terms in equation (3.15). This ensures that if the production of k increases rapidly then the dissipation rate increases accordingly.

Conversely the formulation also ensures that ε decreases at a fast enough rate so as to avoid non-physical values of k.

As one of the most widely used and validated turbulence models, standard k-ε is an adequate foundation for any flow study with successes in a variety of free shear, boundary layer and simple turbulent flows (Launder *et al,* 1972; Launder and Spalding, 1974; Sarkar *et al*, 1997). However, it is well known that the standard k-ε model can give rise to highly inaccurate predictions of the normal Reynolds stresses $\overline{u'u'}$, $\overline{v'v'}$ and $\overline{w'w'}$. The model predicts the normal Reynolds stresses in a fully developed turbulent channel flow to be equal (Speziale, 1987) where in reality for fully separated flows $\overline{u'u'} \neq \overline{v'v'} \neq \overline{w'w'}$. This occurs because the applied formulation of the Boussinesq assumption, equation (3.11), uses an isotropic assumption for the normal Reynolds stresses assigning an equal third to each of normal components with viscosity assumed equal in all directions. This simple assumption is insufficient to adequately describe the complexity of a highly anistropic flow field therefore the standard k-ε model generally performs poorly for flows in which the normal Reynolds stresses play an important role in describing the flow e.g. recirculating and secondary flows. In particular the standard k-ε model tends to under predict the separation length over a backward facing step (Speziale, 1987; Thangam and Hur, 1991). However the standard k-ε model has shown reasonable agreement in the prediction of vehicle wakes (Williams *et al*, 1994; Basara *et al*, 1996). In high Reynolds numbers flows the standard k-ε does not apply close to a wall where viscous effects dominate. Instead the model employs the universal behaviour of near wall flows, wall functions. All of the turbulence models applied here use these functions, which are briefly described below.

3.4.1.1 Wall functions

The behaviour of a fluid flow close to a wall is significantly different from that in a free stream flow. Far from the wall inertia forces dominate but closer to the wall viscous effects govern the flow i.e. air near to the wall is slowed and air in contact with the wall has zero velocity, the fluid fulfils a 'no-slip' condition. High Reynolds number models such as those used here are not valid in this region because molecular

and turbulence effects are comparable in magnitude. Special algebraic formulae known as wall functions are applied to represent the distribution of velocity within this region (Computational Dynamics, 1998a),

$$u^+ = \begin{cases} y^+ & , y^+ \le y_m^+ \\ \frac{1}{\kappa}\ln(Ey^+) & , y^+ > y_m^+ \end{cases} \qquad (3.16)$$

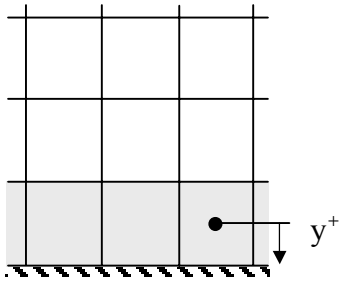

with $u^+ = (u - u_w)/u_\tau$ and $u_\tau = (\tau_w/\rho)^{1/2}$.

u is the tangential fluid velocity, u_w is the wall velocity, τ_w is the wall shear stress, y^+ is the non-dimensional wall distance and κ and E are empirical coefficients. y_m^+ must satisfy $y_m^+ - \frac{1}{\kappa}\ln(Ey_m^+) = 0$. For reasons of accuracy it is recommended that the non-dimensionless parameter y^+ be kept within the limits $30 < y^+ < 100$ where $y^+ = \rho C_\mu^{1/4} k^{1/2} y/\mu$. Generally for $y^+ \ge 11.63$ the flow is turbulent and wall functions are applied. The flow is laminar for $y^+ < 11.63$. Wall functions are also applied to represent the distribution of turbulent energy (Computational dynamics, 1998a).

3.4.2 The Chen k-ε model

An improvement in the standard k-ε model's performance was achieved by Chen and Kim (1987), through adding a second time scale of production range of turbulence kinetic energy spectrum to the dissipation rate equation. This additional time scale allowed the energy transfer mechanism of the turbulence model to respond more effectively to the mean strain. The turbulent kinetic energy equation remains unchanged and is expressed as in equation (3.14), but the turbulence dissipation rate equation now has an extra term on its right-hand side in addition to an extra modelling constant (Computational Dynamics, 1998a),

$$\frac{1}{\sqrt{g}}\frac{\partial}{\partial t}\left(\sqrt{g}\,\rho\varepsilon\right)+\frac{\partial}{\partial x_j}\left(\rho\tilde{u}_j\,\varepsilon-\frac{\mu_{eff}}{\sigma_\varepsilon}\frac{\partial\varepsilon}{\partial x_j}\right)=\frac{\varepsilon}{k}\left[\left(C_{\varepsilon 1}2s_{ij}\frac{\partial u_j}{\partial x_i}+C_{\varepsilon 3}P_B\right)-\frac{2}{3}\left(\mu_t\frac{\partial u_i}{\partial x_i}+\rho k\right)\frac{\partial u_i}{\partial x_i}\right]$$
$$-C_{\varepsilon 2}\,\rho\frac{\varepsilon^2}{k}+C_{\varepsilon 4}\,\rho\varepsilon\frac{\partial u_i}{\partial x_i}+\boldsymbol{C_{\varepsilon 5}\mu_t\frac{P^2}{k}} \qquad (3.17)$$

where $P=2s_{ij}\dfrac{\partial u_i}{\partial x_j}$ and $C_{\varepsilon 5}$ is an empirical constant. The values assigned to the model coefficients σ_ε, σ_k, C_μ, $C_{\varepsilon 1}$, $C_{\varepsilon 2}$, $C_{\varepsilon 3}$, $C_{\varepsilon 4}$, $C_{\varepsilon 5}$ are defined in Table A1-2, Appendix 1.

This additional expression, $C_{\varepsilon 5}\mu_t\left(P^2/k\right)$, allows for the energy transfer rate from the large-scale turbulence to the small-scale turbulence to be controlled by the production range time scale and the dissipation rate time scale. Therefore when the mean strain is strong or production rate is large the presence of this energy transfer function enhances the development of ε. Conversely the generation of ε is suppressed when the mean strain is weak or there is a small production rate (Chen and Kim, 1987). Consequently the production of the turbulent energy is controlled more effectively. Chen and Kim (1987) showed improvements in the prediction of reattachment length over a backward facing step when compared with the standard k-ε model.

3.4.3 The RNG k-ε model

A criticism of Reynolds averaged models is that the Reynolds averages can smooth out many of the important features of turbulence. A more desirable approach is to remove the smallest scales of turbulence to such a point where the only remaining scales are resolvable by available computer resources. This approach, known as the renormalisation group (RNG) methods, was used by Yakhot and Orszag (1986) in the development of the RNG k-ε model. The model used here is based a more recent version by Yakhot *et al* (1992). The model equation for the turbulent kinetic energy is the same as defined in equation (3.14). The difference as with Chen's k-ε model

appears in the turbulence dissipation rate equation (Computational Dynamics, 1998a),

$$\frac{1}{\sqrt{g}}\frac{\partial}{\partial t}\left(\sqrt{g}\,\rho\,\varepsilon\right)+\frac{\partial}{\partial x_j}\left(\rho\,\tilde{u}_j\,\varepsilon-\frac{\mu_{eff}}{\sigma_\varepsilon}\frac{\partial \varepsilon}{\partial x_j}\right)=\frac{\varepsilon}{k}\left[\left(C_{\varepsilon 1}P+C_{\varepsilon 3}P_B\right)-\frac{2}{3}\left(\mu_t\frac{\partial u_i}{\partial x_i}+\rho\,k\right)\frac{\partial u_i}{\partial x_i}\right]$$
$$-C_{\varepsilon 2}\,\rho\frac{\varepsilon^2}{k}+C_{\varepsilon 4}\,\rho\varepsilon\frac{\partial u_i}{\partial x_i}-\frac{\boldsymbol{C_\mu\,\eta^3(1-\eta/\eta_0)}}{\boldsymbol{1+\beta\eta^3}}\frac{\boldsymbol{\rho\varepsilon}}{\boldsymbol{k}} \tag{3.18}$$

where β and η_0 are empirical coefficients. The additional term is a modelled form of a term that arises from the RNG analysis and represents the effect of the mean flow distortion on ε (Rodi, 1979) where η is an extra expansion parameter that is the ratio of the mean strain time scale;

$$\eta = S\frac{k}{\varepsilon} \qquad \text{and} \qquad S=\left(2s_{ij}s_{ij}\right)^{1/2} \tag{3.19a-b}$$

The additional expression essentially allowing the turbulent kinetic energy budget to respond more effectively to changes in strain rate making the model better suited in predictions in regions of flow separation and curvature. The RNG k-ε model has shown improvements over the standard k-ε for a variety of complex two- and three-dimensional flows and in particular vehicle wake flow predictions (Choudhury *et al*, 1993; Kim *et al*, 1994; Williams *et al,* 1994; Gaylard *et al* 1998). When compared with the standard k-ε the RNG k-ε model described above showed improved predictions of the mean reattachment point for flow over a backward facing step, predicting within 5% of the experimental value (Speziale and Thangam, 1992). However as with the Chen k-ε model, the RNG k-ε model is still based on the linear Boussinesq approximation, equation (3.11). The coefficients in both the model equations are defined in Table A1-3, Appendix 1.

3.4.4 The non-linear (quadratic) k-ε model

In reality fluid flows are generally anisotropic and while the RNG and Chen k-ε models endeavour to improve predictions through the dissipation rate equation the main source of error lies with the linear Boussinesq approximation and the isotropic eddy viscosity concept. Non-linear models compensate by using non-linear relationships for the Reynolds stresses. Many different forms of the non-linear model have been developed expressing different forms of the Boussinesq approximation including Speziale (1987) and Craft *et al* (1996). Similar to the expression given by Craft *et al* (1996), the extended form of the Boussinesq approximation used in STAR-CD V3.05 is (Computational Dynamics, 1998a),

$$\rho\frac{\overline{u_i'u_j'}}{k} = \frac{2}{3}\delta_{ij} - \frac{\mu_t}{k}S_{ij} + C_1\frac{\mu_t}{\varepsilon}\left[S_{ik}S_{kj} - \frac{1}{3}\delta_{ij}S_{kl}S_{kl}\right] + C_2\frac{\mu_t}{\varepsilon}\left[\Omega_{ik}S_{kj} + \Omega_{jk}S_{ki}\right] + C_3\frac{\mu_t}{\varepsilon}\left[\Omega_{ik}\Omega_{jk} - \frac{1}{3}\delta_{ij}\Omega_{kl}\Omega_{kl}\right] \tag{3.20}$$

S_{ij} and Ω_{ij} the mean strain and vorticity tensors. C_1, C_2, C_3 and C_μ are defined through a range of empirical constants, which are not detailed here but maybe found in Computational Dynamics (1998a). The model equations for the non-linear k-ε model are (Computational Dynamics, 1998a),

Turbulent kinetic energy;

$$\frac{1}{\sqrt{g}}\frac{\partial}{\partial t}\left(\sqrt{g}\,\rho k\right) + \frac{\partial}{\partial x_j}\left(\rho\tilde{u}_j\,k - \frac{\mu_{eff}}{\sigma_k}\frac{\partial k}{\partial x_j}\right) = \mu_t\left(2s_{ij}\frac{\partial u_i}{\partial x_j} + P_B\right) - \rho\varepsilon - \frac{2}{3}\left(\mu_t\frac{\partial u_i}{\partial x_i} + \rho k\right)\frac{\partial u_i}{\partial x_i} + \boldsymbol{P_{NL}} \tag{3.21}$$

Turbulence dissipation rate;

$$\frac{1}{\sqrt{g}}\frac{\partial}{\partial t}\left(\sqrt{g}\,\rho\varepsilon\right)+\frac{\partial}{\partial x_j}\left(\rho\tilde{u}_j\,\varepsilon-\frac{\mu_{eff}}{\sigma_\varepsilon}\frac{\partial\varepsilon}{\partial x_j}\right)=\frac{\varepsilon}{k}\left[\left(C_{\varepsilon 1}2s_{ij}\frac{\partial u_i}{\partial x_j}+C_{\varepsilon 3}P_B\right)-\frac{2}{3}\left(\mu_t\frac{\partial u_i}{\partial x_i}+\rho k\right)\frac{\partial u_i}{\partial x_i}\right]$$
$$-C_{\varepsilon 2}\,\rho\frac{\varepsilon^2}{k}+C_{\varepsilon 4}\,\rho\varepsilon\frac{\partial u_i}{\partial x_i}+\boldsymbol{C}_{I\varepsilon}\frac{\boldsymbol{\varepsilon}}{\boldsymbol{k}}\boldsymbol{P}_{NL} \qquad (3.22)$$

In comparison with the model equations of the standard k-ε model, equations (3.14) and (3.15), the additional expression which appears on the right hand side of both the turbulent kinetic energy and turbulence dissipation rate equation accounts for non-linear contributions within the flow field (Computational Dynamics, 1998a). The empirical coefficients σ_ε, σ_k, C_μ, $C_{\varepsilon 1}$, $C_{\varepsilon 2}$, $C_{\varepsilon 3}$, and $C_{\varepsilon 4}$ are found in Table A1-1, Appendix 1.

The non-linear models have been shown to give significant improvement in predictions for separated turbulent flows (Speziale, 1987; Speziale and Ngo, 1988, Rabbitt, 1997; Wright and Easom 1999; Wright *et al*, 2001). For the most common test case, flow over a backward facing step, the standard k-ε model significantly under predicts the reattachment length whereas the non-linear makes a more accurate prediction (Speziale, 1987; Speziale and Ngo, 1988; Thangam and Hur, 1991; Easom, 2000). The quadratic model, as used here, is designed for use in highly anisotropic flow problems and is generally sufficient for use in most wind engineering applications.

There is a 'two-layer' turbulence model available within STAR-CD V3.05, which resolves the boundary layer flow using multiple cells close to the surface instead of applying standard wall functions (section 3.4.4.1). While this model potentially provides a more accurate representation of the flow close the surface of a model it requires significantly more computational cells at the expense of computational effort and for this reason was not considered for this study.

3.5 Numerical validation techniques

Statistical techniques were used to give quantitative assessment of each numerical solution. The mean velocity components $\overline{u}$, $\overline{v}$ and $\overline{w}$, and tracer gas concentration were considered. Data from the numerical solutions were extracted using sensor points within the computational domain.

Two different techniques were employed: i) a direct percentage difference between the numerical and experimental data; ii) prediction error expressed as a number of standard deviations derived from the experimental data.

3.5.1 Absolute percentage difference

The difference between predicted and measured values was expressed as an absolute percentage i.e. for each flow variable at each grid point the percentage difference Q,

$$Q = 100 - \left(\frac{P}{M} \text{ x } 100 \right) \qquad \text{when } M > P \quad \text{(under prediction)} \qquad (3.23)$$

otherwise

$$Q = 100 - \left(\frac{M}{P} \text{ x } 100 \right) \qquad \text{when } M < P \quad \text{(over prediction)} \qquad (3.24)$$

where P is the predicted value and M is the measured value i.e. P is Q% of the measured value M. Q was calculated for each flow variable at all measured distances downstream of the model. The success of the each numerical solution was expressed in terms of the percentage of all predicted values falling within 25, 50 and 75% of the measured values. Care was taken with small measured values, which can result in misleading conclusions. Predictions of wrong direction were considered separately.

3.5.2 Prediction error in terms of standard deviation

The standard deviation σ of a set of data is the measure of how far the individual readings within that set are from the mean of the data set (Kreyszig, 1999),

$$\sigma^2 = \frac{1}{\mathrm{n}-1}\sum_{j=1}^{\mathrm{n}}\left(x_j - \bar{x}\right)^2 \tag{3.25}$$

where $\bar{x}$ is the mean of the set of data values and x_j is an individual value from the data set. Used on large data sets it is assumed that 68% of the data will be within σ, 95% will lie within 2σ and 99.7% will be within 3σ, figure 3.3.

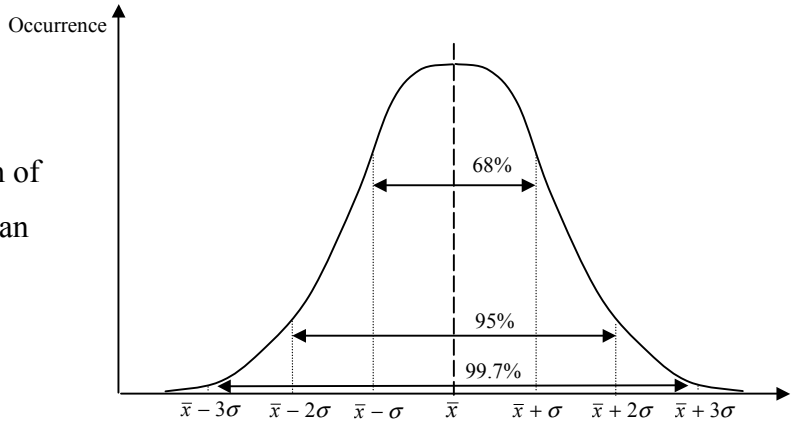

Figure 3.3 – The distribution of large set of data about a mean value

The standard deviation is essentially the root mean square value (rms) of each flow variable and is a basic measure of uncertainty in the mean stated values due to turbulent fluctuations i.e. the degree in which the mean stated value may vary over time. The numerical simulations in essence output only a single mean value whereas the measured mean is the mean of *x* number of instantaneous values over time *t* therefore in using σ to assess prediction error gives the numerical simulations an effective range in which to make a prediction. In the current study both measurement techniques used for the velocity field detailed in Chapter 4 output rms values for all the quantities measured.

Similar to a technique used by Quinn (1996) the prediction error is expressed as the number of standard deviations. The standard deviation is essentially the 'uncertainty' of a measured mean value therefore takes account of experimental

uncertainty in such comparisons and allows predictive and measured quantities to be compared on an equal basis. Equation (3.25) assumes each data set of while $\overline{u}$, $\overline{v}$ and $\overline{w}$ to be normally distributed (section 4.4.1 and Appendix 1e)

To calculate standard deviation of any quantity, equation (3.25), a time-series of that quantity is required. However $\overline{u}_{HW}$, the mean streamwise velocity component obtained using hotwire was calculated from equation (4.2) therefore no time series were available. It was necessary to create a time-series for *u* using

$$u_{HW} = \frac{1}{2}(u'_{uv} + u'_{uw}) \tag{3.26}$$

where u'_{uv} and u'_{uw} are the fluctuating components of *u* in the *uv* and *uw* plane respectively (section 4.2.3) measured using hotwire. The standard deviation for u_{HW} at each measurement point at all downstream locations was established using the time series created from equation (3.26)

The prediction error, $E_{p_{\bar{x}}}$ is expressed as,

$$E_{P_{\bar{x}}} = M_{\bar{x}} - P_{\bar{x}} \tag{3.27}$$

where $M_{\bar{x}}$ is the measured mean quantity and $P_{\bar{x}}$ is the predicted mean quantity. $E_{p_{\bar{x}}}$ is established for each flow variable at each measurement point at all downstream locations and then compared against the equivalent standard deviation for each of these points. If the $E_{p_{\bar{x}}} \leq \sigma$ then the predicted quantity is closer to the measured quantity than if $\sigma < E_{p_{\bar{x}}} \leq 2\sigma$, figure 3.4 and are said to be in good agreement if more then 50% of the predicted results lie within σ of the experimental data and 75% lie within 2σ.

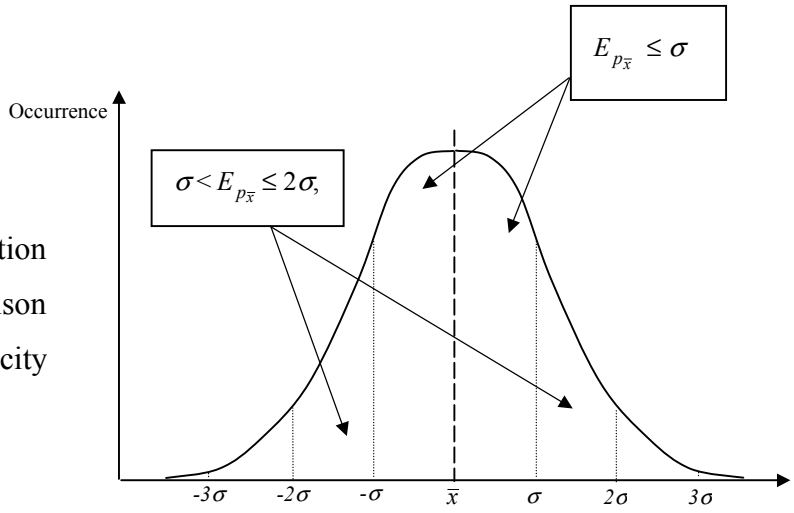

Figure 3.4 – Example of prediction error standard deviation comparison for predicted and measured velocity components.

This method was not however appropriate in the comparisons of predicted and measured values of $\overline{\varpi}_{\mathrm{p}}$, the proportion of propane to air because unlike the velocity data values of $\overline{\varpi}_{\mathrm{p}}$ were derived from calculated values of mean concentration, $\bar{c}$ and not directly from the measured data, equation (5.4). For example to create a time-series for $\overline{\varpi}_{\mathrm{p}}$ at each measured point,

$$\varpi_{\mathrm{p}} = \frac{\mathrm{V}_{act} \cdot C_f}{10^6} \tag{3.28}$$

where V_{act} is the actual instantaneous voltage measured and C_f is the calibration factor (section 5.2.1.1)

$$C_f = \frac{S}{z_{off}} \qquad \text{and} \qquad \mathrm{V}_{act} = \mathrm{V}_{rd} - z_r \tag{3.29a-b}$$

V_{rd} is the instantaneous raw data, z_r is the wind-on zero reading taken at the beginning of each row, S is the maximum source strength and z_{off} being the zero wind-off reading. While data was available to create a time-series for V_{act}, it is the uncertainty contained within C_f through z_{off} that is of concern. It was therefore more

appropriate to use the calculated uncertainty in $\overline{\omega}_p$ [3.1] $E_{\overline{\omega}_p}$ (section 7.3.2.2). This quantity was calculated based on the standard error on the mean S_m that assumes the data to be normally distributed (section 4.4.1). Appendix 2b(i) shows the raw data to be normally distributed therefore it was assumed that the calculated concentration data and thus values of $\overline{\omega}_p$ were also normally distributed. Therefore if the prediction error $E_{P_{\bar{x}}}$ is less than or equal to $E_{\overline{\omega}_{p1,2}}$, $E_{P_{\bar{x}}} \leq E_{\overline{\omega}_{p1,2}}$ then the predicted value is closer to the measured value than if $E_{\overline{\omega}_{p1,2}} < E_{P_{\bar{x}}} \leq 2E_{\overline{\omega}_{p1,2}}$, figure 3.5. The predictions of $\overline{\omega}_p$ were said to be in good agreement if 50% of predictions were within $\leq 4E_{\overline{\omega}_{p1,2}}$.

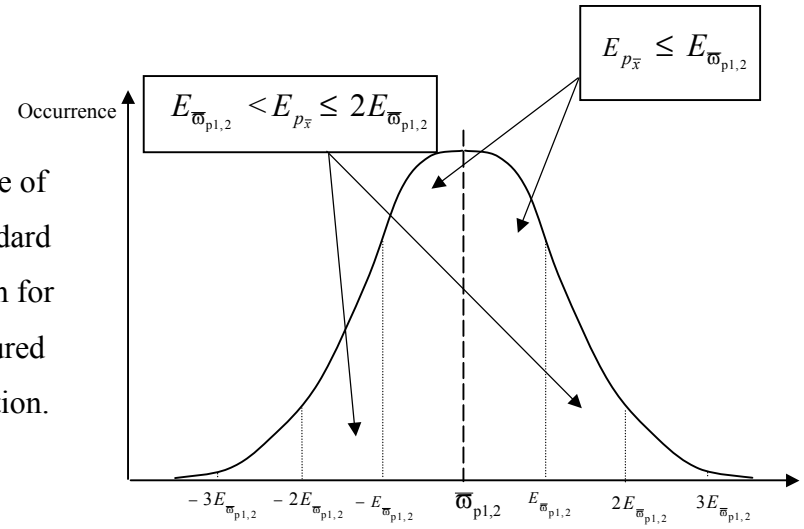

Figure 3.5 - Example of prediction error standard deviation comparison for predicted and measured tracer gas concentration.

[3.1] Mean concentration $\bar{c}$ divided by 10^6 gives $\overline{\omega}_p$

Chapter 4: Experimental Study 1 - Near wake velocity measurements

4.1 Introduction

The following chapter describes an experimental study in which the velocity field within the near wake of the model vehicle was measured. The primary aim of the experiment to be described was to obtain detailed velocity data for the validation of numerical simulations of the near wake flow field of a model vehicle (Chapter 6). Mean velocity data was collected for direct validation and the uncertainty the measured data determined for criteria used in statistical validations. The data collected also provided a valuable insight into the principle near wake flow character of the model vehicle used, information subsequently used in the discussion of the near wake dispersion field (Chapter 5). Velocity vector maps were used to present in some detail the flow structure within the recirculation region of the model vehicle and in particular the significant change in flow structure away from the model centreline. The following chapter describes the experimental techniques used, the data obtained for validation and the main characteristics of the flow field measured.

4.2 Equipment set-up and measurement details

A wake survey was conducted to measure the velocity field at various distances downstream of a model vehicle, a technique commonly used in vehicle wake studies (Howell, 1975; Davis, 1982; Bearman *et al*, 1983; Bearman, 1984; Ahmed *et al,* 1984). Particle Image Velocimetry (PIV) was used to make velocity measurements within the region of recirculation close behind the model vehicle (figure 2.2) and a hotwire anemometer was used to make additional velocity measurements downstream of the recirculation region. In addition static pressure measurements were made along the model centreline.

4.2.1 Wind tunnel and model

The study was conducted in the MIRA model scale wind tunnel using the MIRA 33% scale reference car in the fastback configuration figure 4.1. The test section is open jet, with an average turbulence intensity of 1.1%, over the region typically occupied by a model, at an empty test section free stream velocity of 40m/s (Brown *et al*, 1998). Appendix 2a details the wind tunnel dimensions.

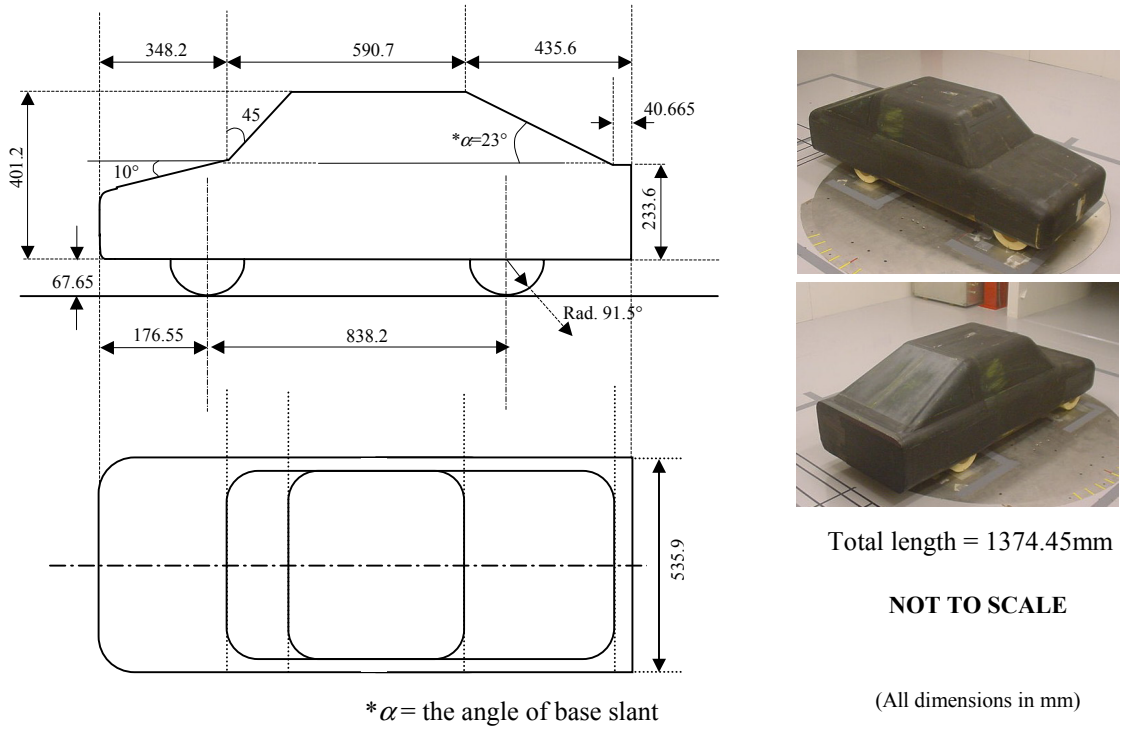

Figure 4.1 – 33% scale MIRA reference model (fastback configuration)

The model was supported by pins beneath each wheel, on a fixed floor at zero angle of incidence to the free stream flow (Appendix 2a). The disadvantage of using a fixed floor is the wake of the model may become engulfed in the boundary layer, which grows along the floor (section 2.3). Boundary layer profiles along the wind tunnel floor, Appendix 2b, suggest a turbulent boundary layer of thickness $\delta = 0.37 x_{ne} / \mathrm{Re}_{x_{ne}}^{1/5}$ (Anderson, 1991). x_{ne} is the distance downstream of the nozzle exit and $\mathrm{Re}_{x_{ne}}$ is the Reynolds number of the flow in the boundary layer expressed as $\mathrm{Re}_x = U_\infty x_{ne} / \nu$ where ν is kinematic viscosity and U_∞ is the velocity upstream of

the model. The boundary layer thickness at the model base, at U_∞=13m/s, was estimated to be 47mm increasing to 58mm at the furthest measurement point downstream of the model. With a model ground clearance of 67.65mm the growing boundary layer could interfere with the development and structure of near wake flow field and as well as its measurement. While Bearman *et al* (1988) showed that for a model vehicle with a smooth flat underside, similar to that used here, the use of a stationary floor made little difference to the actual near wake structure (section 2.3) the inherent disadvantages must not ignored. Boundary layer suction was not used in order that subsequent numerical simulations were kept controlled.

The influence of wind tunnel blockage ratio [4.1] was not considered because the wind tunnel geometry was replicated in the computational domain (Chapter 6). It was for this reason and that comparison made between the numerical simulations and experiment used only absolute measured and predicted values, blockage ratio corrections are not applied. In the few instances where the free stream velocity is used to normalise data the general trend of these quantities remains the same even if blockage correction were applied.

4.2.2 Particle Image Velocimetry (PIV)

Particle Image Velocimetry (PIV) was used to make detailed velocity measurements within the near wake recirculation region as conventional hot-wire techniques are general unreliable in regions of recirculation and high turbulence (section 4.2.3.1). The basic principles of PIV may be found in Appendix 2c. The PIV set-up in the wind tunnel is detailed in figure 4.2. The flow was seeded using Safex fog fluid and the laser light sheet pulsed every 0.01μs. A total of 1000 vector maps were captured at a rate of 2 per second for each measurement location. Figure 4.2a shows the location of the camera with respect to the model and figure 4.2b the location of laser with respect to the model. The system was controlled via computer in the wind tunnel control room.

[4.1] Blockage ratio: ratio between model frontal area and wind tunnel nozzle cross-section.

Cross wake vector maps $\overline{v}-\overline{w}$, where $\overline{v}$ is the mean vertical velocity component and $\overline{w}$ is the mean cross-stream component were captured at 4 locations downstream of the model, x/l = 0.036, 0.073, 0.146, 0.218 (l is the total model length and x is the distance downstream of the model base). The downstream measurement locations were determined from the flow visualisation study which identified the region of recirculation where hot-wire measurements would not be unreliable. Streamwise vector maps of $\overline{u}-\overline{v}$, where $\overline{u}$ is the streamwise velocity component were captured at the model centreline and at z/b = 0.560 (b is half the width of the model base and z is the distance cross-stream from the centreline). Figure 4.3 shows details of the capture region.

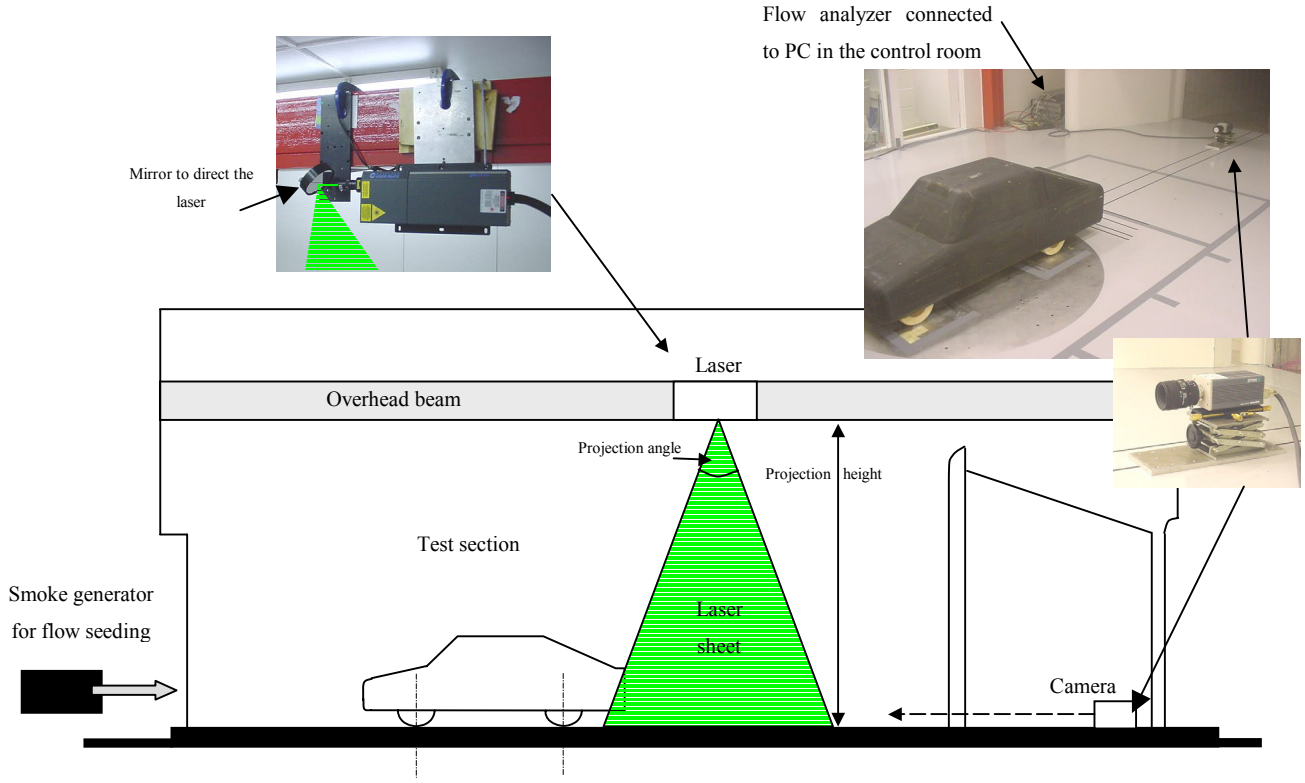

Figure 4.2 – PIV system set-up

The overall size of capture area varied depending in the perpendicular distance from the CCD camera, the laser projection height and angle, figure 4.2. The maximum capture area in each case, while not extensive was sufficient to capture the main features of the flow field under investigation. Each vector map and associated data file provided information on the overall flow structure and the mean velocity components associated with each plotted vector in that map i.e. the mean streamwise, vertical and cross-stream velocities $\overline{u}$, $\overline{v}$ and $\overline{w}$ respectively.

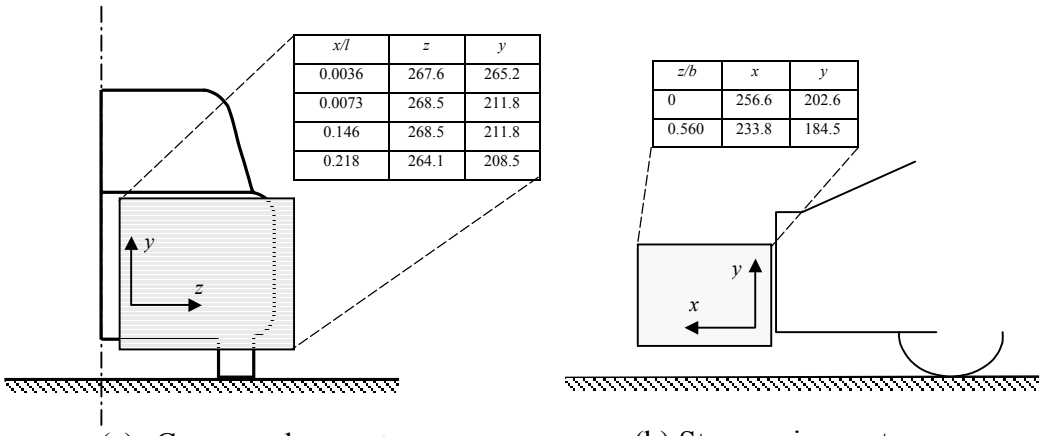

(a) Cross wake capture area (b) Streamwise capture area

Figure 4.3 – PIV measurement capture areas

The co-ordinate system for the velocity components was the same as for the hotwire measurements and is detailed in figure 4.4. A short times series of instantaneous values of each velocity component was also created as a result of the 1000 consecutive image maps captured at each measurement location. The PIV system also outputs the rms values of each component ($\sqrt{\overline{u'^2}}$, $\sqrt{\overline{v'^2}}$ and $\sqrt{\overline{w'^2}}$) as well as values of $\overline{u'v'}$ and $\overline{u'w'}$.

Unlike the hotwire measurements (section 4.2.3) the spatial location of each measured point within the capture area could not be pre-defined as they were dependent on the position of the flow seeding particles. Point data was extracted using Tecplot (Amtec, 2001) for use in the statistical validation of the numerical simulations (section 3.5) according to the points shown in figure 4.4. Measurements were made at a free stream velocity of 13m/s (~30mph). The Reynolds number based on model length was 1.189 x 10^6. It is appropriate at this point to address the issue of Reynolds number effect. At Reynolds numbers typical of road vehicles i.e. Re > 10^4 the boundary layer at separation at the rear of the vehicle is generally turbulent with little sensitivity to changing Reynolds number expected (Hucho, 1998). The free-stream velocity was dictated by unsteadiness in the probe support arm during the hotwire measurements (section 4.2.3).

4.2.3 Hot-wire anemometer

A Hot-wire anemometer was used to make additional velocity measurements outside the near wake recirculation region as the availability of the PIV measurement system was limited. A DANTEC Streamline hot-wire anemometry (HWA) system, with a 55P61 2D sensor (cross-wire, constant temperature type)[4.1], was used to measure both the instantaneous and mean velocity components in the wake of the model, figure 4.4.

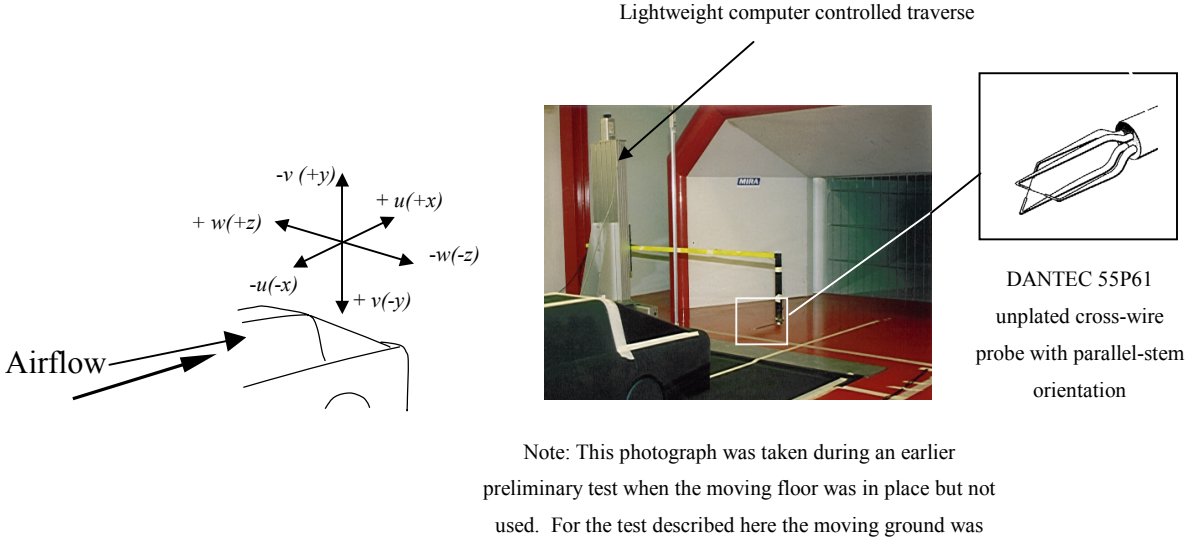

Note: This photograph was taken during an earlier preliminary test when the moving floor was in place but not used. For the test described here the moving ground was

Figure 4.4 - Hot-wire sensor location and traverse co-ordinates

Measurements were made at x/l = 0.291 and 0.437 at 92 spatial locations within a 500mm x 500mm survey area covering one half of the model base, figure 4.5.

The cross-wire allowed simultaneous measurement of two velocity components. All three mean velocity components, $\overline{u}$, $\overline{v}$ and $\overline{w}$ were measured by rotating the probe through 90°. The free stream velocity was 13m/s (~30mph) and the Reynolds number based on model length 1.189 x 10^6. The hotwire system also outputs the rms values of each component ($\sqrt{\overline{u'^2}}$, $\sqrt{\overline{v'^2}}$ and $\sqrt{\overline{w'^2}}$) as well as values of $\overline{u'v'}$ and $\overline{u'w'}$.

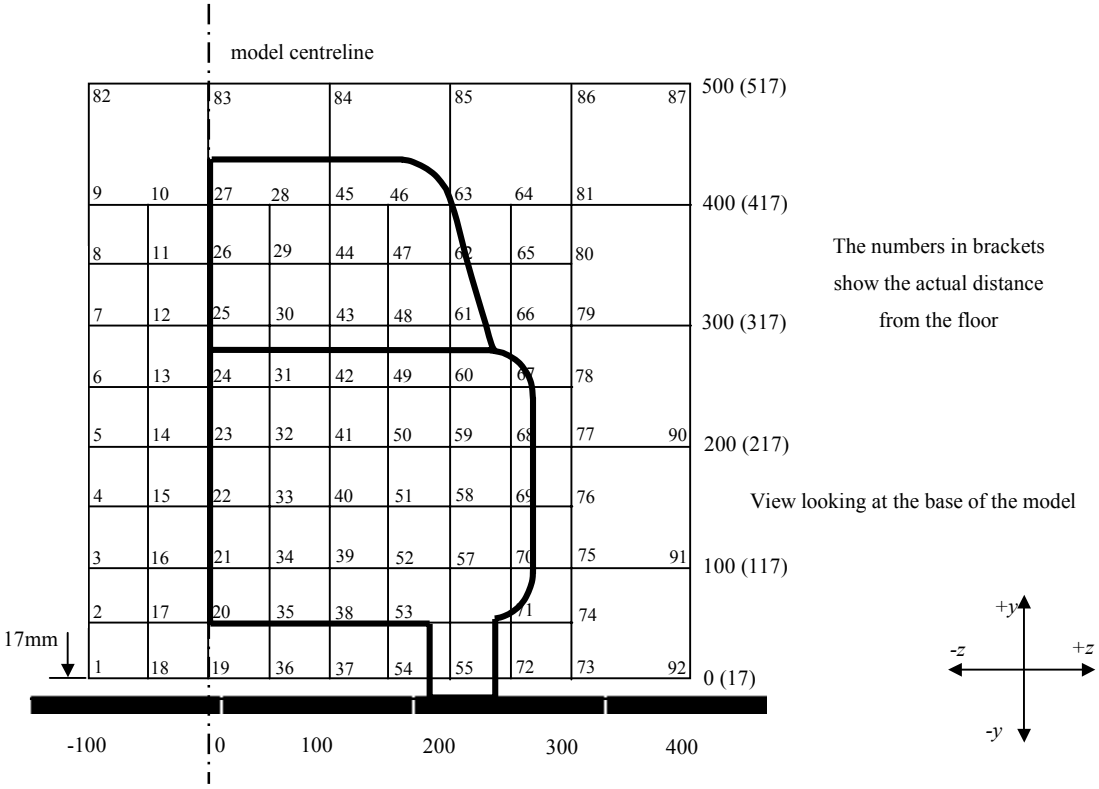

Figure 4.5 – Survey area for hot-wire measurements

The downstream measurement locations were determined from the flow visualisation study which identified the region of recirculation where hot-wire measurements would not be unreliable. The free stream velocity was dictated by the stability of the traverse arm. At higher flow speeds the arm tended to flex and oscillate due to its long length and possibly vortex shedding from the square cross section. The leading edge of the support arm was profiled using modelling foam make the support arm more stable.

4.2.3.1 Calibration of the cross-wire sensor

Calibration of a hot-wire probe was achieved using a calibration procedure built into the system software based on the relationship

$$E^2 = A + BU^n \qquad \text{(King's Law)} \qquad (4.1)$$

where U is the measured velocity, E is the output voltage of the anemometer and A, B and n are constants. For more detail on hot-wire principles and calibration refer to Bruun (1995). Six values of U_∞ were measured between 5 and 15 m/s for each wire and a curve fit analysis used to establish constants A, B, and n, figure 4.6.

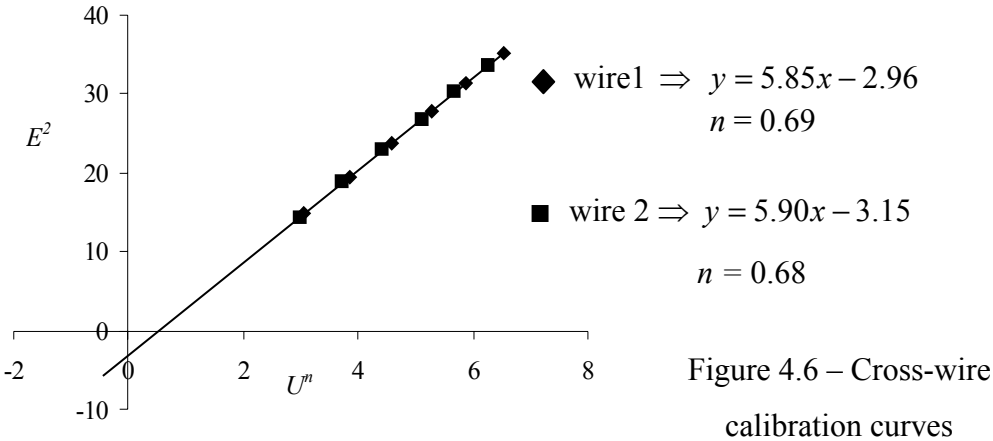

Figure 4.6 – Cross-wire calibration curves

In high turbulence intensities or in regions of flow reversal (>30%) data measured by hotwire is prone to error due to the wire's insensitivity to a flow reversal direction. Therefore due to the turbulent nature of the flow being measured the usability of the data was assessed on the assumption that it looses accuracy if the local turbulence intensity, $\sqrt{\overline{u'^2}}/\overline{u}$, was greater than 30% (Chandrsuda & Bradshaw, 1981). Data is only of qualitative use if $\sqrt{\overline{u'^2}}/\overline{u}$ exceeds 50%. Based on these criteria and taking into account the maximum uncertainty in Iu (section 4.4.2.), over 90% of the data measured at x/l = 0.291 and 0.437 could used with confidence.

4.2.4 Static pressure

Static pressure measurements were taken along the model centreline and on the base of the model to provide data for the validation of the numerical simulations of the flow field over the model (chapter 6). Surface mounted pressure transducers were used with an electronic pressure scanner. The system outputs a mean static pressure coefficient for each point measured. Figure 4.7 shows how the pressure transducers

were attached to the model. The exact locations of all the pressure transducers are detailed in Appendix 2d.

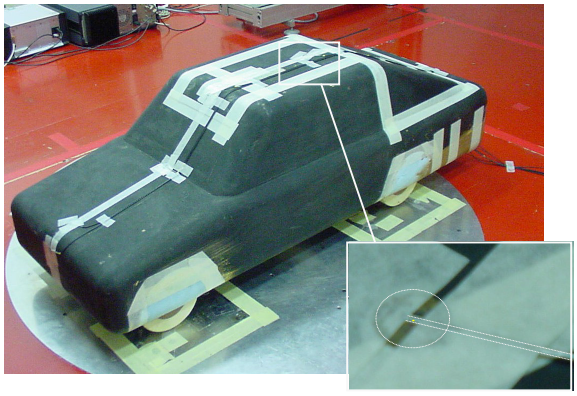

Figure 4.7 – Surface mounted pressure transducers

4.2.5 Flow visualisation

Flow visualisation was achieved using smoke and fluorescence dye. Smoke, known as 'Jem fog' was introduced into the flow through a hand-held injector that could be placed at any point over or around the model. Flow pictures were recorded using a video camera with the individual images 'snap-shot' being created using the image capture software, Adobe Premier 5.

For the fluorescence dye technique a foam board was placed along the centreline extending downstream of the model base. Dye was sprayed on to the model surface, wind tunnel floor and foam board and allowed to trace patterns according to the flow structure. Ultra violet light was shone on the dye traces and images recorded using a digital camera. While the foam board essentially introduces a boundary into the flow field, flow symmetry (figure 4.8) was assumed at the model centreline and therefore thought to have little influence on the flow structure.

4.3 Measured and calculated data

Both mean ($\overline{u}$, $\overline{v}$, $\overline{w}$) and instantaneous (u, v, w) values of velocity were measured by both the PIV and the hot-wire. During the PIV measurements the laser light sheet pulsed every 0.01μs and total of 1000 double vector maps were captured at a rate of

2 per second for each measurement location i.e. double as laser is pulsed twice for each sample (section 4.2.2). Each vector map contained approximately 1215 data points. The mage collection rate of PIV system was limited in order that a data set of 1000 double vector maps could be captured using the camera available for image capture without loss of data during transfer. However the capture rate was sufficient to capture the main flow features of the mean velocity field required for numerical validations. During hotwire measurements the three velocity components were measured at each specified grid point (figure 4.5) for 10.918 seconds at 1500Hz. At equivalent full scale for the same vehicle speed this equates to a 33 second sample time. Ideally for an unsteady flow the sample time would be longer in order to obtain a representative mean but this method of point by point velocity measurement was time consuming therefore in order to obtain sufficient data for validation the sample time was restricted. However subsequent spectral analysis (section 5.5) showed near wake fluctuations at mode1 scale to be of the order 3-84 Hz i.e. 3-84 cycles per second therefore it is believed that the sample time employed was sufficient to obtain mean data for the validation of the numerical simulations.
All measurements were carried out at a wind speed of 13m/s (~30mph).

4.3.1 Mean velocity data

Mean values of the streamwise, vertical and cross-stream velocity measured by PIV, $\overline{u}_{PIV}$, $\overline{v}_{PIV}$ and $\overline{w}_{PIV}$ respectively were used directly in the validation of numerical simulations and in the analysis of the flow field structure. From the hot-wire measurements only the vertical and cross-stream velocities, $\overline{v}_{HW}$ and $\overline{w}_{HW}$ respectively were used directly, the mean streamwise velocity component $\overline{u}_{HW}$ was calculated from using,

$$\overline{u}_{HW} = \frac{1}{2}\left(\overline{u}_{uv} + \overline{u}_{uw}\right) \tag{4.2}$$

where $\overline{u}_{uv}$ and $\overline{u}_{uw}$ are the mean values of u measured by the hot-wire in the uv and uw plane respectively at x/l = 0.291 and 0.437.

4.3.2 Vorticity

The local gradients of the mean cross-stream velocity were calculated to obtain values of mean streamwise vorticity i.e. vorticity about the *x*-axis, ξ_x. ξ_x was defined as,

$$\xi_x = \frac{\partial \overline{w}}{\partial y} - \frac{\partial \overline{v}}{\partial z} \qquad (4.3)$$

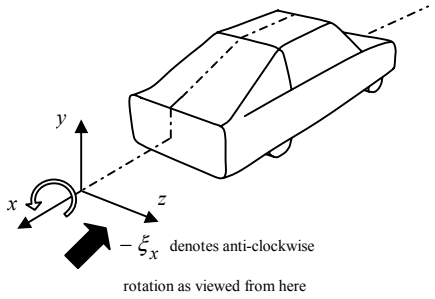

where $\frac{\partial \overline{w}}{\partial y}$ and $\frac{\partial \overline{v}}{\partial z}$ are the local cross-stream and vertical velocity gradients respectively. Vorticity was plotted as contours of constant $\xi_x H / U_\infty$, where U_∞ is the free stream velocity and H is the height of the model (Bearman, 1984). A negative vorticity denotes an anti-clockwise rotation as indicated above. Vorticity was not used in the validation of the numerical velocity field simulations.

4.3.3 Local turbulence intensity

The local streamwise turbulence intensity *Iu*, was calculated along the model centreline and at *z/b* = 0.560 to examine the streamwise turbulence levels within the recirculation region,

$$Iu_{PIV} = \frac{1}{2}\left(\frac{\sqrt{\overline{u'^2_{PIV}}}}{U_\infty} \right) \qquad (4.5)$$

where $\sqrt{\overline{u'^2_{PIV}}}$ is the rms of the streamwise velocity *u* measured by PIV and U_∞ is the free stream velocity. Calculated values of local turbulence intensity were not used in the validation of the numerical because rms values were not output by the solutions due to them being steady state only (section 6.2.3 and 6.3.1). While mean turbulent

kinetic energy, $\bar{k}$ would also provide information on turbulence levels, this quantity could not be calculated as a consequence of the PIV measurements only being 2D i.e. $\bar{k} = 1/2(\overline{u'^2} + \overline{v'^2} + \overline{w'^2})$. Values of $\bar{k}$ could be determined from the hotwire measurements made at *x/l* = 0.291 and 0.437 but it was felt that no gain would be made in calculating *k* at these points alone. In terms of numerical validation using values of $\bar{k}$ at *x/l* = 0.291 and 0.437 only would be secondary as the principle flow structure of interest occurs at *x/l* < 0.291. Further implications of not having $\bar{k}$ for numerical validation are discussed in section 6.2.3. Moreover as the following discussion shows, the near wake recirculation region is dominated by streamwise fluctuations therefore values of streamwise turbulence intensity *Iu* were more beneficial in highlighting these streamwise fluctuations.

Spectral information was not obtained from the PIV velocity data as the frequency of capture, 2 maps per second, was not considered sufficient to capture the unsteady character of the near wake flow. The unsteady character of the recirculation region was examined using the instantaneous concentration data (section 5.4).

4.3.4 Static pressure data

Static pressure data was measured at the points detailed in Appendix 2c. Data was sampled at 20kHz for 30secs at each measurement point. The data acquisition system returned a static pressure coefficient, $C_{P_{stat}}$ at each point. The static pressure coefficient is particularly sensitive in areas such as stagnation (nose of the model) and the leading and trailing edge of the roof, therefore three measurements were taken at each point to check the repeatability of the measurements. An average was taken of the three measurements to obtain $C_{P_{stat}}$ at each measured point. Unfortunately time series data was not available for the pressure data. The Centreline static pressure data was used primarily in the validation of the simulated flow field over the model (chapter 6) and are therefore not discussed in the following sections.

4.4 Experimental data uncertainty and numerical validation criteria

The criteria for statistical validations of the numerical simulations (Chapter 6) are determined and the uncertainties associated with both the measured data and calculated quantities estimated providing a measure of the quality of the data collected.

4.4.1 Criteria for statistical validation

For the statistical validation of the numerical predictions of the measured near wake flow field to be described below in section 4.5 the error in prediction was expressed in terms of the number of standard deviations, σ of the experimental data (section 3.5). The standard deviation is essentially the root mean square value (rms) of each flow variable and is a basic measure of uncertainty in the mean stated values due to turbulent fluctuations i.e. the degree in which the mean stated value may vary over time. The numerical simulations in essence output only a single mean value whereas the measured mean is the mean of x number of instantaneous values over time t therefore in using σ to assess prediction error gives the numerical simulations an effective range in which to make a prediction. RMS values for $\overline{u}$, $\overline{v}$ and $\overline{w}$ were output directly by each of the measurement techniques used and only values of $\overline{u}$, $\overline{v}$ and $\overline{w}$ were considered in the statistical validations (Section 6.3.1). The maximum σ for of $\overline{u}$, $\overline{v}$ and $\overline{w}$ over all distances downstream were determined and are given in Table 4.1,

$\sigma_{\overline{u}_{PIV}}$	$\sigma_{\overline{v}_{PIV}}$	$\sigma_{\overline{w}_{PIV}}$	$\sigma_{\overline{u}_{HW}}$	$\sigma_{\overline{v}_{HW}}$	$\sigma_{\overline{w}_{HW}}$
±3.844m/s	±3.352m/s	±3.271m/s	±2.173m/s	±2.473m/s	±2.243m/s

Table 4.1 – Maximum standard deviation for each flow variable

4.4.2 Experimental data uncertainty

4.4.2 1 Standard error on the mean measured data

The probability of a mean measured value lying within a certain range of its true value may be defined S_m, the standard error on the mean (Pentz & Shott, 1988),

$$S_m = \frac{\sigma}{\sqrt{n-1}} \tag{4.6}$$

where σ is the standard deviation or rms of each flow variable. S_m is a measure of how close the measured mean value of a given sample is to an unknown true value and for that given sample the mean value has a 68% chance of lying within ± S_m of the true value, 95% within ± $2S_m$ and so on. The S_m was evaluated for directly measured mean values only. The mean streamwise velocities $\overline{u}_{HW}$ were considered separately as these values were calculated from equation (4.2) and not directly measured. S_m assumes that the spread of individual readings to fit a normal distribution, Appendix 2e. The standard error on the mean was calculated for all measured values of $\overline{u}_{PIV}$, $\overline{v}_{PIV}$, $\overline{w}_{PIV}$, $\overline{v}_{HW}$, $\overline{w}_{HW}$, $\overline{u}_{uv}$ and $\overline{u}_{uw}$ for all measurement locations and the overall maximum $S_{m(MAX)}$ established for each flow variable i.e. maximum over all measurement locations both streamwise and cross-stream. The uncertainty in each variable considered was expressed with a 95% confidence i.e. $2S_{m_{(MAX)}}$. The uncertainty values listed in Table 4.2 are all with a 95% confidence.

$S_{\overline{u}_{PIV(MAX)}}$	$S_{\overline{v}_{PIV(MAX)}}$	$S_{\overline{w}_{PIV(MAX)}}$	$S_{\overline{v}_{HW(MAX)}}$	$S_{\overline{w}_{HW(MAX)}}$	$S_{\overline{u}_{uv(MAX)}}$	$S_{\overline{u}_{uw(MAX)}}$
±0.244m/s	±0.212m/s	±0.208m/s	±0.04m/s	±0.036m/s	±0.048m/s	±0.052m/s

Table 4.2 –The standard error on the mean (in m/s) for each measured quantity over all measurement locations with 95% confidence.

The standard error on the mean or uncertainty was higher for the PIV measurements because the flow at $x/l \leq 0.218$ was general more turbulent than at $x/l \geq 0.291$ and also because the number of samples, n in equation (4.6) was only 1000 for PIV measurements as opposed to 16000 for the hotwire measurements. The number of samples, or vector maps captured during PIV measurements was limited by the capacity of the PC used for acquisition. Nevertheless the uncertainty in all of the quantities expressed above are no greater than 5% of their maximum mean measured values.

Uncertainties in the measured pressure data could not be calculated, as time series were not available.

4.4.2.2 Uncertainty in calculated quantities

The uncertainties in calculated quantities were evaluated using the methods detailed by Pentz and Shott (1988) and the uncertainties calculated in the previous section. The expressions used from Pentz and Shott (1998) are given in Appendix 2f. Uncertainty was estimated for all the calculated values of $\overline{u}_{HW}$ and ξ_x. The uncertainty in each of these quantities was estimated through the following expressions,

$$E_{\overline{u}_{HW(MAX)}} = \frac{1}{2}\sqrt{(S_{\overline{u}_{uv(MAX)}})^2 + (S_{\overline{u}_{uw(MAX)}})^2} \tag{4.7}$$

$$E_{\xi_{sHW(MAX)}} = \sqrt{4S^2_{\overline{v}_{HW(MAX)}} + 4S^2_{\overline{w}_{HW(MAX)}}} \tag{4.8}$$

The complete descriptions and workings towards these expressions are found in Appendix 2g. Equation (4.7) estimates the uncertainty in $\overline{u}_{HW}$ in terms of the uncertainties in the components $\overline{u}_{uv}$ and $\overline{u}_{uw}$ and equations (4.8) uncertainty in the streamwise vorticity. $\xi_{(x)}$ was only presented for x/l = 0.291 and 0.218 therefore only uncertainty in these values were determined i.e. values calculated using hotwire

data. The uncertainties in calculated $\xi_{(x)}$ and $\overline{u}_{HW}$ with a 95% confidence are given in Table 4.3.

$E_{\overline{u}_{HW(MAX)}}$	$E_{\xi_{sHW(MAX)}}$
±0.068m/s	±0.142 per sec

Table 4.3 –The standard error on the mean for ξ_x and $\overline{u}_{HW}$ with 95% confidence.

The uncertainties in $\overline{u}_{HW}$ and ξ_x are less 1% and 5% their maximum mean values respectively. There was no uncertainty associated with the streamwise turbulence intensity *Iu* as there are no calculated uncertainties associated with the rms quantity $\sqrt{\overline{u'^2_{PIV}}}$ and the free stream velocity U_∞.

4.5 Discussion of experimental results

It should first be made clear that all the measured data presented here corresponds to the time averaged flow structure. In reality the instantaneous near wake field of a road vehicle is highly chaotic and would not exhibit the clear flow structures presented here, refer forward to figure 4.14. To establish a true mean flow field time averaging should ideally be over much longer periods of time than used here but practical limitations did not allow for this. As a consequence while the data presented shows a clear mean flow structure it must be remembered that this is only a time-averaged interpretation of a constantly changing flow structure. Also the assumption that the mean wake flow is symmetric about the model centreline was applied. Dye tracers on the floor of the wind tunnel show evidence that this assumption was valid, figure 4.8.

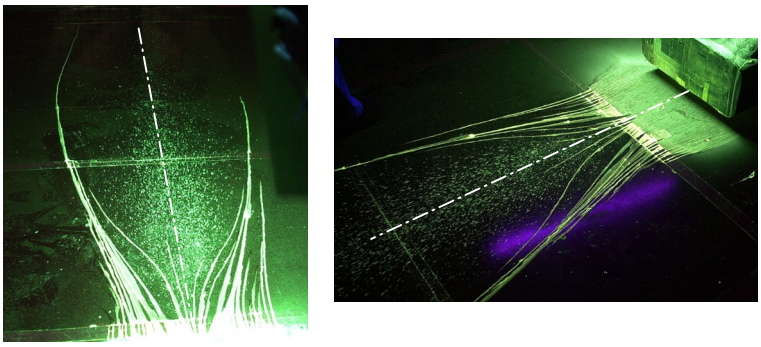

Figure 4.8 – Dye traces showing evidence of flow symmetry.

Images from the flow visualisation give an overall impression of the size and shape of the recirculation region. Figure 4.9a shows a 'snap-shot' of the flow at the model centreline using smoke visualisation.

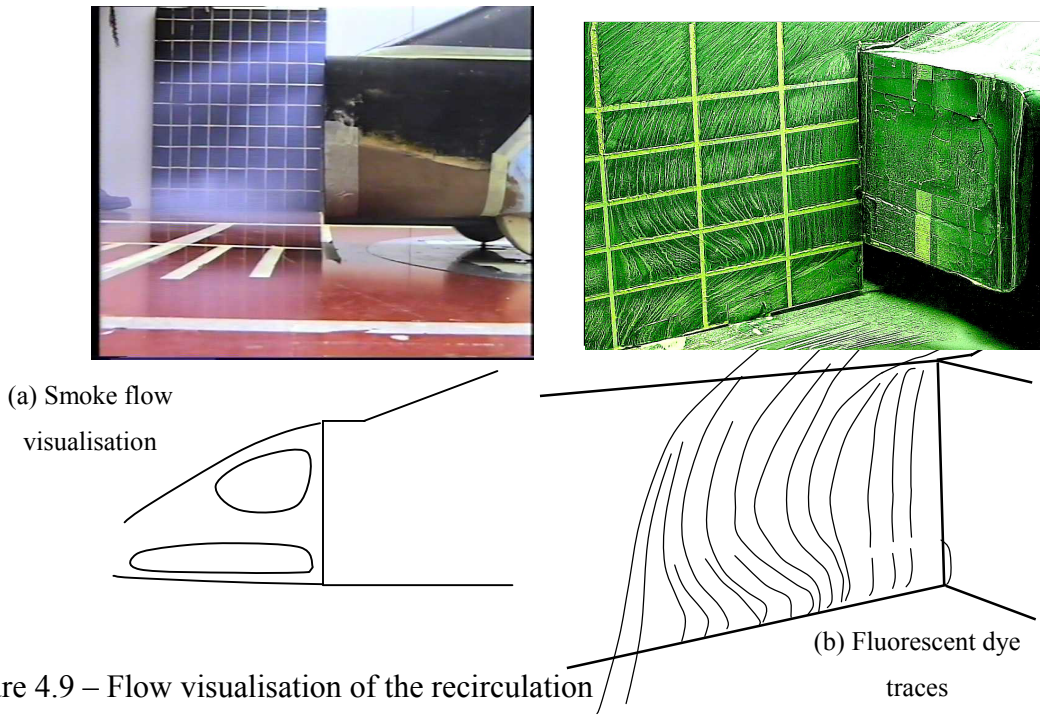

(a) Smoke flow visualisation

(b) Fluorescent dye traces

Figure 4.9 – Flow visualisation of the recirculation region

The images clearly show the general size and shape of the recirculation region and highlight two small regions of smoke build up, one above the other. Further visualisation using dye trace, figure 4.9b, showed streamlines of the vortex structure with the convex streamlines suggesting anti-clockwise rotation and the concave streamlines suggesting clockwise rotation.

From the discussions in section 2.2.1 it was concluded that the build up of smoke was the result of smoke becoming caught in the low velocity recirculation associated with two internal vortices that occur within the near wake recirculation region, refer to figures 2.3 and 2.5. From these images the upper of the two vortices was shown to be larger but generally shorter than the lower vortex. The smoke flow also highlighted the shear layer that forming from the back of the vehicle, separating the recirculation region from the mainstream flow. It was impossible to identify the sense of rotation of the vortices from the still images but the video footage of the smoke flow showed the lower vortex to rotate clockwise and the upper vortex anti-clockwise. The smoke flow visualisation study showed that the near wake recirculation region is a highly unsteady region with its the size and shape of these vortices continually changing.

Despite its unsteady nature it was possible, using a combination of 'snap-shot' images to make an estimate of the mean recirculation length. Figure 4.10 gives examples of the recirculation region, at the model centreline, at its observed minimum, mean and maximum positions. The recirculation length continually varied with a mean value observed at approximately 300mm or $x/l \sim 0.2$. The mean recirculation length is observed from figure 4.10b.

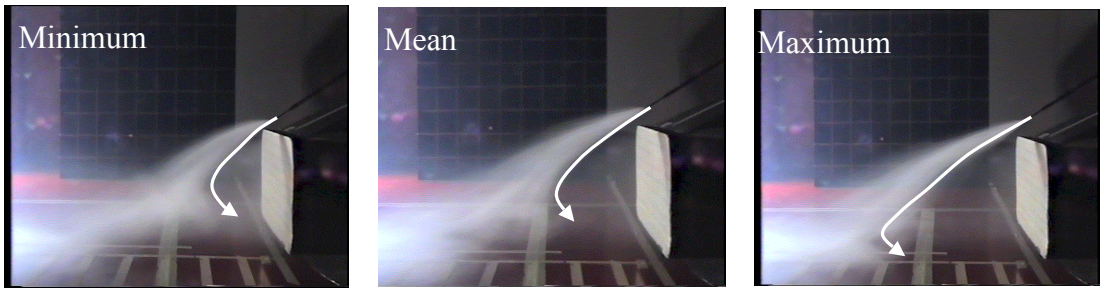

Figure 4.10 – Observed minimum, mean and maximum recirculation length at the model centreline

Figure 4.11a shows the velocity vector map of the near wake recirculation region captured at the model centreline using PIV. A two-tier contra-rotating vortex structure is clearly visible corresponding to the observations made in the flow visualisation study, figures 4.8-4.10. The upper vortex was more circular in shape and generally taller than the lower vortex rotating in an anti-clockwise direction figure 4.11b. The lower vortex was longer extending farther downstream and rotating clockwise. In comparison with the free stream velocity of 13m/s the velocity within the recirculation region was in the range of 1 to -3 m/s with the general rotation of both vortices in the order of ± 1m/s. There was a strong inflow region between the vortices upstream towards the base of the model due to their combined rotation where their upper and lower edges meet. Both the upper and lower vortex did not extend to the model base with the flow split into the vortices occurring at ~ x/l = 0.036, figure 4.11b. This is also shown in figure 4.9b from the dye traces of flow visualisation. As a consequence there was a region of positive streamwise velocity, $+\overline{u}$ very close to the model base albeit low in magnitude. The core of each vortex was identified from the vector map and indicated in figure 4.11a. The core of the upper vortex occurs at x/l ~ 0.070 and y/H ~ 0.289, and the core of the lower vortex is located at x/l ~ 0.076 and y/H ~ 0.174, where y is the distance from the floor and H is the total height of the model in mm.

From observation the mean recirculation length at the model centreline was estimated to be ~ x/l = 0.2, however it is clear from the contour map in figure 4.11a that the recirculation length is less than x/l = 0.2. The recirculation length was identified by the local minimum of $\overline{u}/U_{\infty}$ where U_{∞} is free stream velocity and $\overline{u}$ is the local mean component of u (Duell and George, 1999). Figure 4.11c presents a contour plot of $\overline{u}/U_{\infty}$ and shows the minimum of $\overline{u}/U_{\infty}$ at the model centreline to occur at x/l = 0.180, therefore the mean recirculation length at the model centreline was x/l = 0.180 or 248mm, slightly less than the observed estimate of x/l ~ 0.2. However the mean recirculation length was seen to change with distance from the model centreline due to a change in the relative size of the internal vortex structure. Figure 4.12 illustrates the vector map captured at z/b = 0.560 and shows clearly a different vortex structure than that seen at the model centreline

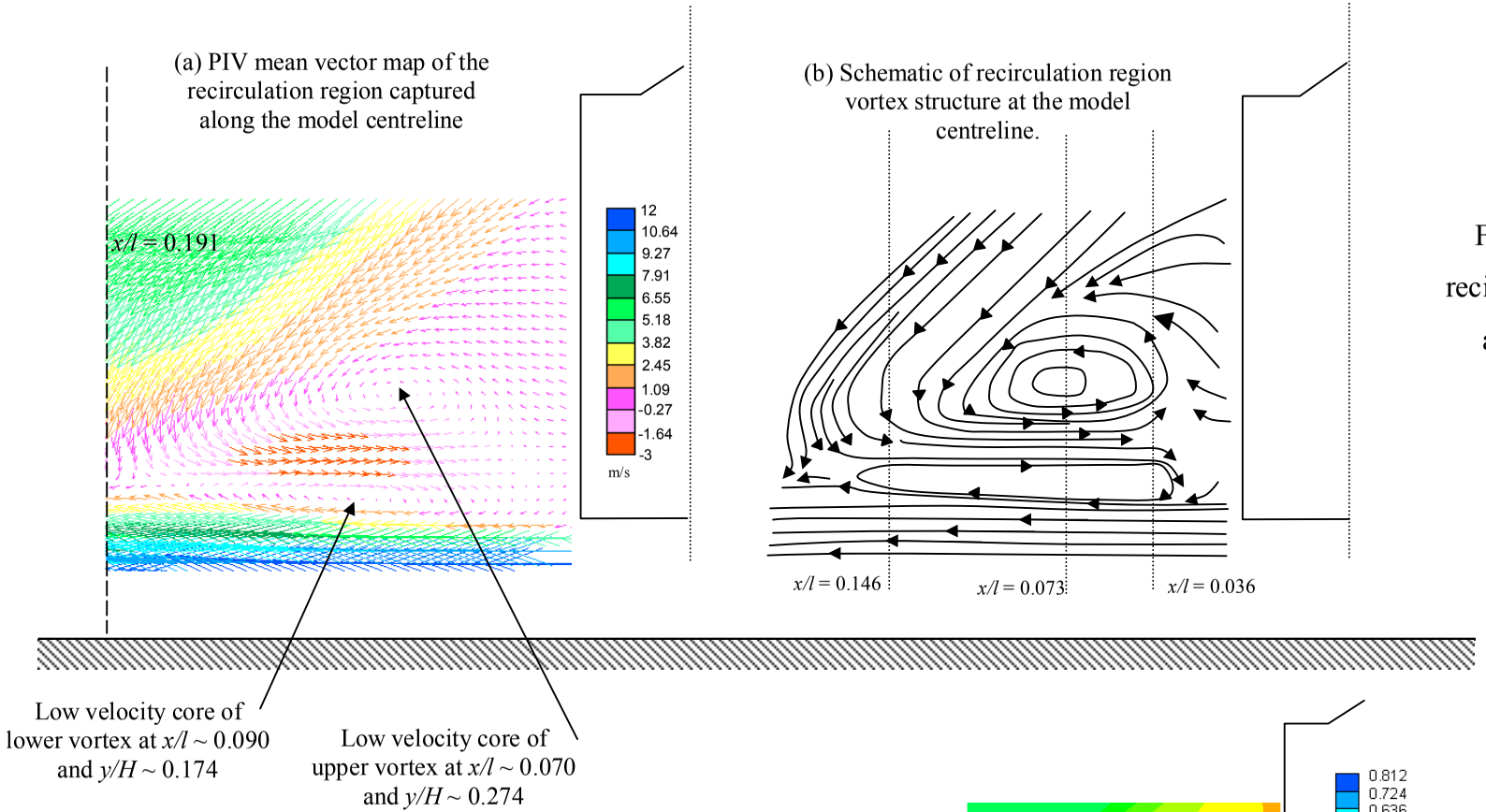

Figure 4.11 –Near wake recirculation region structure at the model centreline

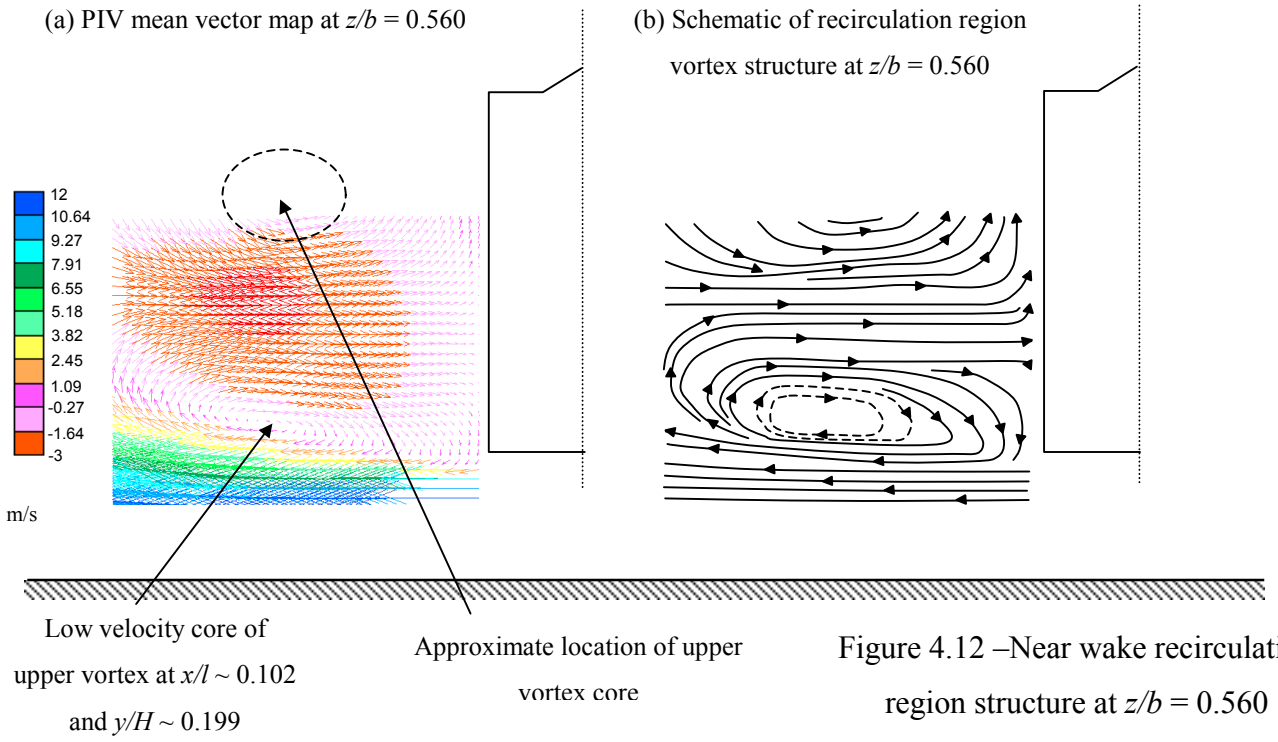

Figure 4.12 –Near wake recirculation region structure at $z/b = 0.560$

Cross-stream location $z/b = 0.560$ corresponds to the location of the representative exhaust used for the tracer gas measurement (chapter 5) therefore an insight into the flow structure at this location proves useful in understanding of the dispersion of a pollutant at this point. Comparing figures 4.11b and 4.12b, sketches of vortex structure at the centreline and $z/b = 0.560$ respectively, it is shown that the lower internal vortex becomes larger and more dominant with distance from the model centreline. Also figure 4.12 shows both vortices to extend closer into the model base with no region of $+\overline{u}$ as shown in figure 4.11a.

Due to a limited capture area (section 4.2.2) only part the of upper vortex was identified nevertheless it is clear from figure 4.12 that the upper vortex forms higher up within the recirculation region and that the upper and lower vortices become more equal in size at $z/b = 0.560$. The sense of rotation of the individual vortices remains the same but there is a stronger and wider inflow region between the two vortices, which results in a stronger rotation in the lower part of the upper vortex and in the upper part of the lower vortex. In addition the location of the core of each vortex is different with the core of the lower vortex located at $x/l \sim 0.110$ and $y/H \sim 0.199$,

farther downstream than at the model centreline. With only part of the upper vortex visible in figure 4.11a it was not possible to locate the core but the estimated location of the upper vortex core is indicated. Nevertheless it is evident from figure 4.12a that the core of the upper vortex occurs much higher up within the region than at the model centreline. While figure 4.12 also indicates the recirculation length at z/b = 0.560 to extend further downstream it was not possible to define this length as it extended further than the area of actual measurement. Nevertheless the estimated recirculation length at the model centreline, sense of rotation, structure and the locations of the vortex cores are sufficient for comparisons with the numerical simulations in chapter 6. Due to the change in vortex structure it is also anticipated that the location of the mean stagnation point i.e. point of minimum $\overline{u}/U_{\infty}$ will occur higher than y/H = 0.234 for z/b = 0.560, figure 4.11c (section 6.3). The change in recirculation region structure with distance from the model centreline is the result of the three-dimensional character of the flow field away from the model centreline and influences from the flow around the side edges and underneath the model close to z/b = 0.560.

The other important feature of the near wake flow field is the formation of the streamwise longitudinal vortices, (section 2.2). Figure 4.13a shows the cross-wake vector maps captured at x/l = 0.036, 0.073, 0.146 and 0.218 for one half side of the model base. The vector maps are presented in black and the relative vector length magnified by a factor of 4 (grid units/magnitude) for better clarity. The downstream development of the streamwise longitudinal vortex is shown by the increased anti-clockwise rotation within the flow field. An increased density of vector arrows denotes an increase velocity and therefore in rotational strength. At x/l = 0.036 there is little cross-flow $\overline{w}$ and only very weak positive and negative components of $\overline{v}$ due to the splitting of the flow into the upper and lower vortices figure 4.11. At both x/l = 0.073 and 0.146 there is only weak anti-clockwise rotation again due to the dominance of the streamwise rotation within the recirculation region. The anti-clockwise rotation becomes stronger with distance downstream i.e. at x/l = 0.218 as the dominant influence of the recirculation region lessens i.e. the vortex begins to grow around the trailing edge of the recirculation region (figure 2.2 and 2.3).

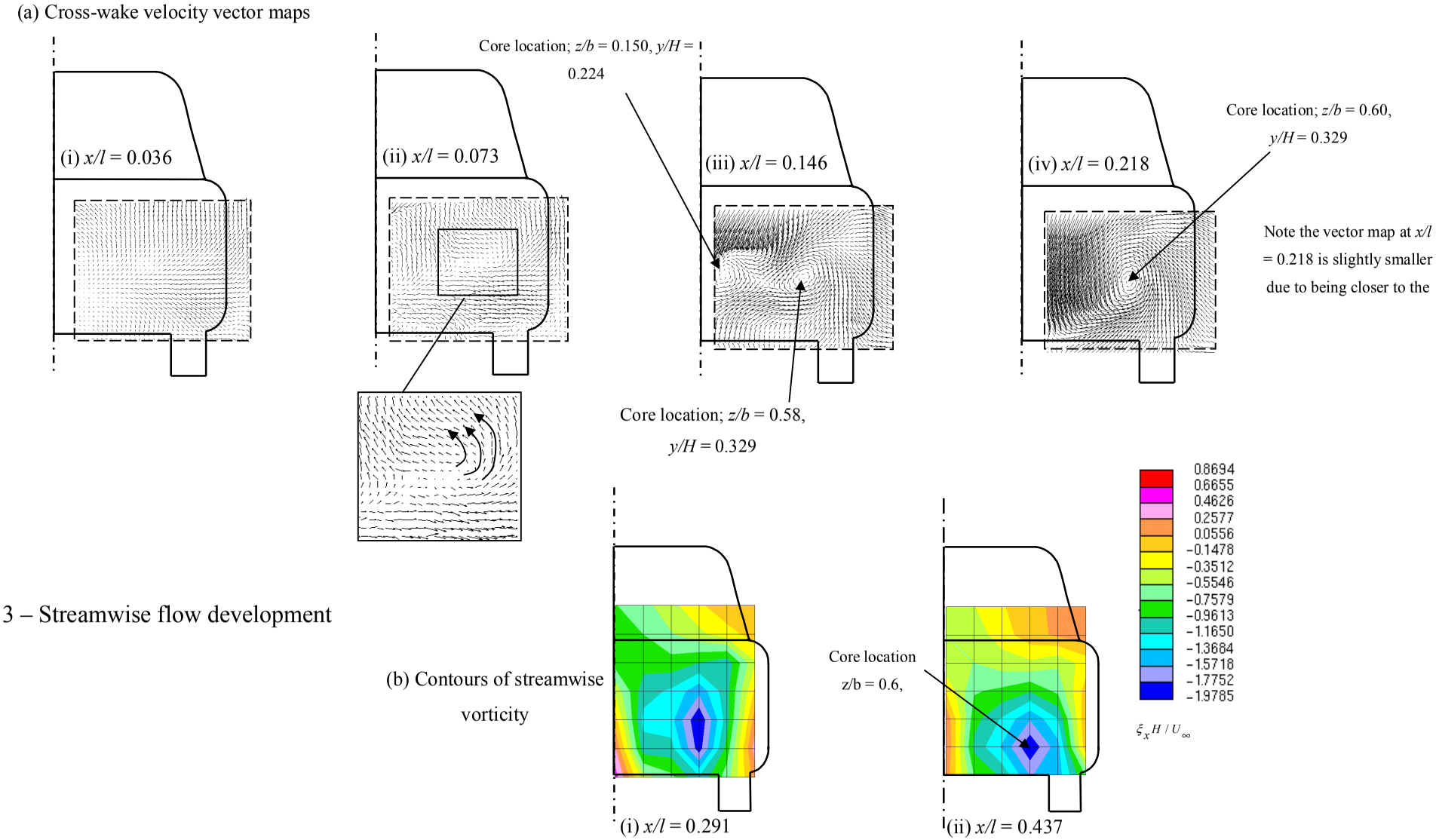

Figure 4.13 – Streamwise flow development

The longitudinal vortex develops with a low velocity core at z/b = 0.61, y/H = 0.348, at x/l = 0.218. Further downstream development of this vortex i.e. x/l > 0.218 is illustrated using streamwise vorticity, ξ_x calculated from the hotwire data, figure 4.13b (section 4.3.2). The spatial density of the hotwire measurements was insufficient[4.2] to create effective vector maps. Figure 4.13b presents contours of constant $\xi_x H / U_\infty$, where U_∞ is the free stream velocity and H is the height of the model where negative vorticity denotes anti-clockwise rotation. Peak negative vorticity corresponds to the vortex centre and is shown, in figure 4.13b(ii) to occur at y/H = 0.250, z/b = 0.56 as opposed to y/H = 0.348, z/b = 0.61 at x/l = 0.218. This suggests that the vortex core moves inwards and down towards the floor with increasing distance downstream behaviour similarly observed by Howell (1975) and Ahmed and Baumert (1979). It is likely that the increased rotation in the flow due to this vortex growth is responsible for the change in recirculation region structure. In addition the increased rotational strength of the vortex with distance downstream may have the effect of stretching the recirculation region thus resulting in the longer recirculation length in this region i.e. z/b = 0.560.

It should be noted that the vector map presented for x/l = 0.073 is slightly discomposed. This might be the result of inconsistent seeding particle concentration due to the unsteadiness within the recirculation region resulting in fewer image pairs for integration and thus a less accurate representation of the velocity field.

At x/l = 0.146 a second weak rotation close to the model centreline, similar in strength to the first was observed, figure 4.13c. From this brief investigation it is unclear whether this is a real effect or whether a consequence of short time-averaging i.e. the sample time was not long enough to resolve the true flow and the vortex shown is a more time dependent structure. A similar flow structure with two vortices was observed by Wang *et al* (1996) but when making instantaneous flow measurements in the wake of a vehicle using PIV. The instantaneous near wake flow structure of a road vehicle is highly chaotic with a constantly changing random-like

[4.2] Measurements using hotwire are time consuming as data is recorded point by point thus limiting the number of points to be measured in the time available.

flow structure. Figure 4.14 shows 4 instant vector maps captured at x/l = 0.146 illustrating this clearly. The time interval between each vector map is 4 seconds

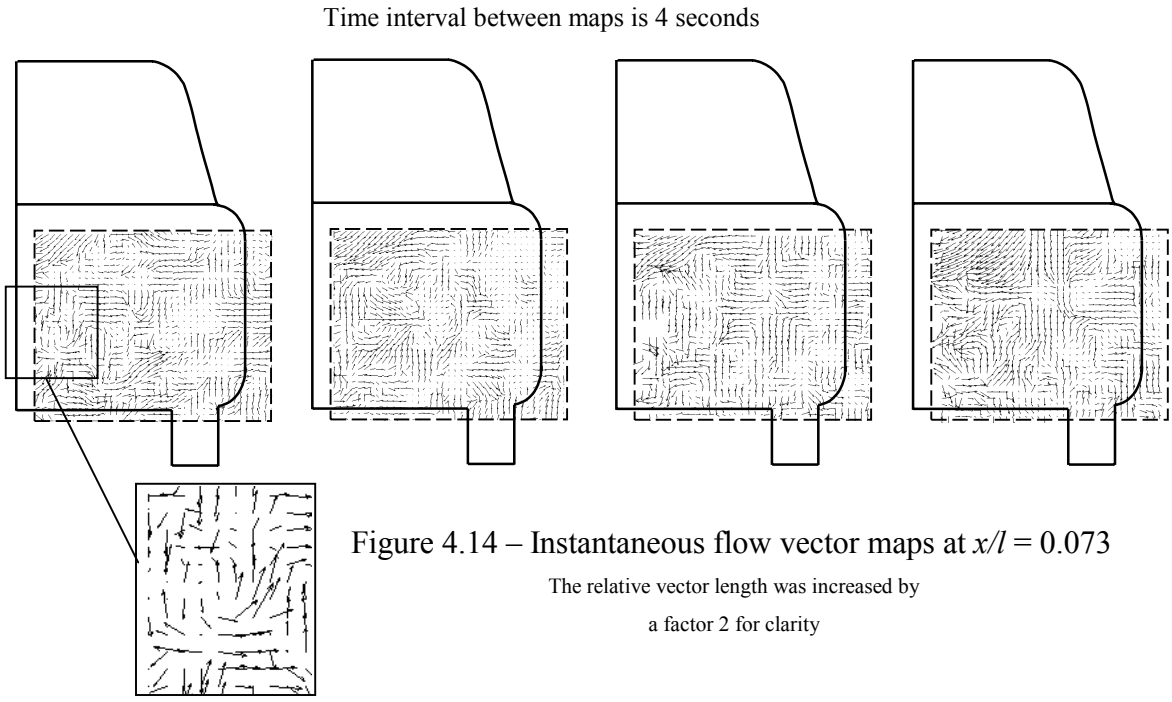

Figure 4.14 – Instantaneous flow vector maps at x/l = 0.073

The relative vector length was increased by a factor 2 for clarity

There is no clear definable structure in these or any other the vector maps examined. While some vector maps did show the small rotation close to the model centreline (as shown in figure 4.14) it is impossible to conclude that they contribute to the presented mean flow structure as the individual vector maps also show no indication of the other expected vortex.

The local streamwise turbulence intensity, *Iu* (equation 4.5) provides a measure of the intensity of streamwise turbulent fluctuations within the flow field. Figure 4.15 shows contour plots of percentage of *Iu* at the model centreline and at z/b = 0.560.

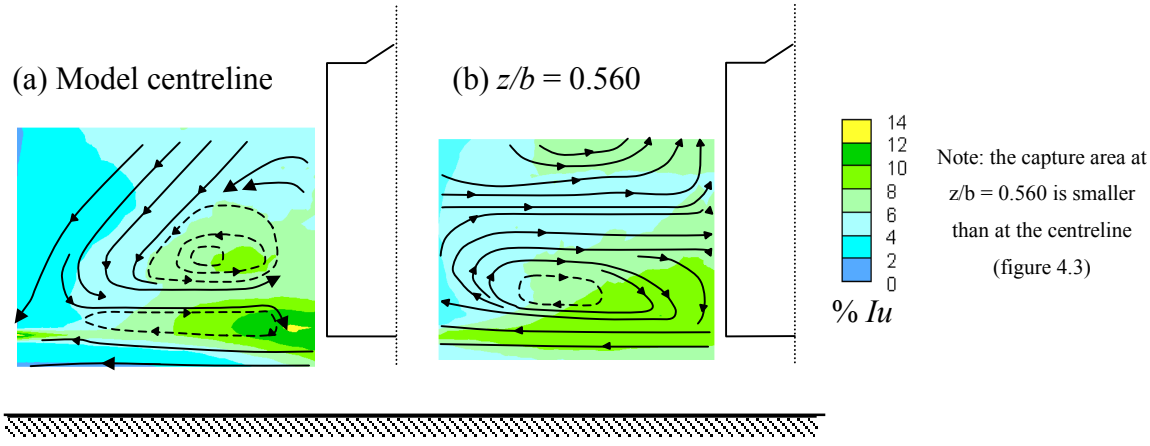

Figure 4.15 – Local streamwise turbulence intensity, *Iu*

In general levels of streamwise turbulence intensity are higher within the regions of unsteadiness which further supports the observations made during the flow visualisation study that the recirculation region is a highly unsteady in the streamwise direction. This unsteadiness is caused by a constantly changing flow structure within recirculation region. Figure 4.16 shows four consecutive vector maps captured at the model centreline with a time interval between each map of 0.5 sec.

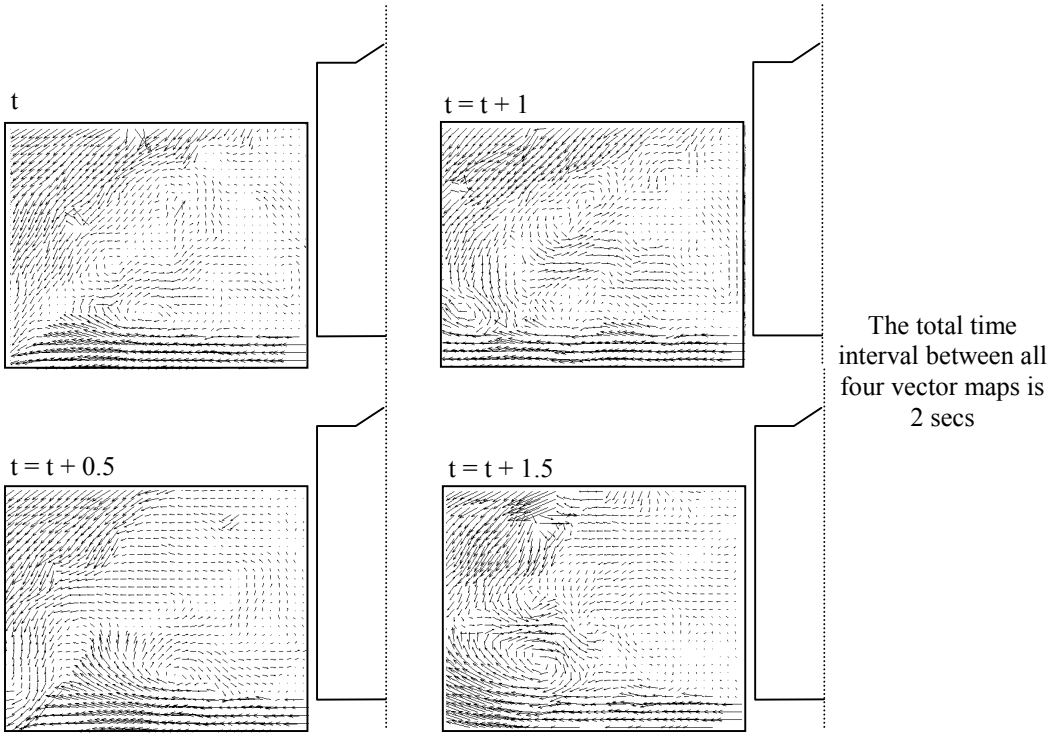

Figure 4.16 – Instantaneous flow structure at the model centreline

Note the vector maps are not aimed at illustrating any particular unsteady sequence but highlighting unsteadiness in the flow structure. The change in flow structure even over 2 seconds is clearly visible with many smaller vortices within the recirculation region as opposed to the two large contra-rotating vortices recorded in the mean flow structure. The streamwise unsteadiness in the flow field is caused by shedding of these vortices into the shear layer from the base of the model (section 2.2.2) with the frequency of this shedding dictating the unsteadiness within the region. The regions of high streamwise turbulence intensity shown in figure 4.15a are the result of vortex shedding from the lower edge of the model base and at the free stagnation point. It is the vortex shedding from the free stagnation point that causes fluctuations in free stagnation point and thus the recirculation length. Figure

4.15a showed an increase in Iu towards x/l = 0.180 illustrating the increase in streamwise fluctuations due to the fluctuations in the free stagnation point. The increase in energy fluctuations towards this point was observed in the spectral calculations (section 5.5). Spectral information was not obtained from the PIV velocity data as the frequency of capture, 2 maps per second, was not sufficient all spectral calculations but were performed using the instantaneous concentration data recorded and detailed in section 5.4, Chapter 5 i.e. the concentration field is driven by the unsteadiness in the flow field.

At this point the influence of the floor boundary layer should be mentioned. The boundary layer growth along the wind tunnel floor for the given flow speed, 13m/s was estimated to be 47mm at the model base increasing to 58mm at the furthest measurement point. From the vector plots presented for $x/l < 0.218$ it is unclear as to whether the floor boundary has influenced the flow, as the streamwise velocity component was not captured. However for the streamwise measurements at the centreline and at z/b = 0.560 the magnitude of velocity just below the model base is still close to a free stream value (figure 4.11a and figure 4.12a) therefore it may be implied that the floor boundary estimated has little or no influence on the flow.

4.6 Conclusions

The primary aim of the experimental study discussed was to obtain detailed velocity data for the validation of numerical simulations of the near wake flow field of a model vehicle (Chapter 6). Using both Particle Image Velocimetry (PIV) and hotwire techniques detailed velocity measurements of the near wake recirculation region were made and a comprehensive data set obtained for use in the validation of the numerical simulations. The data collected also provided a valuable insight into the principle near wake flow character of the model vehicle used, information subsequently used in the discussion of the near wake dispersion field (Chapter 5). Particular attention was paid to the structure of the near wake recirculation region close to the location of a representative exhaust used for the release of tracer gas during tracer gas measurements (Chapter 5).

Using detailed velocity vector maps the mean near wake recirculation region was shown to consist two contra-rotating vortices one on top of the other bounded on all sides by shear layers developing following flow separation at the model base edges. The upper and lower vortices rotated anti-clockwise and clockwise respectively. At the model centreline the upper vortex was shown to be more circular and greater in height than the lower but with the lower extending further downstream. At the model centreline both the upper and lower vortex did not extend to the model base with the flow split into the two vortices occurring at ~ x/l = 0.036, figure 4.11b. As a consequence there was a region of positive streamwise velocity, $+\overline{u}$ very close to the model base albeit low in magnitude. The mean recirculation length was at the model centreline was estimated to be x/l = 0.180. More importantly it was shown that the relative size of the internal vortices changed with distance from the model centreline becoming more equal in size and strength but maintaining their sense of rotation. The understanding of the flow character at this point provided valuable information to help in the discussions of tracer gas dispersion within the same region (Chapter 5). Both vortices extended closer in towards the model base at z/b = 0.560. The recirculation length was also observed to be longer at distance from the model centreline. One of a pair of streamwise longitudinal vortices was shown to develop from x/l = 0.146 downstream of the model base, rotating anti-clockwise and increasing in strength with distance downstream. The core of the vortex moved towards the floor with increasing x/l. After initial estimates of its size the wind tunnel floor boundary layer was believed to have no significant influence on the measured flow field.

Flow visualisation showed the instantaneous near wake flow and in particular the recirculation region to be highly unsteady. Instantaneous vector maps spanning 2 seconds were used to illustrate the significant changes in flow structure even over such a short period. The recirculation region structure was seen to be highly chaotic with many smaller vortices as opposed to the two large contra-rotating vortices recorded in the mean flow structure. Calculated values of streamwise turbulence intensity showed peaks at the model base and close to the mean stagnation point at the model centreline, which were believed to be the result of these smaller vortices being shed from the model base edges into the shear layers and their subsequent shedding from the free stagnation point. Vortex shedding from the free stagnation

pint causes the primary unsteadiness and fluctuations in the near wake recirculation length. It was therefore clear that in reality the near wake field is highly chaotic and that while it was necessary for the validation of numerical simulations to obtain detailed data on the mean flow field, in nature the neat organised structures presented do not exist over short time periods. As a consequence the data presented is only a time-averaged interpretation of a constantly changing flow structure and has shown can reveal flow characteristics, which might not necessarily represent the mean flow structure i.e. a double vortex streamwise rotation in a region where it would not normally be anticipated due to insufficient time averaging.

Chapter 5: Experimental Study 2 – Measurement of tracer gas concentration within the near wake of a model vehicle

5.1 Introduction

The following chapter describes an experimental study in which measurements of the mean concentration of a tracer gas within the near wake of the model vehicle were made. The primary aim of the experiment was to obtain mean concentration data for the validation of numerical simulations of the same dispersion field (Chapter 7). Mean concentration data was collected for direct validation and their uncertainties determined for criteria used in statistical validation. The data collected also provided a valuable insight into the dispersion character of the near wake of the model considered.

Flow visualisation study was conducted to provided additional information on the dispersion character of the near wake flow of the model vehicle considered. Spectral methods were used to analyse the unsteady character of the near wake dispersion field (section 5.5).

While the technique used to measure tracer gas concentration is well established its application for detailed dispersion measurements in the near wake at the model scale road vehicle is relatively unfamiliar. Tracer gas was introduced into the near wake flow using a novel approach in that involved releasing the tracer through a representative exhaust.

5.2 Equipment set-up and measurement details

An experiment to measure the concentration distribution of a tracer gas in the near wake of the MIRA 33% scale reference car is detailed. For model and wind tunnel specifications refer to section 4.2.1. The experimental study had two parts: the

measurement of the concentration distribution of a tracer gas using a flame ionisation detector (FID) and flow visualisation using smoke.

5.2.1. Flame ionisation detector (FID)

A Flame Ionisation Detector (FID) was used to measure the concentration of a tracer gas introduced into the near wake of the MIRA 33% scale reference model (fastback). A FID detects the presence of any hydrocarbon (HC) and works by measuring the quantity of ions generated when a sample containing a HC is burnt in a hydrogen flame. The ions are detected by means of a high voltage collector, and as the leakage current from the collector is proportional to the number of ions generated, the leakage current gives a measure of the HC concentration in the sample, figure 5.1.

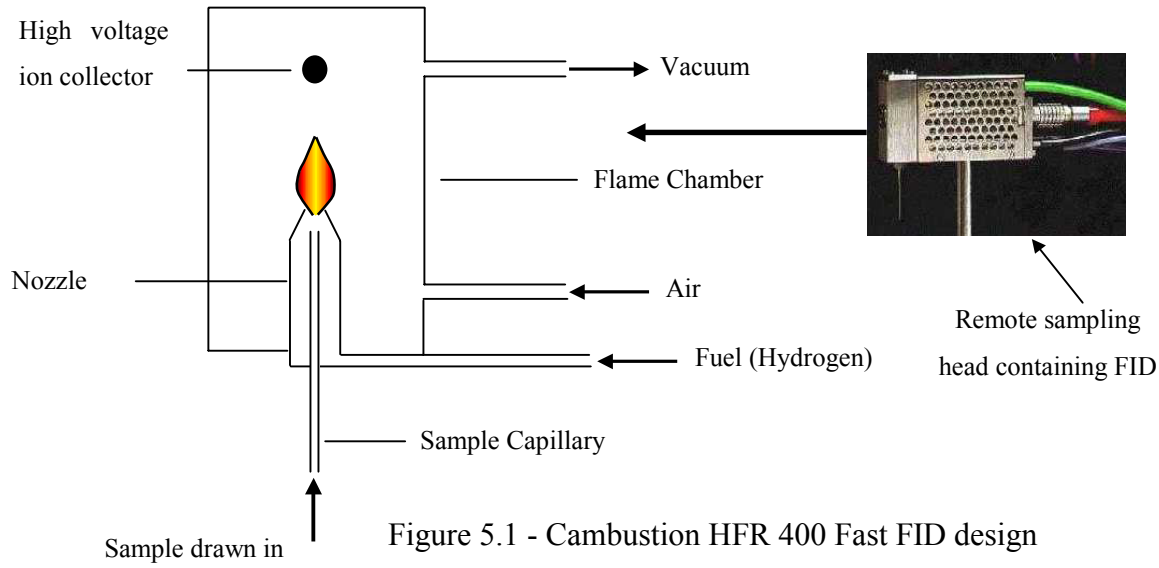

Figure 5.1 - Cambustion HFR 400 Fast FID design

Two remote sampling heads were used (figure 5.1) and are referred to as FID 1 and FID 2 from this point forward. The system used was dual channel enabling simultaneous real time measurement at two separate locations in the flow. The FID gave millisecond time-scale response times. (The response time of standard FID equipment is often much slower - 1-2 seconds) and was capable of reliable measurement of a hydrocarbon gas at levels down to 0.1ppm by volume. Full system specification is given in Appendix 3a. The FID MCU (Main Control Unit) was

located to one side of the wind tunnel working section in the plenum region, figure 5.2. The FID heads were mounted on a computer controlled 2D light-weight traverse using a custom-made support arm and were fixed 250mm apart allowing measurements to be made at two separate points simultaneously. From the photographs shown in figure 5.2 it is clear that the FID heads may have interfered with the flow field in the near wake at the lowest measurement points.

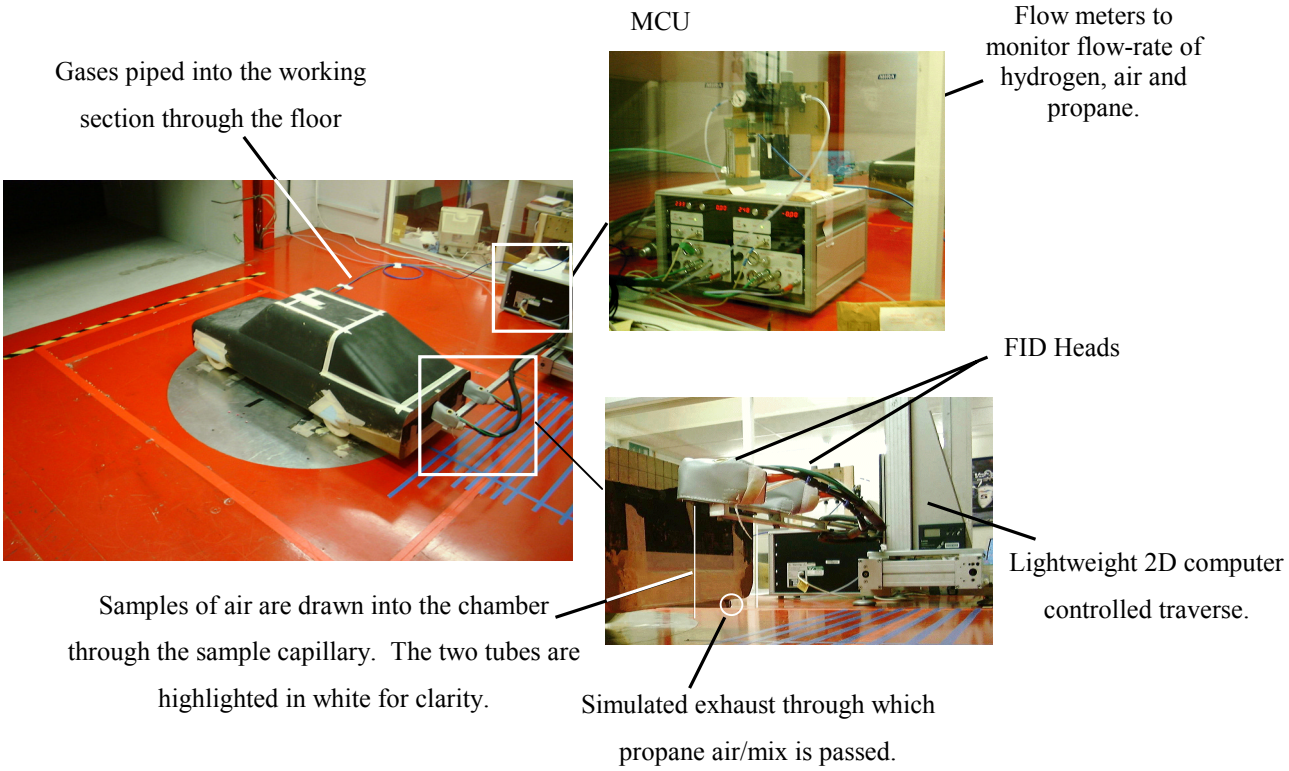

Figure 5.2 – Experimental set-up

Temperature sensors monitored the operating temperature of each FID head (typically 150-450°C) and if the FID temperature dropped below the minimum operating temperature the hydrogen supply was automatically cut-off and the flame in the FID head extinguished. The FID heads were covered with insulating jackets to help maintain temperature in the cooling airflow of the wind tunnel. Each sample capillary was 200mm long. The model position was the same as for the wake survey, Appendix 2a

FIDs are commonly used for the study of pollutant and odour dispersion but generally operated at much lower wind speeds than used in the current study i.e. 13m/s or 30mph model scale. While Hargreaves (1997) also used FIDs to measure gas concentrations in the wake of a $1/50^{th}$ scale lorry the application of a FID system for the detailed concentration measurements close behind a model vehicle at this scale, 33% and in a wind tunnel of this type was new.

A 1.1% propane/air mix was used as the tracer gas with a density of 1.3309 kg/m^3 at 17°C. A safety assessment was carried out to assess the potential risks in using a propane/air mix in the confined environment of the wind tunnel and safety precautions and emergency procedures put in place. However with the maximum source strength of 1.1% the level of concentration remained below the lower explosive limit of propane (2.2%) at all times. Gas cylinders containing the supplies of compressed air, hydrogen and 1.1% propane/air mix were located away from the test area therefore supplies were piped to the wind tunnel working section via nylon tubing. The tracer gas was introduced into the near wake flow using a novel approach in that the propane/air mix was delivered through a representative exhaust pipe located as typical for most road vehicles, to one side of the model base, figure 5.2. A copper pipe 12mm in diameter was fixed 150mm (z/b = 0.560) from the model centreline. The representative exhaust was not in place during the wake survey but it was anticipated that its inclusion would have negligible influence on the structure of the near wake itself. The recirculation region develops due to streamwise separation from the model base and with the exhaust being parallel to the streamwise flow it was unlikely to have a significant influence on flow separation. The exhaust height represented only 17% of the total ground clearance therefore while its presence would slightly modify the flow underneath the model it was believed that it would not significantly effect the development of the longitudinal vortices (section 2.2.1).

5.2.1.1 Calibration of the FID

Calibration of the FID was carried out in the wind tunnel, with no wind. Teflon bags were used to hold a sample of the compressed air and propane/air mix. Each sample

of gas with known concentration was placed over the sample capillary of each FID head until a steady output voltage was achieved, figure 5.3. The compressed air was hydrocarbon free air or 'clean air' and used to obtain a static zero reading for both FID 1 and 2. The propane/air mix was used to obtain a maximum or 100% source reading for each FID.

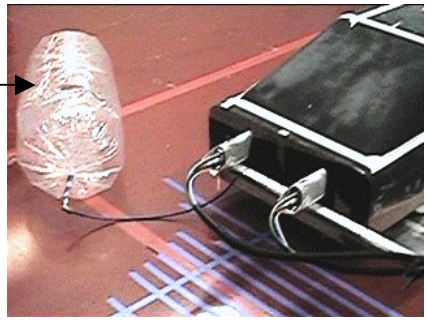

Figure 5.3 – FID calibration

A calibration factor C_f, determined using,

$$C_f = \frac{S}{z_{off}} \tag{5.1}$$

where S is the maximum source strength (ppm of propane) and z_{off} is the zero wind-off reading and thus a standard or mean calibration factor determined. The calibration factor applied to the raw data was 596.15ppm/volt (parts per million/volt) to obtain actual concentration of propane, equation (5.4).

5.2.2 Flow visualisation

A flow visualisation study was conducted to gain additional insight into the dispersion characteristics of the near wake of the model vehicle. Smoke was introduced through the representative exhaust and images recorded using a video camera. Details of the equipment used are given in section 4.2.5. The study was conducted at a free stream velocity of 13m/s, the same as for the concentration and velocity measurements.

5.2.3 Measurement area

Measurements were made at 92 spatial locations at four positions downstream of the model: x/l = 0.036, 0.073, 0.146, 0.218, figure 5.4. These downstream measurement locations correspond to those used for velocity measurements (section 4.2.2) thus enabling the concentration field in relation to the velocity field to be discussed with some confidence. For convenience a similar survey grid to that defined for the hotwire measurements (section 4.2.3) was used applying the same point numbers. There was a minor difference in the spatial location of the points due to a different datum position. The red square in figure 5.4 highlights the actual measured area for the concentration field. Measurements were not taken any further downstream than x/l = 0.218 due practical difficulties discussed in section 5.4.2. As a consequence the survey area only covered the near wake recirculation region and measurements within the developing flow downstream were not obtained. Only the dispersion character of the recirculation region is therefore discussed.

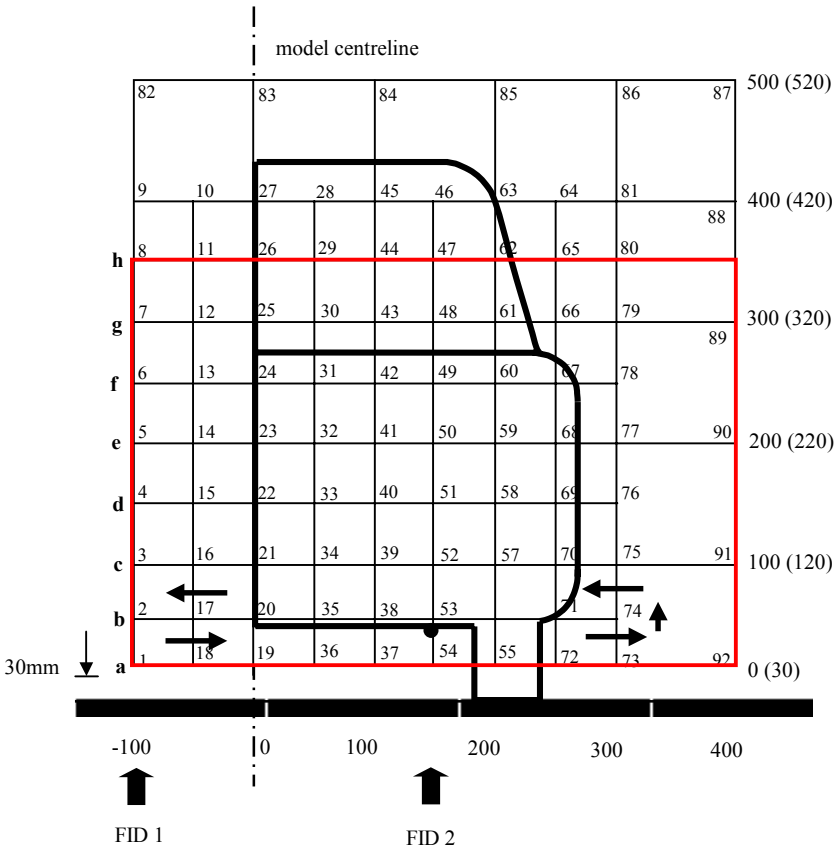

Figure 5.4 – Survey grid for gaseous measurements

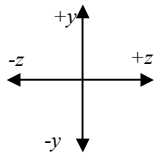

Numbers in brackets show the actual distance above the ground

View looking at the base of the model

Measurements were made one row at a time as the traverse could not be fully automated and only one half of the model base was considered. Figure 5.4 shows the initial position of FID1 and FID2 with the arrows showing the direction of traverse movement. The arrangement of the fids meant that certain points were measured twice

5.2.4 Measured data

Measurements were made at each grid point for all downstream locations at 1500Hz collecting, a total 16384 data per measurement point over a period of 11secs. At equivalent full scale for the same vehicle speed this equates to a 33 second sample time. Ideally for an unsteady flow the sample time would be longer in order to obtain a representative mean but this method of point by point concentration measurement was time consuming therefore in order to obtain sufficient data for validation the sample time was restricted. However subsequent spectral analysis of the concentration data (section 5.5) showed concentration fluctuations at mode1 scale to be of the order 3-84 Hz therefore it is believed that the sample time employed was sufficient to obtain mean concentration data for validation.

Data was recorded initially as a voltage and converted to actual concentrations after the test. Both instantaneous and mean voltages were recorded. The test was conducted at 13m/s, the same flow speed as used in the wake survey with a Reynolds number based on model length of 1.189×10^6.

While it was not the intention to reproduce exact exhaust conditions in the experimental study it was thought appropriate to base the flow rate of the tracer gas on that typical of an average road vehicle. The effect of high temperature and plume buoyancy were not considered. For a 1.6 litre engine vehicle in a typical urban cycle the volume flow rate at exhaust was calculated to be $0.005782 m^3/s$[5.1], which at 33% model scale equates to $0.00064244 m^3/s$. However subsequent restrictions on the supply of tracer gas meant the flow rate used was $0.0000527 m^3/s$ and while this was

[5.1] Information supplied by Les Smith, Motor Industry Research Association.

less than anticipated it was of not as the main aim was to obtain concentration data for validation of numerical simulations of the same concentration field.

5.2.4.1 Concentration data

Both mean and instantaneous voltage data were recorded at each grid point for all distances downstream of the model and stored as voltages in data files. The mean data values were established through the time-average of the instantaneous data,

$$\overline{\mathrm{V}}_{rd} = \frac{1}{\mathrm{n}} \sum_{i=1}^{\mathrm{n}} \mathrm{V}_{rd}{}^{i} \tag{5.2}$$

where $\overline{\mathrm{V}}_{rd}$ is the mean of the raw voltage data and V_{rd} is the instantaneous raw voltage data and n is the number of samples. In addition to the wind-off zero obtained during the calibration zero readings, z_r were also taken at the beginning of each row of data points i.e. rows a-h shown in figure 5.4. The actual mean voltage, $\overline{\mathrm{V}}_{act}$, at each point was determined by,

$$\overline{\mathrm{V}}_{act} = \overline{\mathrm{V}}_{rd} - z_r \tag{5.3}$$

where z_r is the wind-on zero reading taken at the beginning of each row. This additional new zero took into account any zero drift between the start and end of each row. The actual mean voltage data was converted in to actual mean concentration data using,

$$\overline{c} = \overline{\mathrm{V}}_{act} \cdot C_f \tag{5.4}$$

where $\overline{c}$ is the mean concentration expressed in parts per million concentration. For the points at which two sets of data were measured an average of the two calculated values of $\overline{c}$ was taken.

5.3. Experimental data uncertainty and numerical validation criteria

The uncertainties associated with both the raw voltage data and calculated quantities are estimated with the uncertainties in recorded mean concentration $\overline{c}$ required for statistical validation of the numerical simulations of tracer gas dispersion (section 3.5). The calculated uncertainties also provide a measure of the quality of the measured data.

With reference to the analysis in section 4.4 the uncertainty of the direct measured data or raw data is expressed in terms of the standard error on the mean, S_m and the uncertainty of data calculated from a combination of values is determined through combining S_m of the individual values as in section 4.4.2. The analysis was performed essentially to establish the criteria used in the statistical validation (section 3.5) of the numerical simulations of tracer gas concentration but also provided information on the uncertainty of the mean data presented here.

The analysis assumed the data to be normally distributed and Appendix 3b(i) shows the measured raw data to generally fit a normal distribution with the exception of points at the maximum local concentration i.e. point 53 was lies within 50mm (x/l = 0.036) of the source. The distribution of concentration at this point was slightly skewed, which may be due to the close proximity of the source and irregularities in the tracer gas flow rate causing high peaks in concentration, see Appendix 3b(ii). For this reason point 53 at x/l = 0.036 and 0.146 and point 54 at x/l = 0.073 were not considered in the analysis.

5.3.1 Uncertainty in raw data

The raw voltage data included voltage data measured at each point and the calibration or 'wind-off' zero data. In accordance with section 4.4.2 the overall maximum in $S_{\overline{rd}}$, $S_{\overline{rd}\,(MAX)}$, for each FID head was determined and expressed with a 95% confidence i.e. $2\,S_{\overline{rd}\,(MAX)}$ and are given in Table 5.1, where $S_{\overline{rd}}$ represents the

standard error on the mean or uncertainty in the raw voltage data. The uncertainty in the calibration data is represented by the standard error on the mean of the wind-off zero data, $S_{\bar{z}_{off}}$ i.e. the uncertainties in the wind-off zero readings used to calculate the calibration factor. The value of $S_{\bar{z}_{off}}$ is also given in Table 5.1.

$S_{\overline{rd}_{(MAX\ FID1)}}$	$S_{\overline{rd}_{(MAX\ FID2)}}$	$S_{\bar{z}_{off\,(FID1)}}$	$S_{\bar{z}_{off\,(FID2)}}$	$S_{\overline{V}_{off\,(FID1)}}$	$S_{\overline{V}_{off\,(FID2)}}$
±0.0088	±0.0132	±0.0066	±0.0072	±0.0182	±0.0064

Table 5.1 – Maximum uncertainties in raw data with 95% confidence (in volts)

$S_{V_{off\,(FID1)}}$ and $S_{V_{off\,(FID2)}}$ represent the uncertainty in the voltage readings taken at maximum concentration during the wind-off calibration. The maximum voltage readings corresponding to $S_{V_{off\,(FID1)}}$ and $S_{V_{off\,(FID2)}}$ are 6.147volts and 6.460volts respectively. The overall maximum uncertainty occurs at *x/l* = 0.0036 closest to the source.

5.3.2 Uncertainty in actual data

The actual mean voltages, $\overline{V}_{act}$ were calculated by applying the zero readings to the mean raw voltage data $\overline{V}_{rd}$, equation (5.3). However these zero readings also had an associated uncertainty, therefore the uncertainty in the actual measured voltages were calculated using the methods detailed by Pentz and Shott (1988), Appendix 2f. Using expression A2f-1 the maximum uncertainty wit in the actual mean voltages h 95% confidence were expressed as,

$$E_{\overline{V}_{act\,(MAX)}} = \sqrt{(S_{\overline{rd}\,(MAX)})^2 + (S_{z_r\,(MAX)})^2} \qquad (5.5)$$

where $S_{\overline{rd}\,(MAX)}$ and $S_{z_{r\,(MAX)}}$ are the maximum standard error on the mean for the mean raw voltage data and wind-on zeros at the beginning of each row respectively, with

95% confidence. $E_{\overline{V}_{act(MAX)}}$ was calculated for FID 1 and FID 2. The maximum uncertainty in actual voltage data from FID 1 was $\overline{V}_{act} \pm 0.008$ volts and for FID 2 $\overline{V}_{act} \pm 0.013$volts. Higher uncertainties occurred generally where the concentration was higher.

The actual mean concentration, $\overline{c}$ of tracer gas was calculated using equation (5.4). Both $\overline{V}_{act}$ and C_f have an uncertainty associated with them therefore the uncertainty in $\overline{c}$ maybe expressed with 95% confidence as, refer to Appendix 3d for workings,

$$E_{\overline{c}} = SA\sqrt{\frac{(S_{\overline{rd}})^2 + (S_{z_r})^2}{\left(\overline{V}_{rd} - z_r\right)^2} + \left(\frac{S_{z_{off}}}{z_{off}}\right)^2} \tag{5.6}$$

where $A = \dfrac{\overline{V}_{rd} - z_r}{z_{off}}$ and S is the maximum source strength. $E_{\overline{c}}$ was calculated for all values of $\overline{c}$ for FID 1 and FID 2 as appropriate. The analysis showed the uncertainty in $\overline{c}$ to be highest at $x/l = 0.036$ at the point of maximum concentration. However the distribution of c' at the point of maximum concentration was shown to be non-normal (Appendix 3bii) therefore the uncertainty value at this point was not reliable. With this is mind it was appropriate to express the uncertainty in $\overline{c}$ in terms of the second highest uncertainty at $x/l = 0.036$. The maximum uncertainty in $\overline{c}$ at $x/l = 0.036$ for FID 1 was $\overline{c} \pm 5.96$ppm of propane and for FID 2 was $\overline{c} \pm 4.02$ppm of propane with a 95% confidence. The maximum calculated value of $\overline{c}$ at $x/l = 0.036$ was 744ppm of propane.

5.4 Discussion of experimental results

Flow visualisation was achieved by introducing smoke into the near wake flow via the representative exhaust and revealed several interesting features. Figure 5.5 shows a sample of still images taken from the video footage. A simplified schematic of the vortex structure measured at the exhaust location i.e. $z/b = 0.560$ is shown in figure 5.5a(i) to aid in the discussion.

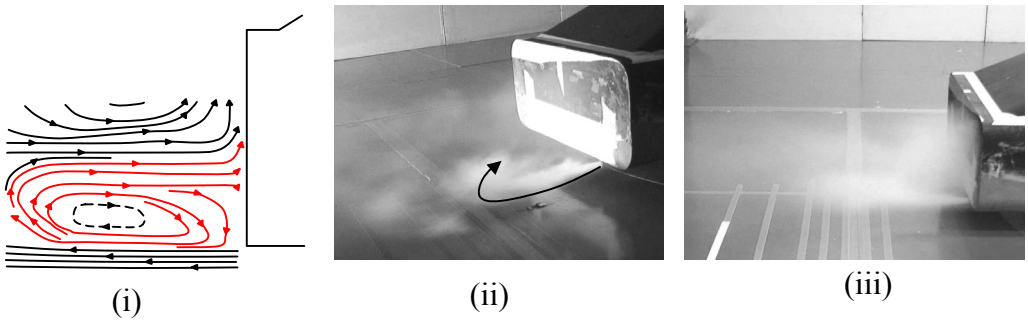

(i) (ii) (iii)

(a) – Smoke distribution within the recirculation region

(b) – Uneven smoke distribution.

Figure 5.5 - Still images of smoke flow visualisation

The first image, figure 5.5a(ii) shows the smoke from the exhaust plume to be drawn upwards into the near wake recirculation region. The smoke is 'picked-up' by the lower inner vortex and then fed in to the upper vortex of the recirculation region the mechanism of which is highlighted in red in figure 5.5a(i). The smoke distribution within the recirculation region was highly unsteady with the density of smoke within the upper region seen to lessen every 1-2 seconds. This behaviour was typical of that observed during the study.

Flow visualisation also showed a constantly changing smoke flow around the exhaust plume. The exhaust plume was seen to fluctuate rapidly while at the same time smoke was being drawn into the near wake. Similar fluctuations were observed at the bottom edge of the model base during the flow visualisation described in section 4.5 and were thought to result from fluctuations in the recirculation length and unsteadiness in the shear layer emanating from the lower edge of the model base (section 2.2.2). This behaviour highlights the fluctuating and unsteady nature of the near wake recirculation region. More detail on the unsteady character of the near wake and the exhaust plume are discussed in section 5.5.1.

The representative exhaust was positioned, typical of most road vehicles, to one side of the vehicle the dispersion pattern of the smoke was therefore concentrated to one side of the model base with a greater concentration closer to the exhaust, figure 5.5b. A small amount of smoke was observed on the opposite side of the model base most likely carried across through a combination of recirculation and weak cross flow within the recirculation region, to be discussed in the following section. This brings in to question the assumption of centreline made in the numerical simulations of the tracer gas dispersion and will be discussed further in the following section.

5.4.1 Mean concentration $\overline{c}$

The following discussion focuses on the mean or time averaged concentration distribution. However in reality the instantaneous near wake field of a road vehicle is highly chaotic therefore the instantaneous dispersion patterns would also be random and not necessarily exhibit the clear flow structures presented here. To establish a true mean flow field time averaging should ideally be over much longer periods of time than used but practical limitations did not allow for this. As a consequence while the data presented shows a clear mean distributions of concentration it must be remembered that this is only a time-averaged interpretation of a constantly concentration field. This is discussed further in section 5.5.

Both mean and instantaneous values of the tracer gas were determined at x/l = 0.036, 0.073, 0.146, 0.218 downstream of the model according to the measurement grid shown in figure 5.4. Mean concentration measurements at x/l = 0.218 were not used as dropping fuel pressure in the FID system rendered the data unreliable. It was for this reason that any measurements further downstream of x/l = 0.218 were not taken therefore the ensuing discussion focuses on the dispersion character of the recirculation region only.

During the test the readings at each point were closely monitored and where it was apparent that the FID was no longer detecting any tracer gas no more readings were made. For plotting purposes the concentration at these points was set to zero.

Figure 5.6 (a-c) shows the measured concentration field (ppm of propane) at x/l = 0.036, 0.073 and 0.146 with vector maps showing the flow structure at the model centreline and z/b = 0.560 in (d) and (e) respectively. It should be noted that while the maximum measured mean concentration $\overline{c}$ recorded at x/l = 0.036 and 0.073 was 744 and 229 ppm of propane respectively the scale shown in figure 5.6 only reaches 60 ppm of propane. This was because rapid dispersion away from the source reduced the value of $\overline{c}$ quickly thus the scale shown was more appropriate for illustrating the main features of the dispersion.

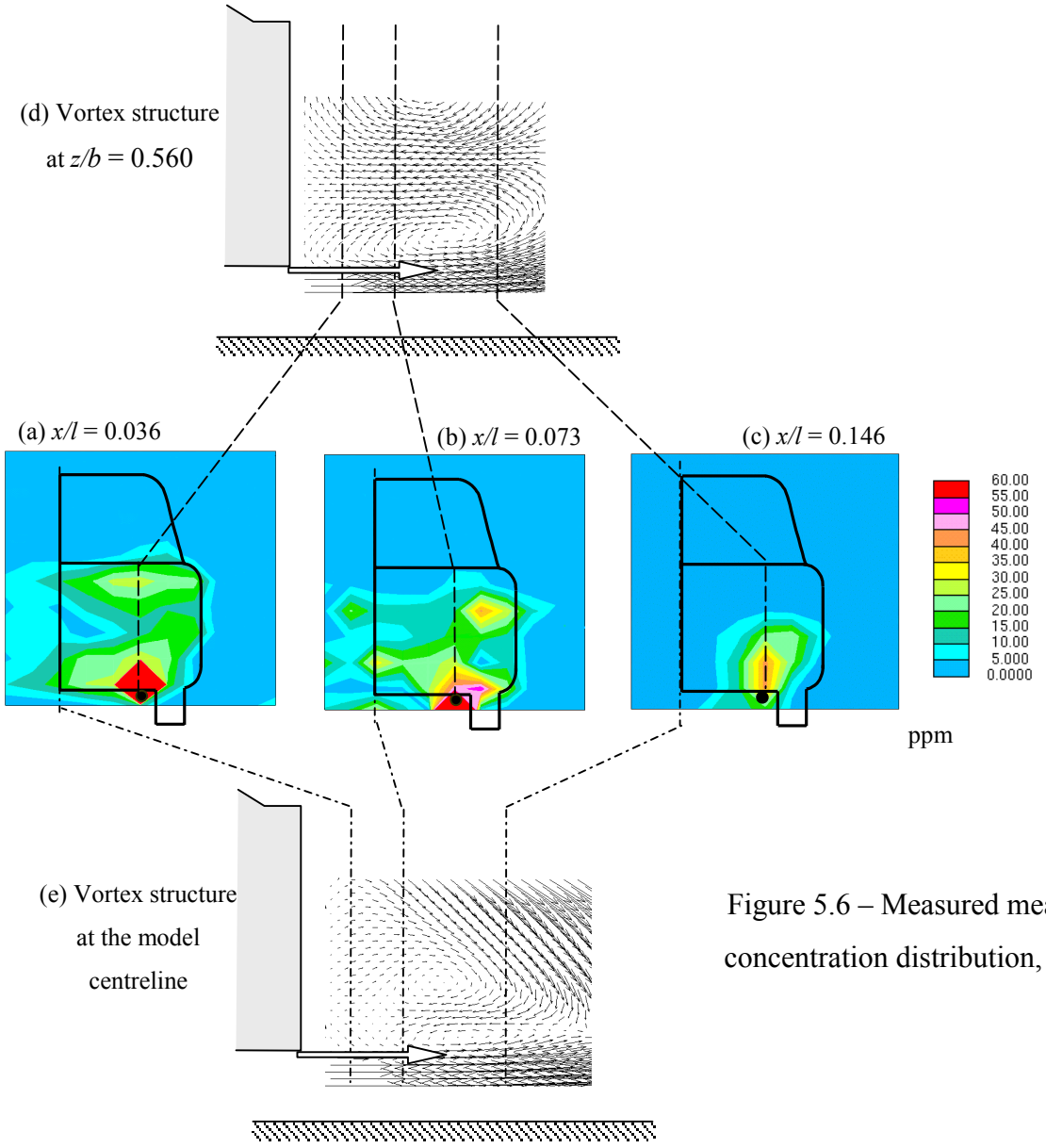

Figure 5.6 – Measured mean concentration distribution, $\overline{c}$

The overall distribution of $\bar{c}$ shows a general upward dispersion of tracer gas reinforcing the observations made during flow visualisation that pollutant is drawn up into the recirculation region through the lower internal vortex. With reference to the concentration fields figure 5.6 (a-c) and the corresponding vector plots of vortex structure the recorded distribution of $\bar{c}$ may be explained.

The distributions of $\bar{c}$ at x/l = 0.036 and 0.073 are significantly different than at x/l = 0.146. With reference to the vortex structure at z/b = 0.560 figure 5.6d it is clear that x/l = 0.146 is a primary "pick-up" point for tracer gas from the exhaust plume, with initial pick-up occurring just downstream of the lower vortex core i.e. at ~ x/l > 110 figure 5.6e. Tracer gas is being drawn up into the recirculation region by the anti-clockwise rotation of the lower vortex hence the elongated distribution of $\bar{c}$ in comparison to that at x/l = 0.036 and 0.073 for z/b = 0.560. From this point tracer gas is then recirculated by the lower vortex back towards the base of the model and in to the upper vortex. The overall distribution of $\bar{c}$ at x/l = 0.146 is not as wide spread due to changes in the relative vortex sizes within the recirculation region with increased distance from the model centreline. Comparing velocity vector plots for the model centreline and z/b = 0.560, figure 5.6 d-e it is seen that while both x/l = 0.036 and 0.073 always fall within the recirculation region, x/l = 0.146 falls towards the end at the model centreline and as a consequence is under the influence of a significantly different flow pattern at the centreline than at z/b = 0.560. As a result any cross-stream spread of tracer gas towards the centreline is carried away by the faster flow within the surrounding shear layers which are more dominant at this point thus resulting in a smaller cross-stream concentration field. Cross-wake velocity measurements made at x/l = 0.146 showed two cross-wake vortices side by side in the flow, figure 4.13 however it was believed that the second of these vortices close to the model centreline was result of insufficient flow time-averaging and therefore would have influence on the concentration field. The results presented for x/l = 0.146 show this to be the case.

The distribution of $\bar{c}$ at x/l = 0.036 and 0.073, figure 5.6 a-b, are similar in that they both clearly show the dispersion of tracer gas under the influence of the two-tier vortex structure. This is further shown by the example vertical profiles of concentration x/l = 0.073 for various distance from the model centreline, figure 5.7.

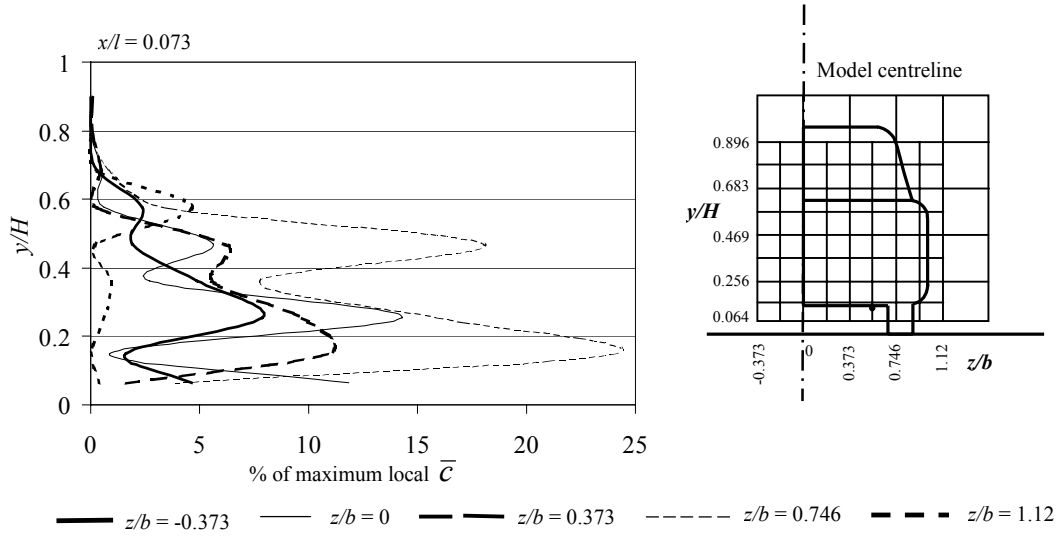

Figure 5.7 – Vertical profiles of percentage concentration at $x/l = 0.073$

The local maximum in this instance occurred at $z/b = 0.560$ but is not shown in figure 5.7. In general local increases in $\overline{c}$ either coincide with the regions of low velocity or actual vortex centres. For example at $x/l = 0.036$ the increase in concentration towards the top of the model base, albeit only 3% of the local maximum, is most likely due to tracer gas build up in the low velocity region towards the centre of the upper vortex.

At both $x/l = 0.036$ and 0.073 there is no "pick-up" of pollutant by the lower vortex and therefore the concentration fields are primarily due to the recirculation of tracer gas via the lower vortex into the upper vortex. The magnitude of the concentration field is therefore lower further into the recirculation towards the model base i.e. turbulent mixing due to recirculation and unsteadiness dilutes the concentration resulting in a weaker concentration field at $x/l = 0.036$.than at $x/l = 0.073$. Also the much lower concentrations within the recirculation region suggest that only a percentage of the plume content was drawn up into the recirculation region.

With no visible sign, at $z/b = 0.560$ of tracer gas "pick-up" for $x/l = 0.036$ and 0.073 the higher values of $\overline{c}$ close the source are believed to be due to the expansion of the exhaust plume, into the recirculation region through the lower velocity layer at the lower edge of the model base, figure 5.8.

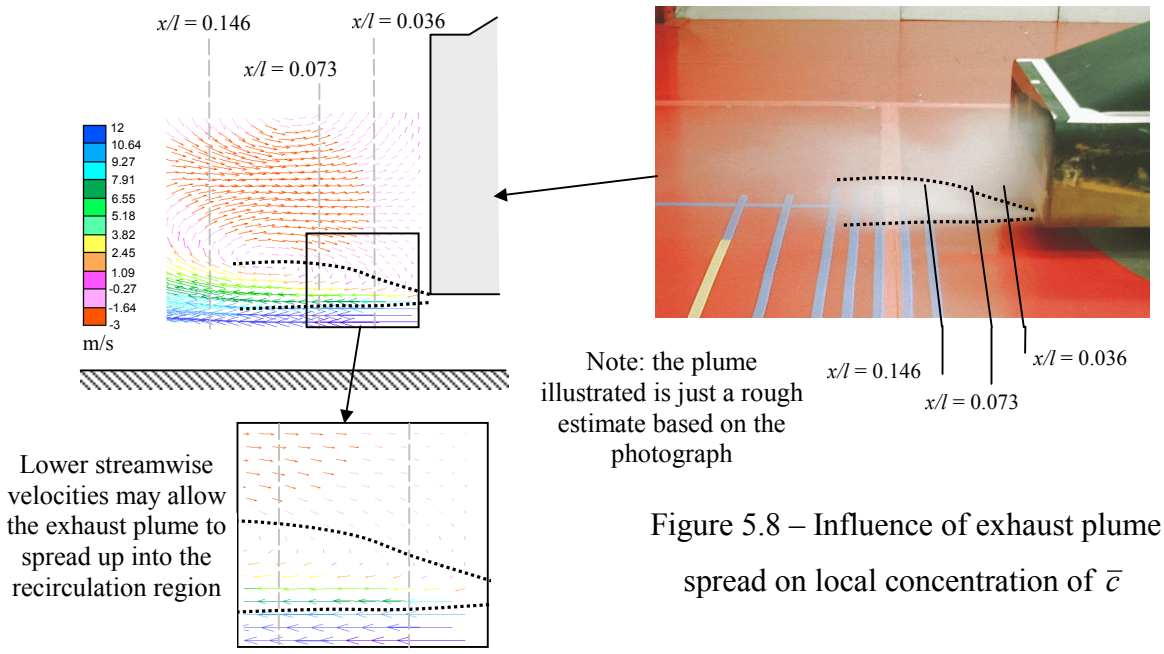

Figure 5.8 – Influence of exhaust plume spread on local concentration of $\overline{c}$

The influence of the change in relative vortex size within the recirculation region maybe shown through the local increase in concentration, figure 5.9 which shows the vertical profile of concentration at x/l = 0.146 for two cross-stream locations either side of the exhaust plume.

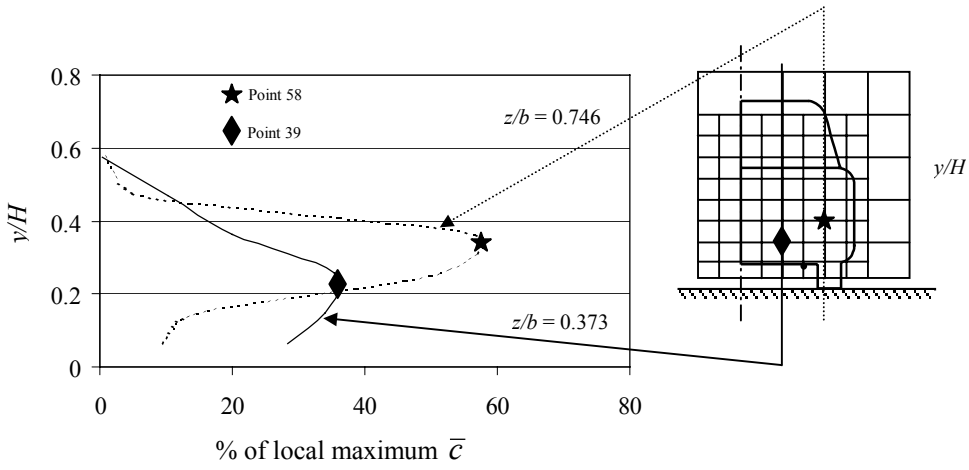

Figure 5.9 – Comparison of concentration profile at z/b = 0.746 and 0.373 for x/l = 0.146

The local increase in concentration at each cross-stream locations occurred at different y/H (where y is the vertical distance from the floor and H is the overall height of the model) with the local increase in concentration occurring higher up at

z/b = 0.746 than at z/b = 0.373. It may therefore be said that the changes in concentration profile between z/b = 0.746 and 0.373 are caused by a increase in size of the lower vortex, refer to figure 4.11-4.12 and that the lower vortex is the primary influence on the dispersion of the tracer gas.

The concentration fields presented for x/l = 0.036 and 0.073 show significant cross-stream dispersion and in particular across the model centreline behaviour also observed during flow visualisation, figure 5.5b. The cross-stream spread of tracer gas is the result of continual recirculation, the general unsteadiness within the recirculation region and a weak cross-flow. Figure 5.10 shows the mean concentration field at x/l = 0.036 compared against the mean vector field for the same location.

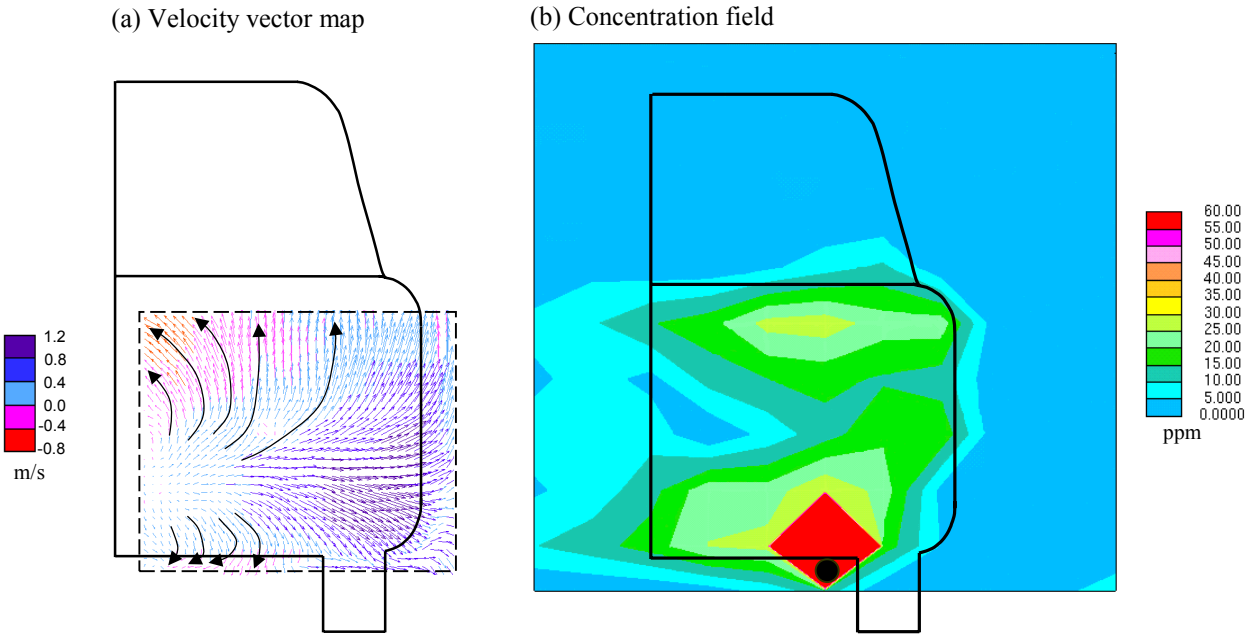

Figure 5.10 - Concentration distribution due to cross-flow at x/l = 0.036

The distribution of $\bar{c}$ at the lower half of the model base is the result of recirculation by the lower vortex and the cross-wake spread of concentration due to low velocities and the change in flow direction towards the centreline. The cross-wake spread in the upper half is due to the cross flow towards the centreline. The distribution of tracer gas across the centreline brings in to question the assumption of centreline made in the numerical simulations of the tracer gas dispersion. The vector map shown in figure 5.10 also shows clearly the reversed flow within the recirculation

split into the upper and lower vortices resulting in a two-tier concentration distribution.

The position of the local maximum in $\bar{c}$ between x/l = 0.036 and 0.073 is visibly seen to change in figure 5.6a-b. At x/l = 0.036 and 0.146 the local maximum concentration occurs at a height y/H = 0.149 above the floor but at x/l = 0.073 only 20% of the local maximum was measured at the same height even though this point is inline with the source. The maximum local concentration at x/l = 0.073 is observed closer to the floor at y/H = 0.064 figure 5.11a. If this difference in location of the local maximum were a consequence of applying a fixed floor condition (section 2.3) then the local maximum concentration at x/l = 0.146 would also be closer to the floor i.e. the thickening boundary layer might draw the plume towards the floor. However these differences in location observed are more likely the result of the vertical fluctuations observed within exhaust plume as the floor boundary was not believed to be of significant influence at this point (section 4.5) i.e. the plume is drawn towards the floor at x/l = 0.073 due to turbulent fluctuations.

Figure 5.11 also clearly illustrates the rapid dispersion of tracer gas away from the source. The maximum source value of the tracer gas was 11000ppm of propane but within 50mm of this source i.e. at x/l = 0.036 the concentration fell to 744ppm of propane, 7% of the maximum source value. The rapid dispersion of tracer gas away from the source results through a combination of recirculation, internal cross-flow and unsteadiness in both the recirculation region and the exhaust plume itself. The unsteadiness in the recirculation region is discussed in section 5.5. The rapid dispersion and low measured concentrations may also be exaggerated by the less than ideal flow rate.

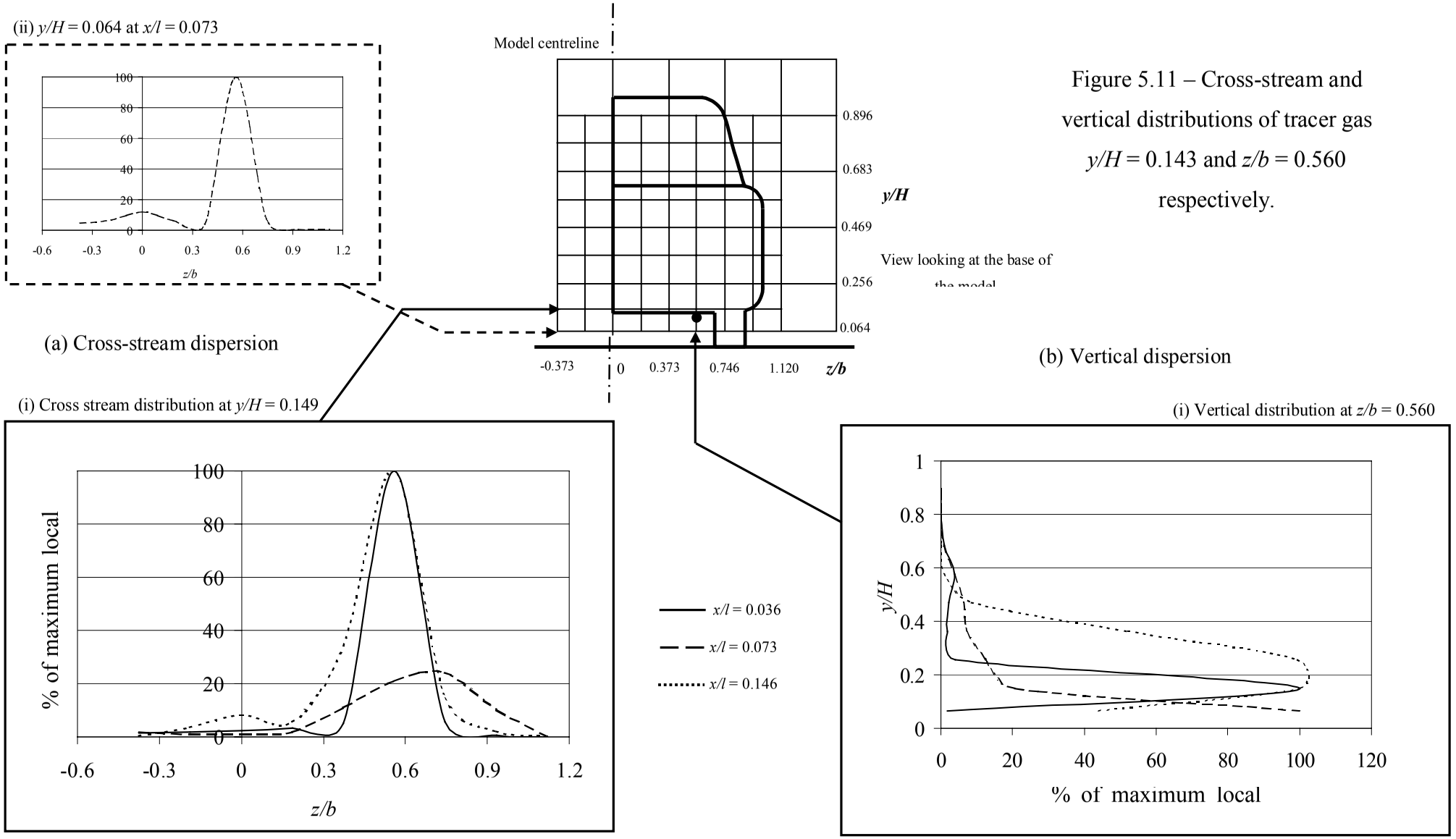

Figure 5.11 – Cross-stream and vertical distributions of tracer gas $y/H = 0.143$ and $z/b = 0.560$ respectively.

The distributions described above are based on a less than ideal flow rate and as a consequence it is possible the momentum jet close to the source was not modelled adequately i.e. too slow. While this may compromise the distribution close to source, away from the source where convective effects dominate the modelling should be adequate. However as it was not the intention to reproduce real exhaust conditions but gain understanding of the dispersion character of the near wake a less than ideal flow rate was accepted. However it was believed that the general distribution would remain unchanged at an increased exhaust mass flow rate (Chapter 7, section 7.4.1).

Despite the less than ideal flow rate and the low concentration values the study still gave a good overall representation of the dispersion character within the near wake recirculation region of the model vehicle. However it should be remembered that the effects of heat in the exhaust flow were not considered. A hot exhaust flow would be less dense and thus more vertical dispersion would be expected. The inclusion of a heated gas flow in the current study would however have further complicated the test. The intention was to obtain data on the dispersion characteristics in a controlled test environment, one that could be easily replicated using CFD. A successful numerical model of the test could then be used to investigate the effects of heat on the dispersion of pollutant within the near wake.

The smoke flow visualisation study showed the near wake recirculation region to be highly unsteady therefore the continually changing smoke distribution observed would also imply the concentration distribution of the tracer gas to continually change. The following section uses spectral analysis to investigate the unsteady characteristics of the velocity and concentration fields.

5.5 Spectral analysis

Spectral methods were used to identify the unsteady character of the near wake dispersion field. The technique essentially transforms data from the time domain into the frequency domain providing information on the amount of power associated with different frequencies. Spectra were produced using the technique of Fourier

analysis which essentially decomposes the measured data into an infinite number of sine waves of differing frequencies and amplitudes that when combined represent the original data series i.e. spectral density, SD. The specific details of the technique are not described and further detail may be found in Bendat & Piersol, (1980, 1986) and Canuto *et al* (1988). All spectral calculations were carried out using MathSoft MathCad® 8 Professional and the Fast Fourier Transform (FFT) technique which uses the Cooley-Tukey Procedure (Bendat & Piersol, 1980).

The unsteadiness in the concentration field is directly influenced by the unsteadiness in the velocity field therefore spectral information obtained from the concentration data may also identify unsteadiness in the velocity field and identify different vortex sizes through frequency and energy content. Spectral information obtained from the concentration data highlights unsteady features within the near wake recirculation region i.e. $x/l < 0.146$. In addition velocity data measured at $x/l = 0.291$ and 0.437 were also used in the analysis. The results of the following analysis were not used in the validation of the numerical simulations as these were concerned with mean data only.

Before the results of the analysis are discussed the problem of aliasing must be addressed. Aliasing occurs when energy at unanticipated frequencies is folded into the band of interest. This occurs for energy at frequencies greater than half the sample frequency or critical frequency f_c . If the Fourier Transform approaches zero as the frequency enters the critical range i.e. $\pm f_c$ then aliasing is likely. Figure 5.12a gives an example of a spectrum from the current study that contains aliasing. Filtering a signal, before it is sampled, to guarantee that no components of frequency higher than the critical frequency are present, may prevent aliasing. It is also possible to filter the digital frequency after sampling and was approach used for the data collected in the current study and will now be described.

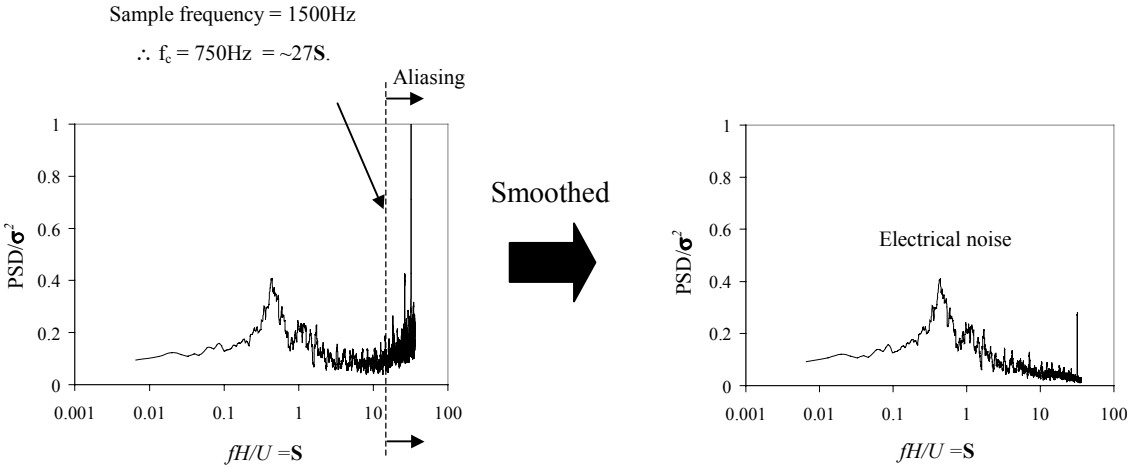

(a) Spectra with (b) Smoothed spectra

Figure 5.12 – The effects of aliasing on spectra

The example spectra shown in figure 5.12 are plots of dimensionless Spectral Density (SD) vs non-dimensional frequency or Strouhal number **S** respectively where the Strouhal number is given by,

$$\mathbf{S} = \frac{fH}{U} \tag{5.6}$$

where f is frequency in Hz, U is the free stream velocity and H is the height of the model above the floor. The non-dimensional spectral density (SD) represents the overall power and energy content of the flow and is the calculated spectral density multiplied by frequency and divided by the variance. The variance is the integral of the spectral density over the entire frequency range. The data smoothing function 'medsmooth' available in Mathcad® was applied to the data, when appropriate, to filter or smooth the sampled data before spectral calculations were performed (Mathcad 8, 1998). This function effectively filters the data at a chosen frequency. In this case the data was filtered at a frequency of 500Hz with the critical frequency being 750Hz i.e. the sample frequency was 1500Hz. Figure 5.12b shows the results of applying the medsmooth function.

5.5.1 Spectral information

The energy contained within the flow at different frequencies is represented using graphs similar to that shown in figure 5.12, which enable dominant frequencies within the flow field to be identified. The analysed concentration data provides spectral information at x/l = 0.036. 0.073 and 0.146. The data measured at x/l = 0.218 was not used for reason the given in section 5.3.2. The spectra for the streamwise component of velocity u (at x/l = 0.291 and 0.437 only) was obtained using the time series data established through combining the data sets of u_{uv} and u_{uw} to give a time series of u i.e. at each point $u = ½(u_{uv} + u_{uw})$. A time series for each point at each downstream distance was established.

Spectral analysis of the concentration data at x/l < 0.146, revealed a division in spectral types between the top and bottom of the recirculation region with the energy content of the flow moving to higher frequencies lower down, figure 5.13. The two distinct spectral types are associated with the different size vortices, which occur inside recirculation region, figure 4.12 i.e. lower frequency energy associated with larger vortices and higher frequency energy associated with smaller vortices. With reference to figure 5.13a-b the broad band low frequency energy ~ 0.1 – 1**S** (~3 – 30Hz) at points 22-24 represents the larger upper vortex and the change to moderate frequency energy ~ 0.3 – 3**S** (~ 8 - 83Hz) at points 20 and 21 might be associated with the smaller lower vortex. **S** is the Strouhal number based on vehicle height H given by equation (5.6). The high frequency energy at both points 23 and 24 (+3**S**) might suggest additional high-energy fluctuations but for the same points 50mm further downstream at x/l = 0.073 high frequency activity is not as significant. The high frequency part of the spectrum (indicated in figure 5.13b) results from the spectral method itself and not the flow characteristics where the general concentration does not change significantly but high concentration peaks occur resulting in a time-series which is ‘peaky’ or non-stationary. The FFT technique is trying to fit a sine wave to a ‘peaky’ time series resulting in a very noisy high frequency spectrum. Figure 5.13c shows the spectra at points 20 and 22 at x/l = 0.073 to also illustrate the change in spectral types identifying the presence of the upper and lower vortices within the near wake recirculation region.

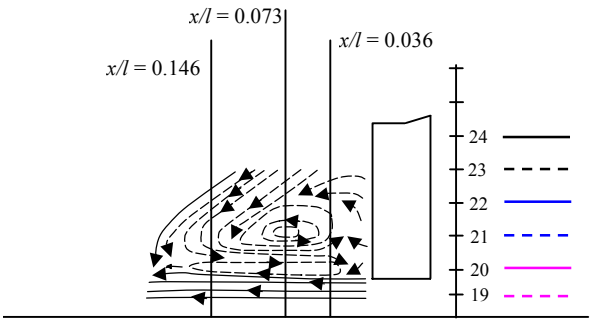

(a) Vertical location of points

(refer to figure 5.4 for exact spatial locations).

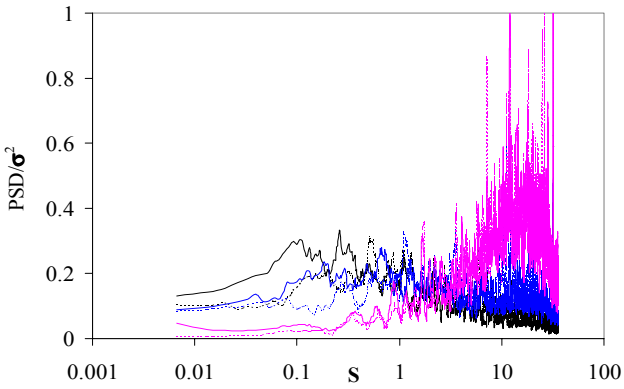

(b) Spectrum at points (19-24) along the model centreline at x/l = 0.036.

Figure 5.13 – Example spectra showing different spectral types.

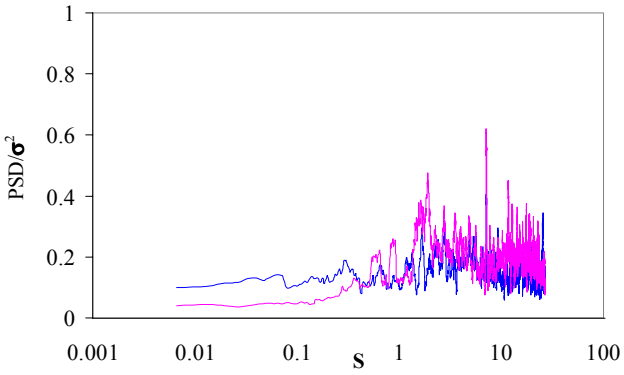

(c) Spectrum at points (20-22) along the model centreline at x/l = 0.073.

The distinct division in spectral types diminishes away from the model centreline as the internal vortices become more equal in size and their energy content similar.

Figure 5.14a presents the spectrum at point 22 for x/l = 0.036 and 0.146 and shows the level of low frequency energy (0.1 – 1**S**) associated with the larger upper vortex to be less at x/l = 0.146 than that at x/l = 0.036 (refer to figure5.12a for point location). This implies, as observed during the wake survey measurements (figure 4.11, section 4.5) that only the trailing edge of the upper vortex was encountered at x/l = 0.146, at the model centreline. The moderate frequency energy 0.3 – 3**S** associated with the lower vortex is still significant at x/l = 0.146 confirming the results of the wake survey that the lower vortex is longer than the upper.

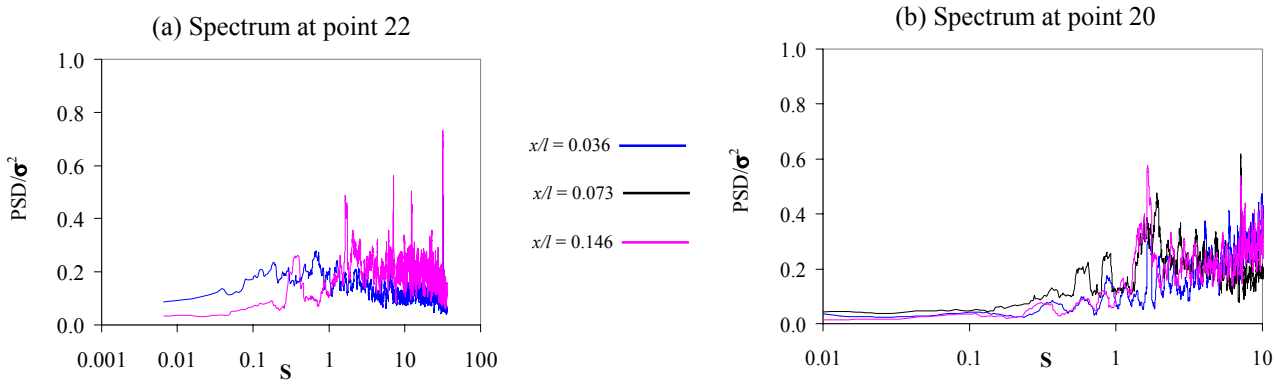

Figure 5.14 – Spectrum at points 20 and 22 for various *x/l*

In addition the spectrum analysed for all points showed frequency peaks at 1-1.7**S** in the lower half of the recirculation region. This frequency peak tended to increase in magnitude to 1.7**S** towards *x/l*=0.146. Figure 5.14b presents the spectrum for point 20, at the model centreline, for *x/l* = 0.146. Point 20 represents the approximate location of the lower vortex refer to figure 5.13a. The increase in level of moderate energy within this region towards *x/l* = 0.146 implies that the lower vortex fluctuations are stronger towards this location satisfying the observation made in flow visualisation study, section 4.5 that the recirculation length to fluctuates around *x/l* = 0.180. This increase in energy towards the mean recirculation length, at the model centreline is mirrored by the increase in streamwise turbulence intensity towards the same point figure 4.15.

The velocity spectra[5.2] (*u* only) showed moderate energy at **S** = 1.5 (42Hz) at the model centreline for points in the lower part of the recirculation region at *x/l* = 0.291 and 0.437. From these observations it may therefore be concluded that the recirculation length fluctuates at a peak between ~ 1.5-1.7**S** or 42-47Hz close to the mean recirculation length, *x/l* = 0.180 at the model centreline. Both flow visualisation studies (section 4.5 and 5.3.1) showed the smoke distribution unsteadiness within the near wake to be governed by the unsteadiness in the flow field therefore it may be said that the concentration field also fluctuates at a peak ~ 1.5-1.7**S** or 42-47Hz close to the model centreline. Moderate energy fluctuations about *z/b* = 0.560 were of the order 0.5-0.7**S** (14-19Hz), with fluctuations at 0.7**S**

[5.2] Spectra calculated using velocity data measured by hotwire at *x/l* = 0.291 and 0.437 only.

occurring at x/l = 0.291, falling to 0.53**S** by x/l = 0.437. This implies that either a peak of 0.7**S** occurs at x/l = 0.291 or a higher peak occurs at $0.291 < x/l > 0.437$ further illustrating the recirculation length to be longer at z/b = 0.560 than at the model centreline. The mean recirculation length at z/b = 0.560 could not be determined using the vector map presented, figure 4.12 due to the size of the capture area but it may be concluded here that the mean recirculation length at z/b = 0.560 lies between x/l = 0.291 and 0.437.

As briefly discussed in Chapter 4 (section 4.5, figure 4.16) the unsteadiness in the recirculation region is the result of a continually changing velocity field caused by vortex shedding. Figure 5.15 shows some instantaneous vector maps from the centreline showing clearly the presence of vortices, in particular close to the free stagnation point.

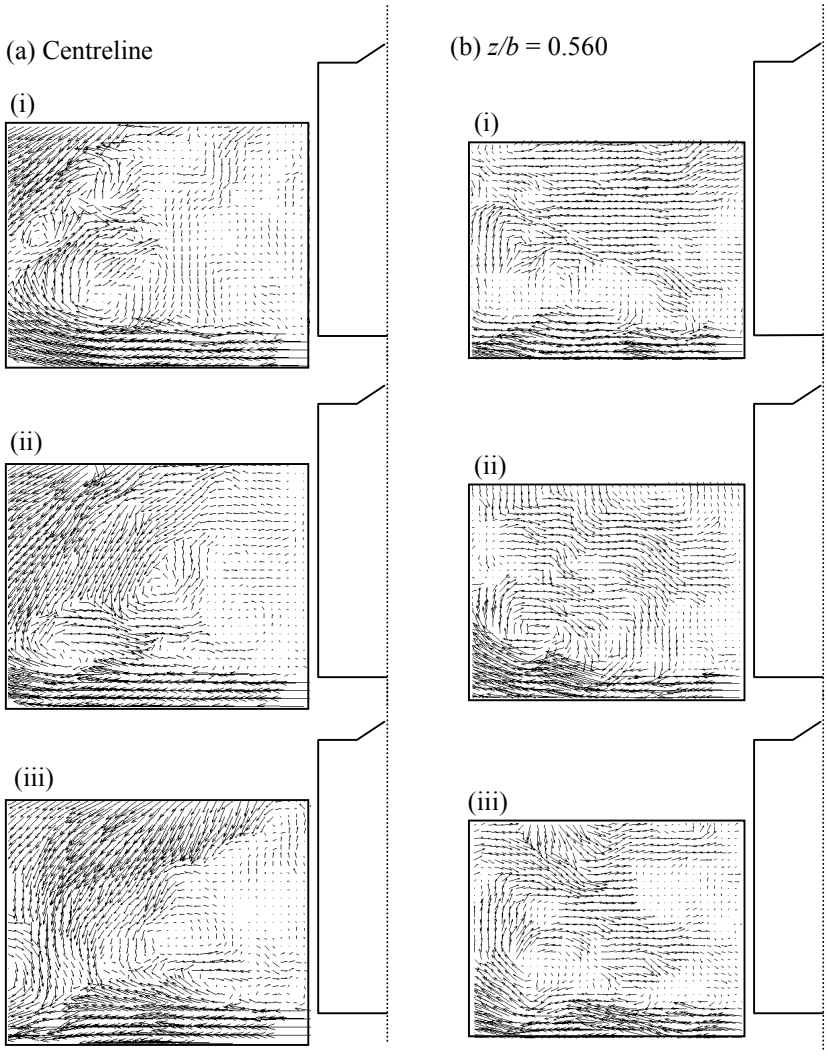

Figure 5.15 – Streamwise instantaneous flow structure

Figure 5.15a(iii) clearly shows the shedding of a vortex from the free stagnation point, the mechanism responsible for the high-energy fluctuations at this point. Similar vectors maps for $z/b = 0.560$ are shown in figure 5.15b for the same instances in time for those shown in 5.15a. The frequency of capture of these images i.e. 2Hz was not sufficient to capture the true instantaneous flow character, in a sequence of pictures, responsible for 42-47Hz unsteadiness observed at the model centreline nevertheless the images presented still capture the principle flow structure responsible for the recirculation region unsteadiness. The vector maps at $z/b = 0.560$ generally presented less vortices within the recirculation region hence the lower frequency of fluctuations observed at this location i.e. 0.7**S** or 19Hz. The total time between each image shown in figure 5.15 is 5 seconds.

While the nature of PIV measurements allows a "snap-shot" of the flow to be assessed it is not possible with the same ease to view a similar image using point concentration measurements. However as it is clear that the character of the velocity field drives the concentration field it may be concluded that the concentration field changes with a similar chaotic behaviour.

The flow visualisation study using smoke flow through the representative exhaust (section 5.3.1) showed the exhaust plume itself to be highly unsteady. This was reflected by high frequency energy at point's inline with and close to the exhaust plume. Figure 5.16 shows the energy spectrum, from concentration data at points 49-54 at $x/l = 0.073$, at $z/b = 0.560$. Within the vicinity of the exhaust plume high-energy fluctuations of the order 7-10**S** (28-280Hz) were observed. The number of points within the vicinity of the plume experiencing high frequency fluctuations increased with distance downstream illustrating the spread of the exhaust plume and its influence on the surrounding flow. These higher frequency fluctuations are not believed to be associated with the recirculation region vortex structure as the larger lower vortex at $z/b = 0.560$ (figure 4.12) would be associated with lower frequency energy. This is reflected in the drop-off in flow energy away from the plume towards points 52 and 51.

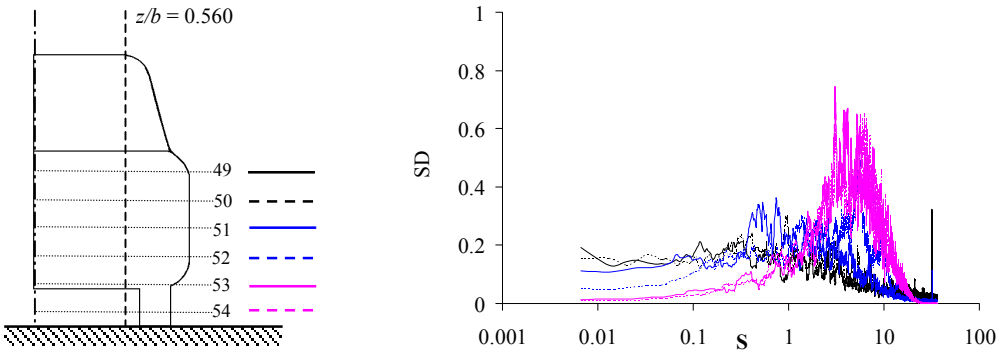

Figure 5.16 – Energy spectrum from concentration data at points inline with the exhaust at $x/l = 0.036$ at $z/b = 0.560$.

To summarise; there was general unsteadiness within the recirculation region with low frequency energy ~ 0.1 – 1**S** (~3 – 30Hz) associated with the larger upper vortex and moderate frequency energy ~ 0.3 – 3**S** (~ 8 - 83Hz) associated with the smaller lower vortex. The recirculation region and thus concentration within this region was shown to fluctuates at ~ 1.5-1.7**S** or 42-47Hz about the mean recirculation length, or mean free stagnation point, $x/l = 0.180$ i.e. the concentration field is driven by the unsteadiness in the velocity field. These frequencies do fully account for the lower frequency changes in smoke distribution of (~0.01 – 0.1**S**) i.e. the regular purging observed in the flow visualisation study. It is probable that the lower frequency end of the spectrum was lost due to the length of sampling chosen suggesting a longer sample time to be more desirable for future investigations.

The results from current study show energy at a wide range of frequencies within the near wake recirculation region i.e. range from ~3-83Hz. For the full-scale equivalent of the model tested the near wake fluctuations and thus fluctuations in concentration would occur between 1-28Hz. Baker (2001) compared spectral data from wake, including initial results from the current study, and urban pollution studies to show that peaks in pollution often occurred close to the period of the breathing cycle (~0.5Hz). The additional results presented here further show that near wake and thus fluctuations in levels of pollutant from the recirculation region, of the vehicle configuration tested, to be close to the frequency of the breathing cycle. The structure and unsteady character of the recirculation region are dependent on the base

slant angle (α) of the vehicle (section 2.2) therefore the frequency at which pollutant concentrations fluctuate within this region will vary. Xia and Bearman (1983) showed the frequency fluctuations within the recirculation region of a simple vehicle geometry to increase from 0.28**S** at α = 10 (a squareback) to more general unsteadiness at 0.36**S** for α = 40 (a fastback). From the findings of the current study this would imply that the concentration of a gaseous pollutant in the recirculation region of a squareback vehicle would fluctuate at frequencies closer to that of the breathing cycle than a fastback geometry. This has potential health implications for the pedestrian at the roadside. While the numerical technique for modelling pollution dispersion demonstrated in Chapter 7 only considers the mean concentration field the method has the potential to investigate the relationship between vehicle geometry and unsteadiness in the concentration field.

5.6 Conclusions

The primary aim of the experimental study described was to obtain the mean concentration within the near wake of a model vehicle for the validation of numerical simulations of the same dispersion field (Chapter 7). Mean concentration data was collected for direct validation and their uncertainties determined for the criteria used in statistical validation. The data collected also provided a valuable insight into the main dispersion mechanism within the near wake of the model considered. Through flow visualisation and measurement using Flame Ionisation detectors (FIDs) the two-tier vortex structure of the recirculation region was shown to be the primary dispersing mechanism close behind the model with tracer gas from the exhaust plume being drawn up into the region via the lower vortex. Tracer gas was then recirculated back towards the base of the model and further dispersed through the upper inner vortex. The concentration distributions within the recirculation region reflected the two-tier vortex structure illustrating the concentration distribution to be driven by the character of the velocity field. While only a proportion of the tracer gas within the exhaust plume was drawn into the recirculation region dispersion away from the plume was rapid in all directions. A significant cross-wake spread of pollutant over the model centreline was observed through both flow visualisation and

data measurement therefore questioning the assumption of centreline symmetry applied for the numerical simulations, to be discussed further in Chapters 6 and 7.

The use of FIDs and the novel approach of releasing tracer gas through a representative exhaust proved effective combination to obtain the dispersion field in the near wake of a model vehicle. Practical limitations meant that the sample time at each point was only 11secs at 1500Hz, which at equivalent full scale for the same vehicle speed equated to a 33-second sample time. However subsequent spectral analysis of the concentration data showed this to be sufficient with fluctuations in the velocity and concentration field at mode1 scale to be of the order 3-84 Hz i.e. 3-84 cycles per second. While only concentration data was obtained at three downstream locations within the recirculation region the importance of this region in dispersing pollutant close behind a vehicle has nevertheless been highlighted. The implications on the validation of the numerical simulations (Chapter 7) were that only predictions within the recirculation region could be validated. However as the near wake recirculation region was shown to be the primary dispersing mechanism this was not considered to be a disadvantage. Moreover in combination with the velocity data measured for the same downstream locations during the wake survey (Chapter 4) the mean concentration data obtained was sufficient for the validation of the dispersion and underlying velocity field within the recirculation region.

While for the purposes of numerical validation the mean or time-averaged concentration field was recorded the inherent unsteadiness and chaotic nature of the time-dependent flow implied the actual instantaneous concentration, similar to the instantaneous velocity field to bear no resemblance to the ordered distribution of tracer gas. Unsteadiness in the distribution of pollutant with the recirculation region was observed through flow visualisation with purging of smoke from the region at 1-3sec intervals. Nevertheless spectral analysis of both concentration and velocity data revealed the general unsteadiness to occur between ~0.1-3**S** (~3-83Hz). Low frequency energy of ~ 0.1 – 1**S** (~3-30Hz) was associated with the larger upper inner vortex and moderate frequency energy of ~ 0.3 – 3**S** (~8-83Hz) with the lower vortex. The inherent unsteadiness in the flow is the result of a constantly changing flow structure with small vortices being continually shed from the free stagnation point. The recirculation region and thus concentration within this region was shown

to fluctuate at a peak ~ 1.5-1.7**S** or 42-47Hz about the mean recirculation length, or mean free stagnation point, x/l = 0.180. At equivalent full scale fluctuations in the recirculation region and thus concentration distribution were shown to be close to the frequency of the breathing cycle i.e. ~ 0.5Hz which might have implications on the health of pedestrians at the roadside. From this it is clear that for future investigations the time-dependent velocity and concentration fields are of particular interest.

Chapter 6: Numerical Simulations 1 - Simulation of the near wake flow field of a model vehicle

6.1 Introduction

The following chapter describes the first part of a two part computational study in which commercially available Computational Fluid Dynamics (CFD) software, namely STAR-CD was used to simulate the dispersion of pollution in the near wake of a model road vehicle. Part 1 discussed here aspires to simulate the near wake flow measured and detailed in Chapter 4. Part 2 (detailed in Chapter 7) endeavours to simulate the tracer gas distribution measured in Chapter 5 using the simulated near wake flow field from the following chapter.

The primary aim of the computational study to be discussed was to obtain a numerical simulation of the near wake flow measured and detailed in chapter 4 which could be used as the foundation for subsequent numerical simulations of pollutant dispersion within the same near wake region. Refer to figure (1.1) for the project strategy. In doing this it was also the intention to assess the capability of STAR-CD, a commercially available CFD code, in obtaining a good numerical simulation of the near wake without the need for detailed changes to modelling parameters.

The performance of different turbulence models and differencing schemes in predicting the measured near wake flow field (chapter 4) were assessed. The study focused on the mean flow field only. Mesh refinement was used to improve solution accuracy and flow detail. Numerical results are compared against both experimental data and each other, to assess the capability of the turbulence models and differencing schemes chosen and to validate the predicted velocity field. Detailed validation was achieved using statistical methods (Chapter 3, section 3.5) and the validation criteria established in Chapter 4, section 4.4.

6.2 Problem definition

The commercial code STAR-CD (V3.05) was used to perform the numerical simulations of the near wake flow field of the MIRA 33% scale reference model (fastback). The analysis was carried out (except where otherwise stated) using a Silicon Graphics workstation with a 225Mhz R11000 chip and 512 MB of RAM. This effectively put a constraint on the maximum size of the CFD model.

6.2.1 Mesh definition

An existing block-structured[6.1] hexahedral mesh of one-half of the MIRA 33% scale reference car (fastback) created using ICEMCFD/HEXA™ was utilised. Centreline symmetry was assumed and is discussed further section 6.2.2.1. The additional features of the wind tunnel geometry (Appendix 2a) were included using the meshing facility within STAR-CD to include the inlet, plenum, collector and diffuser (figure 6.1a). The inlet was positioned approximately two model lengths upstream to ensure a uniform velocity distribution ahead of the model (Appendix 4a). The collector/diffuser mesh was 'joined' to the main mesh using an arbitrary interface figure 6.1a, which enabled to blocks of dissimilar mesh to be joined without out compromising the solution. The main features of the wind tunnel geometry were included in the computational mesh in order that any comparisons between the predicted and experimental data were fair. This meant blockage correction need not be applied (section 4.2.1). The complete mesh contained 667560 cells.

The complexity of the flow being solved and the level of flow detail required dictated the density of the mesh i.e. a higher density mesh was used downstream of the model where regions of recirculation were more difficult to solve, figure 6.1b(i). The change in grid density through the mesh is illustrated in figure 6.1a where the density of mesh in region A is twice the density in region B that is three times the density of region C.

[6.1] In STAR-CD the mesh used is considered unstructured (Computational Dynamics, 1998b).

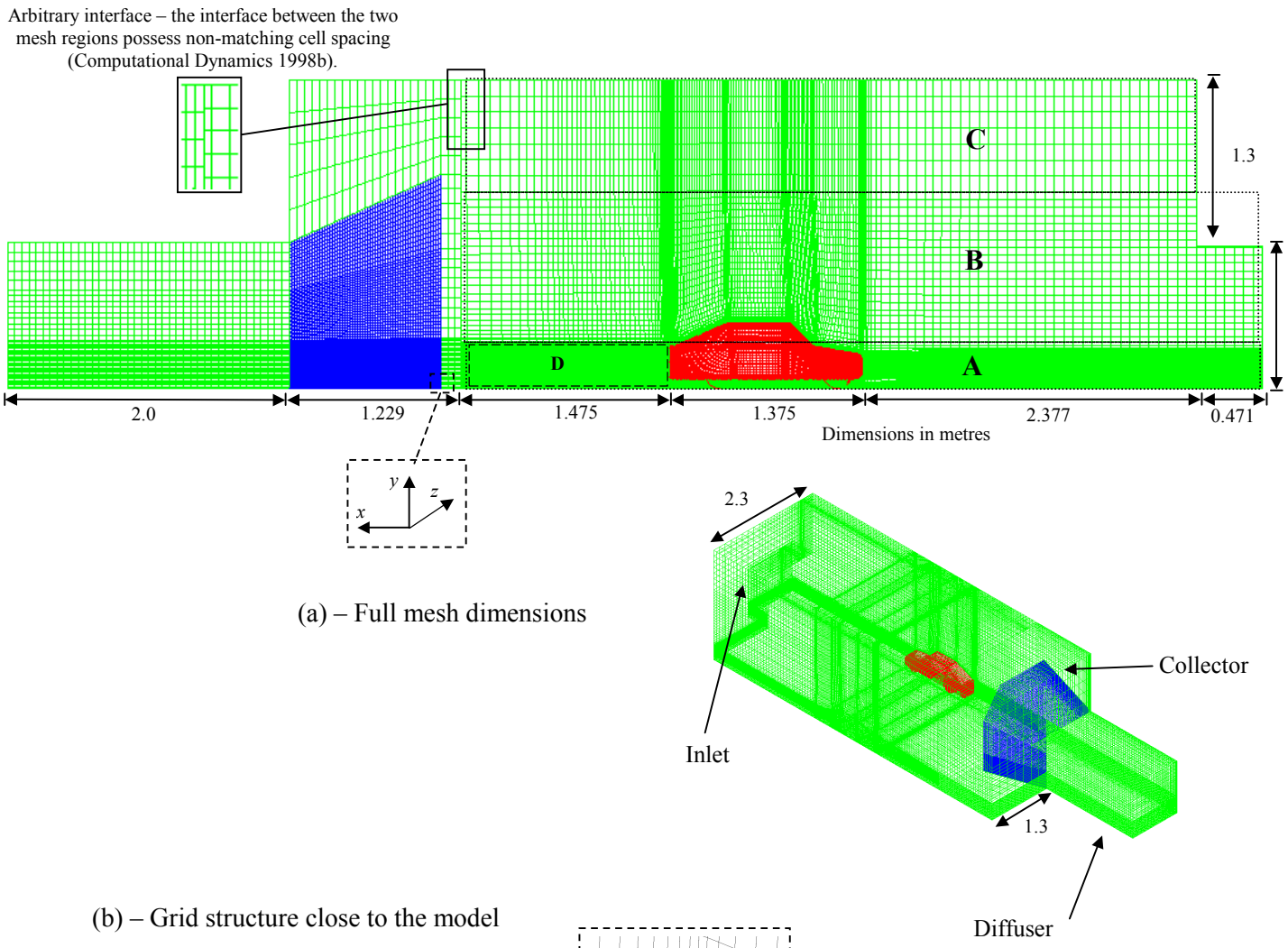

(a) – Full mesh dimensions

(b) – Grid structure close to the model

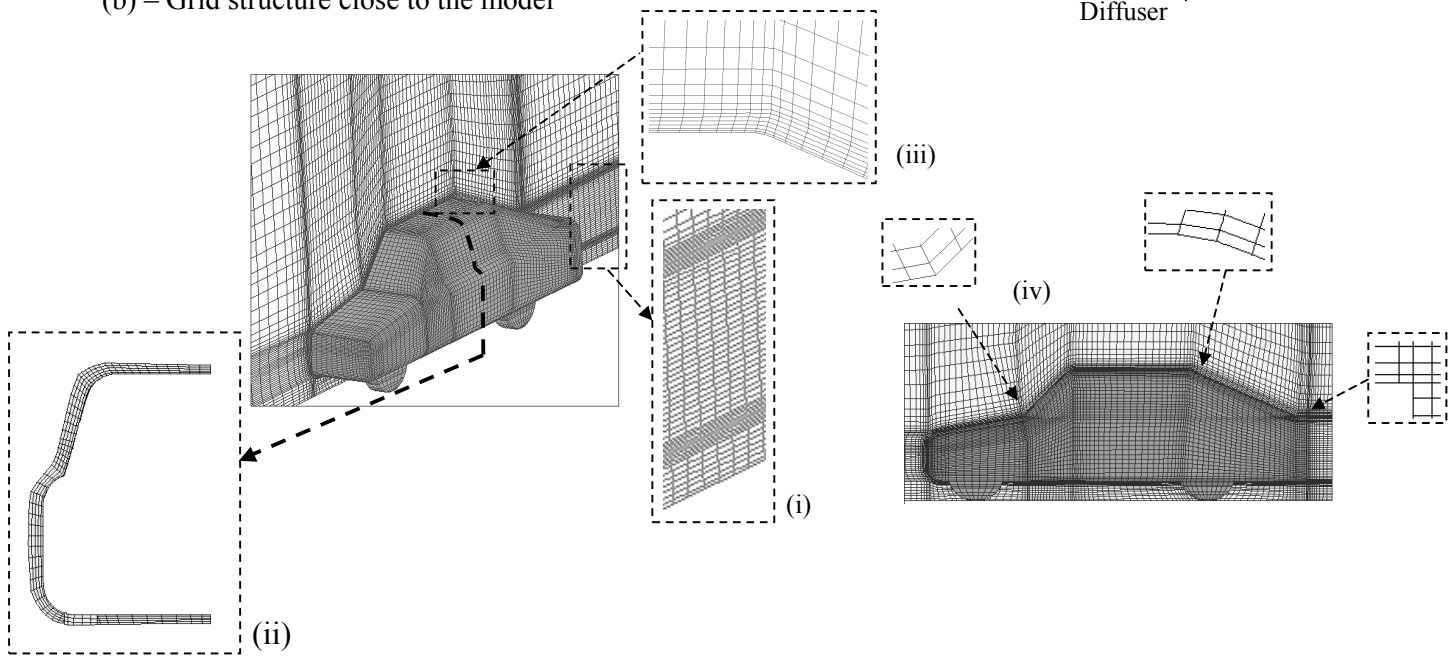

Figure 6.1 Mesh Definitions

The number of cells within the wake of the model, region D, which spanned the width of the model base area and extended downstream to the collector, was approximately 32,000. Similar mesh density ratios were applied in the collector/diffuser region of the mesh.

An "O-grid" was used to define the surface shape of the model, figure 6.1b(ii) while the remaining grid was an H-grid. The use of algebraic wall functions required the mesh at the surface of the model to be fine, figure 6.1b(iii). The mesh also employed a 'corner block' structure to ensure that the mesh followed the streamwise direction of flow, figure 6.1b(iv). The quality of mesh close to the model surface was important as inappropriate mesh structure, particularly at corners, could lead to inaccurate results (Bickerton *et al*, 1996). The use of algebraic wall functions (section 3.4.4.1) required the mesh to be finer close to the model surface, figure 6.1b(iii).

For part of the study embedded mesh refinement was used in the near wake to gain more resolution while keeping the mesh points to a minimum. Embedded refinement is a technique commonly used which allows a finer mesh to be used in regions of rapid variations and a coarser mesh in areas of relatively little change. Improved solution accuracy may be achieved without significant increases in computational costs. The finer mesh was created within the coarser mesh with the two regions being joined using an integral interface, figure 6.2.

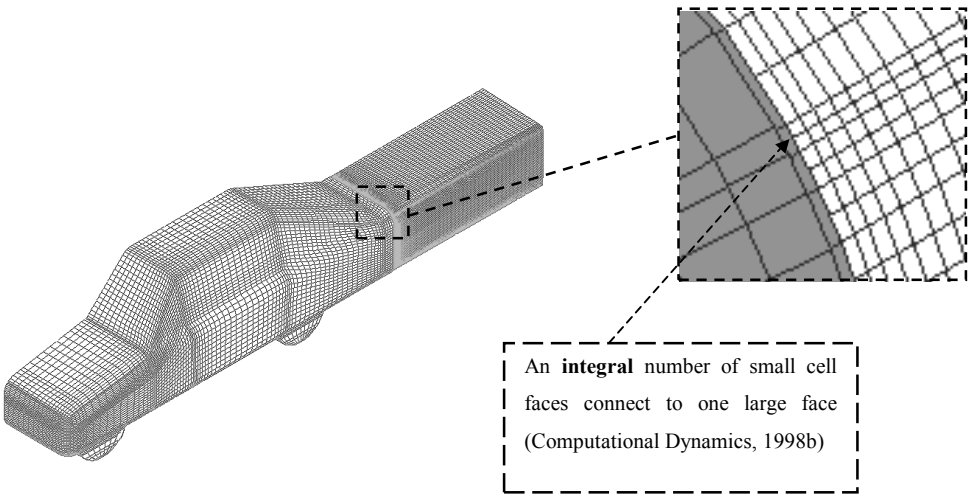

Figure 6.2 – Embedded mesh refinement

The area of refinement extended approximately 650mm downstream of the vehicle base i.e. $x/l = 0.473$, and covered the entire base area as illustrated. The numbers of cells in this region were 141416 increasing the cell count of the entire mesh to 803996.

6.2.2 Problem set-up

The boundary and initial conditions described ensured the computational model represented the conditions of the experimental study described in Chapter 4. No attempt was made to simulate on road conditions in the numerical simulations.

6.2.2.1 Boundary location

The defined boundaries within the computational domain are illustrated in figure 6.3. All the numerical calculations in the study were steady state simulating only the time-averaged wake flow structure. It is for this reason that only one half of the model vehicle and wind tunnel domain were modelled as it is generally accepted that the structure, about the centreline, of the time-averaged wake structure of a vehicle coincident with the free stream flow is symmetric (Howell, 1975; Ahmed, 1981; Bearman, 1984, 1997; Williams *et al*, 1994). Flow visualisation from the current study also illustrates this clearly, figure 4.8. A symmetry plane was therefore applied along the domain centreline, figure 6.3. An outlet boundary was set at the end of the diffuser section and the surface of the collector represented by a baffle boundary. Baffles are zero thickness cells representing a solid/porous region whose thickness is much smaller than the local cell thickness. Using a baffle boundary was a simple but effective method for modelling the influence of the collector without the need for a complicated mesh structure. The remaining mesh boundaries including the surface of the model vehicle were defined as wall boundaries.

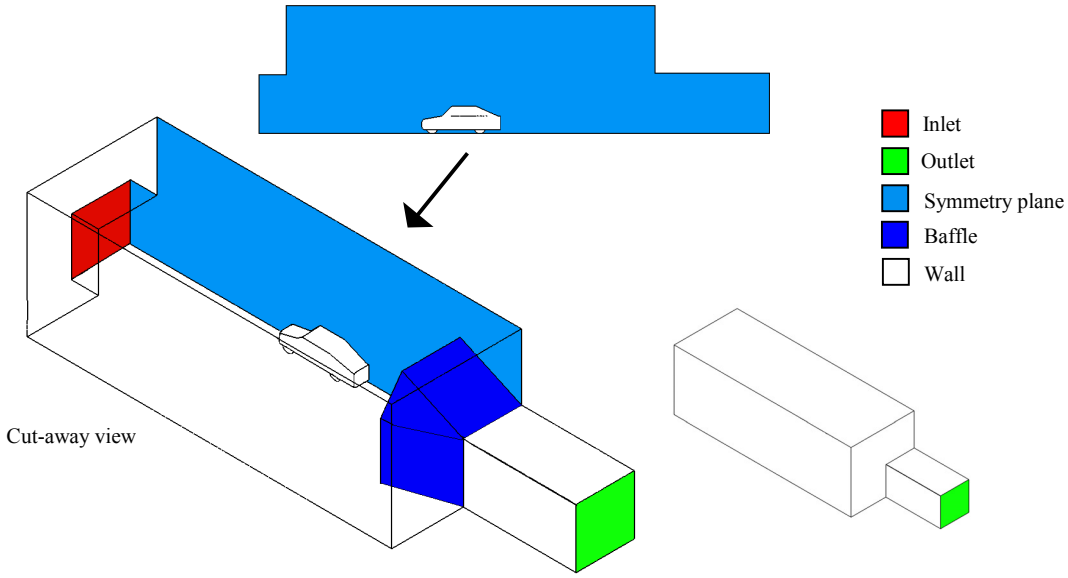

Figure 6.3 – Boundary locations

6.2.2.2. Boundary conditions and flow properties

The boundary conditions for the flow problem were defined as follows;

- Inlet Inlet velocity $U = 13$m/s
  Density $\rho = 1.205$kg/m^3

  The fluid flow properties were set for an incompressible constant viscosity airflow. In addition it was necessary to define turbulence quantities that were dependent on the turbulence models to be use. For the standard k-ε model and variants used in the current study the turbulence intensity (dimensionless) and the turbulence length scale (m) at the inflow boundary were defined. A turbulence intensity of 1.1 % was defined based on the average wind tunnel test section turbulence intensity at maximum test section velocity (section 4.2.1). The turbulence length scale was based on the height of the inflow boundary i.e. the inlet and set at 1.0m.

- Outlet: At the outlet the distributions of variables were evaluated through extrapolation of upstream values based on the assumption of zero gradients along

the mesh lines intersecting this surface. The estimated velocities were then adjusted to give a required outlet flow rate to satisfy continuity.

- Baffle: The boundary was defined as a smooth, stationary, impermeable, adiabatic wall.
- Symmetry plane: Normal velocity and normal gradients of all other variables assumed zero at the surface.
- Wall: All wall boundaries were assumed to be smooth, stationary and impermeable with a no-slip condition applied to include a fixed floor condition to match the experimental conditions (section 2.3 and section 4.2.1).

6.2.2.3. Turbulence models

The turbulence models used in the study were the standard k-ε, the Chen k-ε, the RNG k-ε, and the non-linear (quadratic) k-ε models and no changes were made to any of the modelling constants listed in table A1-1 - A1-3, Appendix 1. The turbulence length scale was defined based on the height of the model vehicle from the wind tunnel floor, 0.469m and is used to calculate the initial values of k and ε.

6.2.3 Modelling strategy

The primary aim of the computational study to be discussed was to obtain numerical simulations of the near wake flow behind a model vehicle that could be used as a foundation for numerical simulations of pollutant dispersion within the same near wake region. Refer to figure (1.1) for the project strategy. At the same time the capability of STAR-CD in obtaining a fair numerical representation of the near wake flow of a model vehicle without the need for any changes to modelling parameters was assessed (section 6.2.2.3). The modelling approach taken to achieve these aims is detailed below in figure 6.4. The objective of the strategy was to systematically obtain a numerical solution for the near wake flow field using different turbulence models and various differencing schemes of increasing order of accuracy.

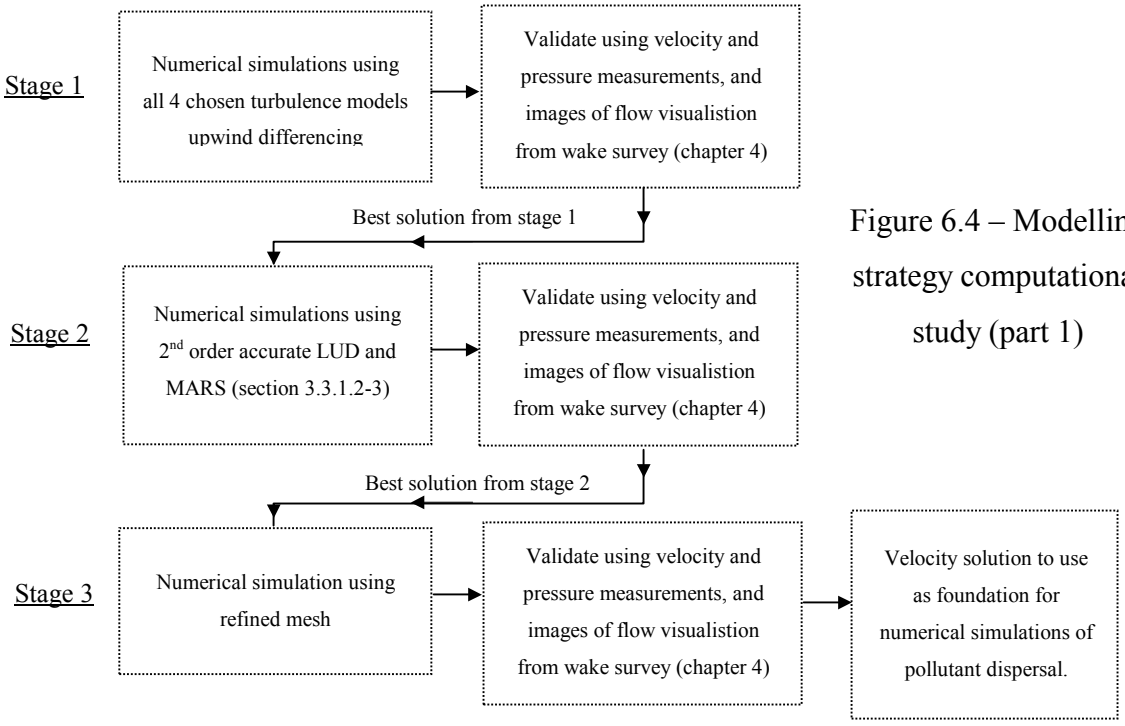

Figure 6.4 – Modelling strategy computational study (part 1)

At each stage the experimental data collected during the wake survey (chapter 4) was used to make general observations and discuss the relative success of each solution. The near wake recirculation region has a primary role in the dispersion of a pollutant close behind the model (section 5.4.1) therefore in order that the velocity solutions could be used as a foundation for numerical simulations of pollutant dispersion within this region it was essential that the flow field be adequate represented and in particular the flow field close the location of the representative exhaust (section 5.2). Thus the main focus of the investigation was on the prediction of the size, shape and internal structure of the recirculation region. Direct validation of the predictions of the main flow field structures was carried out using vector maps, contour plots and velocity profile graphs to assess the success of each numerical solution against the experimental data.

Statistical techniques (chapter3, section 3.5) were used to make additional more global validation of each solution using mean values of streamwise, vertical and cross-stream velocity $\overline{u}$, $\overline{v}$ and $\overline{w}$ respectively. Mean turbulent kinetic energy $\overline{k}$ was not used in validation as $\overline{k}$ could not be calculated as a consequence of the PIV measurements only being 2D i.e. $\overline{k} = 1/2(\overline{u'^2} + \overline{v'^2} + \overline{w'^2})$ and while $\overline{k}$ could be

determined from the hotwire measurements made at x/l = 0.291 and 0.437 it was felt that no gain would be made in using data at only these points for validation of the recirculation region. Also the predicted values are essentially calculated from an isotropic assumption (equation 3.11-3-13) and as the measured values are calculated from an inherently anisotropic flow field it was felt that there would be no benefit in making these comparisons as there already exists a disparity in the data making comparisons unfair. Even though the non-linear k-ε model takes some account of flow anisotropy through non-linear relationships for the Reynolds stresses all k-ε models only account for small scale/high frequency turbulence and not the full spectrum and therefore do not fully represent turbulence and thus turbulent kinetic energy on all scales (Richards and Hoxey, 1993). Validation of the primary flow features using measured values of $\overline{u}$, $\overline{v}$ and $\overline{w}$ was believed sufficient, as they are the foundation of the flow field structure being analysed.

At the end of each stage the "best" solution was chosen to take forward and use as the base for the next stage in the study. In stage 1 the standard k-ε model/upwind differencing scheme combination was used to obtain an initial solution of the near wake flow. All other solutions within stage 1 were initiated from this solution using the *restart* facility available in STAR-CD which enables the user to restart a velocity solution, using the *restart* post data file of that solution to form the basis of a new calculation and which saves on processing time (Computational Dynamics, 1998b). The *restart* post data file contains all the information and values of flow variables solved in the last iteration of the calculation, which are used as the starting point or initial conditions for the new calculation. Solution restart was used at the beginning of each stage in the modelling strategy using the "best" solution bought forward from the previous stage. All the solutions are listed in Table 6.1. Each solution is referred to by the given index in the following discussions i.e. standard k-ε model/upwind differencing scheme combination will be referred to as solution A and so on. Additional detail of each solution may be found in Appendix 4b.

Solution description	Index
Standard k-ε/Upwind differencing	A
Chen's k-ε/Upwind differencing	B
RNG k-ε/Upwind differencing	C
Non-linear k-ε/Upwind differencing	D
Non-linear k-ε/Linear upwind differencing	E
Non-linear k-ε/MARS differencing scheme	F
Standard k-ε/Linear upwind differencing	G
Non-linear k-ε (refined)/Linear upwind differencing	H

Table 6.1 – Solution description and index

Although flow visualisation studies (chapter 4 and 5) have shown the near wake to be highly unsteady all the numerical solutions obtained here use the steady state modelling approach described in chapter 3 i.e. the unchanging flow pattern under a given set of boundary conditions is obtained through a number of numerical iterations. To obtain numerical simulations of the unsteady flow field would require time-dependent or transient calculations which essentially involve starting from well-defined initial and boundary conditions and proceeding to a new state in a series of discrete time steps thus simulating the change in flow field at the specified time interval. This approach is both time and computationally intensive. The aim of the current work was to determine whether STAR-CD could be used to simulate the dispersion of a pollutant in the near wake of a model vehicle and therefore as a feasibility study it was more appropriate, and common place, to begin with the simulation and validation time-averaged flow and dispersion field. To begin such a study using transient calculation would be ambitious. The relative success of the current work could then be used as a foundation for further transient studies.

6.2.4. Solution control and monitoring

Solution control was achieved using under relaxation factors applied to the flow variables u, v, w, p, k and ε to suppress any numerical instability in the solution underlying velocity solution (section 3.3.2) and to assist in maintaining an adequate convergence level. The progress of each solution was monitored using the global residuals, equation (3.9), of each variable and a user specified monitoring cell giving

absolute values of the flow variables at a specified point in the flow. The monitoring cell was placed in the near wake recirculation region in order to monitor any rapid changes in the absolute values of flow variables. For a satisfactory solution these absolute values of flow variables should remain consistent. The solution convergence criterion was set based on the value of the global residual for each flow variable. At least 10^{-3} was achieved for all flow variables, Appendix 4b.

6.3 Stage 1 – Direct validation of near wake flow field simulation using upwind differencing (solutions A-D)

The following section discusses the results from the numerical simulations using the standard k-ε, the Chen k-ε, the RNG k-ε, and the non-linear (quadratic) k-ε models where the first order upwind differencing scheme (section 3.3.1.1) was used to discretise the momentum and turbulent transport equations in all cases i.e. solutions A-D respectively. The solver used was the SIMPLE algorithm (section 3.3.2). The initial discussion is a direct validation comparing velocity vector maps, contour plots and velocity profiles from both the experimental and predicted data. Validation using statistical techniques is detailed in section 6.3.1.

Figure 6.5 presents a direct comparison between the measured and predicted recirculation region structure at the model centreline. Although the vector map depicting the measured recirculation region structure, figure 6.5e, is some what smaller[6.2] than the predicted vector maps the comparison nevertheless shows all four solutions to make very similar and good predictions of the general two-tier recirculation region vortex structure. Due to the limited capture area it was difficult to accurately assess whether the relative size of the upper vortex in terms of height was predicted in good agreement however figure 6.5 does show the streamwise length of the upper vortex to be over predicted by all the solutions.

[6.2] The total capture area depended on the distance from the CCD camera, the laser projection height and angle (section 4.2.2)

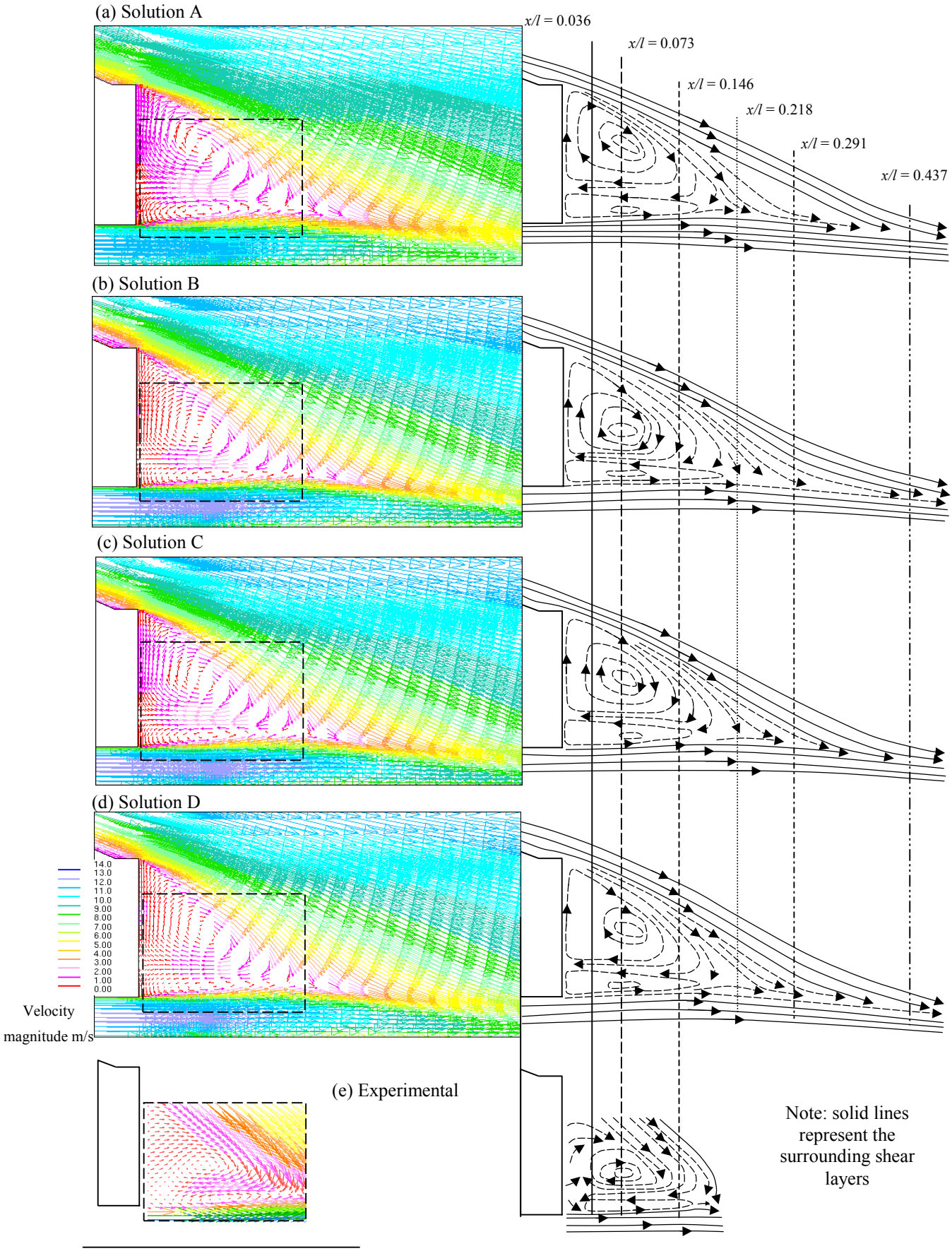

Figure 6.5 – Comparison of predicted and measured recirculation structure at model centreline.

From the vector maps presented in figure 6.5a-d it is shown that all solutions predicted both vortices to extend further upstream close to the model base whereas the experiment showed both vortices to extend only to $x/l = 0.036$, figure 6.5e. Also the downstream lengths of both vortices were generally over predicted. As a consequence of the inaccurate prediction of the proximity of the vortices to the model base the region of low positive mean streamwise velocity, $+\overline{u}$ close to the model base. This is not entirely clear from figure 6.5 as the vector maps show velocity magnitude but may be illustrated effectively through contour maps of $\overline{u}$. Figure 6.6 compares contour maps of $\overline{u}$ for the measured flow field and solutions A at the model centreline and shows clearly the failure to predict the region of $+\overline{u}$ close to the model base. Solutions B C and D made similar comparisons. However despite the prediction of wrong flow direction the actual magnitude of the velocity field was comparable for all solutions with predictions in the remainder of the recirculation flow in good agreement.

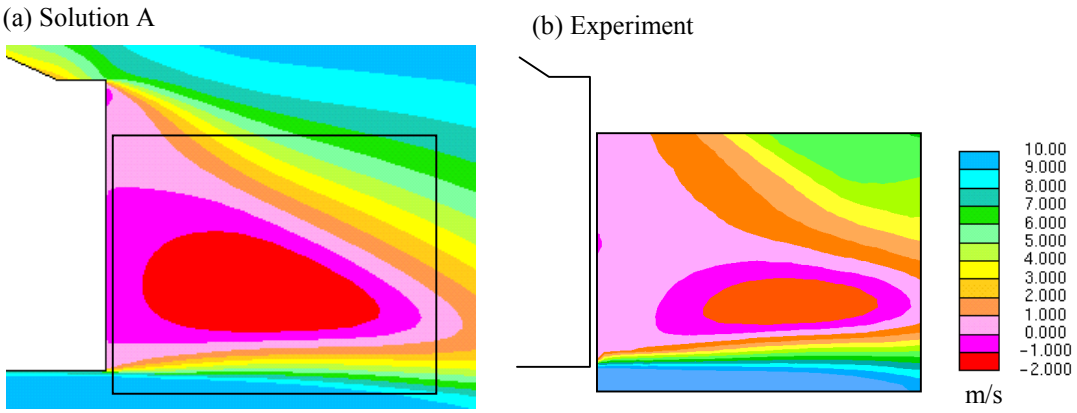

Figure 6.6 – Comparison of contour maps of $\overline{u}$ at the model centreline

Despite these disparities all four solutions made good predictions of the actual location of the core of each vortex. Solution B predicted a slightly longer lower vortex downstream in comparison with the experiment the predicted location of its core was the closest. Predictions of the streamwise position (~ x/l) of the upper vortex core were good but height of the core i.e. y/H was not so well predicted. Solution B also made the closet prediction for the location of the upper vortex core. In general the vertical location of the upper vortex core was over predicted by on average $y/H = 0.112$ most likely a consequence of disparity in velocity direction very close to the model base and the relative size of the upper vortex. The predicted

rotation within the upper vortex was larger due to the flow split into the two vortices occurring closer to the model base providing essentially a larger area for rotation.

	Upper vortex		Lower vortex	
	~x/l	*~y/H*	*~x/l*	*~y/H*
Experimental	0.070	0.289	0.076	0.174
Solution A	0.076	0.433	0.075	0.199
Solution B	0.076	0.349	0.080	0.174
Solution C	0.076	0.433	0.088	0.199
Solution D	0.077	0.389	0.077	0.184

Table 6.2 – Measured and predicted vortex core location for centreline recirculation region structure; Solutions A-D

The measured recirculation region was on the whole more compact than shown in the predictions and as a consequence all solutions slightly over predicted the mean recirculation length. The experimental mean recirculation length was estimated to be approximately 248mm or $x/l \sim 0.180$. The predicted recirculation length was estimated using the local minimum of $\overline{u}/U_\infty$ where U_∞ is free stream velocity and $\overline{u}$ is the local mean component of u (Duell and George, 1999). Figure 6.7 shows a contour map of $\overline{u}/U_\infty$ at the model centreline for solution C where the recirculation length is estimated as the distance between the model base and the furthest point at which $\overline{u}/U_\infty = 0$.

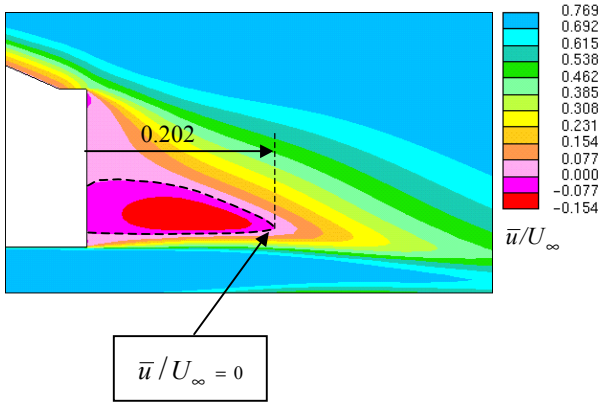

Figure 6.7 – Contour plot of $\overline{u}/U_\infty$, at the model centreline, for the Chen k-ε model using upwind differencing (solution B)

Solutions A B and C made very similar predictions of the mean recirculation length predicting within 10%, 12% and 11% of the experimental value respectively. While

the experimental mean recirculation length is essentially the mean of continually fluctuating point all predictions were to within 12%, which was encouraging, Table 6.3.

	Mean recirculation length ~*x/l*	Vertical location of $\overline{u}/U_\infty = 0$ *y/H*
Experimental	0.180	0.234
Solution A	0.198 (+10%)	0.249 (+6%)
Solution B	0.202 (+12%)	0.214 (-9%)
Solution C	0.2 (+11%)	0.214 (-9%)
Solution D	0.188 (+4%)	0.224 (-4%)

Table 6.3 – Measured and predicted mean recirculation length and location of $\overline{u}/U_\infty = 0$ at the centreline

The numbers in brackets denote the % difference from the experimental value. The solution D made the closest prediction to within 4%. The mean recirculation length was over predicated in all cases. The predictions of the vertical location of the minimum $\overline{u}/U_\infty = 0$ i.e. the mean stagnation point, were also assessed and are given in Table 6.4 showing solution D to make the best prediction. Taking into consideration both prediction of the mean recirculation length and the location of $\overline{u}/U_\infty = 0$ solution D made the best predictions overall.

The velocity gradients across the shear layers that surround the recirculation region were in good agreement with the measured profiles. Figure 6.8 compares the velocity profile of the streamwise velocity component $\overline{u}$ for *x/l* = 0.146 at the model centreline. Downstream distance *x/l* = 0.146 was chosen for comparison as it provides the most detail across the shear layer from the experimental data available. The predicted profiles of velocity $\overline{u}$ through the upper and lower shear layers are similar and in good agreement with the experimental data. However the predicted profiles of $\overline{u}$ through the recirculation region at this point are not so good primarily because all the numerical solutions, A to D over predicted the recirculation length at the model centreline (Table 6.3). The predicted profiles therefore show a significant region of $-\overline{u}$ when the experimental profile shows the end of the recirculation region, the measured recirculation length being ~ *x/l* = 0.180, figure 6.7b.

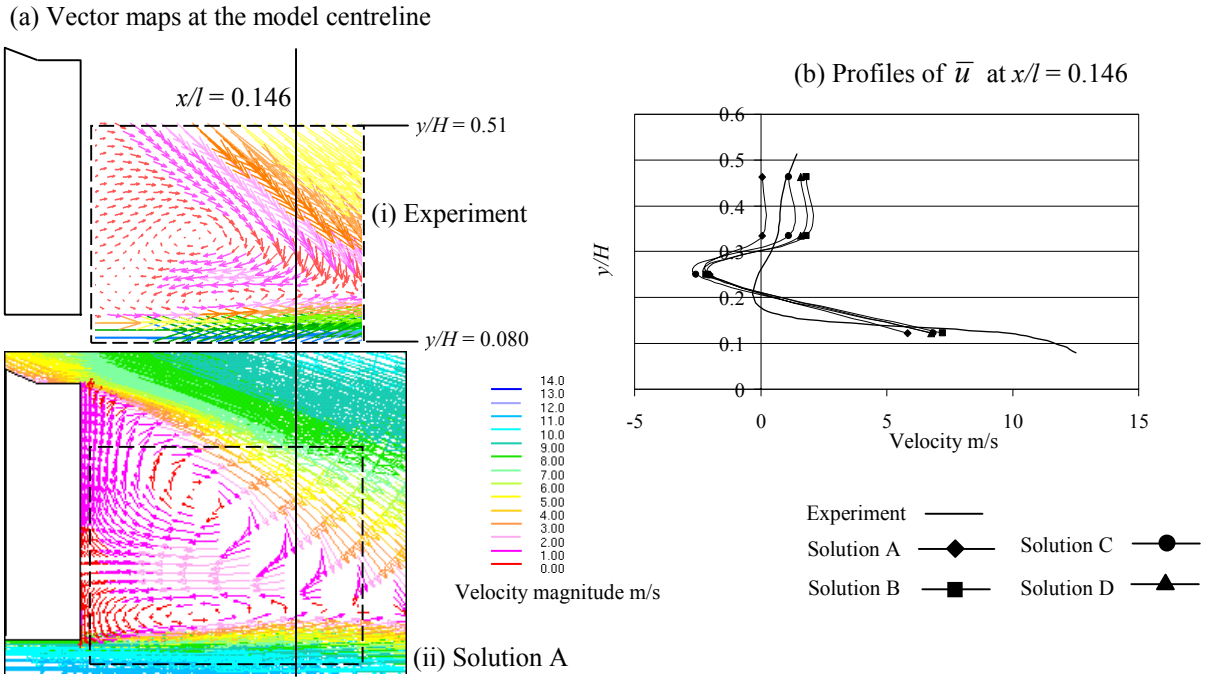

Figure 6.8 – Comparisons of velocity profile $\bar{u}$ for $x/l = 0.146$ at the model centreline

Observations made during tracer gas measurements within the recirculation region of the model vehicle (Chapter 5) showed vortex structure within the vicinity of a representative exhaust to be a primary influence on the dispersion of a gaseous pollutant within the recirculation region. Therefore predictions of the flow structure at this point were of particular importance if a solution was to be used as the foundation for numerical prediction of tracer gas dispersion. A similar assessment to that made in figure 6.5 was made for the predicted vortex structure at $z/b = 0.560$. Figure 6.9a shows a direct comparison between the predicted and measured vortex structures at $z/b = 0.560$. Only solutions A and D are presented, figure 6.9a(i-ii) as all solutions produce near identical vortex structures in which upper and lower vortices were seen to be more equal in size but further apart towards the top and bottom of the recirculation region. Again while the vector field presented for the experimental data was limited in size, figure 6.9a(iii) shows the general vortex structure at $z/b = 0.560$ to be predicted in good agreement with the measured flow field and a significant improvement in comparison to predictions made at the model centreline.

(a) Comparison of predicted and measured velocity vector maps for $z/b = 0.560$

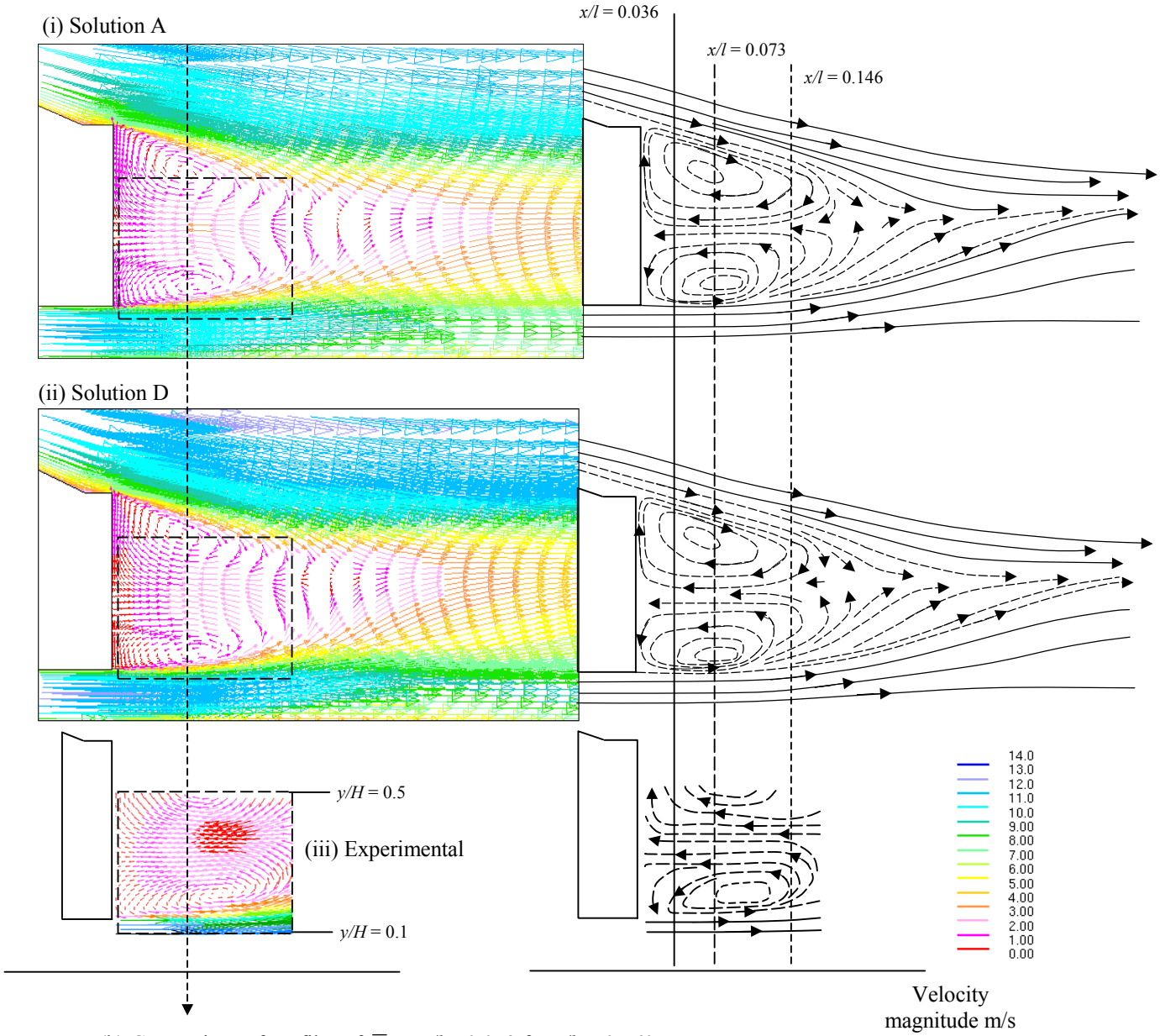

(b) Comparison of profiles of $\overline{u}$ at $x/l = 0.073$ for $z/b = 0.560$

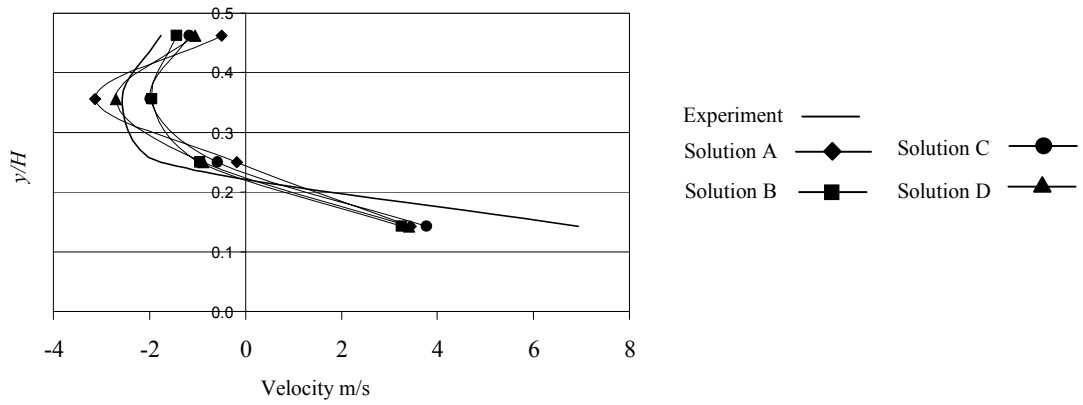

Figure 6.9 – Comparison of predicted and measured flow field at $z/b = 0.560$

Solutions C and D made slightly better predictions than solutions A and B and in particular the very low velocity magnitude close to the model base. Figure 6.9b compares the predicted and measured profiles of streamwise velocity component $\overline{u}$ for $z/b = 0.560$ at $x/l = 0.073$ demonstrating the similar profiles but marginal under and over prediction in the magnitude of the velocity field through the inflow region at this point. Agreement within the lower shear layer was good. The upper shear layer was not captured in the experimental field and is thus not compared. None of the solutions however predicted the low velocity patch within the inflow region between the two vortices shown in the experimental vector map, figure 6.9a(iii).

The location of the upper vortex core at $z/b = 0.560$ was difficult to define using the experimental vector map due to its limited size but as before it was nevertheless useful to compare the predicted and measured location of the lower vortex core, Table 6.4. Similar to the model centreline predictions of the height of the lower vortex above to the floor were in good agreement with the experimental value. However none of the solutions predicted the streamwise location to within closer than 20%, solution D making the best prediction.

	Lower vortex	
	$\sim x/l$	$\sim y/H$
Experimental	0.110	0.199
Solution A	0.076	0.199
Solution B	0.072	0.184
Solution C	0.070	0.180
Solution D	0.082	0.189

Table 6.4 – Measured and predicted lower vortex core location for the recirculation region structure at $z/b = 0.560$

The location and size of the lower vortex at $z/b = 0.560$ was shown in the previous chapter to have a primary influence on the uptake of pollutant from the exhaust plume into the recirculation region (section 5.4.2). Therefore in order that the velocity solutions be used as the foundation for subsequent dispersion simulations it was important that this key feature as well as the general flow structure be adequately predicted. From experimental data the primary "pick-up" region was identified from $\sim x/l > 0.110$ for $z/b = 0.560$ i.e. exhaust location. The pick-up region

being the region of flow downstream of the lower vortex core where upward motion i.e. $+\overline{v}$ becomes significant. Due to the under-prediction in the location of lower vortex core the pick-up region was generally predicted to begin marginally further upstream than observed in the experiment. Solution D made the closest prediction of this point and is demonstrated in figure 6.10. The predicted velocity magnitude at was in general marginally greater than measured suggesting a slightly stronger rotation within the predicted lower vortex.

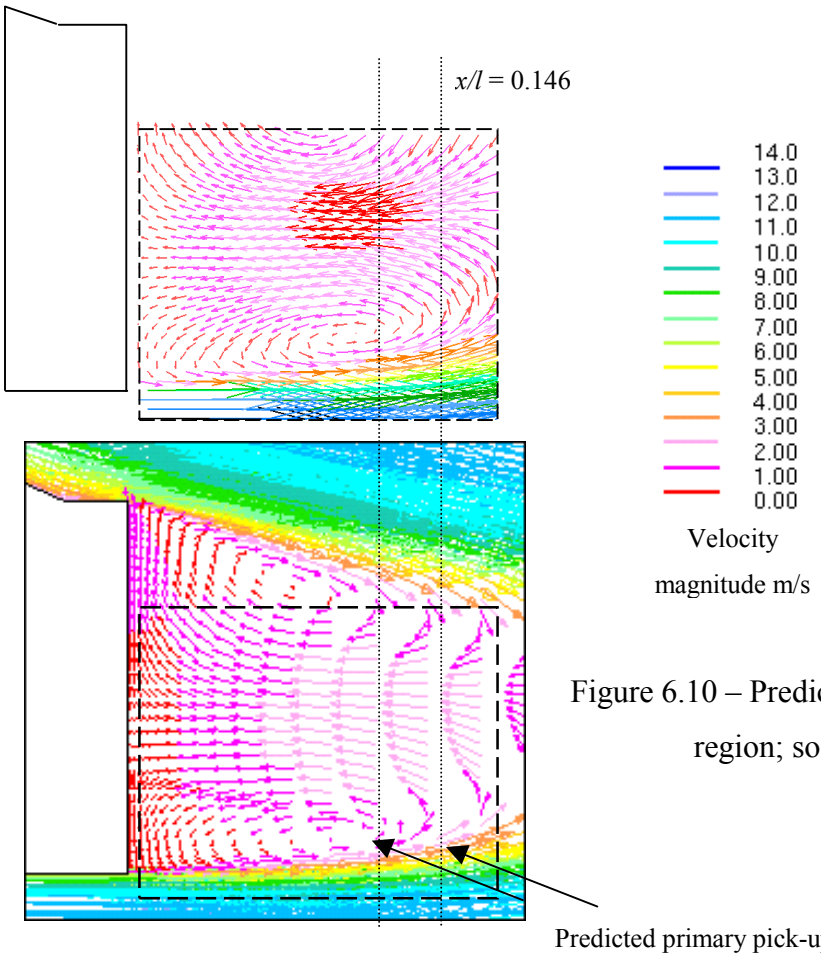

Figure 6.10 – Prediction of "pick-up" region; solution D

From the experimental results presented in figure 4.11 and 4.12 it was clear that the recirculation length at z/b = 0.560 was longer than at the model centreline but due to the limited capture area during measurements it was not possible to determine this length. It was also suggested that due to the change in vortex structure from the centreline to z/b = 0.560 the location of the minimum $\overline{u}/U_{\infty}$ i.e. the mean stagnation point would occur higher up than y/H = 0.234, the location of $\overline{u}/U_{\infty}$ = 0 at the model centreline. The predicted velocity fields were used not to determine these

parameters but to demonstrate that the suggestions made were reasonable. Figure 6.11 shows a contour plot of $\overline{u}/U_\infty$ at z/b = 0.560 for solution B, the Chen k-ε model.

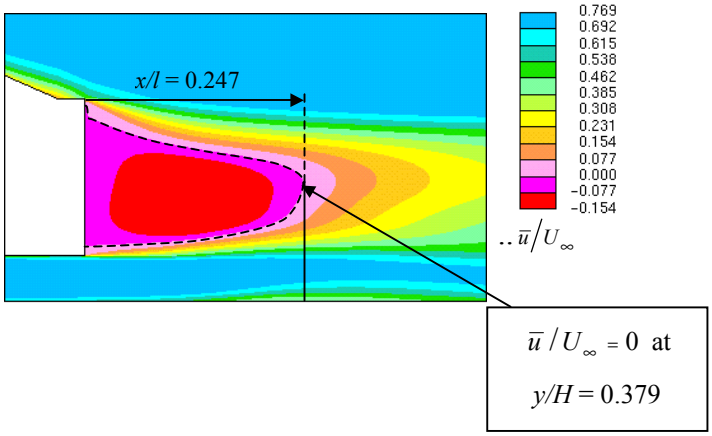

Figure 6.11 – Contour plot of $\overline{u}/U_\infty$, at z/b = 0.560, for solution B

Table 6.5 summarises the predictions of recirculation length and vertical location of $\overline{u}/U_\infty$ = 0 at z/b = 0.560 made by all solutions. Comparing these with the predicted values in Table 6.4 it is clear that the predicted mean recirculation region at z/b = 0.560 is longer than at the model centreline, extending on average x/l = 0.040 further downstream. Even based on the assumption that the numerical simulations over predict the recirculation region at z/b = 0.560 by a maximum of 12% as in the case at the model centreline the recirculation length at z/b = 0.560 is still clearly longer than at the model centreline. Also the point at which $\overline{u}/U_\infty$ = 0 occurs is higher by on average y/H = 0.135 primarily due to the change in vortex structure, Table 6.5.

	Mean recirculation length ~x/l	Vertical location of $\overline{u}/U_\infty$ = 0 y/H
Solution A	0.212	0.338
Solution B	0.247	0.379
Solution C	0.258	0.349
Solution D	0.230	0.373

Table 6.5 –Predicted mean recirculation length and location of $\overline{u}/U_\infty$ = 0 at z/b = 0.560

The other significant time-averaged flow feature within the near wake of a vehicle is the development of a pair streamwise longitudinal vortices from around the model side edges (section 2.2.1). Figure 6.12a compares the predicted and measured cross-stream vortex structure for x/l = 0.146 and 0.218 for solution D. The vector maps are illustrated in black for clarity and the vector lengths magnified by 3 in both cases. In this instance an increase in arrow density did not necessarily correspond to increased rotation. For example the increase in arrow density towards the edge of the model base was due to the computational cells getting smaller and denser. In terms of general flow representation solution D is in good agreement with the measured flow field at x/l = 0.218 showing clear rotation within the flow field. However agreement at x/l = 0.146 is not so favourable with solution D failing to predict the second rotation close to the model centreline. Solutions A, B and C made very similar predictions to that shown in figure 6.12a. Figure 6.12b compares profiles of $\overline{v}$ across the model base at y/H = 0.356 and for x/l = 0.146 and 0.218 for all solutions. The non-prediction of the second rotation at x/l = 0.146 is clearly visible, figure 6.12b(i) where a vortex core is located by $\overline{v}$ = 0. All solutions predict only one location for $\overline{v}$ = 0 as opposed to two shown by the experimental data. It is unclear whether the measured second rotation was a consequence of insufficient sample time (Section 4.5, figure 4.14) and therefore not a true time-averaged flow feature. However this "vortex" was shown not to have an influence over the dispersion of a tracer gas at x/l = 0.146 and therefore its non-prediction was not believed critical in terms of the overall flow structure.

Notwithstanding this failing the development of the primary streamwise longitudinal vortex was generally in good agreement with solutions C and D making marginally better predictions, figure 6.12b(i-ii). The peak in $+\overline{v}$ depicted in both figures 6.12b(i) and (ii) corresponds to the upward rotation on the outer edge of the primary vortex i.e. nearest the model base edge and shows all four solutions to predict the strength of the rotation at this point. However close to the model centreline the downward component $-\overline{v}$ is much stronger than any predicting suggesting solutions A-D to under predict the strength of rotation on this side of the vortex. Each solution made a near identical prediction of location of the vortex core but all predicted marginally closer the centreline than measured i.e. at ~ z/b = 0.560 as opposed to z/b = 0.61.

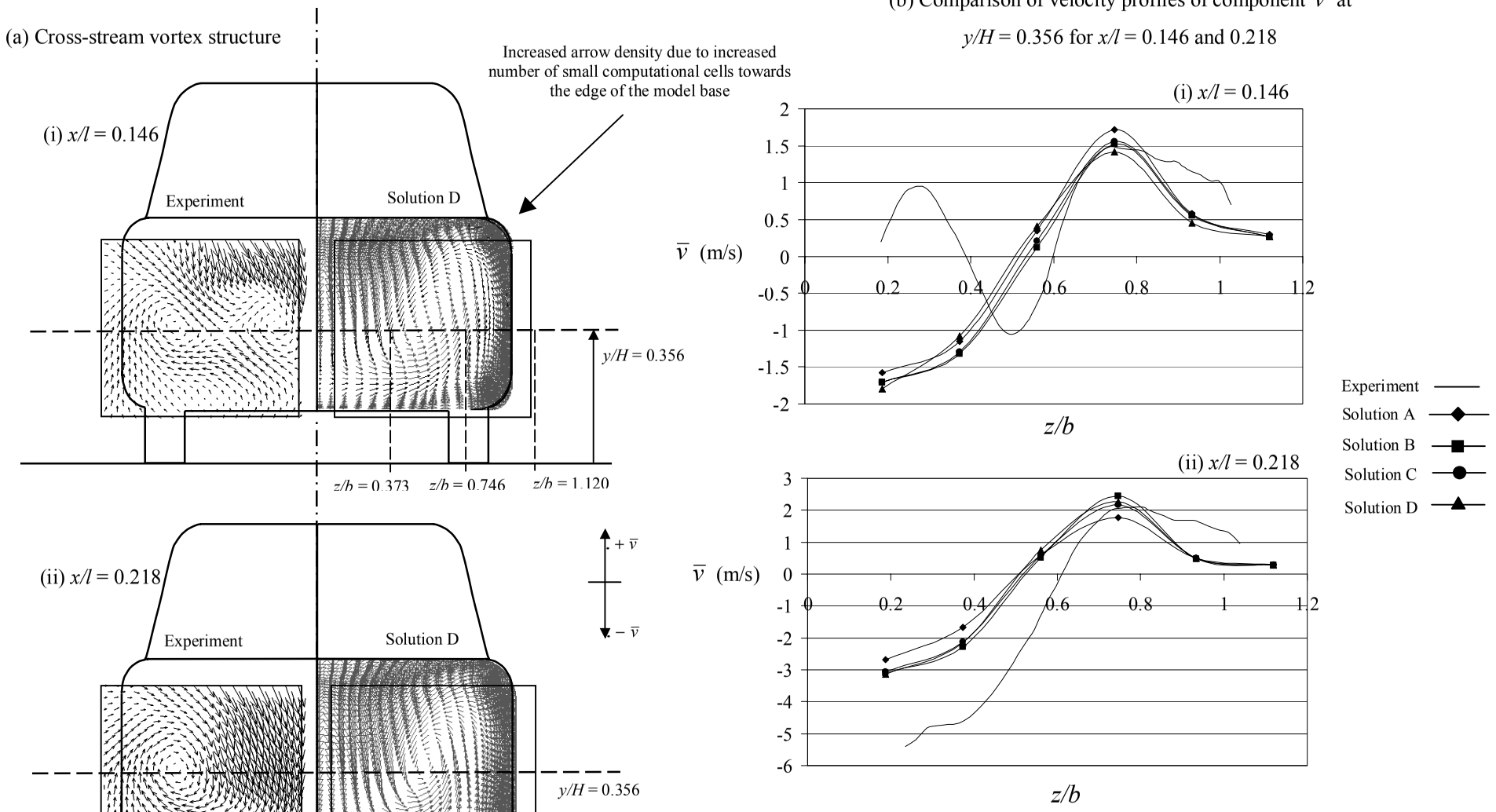

Figure 6.12 – Predictions of streamwise flow development

In order to further assess predictions of the development of this vortex downstream i.e. $x/l > 0.218$ streamwise vorticity, ξ_x was compared using values calculated from the hotwire data (Section 4.3.2). The spatial density of the hotwire measurements at $x/l > 0.218$ were insufficient to create effective vector maps for comparisons (Section 4.5). Figure 6.13a compares contours of $\xi_x H / U_\infty$ where H is the height of the model and U_∞ is the free stream velocity at $x/l = 0.291$ and 0.437 for solution D. The predicted contour maps show good agreement with the measured vorticity field predicting the location of peak vorticity and the movement of this peak with distance downstream. The magnitude of the vorticity field in general was marginally under predicted by solution D. Note that the predicted vorticity field has one less column in the data set due to the way in which ξ_x is calculated and there only being data to the model centreline refer to Appendix 2g. Figure 6.13b compares predicted values of $\xi_x H / U_\infty$ at the $y/H = 0.356$ and 0.250 for $x/l = 0.291$ and 0.437 respectively, the locations of the measured peak negative vorticity.

All four solutions correctly predicted the location of peak negative vorticity but all generally under predicted the magnitude. At $x/l = 0.291$ solutions B- D show similar predictions but solution D made the closest prediction peak negative vorticity to within 12% of the experimental value figure 6.12b(i) and at $x/l = 0.437$ both solutions B, C and D made similar predictions to within 26% of the experimental value. Solution A, using the standard k-ε model made the weakest predictions of vorticity which may be attributed to the isotropic assumption (equation 3.11) on which the model is based where the normal Reynolds stresses are assumed to be equal in all directions i.e. $u'u' = v'v' = w'w'$. For 'real' turbulent flows $u'u' \neq v'v' \neq w'w'$ and as the streamwise vorticity, ξ_x was calculated using local gradients of $\overline{v}$ and $\overline{w}$ Solution A under predicted ξ_x most likely due to less than accurate predictions of $\overline{v}$ and $\overline{w}$. At $x/l = 0.218$ solution A shown to under predict $\overline{v}$ through the centre of the developing vortex, figure 6.11. While solutions B and C, the RNG and Chen k-ε models respectively, also use the same isotropic assumption (equation 3.11) both solutions showed better predictions of ξ_x most likely due to the additional terms that appear in their dissipation rate equations (equations 3.17 and 3.18).

(a) Comparison of contours of streamwise vorticity ξ_x at $x/l = 0.291$ and 0.437 for solution D

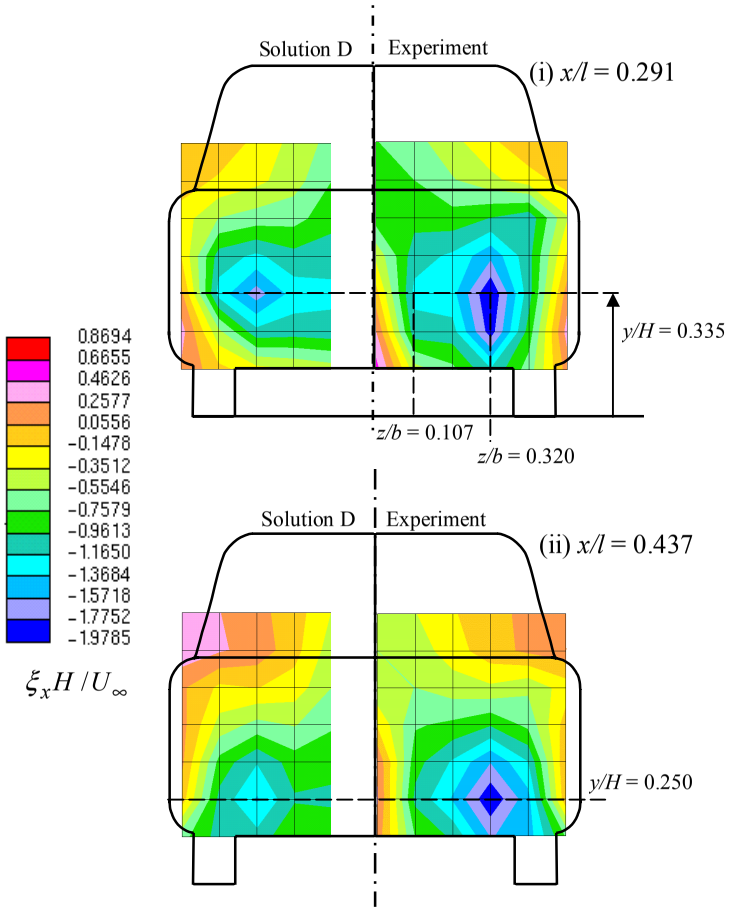

(b) Comparison of profiles of $\xi_x H / U_\infty$ at $y/H = 0.355$ and 0.250 for $x/l = 0.291$ and 0.437 respectively.

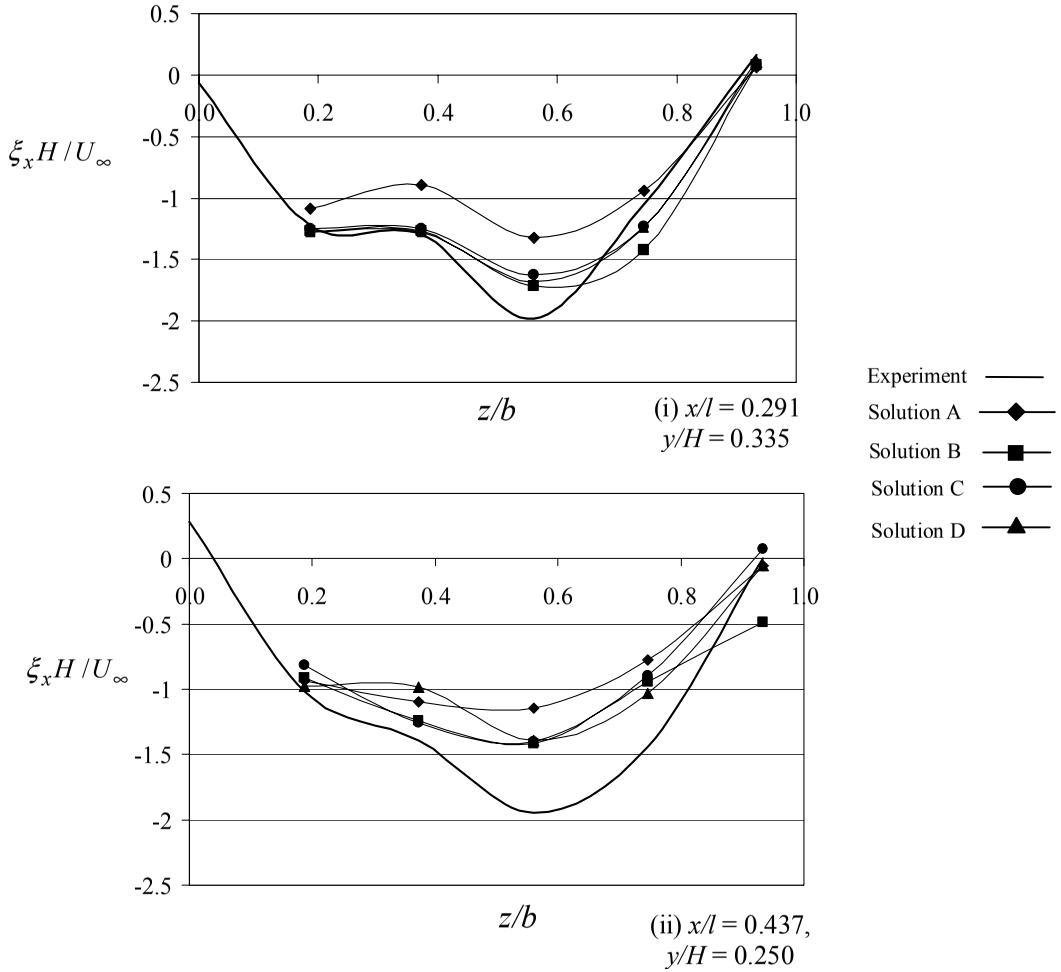

Figure 6.13 – Comparison of predicted and measured streamwise vorticity

It is these terms essentially control the development of ε depending on the mean strain rate of the flow and can result in better predictions of flow separation, rapidly strained flows and anisotropic large scale eddies (Chen and Kim, 1987; Speziale and Thangham, 1992; Choudhury *et al*, 1993; Kim *et al*, 1994). This may also be why solutions B and C made generally good predictions of the mean recirculation length although solution A made a better prediction at the model centreline. Solution D, the non-linear k-ε model made the best prediction of vorticity and thus the development of the streamwise longitudinal vortex due to the non-linear relationship assumed for the Reynolds stresses i.e. $u'u' \neq v'v' \neq w'w'$ (equation 3.20) and the non-linear contributions introduced into both the turbulent dissipation and turbulent energy equations (equations3.21 and 3.22). Similarly solution D made better predictions of recirculation length at both the centreline and $z/b = 0.560$ for this same reason.

Peak negative vorticity corresponds to the centre of the streamwise longitudinal vortex and the observation made from the experimental data that the core moves towards the floor between $x/l = 0.291$ and 0.437 is reflected in the predicted results. The movement of this core closer to the model centreline between $x/l = 0.218$ and 0.291 was not however predicted by any solution with the predicted spatial location of the vortex core at $x/l = 0.218$ also ~ $x/l = 0.560$ for all solutions.

In addition it is useful at this stage in the investigation to assess the quality of flow prediction over the model may be assessed using the measured static pressure coefficients, C_p (section 4.2.4). The predicted upper centreline C_p profiles are in good agreement with the measured centreline static pressure distribution figure 6.14. Both the solution A and C predict C_p at stagnation greater than unity which may be the results of excessive production of $\bar{k}$ at impingement.

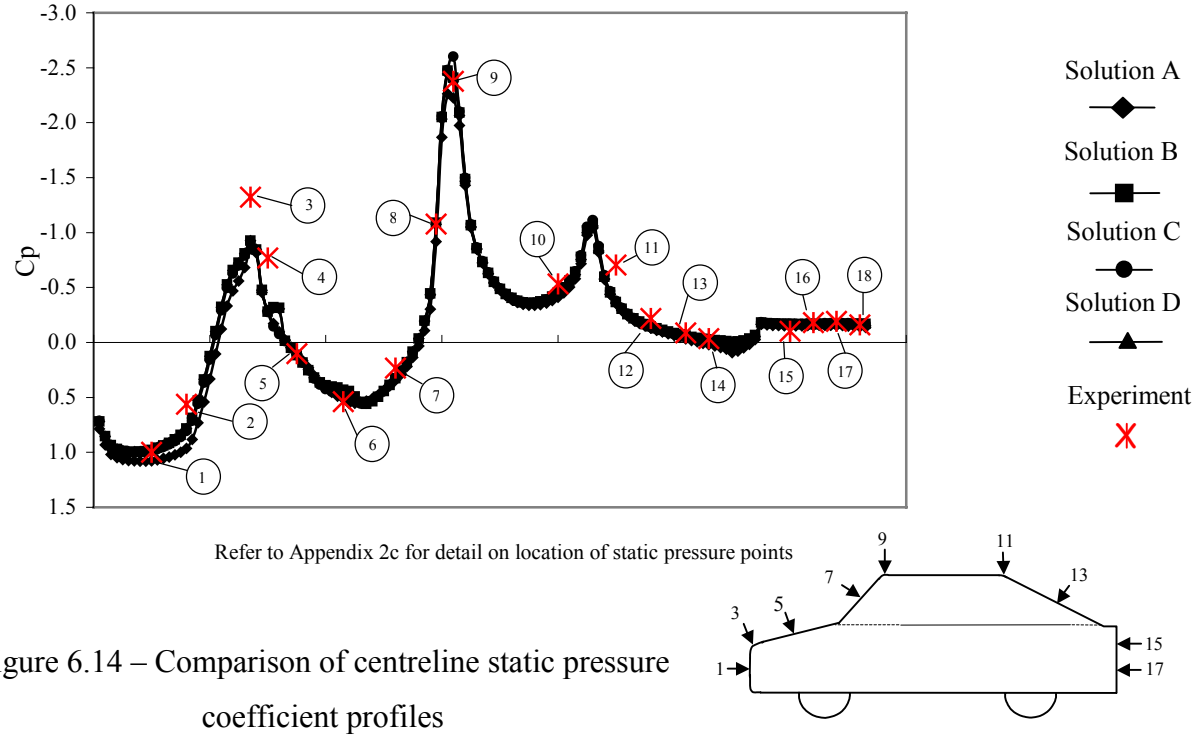

Figure 6.14 – Comparison of centreline static pressure coefficient profiles

The under prediction of the peak minimum pressure at the leading edge of the roof generally results from excessive mixing caused by an over production of $\bar{k}$ at the nose. The experimental values of C_p show there to be no flow separation over the 23° slanted rear surface, which is reflected, in the predicted values by the increased suction around the trailing roof corner.

Overall predictions of the main flow features are in good agreement with the measured data providing a foundation for further modelling. While the comparisons made give a good indication of which turbulence model makes the better prediction of the general flow field structure. However, it is necessary to make a more detailed validation of the solutions obtained.

6.3.1 Statistical validation – solutions A-D

The following section uses statistical techniques for a more global validation of the predicted flow fields, solutions A-D. The first technique compares the absolute percentage difference between the measured and predicted value and is used to assess the overall performance of the solution i.e. the turbulence model (section

3.5.1). The second technique uses the uncertainty in the experimental data to determine the probability of the predicted value falling within the uncertainty range of the measured value (section 3.5.2). Using two different methods allowed for a comprehensive validation of the predicted flow field but also served as a check on each other ensuring meaningful results from each validation. Only predicted and measured values of $\overline{u}$, $\overline{v}$ and $\overline{w}$ were considered in the analysis, as they are the foundation of the predicted flow field and any subsequent calculated values. The only distinction made between the data measured by the hotwire or PIV in the analysis was in the application of the appropriate uncertainty criteria determine in Chapter 4, Section 4.4. The results of the validation are expressed in global terms considering all values of each component measured by both measurement techniques at $x/l \leq 0.218$ and $x/l \geq 0.291$ i.e. because at $x/l \leq 0.218$ the majority of the flow is in recirculation thus prediction should theoretically be more difficult.

The validation of $\overline{u}$ at $x/l \leq 0.218$ is based the velocity field at the model centreline and $z/b = 0.560$ measured using PIV (Section 4.2.2) and for $x/l \geq 0.291$ based on the velocity fields at $x/l = 0.291$ and 0.437 measured using hot-wire (Section 4.2.3). The vertical velocity component $\overline{v}$ was measured at all x/l for all measurement planes and is thus validated for the entire flow field. The validation of $\overline{w}$ at both $x/l \leq 0.218$ and $x/l \geq 0.291$ was based on hotwire and PIV measurements made at all x/l.

Point data was extracted from the PIV data fields (Section 4.2.2) using Tecplot (Amtec, 2001) in accordance with the spatial location of points shown in figure 4.4 for the wake survey grid for the size of capture area i.e. for data at the model centreline all points from wake survey grid, figure 4.4 falling within centreline capture area, figure 4.3 were considered. Tecplot essentially extracts the data from a user specified point by interpolation. PIV measurement did not allow for the exact definition of spatial measurement point as in the wake survey (Section 4.2.2).

6.3.1.1 Absolute percentage difference – solutions A-D

The absolute percentage difference between the experimental and predicted results was calculated according to the description given in section 3.5.1 and the

performance of each solution compared in terms of the percentage of all predicted values falling within a 50 and 75% percentage of all measured values. The results of the validation, summarised in Table 6.6(i-ii) are expressed as the average absolute percentage for each flow variable for $x/l \leq 0.218$ and $x/l \geq 0.291$. The validation was spilt in this way to allow the assessment of prediction within the recirculation region. The total of 328 points were considered for validations. For full solution details refer to Table 6.1 and Appendix 4b.

(i) % of predictions for $x/l \leq 0.218$

	$\overline{u}$		$\overline{v}$		$\overline{w}$	
Solution	≤50%	≤75%	≤50%	≤75%	≤50%	≤75%
A	57%	70%	55%	82%	55%	73%
B	50%	67%	61%	84%	65%	81%
C	51%	69%	62%	85%	62%	82%
D	63%	75%	62%	87%	64%	83%

(ii) % of predictions for $x/l \geq 0.291$

	$\overline{u}$		$\overline{v}$		$\overline{w}$	
Solution	≤50%	≤75%	≤50%	≤75%	≤50%	≤75%
A	95%	100%	56%	79%	58%	82%
B	95%	100%	64%	82%	65%	83%
C	96%	100%	56%	79%	64%	83%
D	96%	100%	61%	83%	66%	84%

Table 6.6 – Results summary of absolute percentage difference comparisons from solutions A-D; % of predicted points at all x/l to fall within x % of the measured data

All four solutions show similar performance when predicting $\overline{u}$ both inside and outside the recirculation region although solution D made marginally better predictions at $x/l \leq 0.218$. The poorer predictions of $\overline{u}$ inside the recirculation region were due to inaccurate predictions of the vortex structure close to the model base and the failure of all solutions to predict the small region of $+\overline{u}$ close to the model base. Outside the recirculation region, $x/l \geq 0.291$ all solutions showed excellent agreement of $\overline{u}$ with the experimental data primarily because resolution of

a flow field with no recirculation was less complicated. All predictions of $\overline{v}$ and $\overline{w}$ were in good agreement with no less than 50% of predictions falling within 50% of the measured values for any solution at any downstream distance based on the criteria set in section 3.5.1.

Note that the PIV vector map presented for x/l = 0.073 (figure 4.13) was slightly discomposed which might have been the result of inconsistent seeding particle concentration due to the unsteadiness within the recirculation region. This would potentially result in fewer image pairs for integration and thus a less accurate representation of the velocity field at x/l = 0.073. As a consequence this might have compromised validations of $\overline{v}$ and $\overline{w}$ at $x/l \leq 0.218$.

On the whole all solutions tended to under predict the three velocity components at all x/l with on average 78%, 73%, 76% and 80% of values being under predicted for solutions A, B, C and D respectively. There was no significant difference between the percentage of under prediction between $x/l \leq 0.218$ and $x/l \geq 0.291$ although the actual magnitude of the under prediction was less for $x/l \geq 0.291$.

The figures shown in table 6.6(i-ii) do not account for incorrect predictions of flow direction. On average 20% of $\overline{u}$, 11% of $\overline{v}$, 10% of $\overline{w}$ were predicted in the wrong direction. The incorrect predictions of both $\overline{v}$ and $\overline{w}$ were the consequence of inaccurate predictions of the recirculation length and the non-prediction of the secondary region of rotation at x/l = 0.146. This was reflected by the highest percentage of wrong-flow direction predictions which occurred at x/l = 0.146. The higher number of wrong predictions for $\overline{u}$ are the result of inaccurate predictions within the recirculation region, close to the model base at the model centreline.

Based on the above analysis solution D, non-linear k-ε/upwind differencing in general showed better predictions both inside and outside the recirculation region. In particular solution D, using the non-linear k-ε model made marginally better predictions of the streamwise velocity component $\overline{w}$ due to the non-linear relationship assumption that $u'u' \neq v'v' \neq w'w'$ as opposed the linear assumption

$u'u' = v'v' = w'w'$ assumed by the standard, Chen and RNG k-ε models used for solutions A, B and C respectively (Chapter 3, Section 3.4).

6.3.1.2 Prediction error in terms of experimental uncertainty –solutions A-D

The standard deviation, σ of the measured mean values were used to represent the prediction error defined in equation (3.27) and to further validate the numerical simulations, solutions A-D using stricter criteria than applied above in section 6.3.1.1. A basic measure of uncertainty in the mean stated values due to turbulent fluctuations the standard deviation provides an effective range for the numerical simulations to predict within. For more detail of the method refer to Section 3.5. The method, previously used by Quinn (1996) accounts for experimental uncertainty allowing the predicted values to be compared against the measured values on a more equal basis on the assumption that the flow variables are normally distributed (Appendix 2d). The prediction error was calculated using equation 3.27 and compared against the maximum standard deviation for each flow variable over all downstream distances, Table 6.7. The maximum standard deviations for the PIV data were used at $x/l \leq 0.218$ and the maximum standard deviations for the hotwire data used for $x/l \geq 0.291$.If the prediction error $E_{p_{\bar{x}}} \leq \sigma$ then the predicted value was closer to the measured value than if $\sigma < E_{p_{\bar{x}}} \leq 2\sigma$, (Chapter 3, figure 3.3). The predicted results were considered to be in good agreement with the experimental data if at least 50% of the predicted results were within σ.

$\sigma_{\bar{u}_{PIV}}$	$\sigma_{\bar{v}_{PIV}}$	$\sigma_{\bar{w}_{PIV}}$	$\sigma_{\bar{u}_{HW}}$	$\sigma_{\bar{v}_{HW}}$	$\sigma_{\bar{w}_{HW}}$
±3.844m/s	±3.352m/s	±3.271m/s	±2.173m/s	±2.724m/s	±2.243m/s

Table 6.7 – Maximum standard deviation for each flow variable

Expressing the prediction error of $\bar{v}$ and $\bar{w}$ in terms of the number of σ shows all solutions to be in good agreement with the experimental data. Despite the predictions of wrong direction all predictions of $\bar{v}$ and $\bar{w}$ were within $\sigma_{\bar{v}_{PIV}}$, $\sigma_{\bar{w}_{PIV}}$ and $\sigma_{\bar{v}_{HW}}$, $\sigma_{\bar{w}_{HW}}$ of the experimental data for $x/l \leq 0.218$ and $x/l \geq 0.291$ respectively.

Figure 6.15 shows the prediction of $\overline{v}$ at x/l = 0.146 illustrating that all predictions fall within $\sigma_{\overline{v}_{PIV}}$ i.e. ± 3.352m/s.

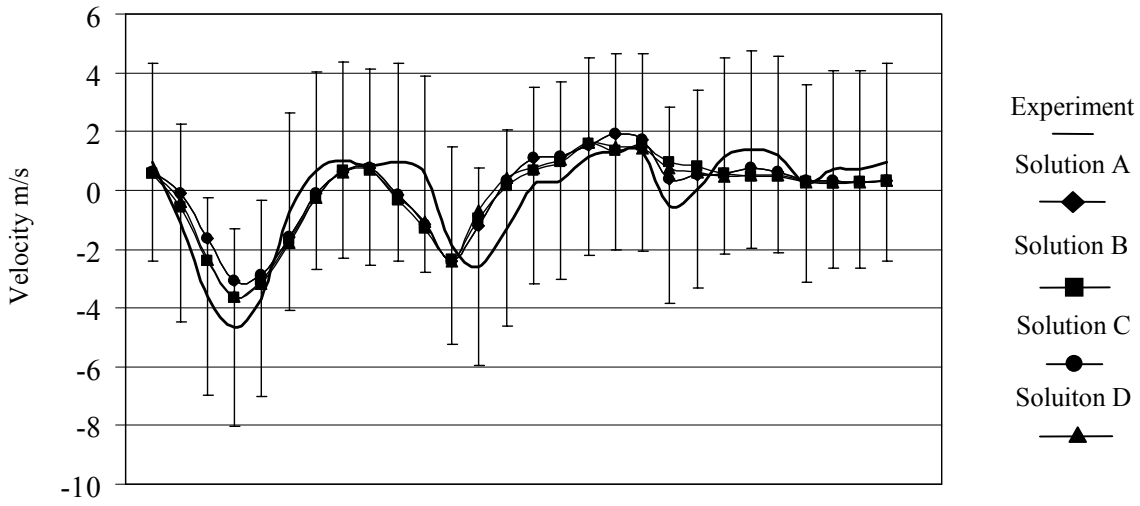

Figure 6.15 – Agreement of predicted values of $\overline{v}$ to within $\sigma_{\overline{v}_{PIV}}$ at x/l = 0.146

Prediction errors in $\overline{u}$ were not as favourable as for $\overline{v}$ and $\overline{w}$ with an average of 70% of predictions falling within either $\sigma_{\overline{u}_{PIV}}$, or $\sigma_{\overline{u}_{HW}}$, of the experimental data for $x/l \leq 0.218$ and $x/l \geq 0.291$ respectively, although 95% of predictions fell to within either $2\sigma_{\overline{u}_{PIV}}$ or $2\sigma_{\overline{u}_{HW}}$, figure 6.16. These unfavourable predictions were the direct consequence of inaccurate predictions within the recirculation region, close to the model base at the model centreline. Nevertheless with over 50% of predicted $\overline{u}$, $\overline{v}$ and $\overline{w}$ within $\sigma_{\overline{u}_{PIV}}$ and $\sigma_{\overline{u}_{HW}}$, $\sigma_{\overline{v}_{PIV}}$ and $\sigma_{\overline{v}_{HW}}$, $\sigma_{\overline{w}_{PIV}}$ and $\sigma_{\overline{w}_{HW}}$ respectively all predictions were considered in good agreement with the measured data in accordance with Section 3.5.2.

6.3.1.3 Solution run times and y^+ *values –solutions A-D*

Solution run times: The relative cost of each calculation is expressed in terms of a CPU time index (Gaylard *et al*, 1998). The CPU time index is calculated as follows;

$$\text{CPU time index} = \frac{\text{Total calculation CPU time}}{\text{Total CPU time for base simulation}}$$

The base simulation refers to the solution using the standard *k-ε*/Upwind differencing combination. The CPU time index for each solution is given in Appendix 4b. The restart facility was used in conjunction with the base simulation to initiate all subsequent calculations and save on processing time (section 6.3).

The solution A had the shortest run time at 402 hours total CPU time requiring 10500 iterations to reach the required level of convergence, Appendix 4b. While solution C needed less than 10,000 iterations the overall CPU time was greater as the RNG *k-ε* model is slightly more complex than the standard model. However in comparison with the solutions B and D, solution C showed the least run time and number of iterations. Convergence difficulties resulted in solution C requiring the greatest number of CPU hours. Significant adjustments were made to the under relaxation factors on both the momentum and transport equations to achieve the desired level of convergence. Solution D used a total of 13100 iterations, compared with 10500 of the standard model but used over twice the total CPU hours because of the increased complexity of the non-linear model *k-ε* used in solution D.

$\underline{y^+}$: The turbulence models used in the current study rely on algebraic wall functions to represent the distribution of velocity, turbulence etc within the boundary layer adjacent to any wall (section 3.4.4.1). In order for these wall functions to be valid the non-dimensional distance from the wall y^+ must be within acceptable limits. It is recommended, for the high Reynolds turbulence models used here that $30< y^+ <150$ (Computational Dynamics, 1998a). Appendix 4b shows $30< y^+ < 45$ y^+ for the surface of the vehicle, thus all y^+ values meet the given criteria.

6.3.1.4 Conclusions –solutions A-D

Generally solution A-D showed favourable agreement with the experimental data with the main flow features within the wake flow represented. The two-tier vortex structure was clearly defined at both the model centreline and *z/b* = 0.560 but at the

model centreline all four solutions failed to accurately predict the size and extent of the vortices very close to the model base. The prediction of the relative vortex sizes at $z/b = 0.560$ were improved showing the overall vortex structure to change with the size of the vortices becoming more equal in strength with distance from the model centreline. The improved predictions of the vortex structure were significant as the location and size of the lower vortex at $z/b = 0.560$ was in Chapter 5 to have a primary influence on the uptake of pollutant from the exhaust plume into the recirculation region (section 5.4.2). Solution D made the better predictions of the flow field within this region.

The recirculation length at the model centreline was predicted to within 12% of measured mean value with solution D making the better prediction to within 4%. The numerical simulations also showed as concluded from the experimental data that due to the change in relative vortex size with distance from the model centreline the recirculation length was longer at distance from the model centreline.

None of the solutions predicted the secondary vortex observed close to the model centreline at $x/l = 0.146$. It is unclear whether the second rotation was a consequence of insufficient sample time (Section 4.5, figure 4.14) and therefore not a true time-averaged flow feature. However this "vortex" was shown not to have an influence over the dispersion of a tracer gas within the near wake flow and as a consequence its non-prediction was not believed critical in terms of the overall flow structure.

While all solutions show good agreement with the measured flow field based on the results of both the direct and statistical validations, solution D, the non-linear k-ε model (solution C) was chosen for stage 2 of study (figure 6.4) based better prediction of the lower vortex and "pick-up" region at $z/b = 0.560$ i.e. the location of the representative exhaust during gaseous measurements. While in terms of CPU run time the solution C took less time than solution D it is often necessary to comprise computational efficiency for solution accuracy. All solutions show favourable y^+ values on the surface of the model falling within the specified criteria for all of the high Reynolds number turbulence models (section 3.4.4.1).

Finally it may be concluded that even using a simple turbulence model such as the standard k-ε model with lower order differencing it was still possible to achieve good simulation of the near wake flow field of a model vehicle without the need for change to any modelling parameters (section 6.3.1).

6.4 Stage 2 – Direct validation of near wake flow field simulation using higher order differencing (solutions E-G)

The Linear Upwind Differencing scheme (LUD) (section 3.3.1.2) and the Monotone Advection and Reconstruction Scheme (MARS) (section 3.3.1.3) were used with the non-linear k-ε model with the aim of improving predictions the near wake flow field, solutions E and F respectively. The standard k-ε model was also used with the LUD scheme in the clarification of certain flow features, solution G. The LUD schemes were used to discretise the momentum equations in solutions E and F where it was blended with the UD in a compromise between accuracy and solution stability. The MARS scheme was used to discretise the momentum equations in solution F and the compression level on the MARS scheme was 0.5 (default), a compromise between accuracy and convergence rate. The upwind differencing (UD) was used to discretise the turbulent transport equations of k and ε in all the solutions.

Because solutions E-G use only standard and non-linear k-ε models predictions from solutions E-G were only compared against solutions A and D, their low order counterparts, in order to assess any improvement in prediction through using higher order differencing. Details of all the solutions may be found in Appendix 4b. The solver used was the SIMPLE algorithm (section 3.3.2). The restart facility (section 6.3) was used with the solution D from stage 1 to initiate the new calculations.

The two-tier vortex structure of the recirculation region at the model centreline was generally represented for solutions E and F, as illustrated in figure 6.16a(i-ii). However again neither of the solutions accurately predicted the upstream extent of the vortices close to the model base. Both solutions over predicted the upstream length of the vortices showing them to extend to the model base when the measured flow field showed them to extend upstream only to $x/l = 0.036$, refer to figure 4.11. As a consequence the region of low positive mean streamwise velocity, $+\overline{u}$ close to the model base was not predicted, illustrated using contour maps in figure 6.16b. However despite the prediction of wrong flow direction the actual magnitude of the velocity field within this region was comparable for solutions E-G with predictions of velocity magnitude in the remainder of the recirculation flow in fair agreement.

The contour maps presented also show a slight distortion in the contour field in the lower shear layer not seen in the measured flow field or predictions by solutions A and D i.e. figure 6.6. As a further assessment an additional solution was obtained using the standard k-ε model and the linear upwind differencing scheme (solution G). Figure 6.16b(iv) shows the predicted contour map of $\overline{u}$ at the model centreline for solution G. Comparing these with those presented in figure 6.16b(i-iii) and figure 6.6 shows solution G to make more comparable prediction with solutions A and D and the measured flow field not predicting the distortion in the contour field. Note that solutions A and D made very similar predictions of the shape of the contour map for $\overline{u}$ at the model centreline.

There was also significant distortion in the vector field for solutions E and F further downstream at $\sim x/l = 0.218$, figure 6.17a(i-ii). Due to the limited capture area of the PIV measurements at the model centreline[6.3] it was not possible to assess whether these further flow distortions were real or a product of the simulation. Figure 6.17 presents the velocity vector field at the model centreline predicted by solution G and shows no significant flow distortions compared with solutions E and F. Solution G also made comparable predictions with solutions A and D which also showed no flow distortions at $\sim x/l = 0.218$.

[6.3] The capture area for PIV measurements was limited by the perpendicular distance fro the camera, laser projection angle and height (Section 4.2.2)

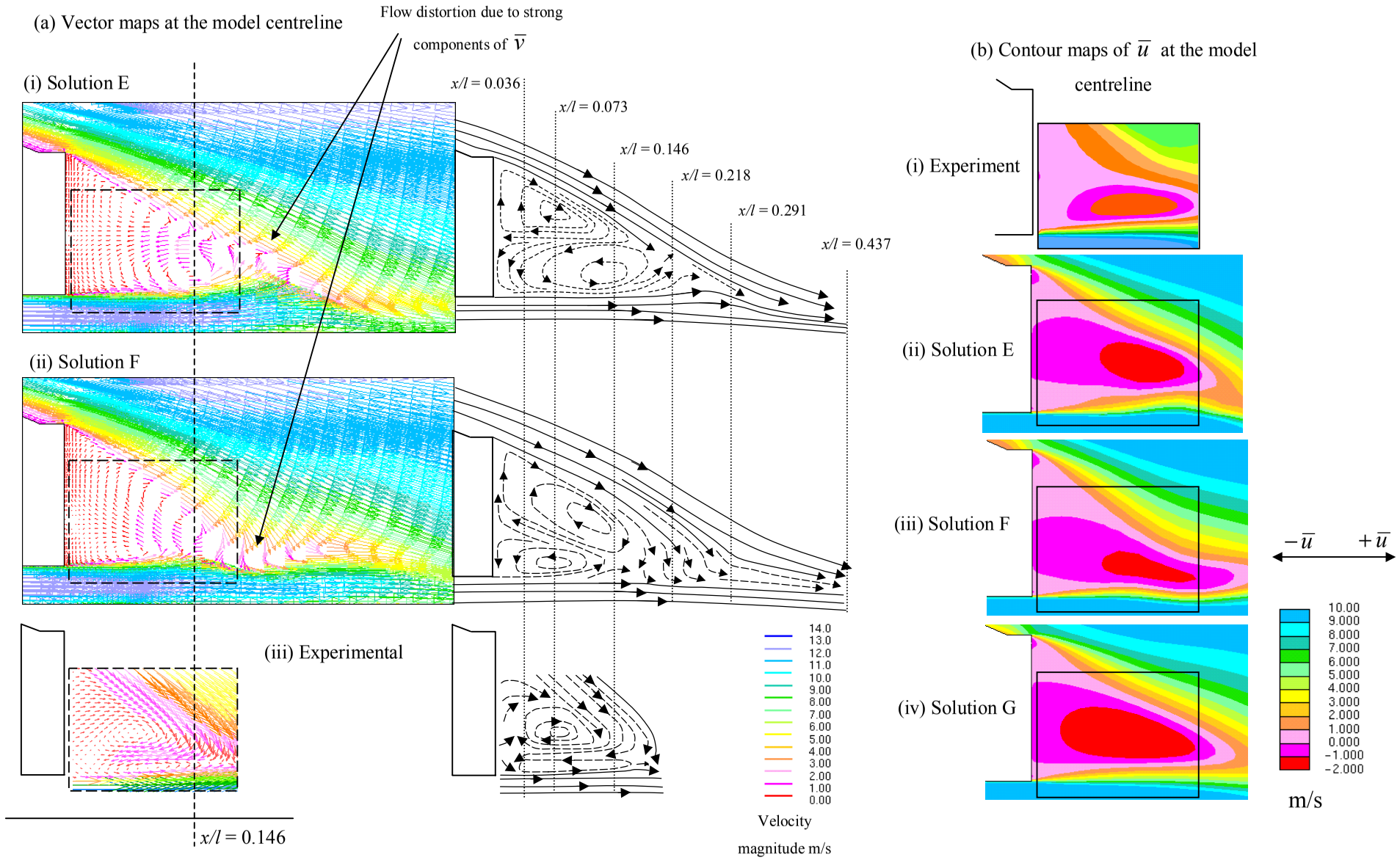

Figure 6.16 Comparison of measured and predicted centreline near wake recirculation region structure

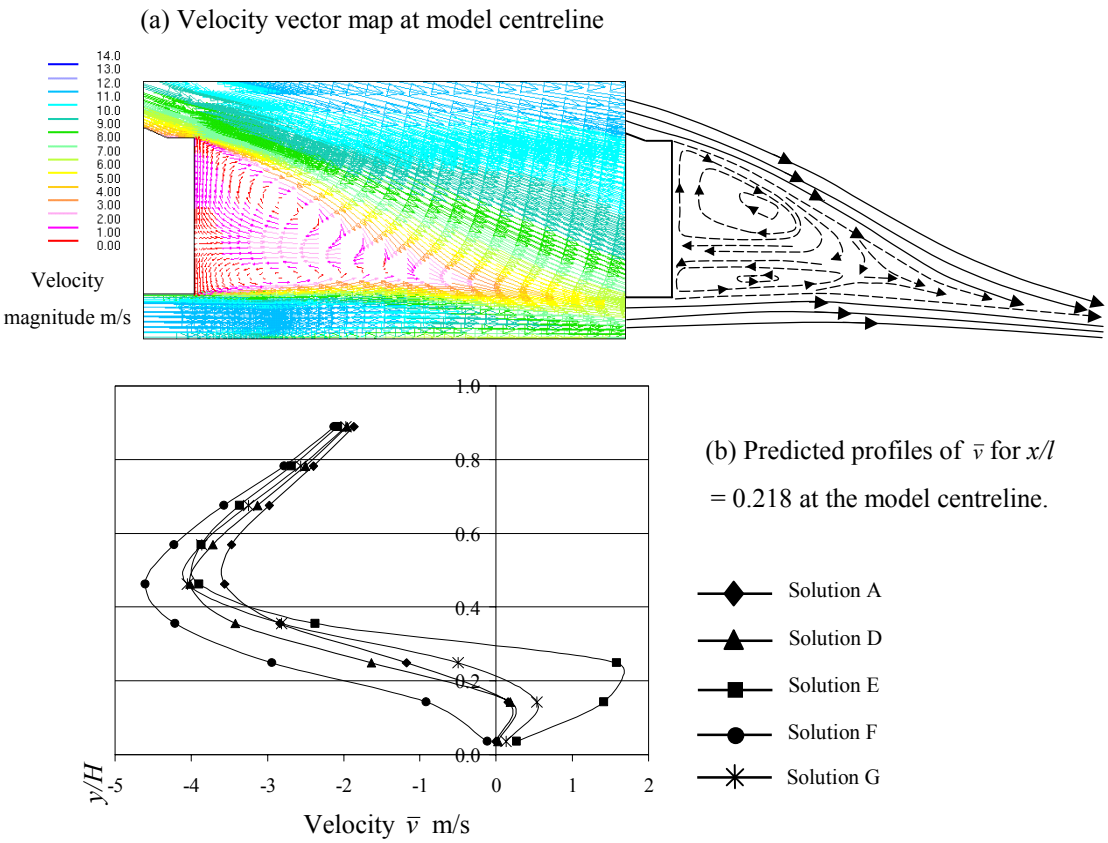

Figure 6.17 - Assessment of flow distortion

The predicted distortions in the flow field were believed to be due to the prediction of a stronger component of $+\bar{v}$ close to the lower shear layer. Figure 6.17b compares predicted profiles of $\bar{v}$ at $x/l = 0.218$ for the model centreline for solutions A, D, E, F and G. Experimental values of $\bar{v}$ at $x/l = 0.218$ along the model centreline were not available because the streamwise capture area was not long enough and for the cross-stream measurements the field did not extend to the model centreline, refer to Section 4.2.2. The velocity profiles show a stronger $+\bar{v}$ at $x/l = 0.218$ for solution E and purely $-\bar{v}$ at $x/l = 0.218$ for solution F which correspond to the distortions predicted flow as indicated in figure 6.16b(i-ii). Predictions from all other solutions, namely A, C, and G at $x/l = 0.218$ predicted no distortion. With solutions B and C also not predicting these distortions it is believed that they were not real and just a consequence of the simulation. It will also be shown in section 6.5 that even using a refined mesh this distortion was not predicted.

Despite the increase in solution accuracy offered by the higher order differencing schemes of LUD and MARS (Section 3.3.1.2 and 3.3.1.3) solutions E, F and G showed no improvement over solutions A and D. In fact solutions E and F made poorer predictions of the relative vortex sizes within the recirculation region in comparison with solutions A and D, figures 6.5 and figure 6.16. Solution E predicted a much to large lower vortex and solution F different vortex size and shapes completely. It was solution G that made the best prediction of the general shape internal vortex structure albeit over predicting there actual downstream length and again failing to accurately predict the flow field close to the model base. At this point, because none of the solutions have accurately predicted the flow close to the model base one might start to doubt the measured flow field. However it should be remembered that regions of recirculation are notoriously difficult to predict even with more sophisticated turbulence models but with the general flow structure in good agreement it was concluded that the measured flow field was a good representation based on the facts of chapter 2, section 2.2.1.

To further assess the predictions of the vortex structure at the model centreline the predicted and measured spatial locations of the core of these vortices are compared, Table 6.8. The table also includes the locations predicted by solutions A and D for comparison. Solution E made favourable predictions in comparisons with the measured locations for the downstream distance (*x/l*) of the upper vortex and the vertical height of the lower vortex (*y/H*) predicting to within 9% and 14 % respectively. Predictions of *y/H* for the upper vortex and *x/l* for the lower were poor.

	Upper vortex		Lower vortex	
	~x/l	*~y/H*	*~x/l*	*~y/H*
Experimental	0.070	0.289	0.076	0.174
Solution E	0.076	0.428	0.137	0.199
Solution F	0.119	0.374	0.076	0.174
Solution G	0.093	0.473	0.093	0.199
Solution A	0.076	0.433	0.075	0.199
Solution D	0.077	0.389	0.077	0.184

Table 6.8 – Measured and predicted vortex core location for centreline recirculation region structure

Solution F predicted the exact spatial location of the lower vortex despite predicting the wrong size and shape in comparison with the experiment but made poor predictions of the location of the upper vortex core. The best predictions were made by solution G predicting 3 of the four locations good agreement. All of the solutions as with solutions A and D over predicted the height of the upper vortex core due to the over prediction in the upstream extent of the vortex close to the model base. As a consequence the predicted rotation in the upper vortex was larger due to the flow split into the two vortices occurring closer to the model base providing essentially a larger area for rotation.

The predicted mean recirculation lengths at the model centreline were established as in section 6.3 and are listed in Table 6.8 along with the vertical location of the mean stagnation point. The numbers in brackets denote the percentage of over or under prediction. Solution E, F and G all over predicted the mean recirculation length at the model centreline by 13%, 32% and 17% respectively. Solution E made the closest prediction. In comparison with the predictions of the equivalent lower order solutions, the use of higher order differencing did not results in closer predictions primarily due to the flow distortions observed in figure 6.16. In predicting the location of the mean stagnation point i.e. $\overline{u}/U_{\infty} = 0$, solutions F and G made comparable predictions to the lower order solutions A and D and were in good agreement with the experiment predicting to within 6%. Solution E made the poorest prediction.

	Model centreline		*z/b* = 0.560	
	Mean recirculation length : ~*x/l*	$\overline{u}/U_{\infty} = 0$ *y/H*	Mean recirculation length : ~*x/l*	$\overline{u}/U_{\infty} = 0$ *y/H*
Experimental	0.180	0.234	-	-
Solution E	0.204 (+13%)	0.274 (+17%)	0.246	0.399
Solution F	0.238 (+32%)	0.224 (-4%)	0.252	0.389
Solution G	0.212 (+17%)	0.244 (+4%)	0.229	0.349
Solution A	0.198 (+10%)	0.249 (+6%)	0.212	0.338
Solution D	0.188 (+4%)	0.244 (-4%)	0.230	0.373

Table 6.9 – Comparing measured and predicted mean recirculation length and location of $\overline{u}/U_{\infty} = 0$ for solutions A, D, E-G

Table 6.9 also includes predictions for the recirculation length at *z/b* = 0.560 and while there were no experimental values to compare against the predictions of solutions E-G were compared with solutions A and D. The higher order solutions, E-G generally predicted a longer mean recirculation length at x/l = 0.560 and a higher location (*y/H*) for $\overline{u}/U_{\infty} = 0$.

Predictions of the vortex structure at *z/b* = 0.560 were in much better agreement with both lower order solutions, A and D and with the measured field. Figure 6.18a compares the predicted vortex structure at *z/b* = 0.560 from solutions E and G and when compared with the vector maps and vortex sketches shown in figure 6.9 the good agreement is clear. Solution F made near identical predictions to solution E. The measured and predicted vertical profiles of $\overline{u}$ at *x/l* = 0.073 for *z/b* = 0.560 are shown in figure 6.18b and show the shape of the profile to be in good agreement but with under prediction by solution E-G through the inflow region between the vortices. While good agreement is desirable for the flow fields at both the model centreline and *z/b* = 0.560 the prediction at *z/b* = 0.560 was more critical as the flow field at this location was shown to have a significant influence on the dispersion of tracer gas expelled from a representative exhaust placed at *z/b* = 0.560 and in particular the lower vortex (Chapter 5).

The prediction of the "pick-up" region of the lower vortex in which tracer gas was drawn up from the exhaust plume into the recirculation region was of primary importance. The pick-up region occurs just aft the lower vortex core i.e. where the vortex rotation becomes dominated by $+\overline{v}$. Table 6.10 shows the prediction of the spatial location of the lower vortex core by all solutions to be in fair agreement with the measured flow field with solution F making the best prediction. Thus it maybe concluded with reference to figures 6.10 and 6.18 that solutions E-G make a fair estimate of the pick up region at ~ *x/l* = 0.146. Note that solution E made very similar predictions to solution F.

(a) Predicted vector maps at $z/b = 0.560$

(i) Solution E

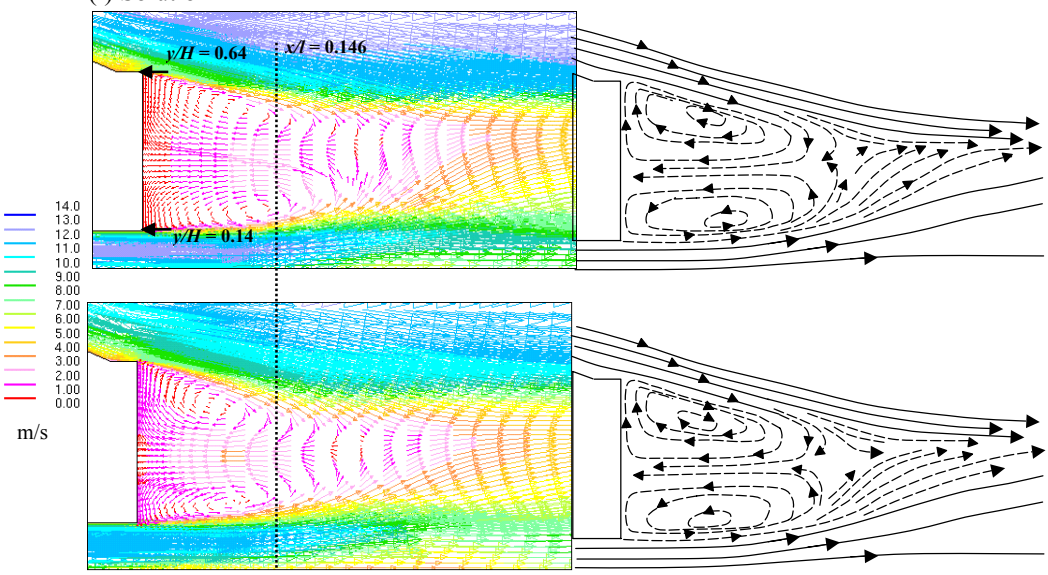

(ii) Solution G

(b) Comparison of profiles of $\overline{u}$ at $x/l = 0.146$ for $z/b = 0.560$

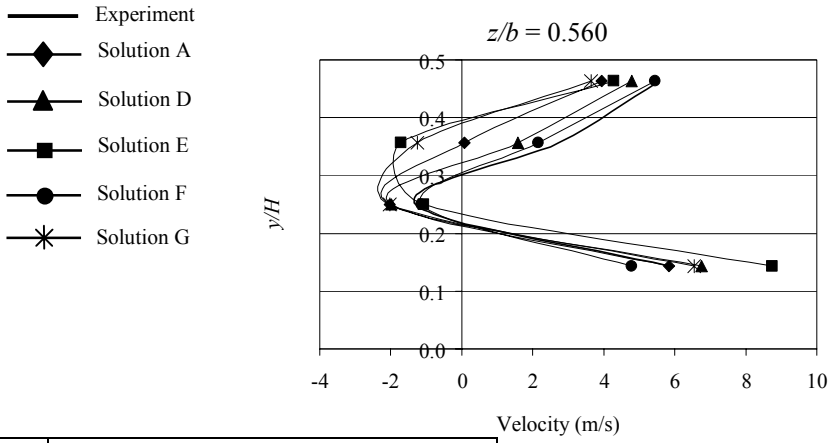

Figure 6.18 – Comparison of predicted and measured flow field at $z/b = 0.560$

	Lower vortex	
	~x/l	~y/H
Experimental	0.110	0.199
Solution E	0.127	0.174
Solution F	0.102	0.189
Solution G	0.093	0.199
Solution A	0.076	0.199
Solution D	0.082	0.189

Table 6.10 – Measured and predicted lower vortex core location for the recirculation region structure at $z/b = 0.560$ (solutions E-G, A and D)

Predictions of the streamwise growth of one of a pair of longitudinal vortices were comparable to those made by solutions A-D. Figure 6.19a compares measured cross-stream flow field for $x/l = 0.218$ with the predicted field from solution E showing the structure of the cross-stream flow to be in fair agreement.

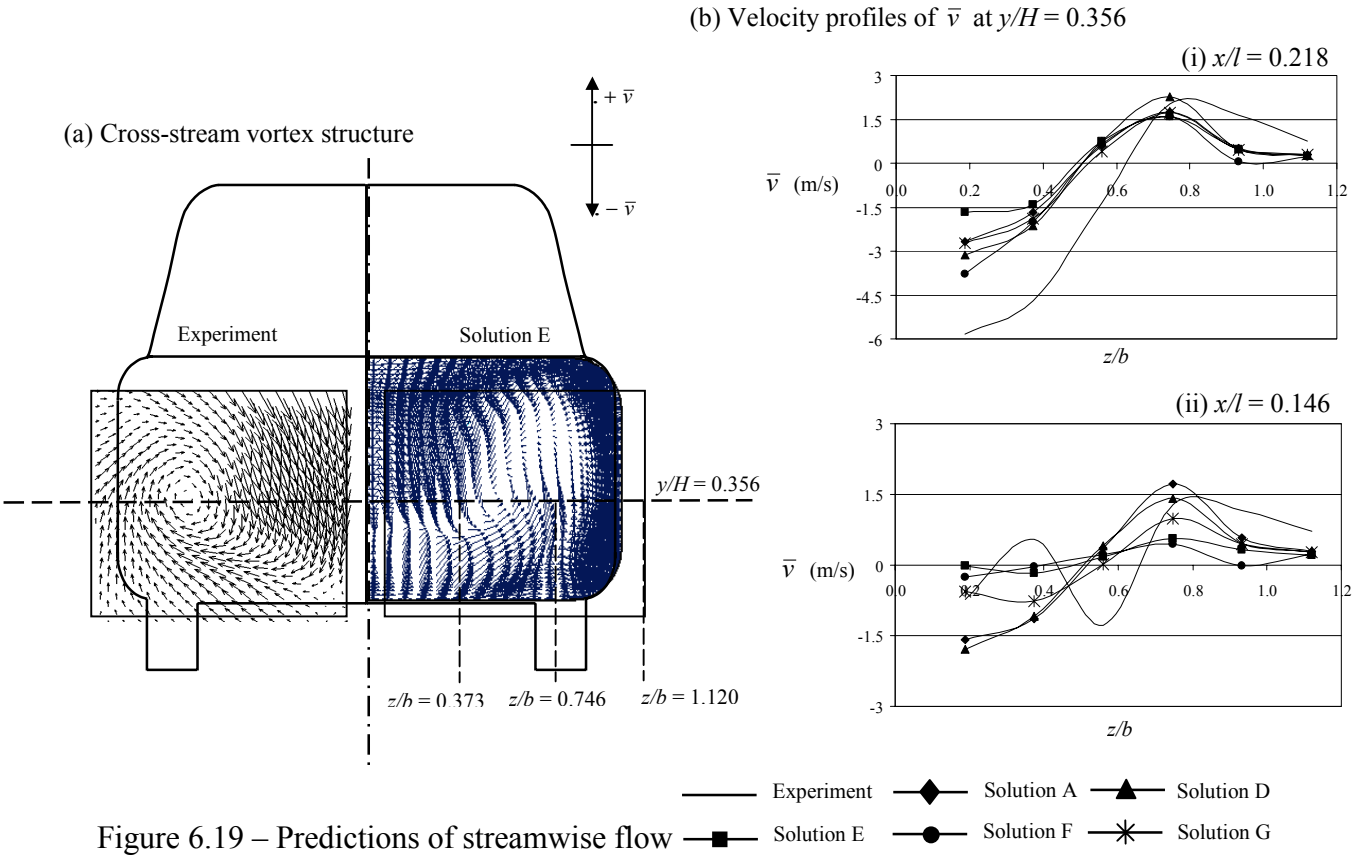

Figure 6.19 – Predictions of streamwise flow development higher order solutions

The vector maps are illustrated in black for clarity and the vector lengths magnified by 3 in both cases. In this instance an increase in arrow density did not necessarily correspond to increased rotation. For example the increase in arrow density towards the edge of the model base was due to the computational cells getting smaller and denser. The measured profile cross-stream profile of $\bar{v}$ are compared against for those solutions E, F. G, A and D at $x/l = 0.218$ for $y/H = 0.356$ the approximate vertical height of the vortex core in each case, figure 6.19b(i). Solutions E-G all made very similar predictions of the cross-stream location of the vortex centre i.e. where $\bar{v} = 0$ comparable to the predictions of solutions A and D. However none of the predictions were in agreement with the measured location of the vortex core. In addition neither solution E, F or G predicted the second cross-stream rotation

observed at *x/l* = 0.146 in the measured data, figure 6.19b(ii) which is denoted by the double change in direction of $\bar{v}$ in the experimental profile, also refer to figure 6.12. To assess further downstream flow development predictions of peak negative streamwise vorticity, ξ_x were compared for distance *x/l* = 0.291 and 0.437[7.4] to assess the movement of the vortex core. The measured flow field showed the vortex core of the streamwise longitudinal vortex to move down towards the floor between *x/l* = 0.291 and 0.437, from *y/H* = 0.356 to *y/H* = 0.250 respectively. Peak negative vorticity corresponds to the vortex centre therefore predicted and measured profiles ξ_x at *y/H* = 0.356 and *y/H* = 0.250 for *x/l* = 0.291 and 0.437 respectively were compared, figure 6.20. Comparison is also made with solutions A and D. At both *x/l* = 0.291 and 0.437 solutions E, F and G predicted the correct location of peak negative vorticity but all generally under predicted the magnitude except solution F at x/l = 0.437 which made an excellent prediction near identical to the measured value. At *x/l* = 0.437 solution F also made the better prediction under predicted the maximum value by only 3%. Solutions E and F made better predictions than solution G as solutions E and F use the non-linear standard *k-ε* model and the anisotropic assumption that $u'u' \neq v'v' = w'w'$. The predictions by solutions E-G were an improvement over solutions A and D.

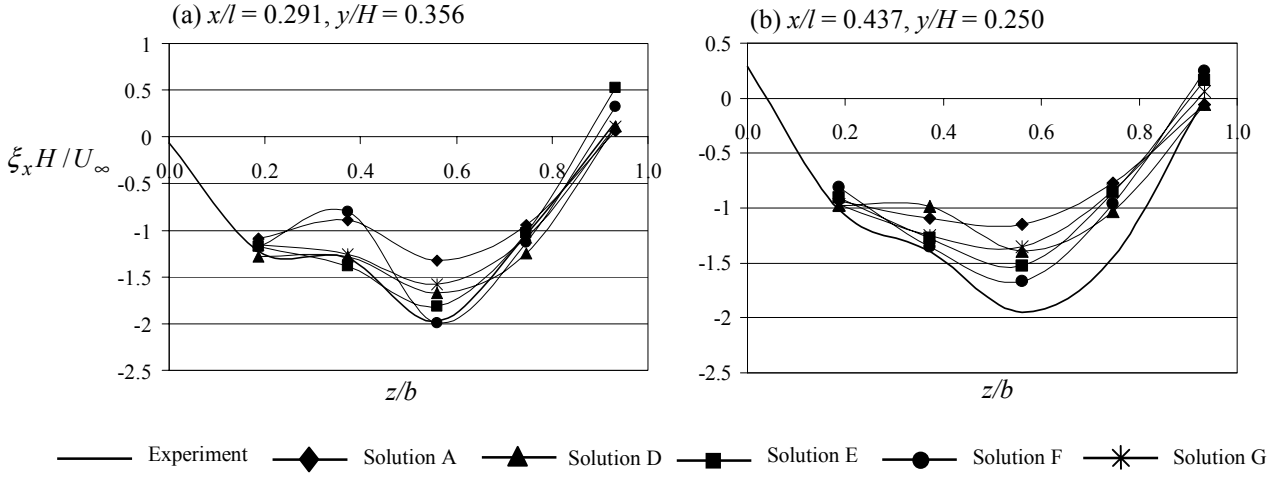

Figure 6.20 – Profiles of predicted and measured $\xi_x H/U_\infty$

[7.4] The spatial density of hotwire measurements was insufficient to create effective vector maps (Section 4.5)

6.4.1 Statistical validation – solutions E-G

The same techniques used in section 6.3.2 were applied here. The performances of solutions E-G are compared against solutions A-D to assess the level of improvement in predictions through using higher order differencing schemes.

6.4.1.1 Absolute percentage difference – Solutions E-G

The absolute percentage differences between the experimental and predicted results were calculated according to the description given in section 3.5.1. The relative performance between the higher order and lower order solutions is expressed as a percentage increase in the number of predicted values falling within 50% and 75% of the measured values. For a example the results of the solutions A-D show on average 83% of predicted values of $\overline{w}$ to lie within 75% of the measured data at $x/l \geq 0.291$ in comparison with 85% from solutions E-G, an improvement of 2%. As before the results of the validation were expressed in global terms considering all values of each component measured by both measurement techniques at $x/l \leq 0.218$ and $x/l \geq 0.291$ (Section 6.3.1). The results of the analysis are summarised in Table 6.10.

The numbers in brackets () denote the percentage improvement over the equivalent low order solutions i.e. for solutions E and F improvement over solution D and for solution G improvement over solution A (Section 6.3).

Solutions E-F showed only minor improvement in predictions of $\overline{u}$ at $x/l \leq 0.146$ over all the lower order solutions, solutions A-D, although when solution F was compared directly with its lower order counterpart, solution D the predictions of solution F were poorer. The general improvements came through the magnitude of predicted $\overline{u}$ being marginally better predicted despite the predicted flow structure being poorer (figure 6.17). This point highlights the importance of using both visual and numerical validations to assess predictive performance.

(i) % of predictions for $x/l \leq 0.218$

	$\overline{u}$		$\overline{v}$		$\overline{w}$	
Solution	≤50%	≤75%	≤50%	≤75%	≤50%	≤75%
E	60%(3)	79%(4)	61%(-1)	85%(-3)	62%(2)	82%(-1)
F	60%(-3)	72%(-3)	57%(-5)	81%(-6)	60%(-4)	80%(-3)
G	56%(-1)	74%(4)	59%(4)	80%(-2)	57%(2)	78%(5)
% Improvement over solutions A-D	3%	3%	-1%	-2%	0%	0%

(ii) % of predictions for $x/l \leq 0.291$

	$\overline{u}$		$\overline{v}$		$\overline{w}$	
Solution	≤50%	≤75%	≤50%	≤75%	≤50%	≤75%
E	97%(2)	100%(0)	67%(6)	86%(3)	71%(7)	87%(3)
F	96%(0)	100%(0)	68%(7)	85%(2)	67%(1)	84%(1)
G	96%(1)	100%(0)	60%(4)	76%(-3)	64%(6)	84%(2)
% Improvement over solutions A-D	0.5%	0%	6%	2.5%	3%	2%

Table 6.11 - Results summary of absolute percentage difference comparisons for solutions E-G with percentage improvement over solutions A-D

The prediction of $\overline{v}$ at $x/l \leq 0.218$ was generally poorer due to the predicted flow distortions close to $x/l = 0.218$. Solution G made the best predictions because no flow distortions were predicted. Predictions of $\overline{w}$ at $x/l \leq 0.218$ showed no significant improvement over the lower order solutions. In fact, in general predictions at $x/l \leq 0.218$ showed only a 1% improvement for all predicted velocity components ≤75% of the measured values, which may be attributed to universal difficulties in prediction in regions of recirculation. In addition a discomposed vector map for the measured data at $x/l = 0.073$ (figure 4.13), thought to be the result of insufficient flow seeding may have contributed to poor improvements in the validation of $\overline{v}$ $\overline{w}$ at $x/l \leq 0.218$. Prediction outside recirculation at $x/l \geq 0.291$ were on the whole much better with a global improvement of 7.5% on prediction ≤75% to the measured values. The improved predictions of $\overline{w}$ were reflected in the improved predictions of streamwise vorticity figure 6.21.

All solutions tended to under predict the three velocity components at all *x/l* with on average 81% for solutions E and F and 85% for solution G. There was no significant difference between the percentage of under prediction between $x/l \leq 0.218$ and $x/l \geq 0.291$ although the actual magnitude of the under prediction was less for $x/l \geq 0.291$. The percentage of predicted values under predicted were marginally higher in comparison with solutions A and D.

The figures given in Table 6.10 do not take account of predictions of wrong flow direction. Incorrect predictions of $\overline{v}$ resulted from inaccurate predictions of the mean recirculation length and were comparable to solutions A and D at 10%. The wrong-direction flow predictions of $\overline{w}$ are generally comparable to those made by solutions A and D primarily due to the absence of the secondary vortex at $x/l = 0.146$ in the predicted velocity fields. Incorrect flow direction predictions of the streamwise velocity component $\overline{u}$ were only significant at $x/l \leq 0.218$ due to inaccurate predictions of the vortex sizes within the recirculation region.

With on average 60% of predictions at $x/l \leq 0.218$ and 76% of predictions at $x/l \geq 0.291$ falling within 50% of the measured values the overall predictions by solutions E, F and G were considered to be in good agreement with the measured data (Section 3.5.1).

6.4.1.2 Prediction error in terms of experimental uncertainty – Solutions E-G

The following analysis used the uncertainty in the measured data to assess the prediction error (section 3.5.2 and 6.3.1.2). The maximum standard deviation for each measured flow variable was used and is given in Table 6.7.

Solutions E-G, despite a number of wrong direction predictions predicted all $\overline{w}$ to fall within $\sigma_{\overline{w}_{PIV}}$ and $\sigma_{\overline{w}_{HW}}$ of the experimental data for $x/l \leq 0.218$ and $x/l \geq 0.291$ respectively. The 2% of predictions of $\overline{v}$ that fell within $\sigma_{\overline{v}_{PIV}} < E_{p_{\overline{x}}} \leq 2\sigma_{\overline{v}_{PIV}}$ resulted from the incorrect predictions of the distribution of $\overline{v}$ at $x/l \leq 0.218$ due to the predicted flow distortions by solutions E and F. However despite these inconsistencies the overall value of prediction error for $\overline{v}$ was generally improved

using higher order differencing schemes. Predictions of $\overline{u}$ were again not as favourable but showed some improvement over solutions A-D with an average of 77% of predictions falling within either $\sigma_{\overline{u}_{PIV}}$, or $\sigma_{\overline{u}_{HW}}$, of the experimental data for $x/l \leq 0.218$ and $x/l \geq 0.291$ respectively, 7% improvement on the lower order solutions. In addition 97% of predictions fell to within either $2\sigma_{\overline{u}_{PIV}}$ or $2\sigma_{\overline{u}_{HW}}$ a 3% improvement on solutions A-D. These unfavourable predictions were the direct consequence of inaccurate predictions within the recirculation region, close to the model base at the model centreline. Also the discomposed vector map presented for the measured data at $x/l = 0.073$ (figure 4.13) may have contributed to poor improvements in the validation of $\overline{v}$ $\overline{w}$ at $x/l \leq 0.218$ (section 6.3.1.1). Nevertheless with well over 50% of predicted $\overline{u}$, $\overline{v}$ and $\overline{w}$ within $\sigma_{\overline{u}_{PIV}}$ and $\sigma_{\overline{u}_{HW}}$, $\sigma_{\overline{v}_{PIV}}$ and $\sigma_{\overline{v}_{HW}}$, $\sigma_{\overline{w}_{PIV}}$ and $\sigma_{\overline{w}_{HW}}$ respectively all predictions were considered in good agreement with the measured data in accordance with Section 3.5.2.

All prediction errors are generally higher in the turbulent wake region because the surrounding flow field is less turbulent and thus less complex to solve. Any improvement in predictions over solutions A-D comes from the increased accuracy offered by the higher order differencing schemes. For example the LUD differencing scheme uses two upwind neighbours in its approximation of convective fluxes as opposed to just one used by the upwind differencing scheme (section 3.3.1.1). In addition the LUD and MARS schemes are both second order accurate which means higher order terms are included in the approximations during the discretisation process improving the overall accuracy. The upwind scheme is only first order accurate. However as it has been illustrated even applying higher order differencing schemes may not necessarily improve predictions in regions of complex flow structure i.e. recirculation

6.4.1.3 Solution run times and y^+ *- Solutions E-G*

Solution run times: Solution G was run on a Silicon Graphics workstation as described at the beginning of section 6.2. Compared with the equivalent upwind solution, solution A, solution G took 5 times as long with over double the number of

iterations (Appendix 4b). Solution E was initiated using the Silicon Graphics workstation but convergence problems required external assistance from the support team at Computational Dynamics. An updated version of STAR-CD, V3.1b, was used but assurance was given of no fundamental differences between the two versions. The new version is however more robust and less prone to numerical instabilities (chapter 3). The subsequent run time was unrepresentative because two different machines were used. Using the Silicon Graphics workstation it took approximately 8 minutes CPU time per iteration. Based on the total number of iterations performed solution E would have taken twice as long as solution G had the solution run to convergence on the Silicon Graphics machine. The solution was completed using a Hewlett Packard L-class workstation. Solution F was also obtained using V3.1b and run on a Hewlett Packard L-Class workstation with 2Gb of RAM. As a consequence the solution run time was much reduced and would be unfair to be compared directly with the other solutions.

$\underline{y^+}$: . It is recommended, for the high Reynolds turbulence models used here that $30< y^+ <150$ (Computational Dynamics, 1998a). Appendix 4b shows $30< y^+ < 45$ y^+ for the surface of the vehicle, thus all y^+ values meet the given criteria.

6.4.1.4 Conclusions - solutions E-G

The use of higher order differencing schemes showed some improvement in the prediction of the near wake flow field but generally only outside of the main area of recirculation i.e. $x/l \geq 0.291$. The two-tier vortex structure near wake recirculation was represented but prediction of the size and shape of the vortices was varied. Only the standard k-ε/linear upwind differencing scheme (solution G) made the best predictions of the relative size and shape of the internal recirculation region vortices. Similar to the lower order solutions (A-D) none of the higher order solutions (E-G) manage to accurately predict the flow field close to the model base. The upstream length of the two vortices were over estimated and as a consequence the small region of $+\overline{u}$ shown in the experimental results was not predicted. With none of the solutions so far making an accurate prediction at this point in the flow one might start

to doubt the measured flow field it must be remembered that regions of recirculation are notoriously hard to predict.

Solution G, standard k-ε/LUD combination made the closest prediction of recirculation length predicting within 4% of the observed length i.e. $x/l \sim 0.218$.

The prediction of the relative vortex sizes and structure were much improved at z/b = 0.560 with all the solution showing similar predictions which were comparable to both the measured flow field and the lower order solutions, A and D. The improved predictions of the vortex structure were significant as the location and size of the lower vortex at z/b = 0.560 was in Chapter 5 to have a primary influence on the uptake of pollutant from the exhaust plume into the recirculation region (section 5.4.2).

Solution E, the non-linear k-ε/LUD combination was chosen for the last stage in the study based primarily on the very good representation of the flow field and pick-up point at z/b = 0.560. While the predictions of flow structure at the model centreline were not in as good agreement it is believed the flow structure at the centreline is not at critical in terms of the initial dispersion of a pollutant from z/b = 0.560. Based on the results of the statistical validations solution E showed better predictions of the velocity components $\overline{v}$ and $\overline{w}$ with on average 85% of $\overline{v}$ and 82% of $\overline{w}$ within 75% of the experimental data at $x/l \leq 0.218$ and 86% of $\overline{v}$ and 87% of $\overline{w}$ within 75% of the experimental data at $x/l \geq 0.291$. While solution F made much better predictions of vorticity at x/l = 0.291 and 0.437 and thus the streamwise development the longitudinal vortex for the purposes of the current study the flow close to the model base was considered to be more critical. Solution E also made fair predictions of streamwise flow development and therefore the general dispersing mechanism of the flow rotation downstream would still be represented.

6.5 Stage 3 – Direct validation of near wake flow field simulation using refined mesh (solution H)

A finer mesh was used within the vicinity of the model base in an attempt to improve solution accuracy and flow detail within the near wake recirculation region. Details of mesh refinement are found in section 6.2.1. The linear upwind differencing scheme was used to discretise the momentum equations and the upwind differencing scheme to discretise the turbulent transport equations. The non-linear (quadratic) k-ε model was applied. Comparisons are made with predictions from solution D, the non-linear k-ε model/UD combination and solution E, the non-linear k-ε model/LUD combination using the non-refined mesh.

Figure 6.21 illustrates the predicted recirculation region vortex structures for both the model centreline and z/b = 0.560. In comparison with vector maps of recirculation region vortex structure presented in figures 6.16 and 6.18 solution H was in agreement with the measured flow field and made similar predictions to solutions G for the flow field structure at the model centreline. Solution H did not predict the flow distortions in the flow recirculation region structure at the model centreline, as shown in figure 6.16a for solutions E and F. Predictions of the recirculation region structure at the model centreline were more comparable with predictions from solutions A-D (figure 6.5) further suggesting the distortions not to be a real feature of the flow but a product of the simulations themselves. The relative size and shape of each vortex at the model centreline was comparable to the measured flow field. However comparing actual predicted vortex size with the measured flow field (refer to figure 6.16) solution H over predicts the downstream length of both the upper and lower vortex.

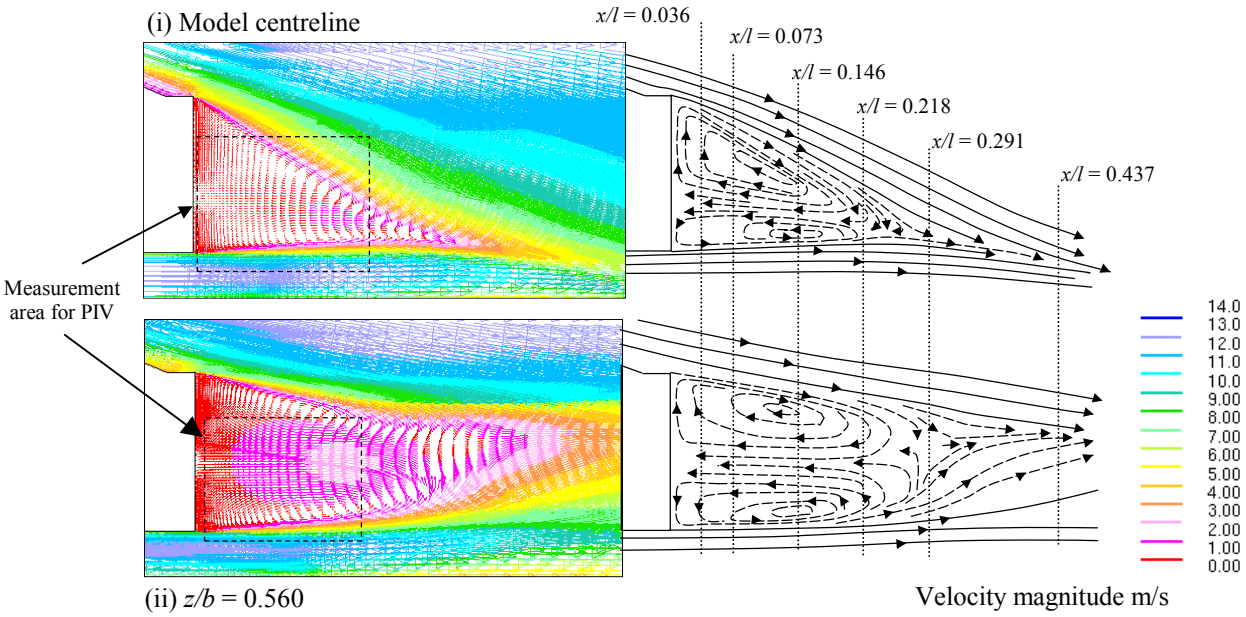

Figure 6.21 - Predicted wake flow structures for solution H

Also similar to the other solutions discussed in previous sections solution H also over predicted the upstream length of both vortices despite the increased mesh resolution and thus failed to predict the small region of $+\overline{u}$ close to the model base. This again brought doubt on the measured flow at the model centreline. However as predictions at distance from the model centreline and in particular at z/b = 0.560 were more critical for the dispersion of a pollutant release away from the model centreline it was not considered vital as the general sense and size of rotation within the vortices at the centreline were represented in fair agreement.

Table 6.12 compares the spatial locations of the predicted upper and lower vortex cores at the model centreline with the measured flow field and solutions D and E. Solution D being the low order equivalent of solution E and solution E being equivalent to H but using a non-refined mesh. Solution H over predicted the location of each vortex core at the model centreline.

	Upper vortex		Lower vortex	
	~x/l	*~y/H*	*~x/l*	*~y/H*
Experimental	0.070	0.289	0.076	0.174
Solution H	0.102	0.399	0.119	0.199
Solution E	0.076	0.428	0.137	0.199
Solution D	0.077	0.389	0.077	0.184

Table 6.12 – Measured and predicted vortex core location for centreline recirculation region structure using refined mesh

The predicted mean recirculation length and location of the mean free stagnation point are given in Table 6.13

	Model centreline		*z/b* = 0.560	
	Mean recirculation length : *~x/l*	$\overline{u}/U_\infty = 0$ *y/H*	Mean recirculation length : *~x/l*	$\overline{u}/U_\infty = 0$ *y/H*
Experimental	0.180	0.234	-	-
Solution H	0.229 (+27%)	0.224(-4%)	0.277	0.399
Solution E	0.204 (+13%)	0.274 (+17%)	0.246	0.399
Solution D	0.188 (+4%)	0.244 (-4%)	0.230	0.373

Table 6.13 – Comparing measured and predicted mean recirculation length and location of $\overline{u}/U_\infty = 0$ for solutions H, E, and D

Solution H over predicts the mean recirculation length by 27%. Comparing this value with those given in Table 6.4 and 6.8 solution H made then second worst prediction of mean recirculation length at the model centreline, solution F making the worst over predicting by 32% despite increased mesh resolution and the potential of improved solution accuracy offered by the LUD scheme. This maybe a consequence of mesh dependency i.e. if overall predictions using different meshes do not change significantly the solution may be said to be mesh independent. Mesh independence is always desirable but not always practical to achieve. Mesh dependency studies are often conducted by computing the same solution using a progressively finer mesh until changes between successive solutions are no longer significant. While progressive mesh refinement improves the overall accuracy of the solution the

computational effort required is increased. Unfortunately available computing resources did not allow any further mesh refinements to be made in order to assess mesh dependency. The predicted location of $\overline{u}/U_{\infty} = 0$ was however in good agreement with the measured flow field.

While solution H also predicted the longest recirculation length at *z/b* = 0.560 the flow structure and relative vortex sizes were in good agreement with the measured flow field. With reference to figure 6.21 and 6.9 solution H clear predicts a much longer upper and lower vortex and a much large region of very low velocity field close to the model base. In comparison with the measured location of the lower vortex core was *x/l* = 0.017 further downstream at *x/l* = 0.127 identical to the prediction by solution E. Comparing the measured and predicted streamwise velocity profile through the recirculation at *x/l* = 0.073 for *z/b* = 0.560, figure 6.22 it is shown that solution H generally under predicts the flow within the region of inflow between the vortices. However in general the shape of the profile is in good agreement.

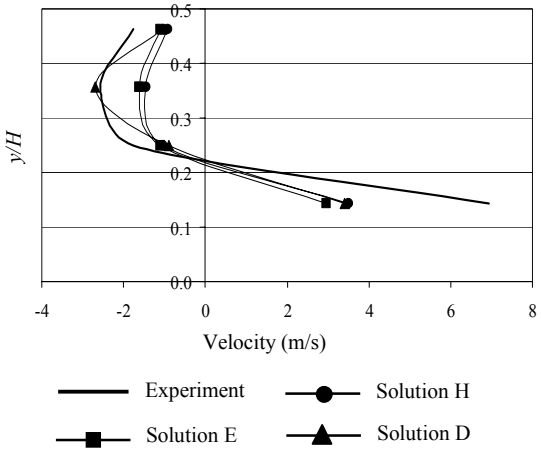

Figure 6.22 - Comparison of profiles of $\overline{u}$ at *x/l* = 0.073 for *z/b* = 0.560; solutions H, E and D.

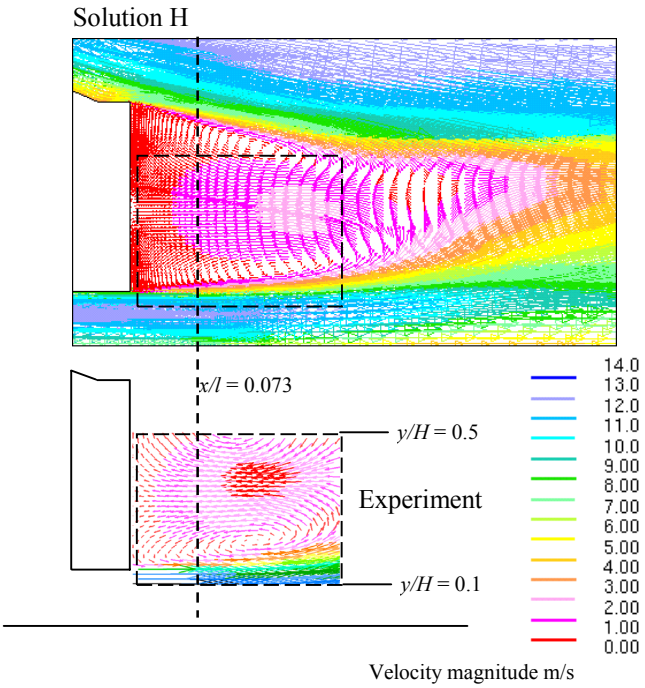

Predictions of the longitudinal vortex structure at *x/l* = 0.146 and 0.218 were comparable with solutions D and E, figure 6.12 and 6.19 respectively. Solution H predicted the general vortex structure at *x/l* = 0.218 however the strength of rotation

around the outer edge of the vortex at *x/l* = 0.218 was under predicted, denoted by the under prediction in peak is $+\bar{v}$, figure 6.23b. The predicted location of the vortex core at *x/l* = 0.218 was comparable to solutions D and E but closer towards the model centreline than measured. At *x/l* = 0.146 the secondary vortex observed close to the model centreline was not predicted and the overall strength in the developing vortex was weaker. This was reflected in the under prediction of streamwise vorticity at *x/l* = 0.437, figure 6.23c, nevertheless solution H did accurately predict the location of peak negative vorticity which corresponds to the vortex centre.

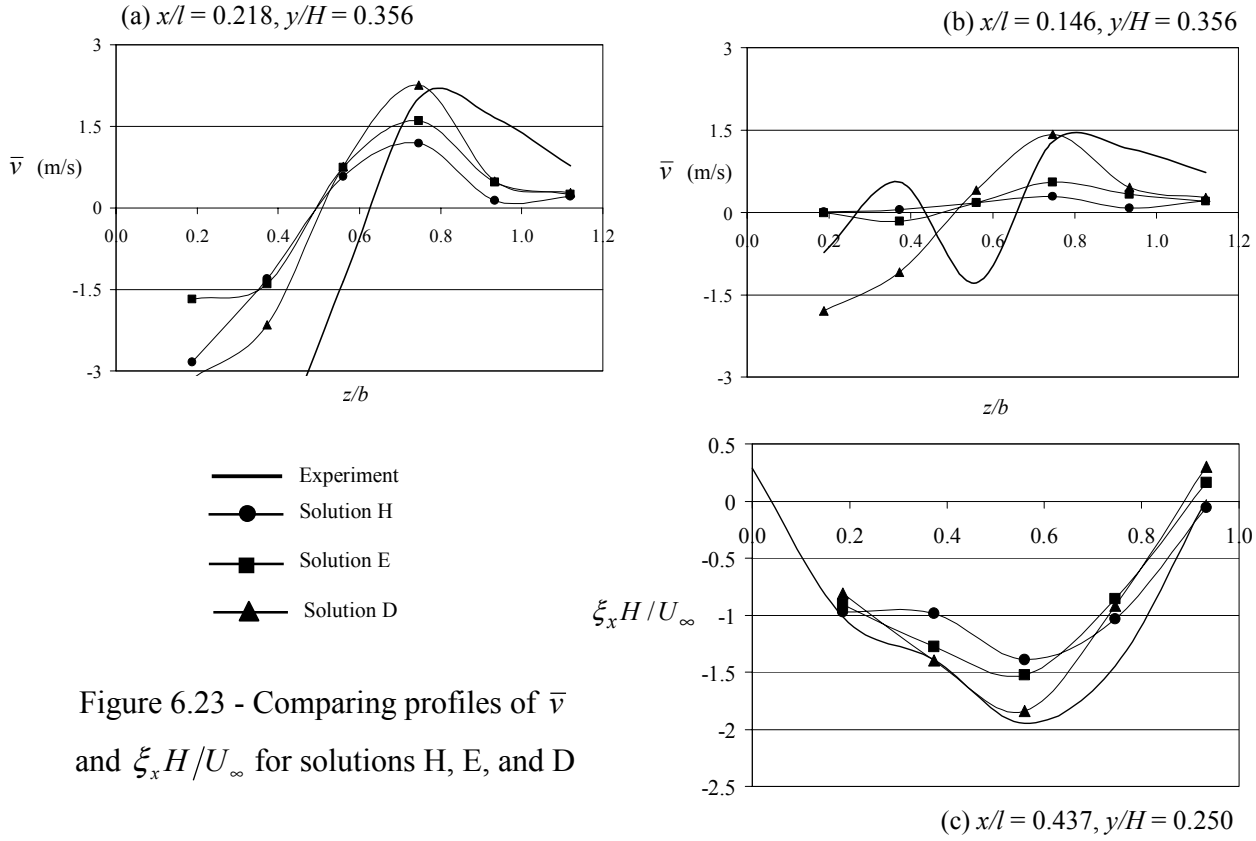

Figure 6.23 - Comparing profiles of $\bar{v}$ and $\xi_x H/U_\infty$ for solutions H, E, and D

6.5.1 Statistical validation – Solution H

The techniques used in sections 6.3.2 and 6.4.2 and described in sections 3.5 were used. The results of the analysis are compared against solutions D, and E.

6.5.1.1 Absolute percentage difference – Solution H

The relative performance of solution H compared with solutions D, and E was expressed as a percentage increase in the number of predicted values falling within 50% and 75% of measured values. Solution D being the low order equivalent of solution E and solution E being equivalent to H but using a non-refined mesh. The results of the analysis were considered as described in section 6.3.2.1 and summarised in Table 6.14. The percentage improvement was estimated based on the difference between the average percentage difference of solution H and the highest percentage difference from solutions D and E e.g. solution H predicts 81% of $\overline{w}$ to lie within 75% of measured $\overline{w}$ an improvement of 1% over solutions D and E.

(i) % of predictions for $x/l \leq 0.218$

	$\overline{u}$		$\overline{v}$		$\overline{w}$	
Solution	≤50%	≤75%	≤50%	≤75%	≤50%	≤75%
H	61%(1)	80%(1)	59%(-2)	82%(-4)	63%(1)	81%(-2)
% Improvement over solution E and D	1%	2%	-3%	-4%	0%	1%

(ii) % of predictions for $x/l \leq 0.291$

	$\overline{u}$		$\overline{v}$		$\overline{w}$	
Solution	≤50%	≤75%	≤50%	≤75%	≤50%	≤75%
H	97%(0)	100%(0)	66%(-1)	87%(1)	66%(7)	85%(1)
% Improvement over solutions E and D	0%	0%	2%	2%	3%	-1%

Table 6.14 - Results summary of absolute percentage difference comparisons for solutions H, E and F.

The numbers in brackets () denote the percentage improvement over solution E, the equivalent solution using the non refined mesh.

The analysis showed there to be no significant improvement in prediction from using a refined mesh within the region of recirculation. The poorer prediction of $\overline{v}$ at $x/l \leq$

0.218 came from the prediction of much weaker cross flow at x/l = 0.146 and 0.218 and the failure to identify the second vortex close to model centreline at x/l = 0.146. Poor improvements in predictions at $x/l \leq 0.218$ may also have be due to the discomposed vector map for the measured data at x/l = 0.073 (figure 4.13), thought to be the result of insufficient flow seeding (section 6.3.1.1).

The percentages of incorrect predictions of flow direction were not included in Table 6. Wrong direction predictions of $\overline{v}$, on average 11%, were the result of inaccurate predictions of mean recirculation length and the failure to predict the second vortex at x/l = 0.146. The percentage of wrong direction predictions was higher for the streamwise component of velocity at 20% due to inaccurate prediction of vortex size very close to the model base. Wrong direction predictions of $\overline{w}$ were on average 13% for all x/l slightly than for solutions D and E.

Despite the overall poor improvement in predictions using a refined mesh solution H nevertheless predicted, on average 61% and 76% of flow variables to be within 50% of the measured values at $x/l \leq 0.218$ and $x/l \geq 0.291$ respectively. With reference criteria set in section 3.5.1 the predictions were still considered to be in good agreement with the experimental results.

Solution H used increased mesh resolution in the recirculation region and combined with the improved solution accuracy offered by the LUD scheme it might be expected for predictions to be improved. The poor overall improvement in predication demonstrated may be due to mesh dependency i.e. if overall predictions using different meshes do not change significantly the solution may be said to be mesh independent. While for any numerical solution mesh dependency is desirable it is often not practical and limitations on available computing resources during the current project did not allow any further mesh refinements to be made in order to assess any mesh dependency in the solutions.

6.5.1.2 Prediction error in terms of experimental uncertainty – Solution H

Details of the technique applied are found in section 3.5.2 and section 6.3.2.2. As in section 6.3.2.2 the maximum standard deviation for each measured flow variable was used (Table 6.7).

Predictions of $\overline{w}$ were comparable with both solutions D and E with all $\overline{w}$ predicted to be within $\sigma_{\overline{w}_{PIV}}$ and $\sigma_{\overline{w}_{HW}}$ of the experimental data for $x/l \leq 0.218$ and $x/l \geq 0.291$ respectively despite 13% of wrong flow predictions. Similar to solution E, solution H showed 97% predictions of $\overline{v}$ to be within $\sigma_{\overline{v}_{PIV}}$ and $\sigma_{\overline{v}_{HW}}$ of the experimental data for $x/l \leq 0.218$ and $x/l \geq 0.291$ respectively and 3% to be within $\sigma_{\overline{v}_{PIV}} < E_{p_{\overline{x}}} \leq 2\sigma_{\overline{v}_{PIV}}$ i.e. the result of poor prediction in $\overline{v}$ at $x/l \leq 0.218$. Nevertheless with over 50% of predicted $\overline{v}$ and $\overline{w}$ falling within $\sigma_{\overline{v}_{PIV}}$, $\sigma_{\overline{v}_{HW}}$ and $\sigma_{\overline{w}_{PIV}}$, $\sigma_{\overline{w}_{HW}}$ the predictions of solution H were considered in good agreement with the measured data based on criteria set in Section 3.5.2.

Similar to solutions D and E predictions of $\overline{u}$ were not so favourable and but showed no significant improvement over predictions by solution E. Solution H predicted 76% of predictions falling within either $\sigma_{\overline{u}_{PIV}}$, or $\sigma_{\overline{u}_{HW}}$, and 23% to within either $2\sigma_{\overline{u}_{PIV}}$ or $2\sigma_{\overline{u}_{HW}}$ of the experimental data for $x/l \leq 0.218$ and $x/l \geq 0.291$ respectively. However with over 70% of the predictions falling with either $\sigma_{\overline{u}_{PIV}}$, or $\sigma_{\overline{u}_{HW}}$ predictions by solution H were considered to be in good agreement despite inaccurate predictions of flow direction close to the model base.

6.5.1.3 Solution run times and y^+ *values –Solution H*

Convergence difficulties required solution H to be run on a HP L-Class workstation using an update version of STAR-CD, STAR-CD, V3.1b (section 6.4.2.3). As a consequence the solution run time is not comparable with solutions A-D, and G. However it is certain that solution H would have required considerably more CPU time than these solutions to reach the stated convergence criteria i.e. the global residual for each flow variable should be at least 10^{-3}, Appendix 4b. Solution E was

only partly run on a HP L-Class workstation therefore run times with solution H are not comparable.

Solution F was run entirely on a HP L-Class workstation and may be compared with solution H. The CPU index defined for previous solutions (section 6.3.1.3) is based on the original solution, solution A and was not be used to compare solutions here to avoid confusion. Solution H took 1.4 times longer than solution F in terms of actual clock time. In general it would be expected for the overall run time of solution H to be longer than any other solution due to added mesh refinement.

$\underline{y^+}$: . It is recommended, for the high Reynolds turbulence models used here that $30< y^+ <150$ (Computational Dynamics, 1998a). Appendix 4b shows $30< y^+ < 45$ y^+ for the surface of the vehicle, thus all y^+ values meet the given criteria.

6.5.1.4 Conclusions - solution H

The use of a refined mesh did not offer significant improvement in prediction over solutions using a non-refined mesh that was believed to be due to mesh dependency. Nevertheless solution H captured the relative size and shape of primary two-tier vortex structure within the recirculation region at the model centreline but generally over predicted the actual length of each vortex. The recirculation length at the model centreline was over predicted by 27%. Similar to solutions D and E prediction of the flow structure at distance from the model centreline i.e. z/b = 0.560 were much improved and in good agreement with the measured flow field. The distortions predicted by solutions E and F were not repeated. Predictions of streamwise velocity $\overline{u}$ were comparable to solutions E and F.

6.6 Chapter Conclusions

This chapter has discussed detail predictions of the near wake flow behind a model vehicle using different turbulence models, discretisation schemes and mesh refinement. The primary aim of the study was to obtain a numerical simulation to adequately represent the near wake flow behind a model vehicle that could be used

as the foundation for numerical simulations of pollutant dispersion within the same region. Through the progressive analysis of the different turbulence model/discretisation scheme combinations numerical solutions of the near wake flow field behind the MIRA 33% reference vehicle (fastback) were obtained using STAR-CD.

While the near wake is inherently unsteady (section 4.5 and section 5.4) all the numerical solutions obtained used the steady state modelling approach described in chapter 3 i.e. the unchanging flow pattern under a given set of boundary conditions is obtained through a number of numerical iterations. The aim of the current work was to determine whether CFD could be used to simulate the dispersion of a pollutant in the near wake of a model vehicle and therefore as a feasibility study it was more appropriate, and common place, to begin with the simulation and validation time-averaged flow and dispersion field. To begin such a study using transient calculation would be ambitious. The relative success of the current work could then be used as a foundation for further transient studies.

The general mean flow structure and relative size of the two-tier recirculation region vortex structure was presented with predictions at distance from the model centreline generally in better agreement than predictions at the model centreline. All the solutions analysed generally over predicted the streamwise length of the two vortices within the recirculation region resulting in inaccurate predictions very close to the model base i.e. the failure to predict small region of $+\overline{u}$. However the flow field at distance from the model centreline and in particular at $z/b = 0.560$ was in much better agreement with the measured flow field, $z/b = 0.560$ being the location of the representative exhaust during tracer gas measurements (Chapter 5). From the tracer gas measurements it was shown that the flow field structure at $z/b = 0.560$ had a primary influence on the initial dispersion from the exhaust and therefore the prediction of the flow field within this region was considered to be more critical particularly as the solutions obtained would be used as the foundation for numerical simulations of dispersion within the same region. Therefore prediction of the flow structure at the model centreline were not considered to be as crucial and that provided the overall flow structure, and sense of rotation was is fair agreement with the measured flow field then the general dispersion mechanisms would be adequately

represented. In addition good representation of the downstream development of a streamwise longitudinal vortex was also demonstrated although none of the solutions predicted the secondary rotation observed at x/l = 0.146. However it was unclear whether this was a real effect or a consequence of short time-averaging i.e. the sample time was not long enough to resolve the true flow and the vortex shown is a more time dependent structure. Moreover the second vortex did not have a significant influence over the dispersion field detailed in chapter 5 and therefore its was believed that its non-predication would not compromise subsequent predictions of tracer gas dispersion.

Numerous turbulence model/differencing schemes combinations of were increasing in order of accuracy and the use of a refined mesh within recirculation region were assessed. However it was clearly demonstrated through vector maps and velocity profiles that increased mesh resolution or improved solution accuracy offered by higher order differencing schemes did not necessarily result in a more accurate prediction. The current study has shown that even using the simplest combination of the standard k-ε model and first order upwind differencing a good representation of the measured flow field could be obtained. The poor performance shown by the solution using the refined mesh and higher second order accurate differencing in comparison with the solutions using the non-refined mesh was believed to be a result of mesh dependency. While it is desirable to obtain a solution that is mesh independent i.e. overall predictions do not change significantly with different mesh densities, it was felt that no benefit would be gained by trying to achieve this as an adequate representation of the flow field had already been demonstrated. Moreover it was felt that even using a more powerful computer there would be no benefit and no significant improvement on the solution already achieved. In addition no further solutions were obtained for the non-refined mesh, as it was believed there would noteworthy improvements over the steady-state solutions already obtained even using a more powerful workstation

It was therefore concluded that CFD, and in this case STAR-CD was able to make adequate predictions of the near wake flow and in particular the recirculation region of a model vehicle. The primary flow features important to the dispersion of a pollutant within the near wake were adequately represented and thus the velocity

solutions obtained could be used as the foundation for numerical simulations of tracer gas dispersions. In addition the study demonstrated that even a basic turbulence model it was possible to achieve a good representation of the flow field without the need to change any of the modelling parameters associated with the turbulence models (section 6.3.1), which from a 'users' point of view enables a relatively inexperienced modeller to obtain a solution capturing the main features of the flow field under investigation with relative ease.

Chapter 7: Computational Study 2 - Simulation of gaseous dispersion

7.1 Introduction

The study to be discussed in the following chapter investigates the feasibility of using commercially available computational software, in this case STAR-CD, to simulate the dispersion of a gaseous pollutant within the near wake of a model vehicle. To the authors knowledge STAR-CD had not previously been used for such an application therefore the following study was conducted as an initial investigation into the application and thus concentrates on the obtaining an agreeable solution as opposed to developing a tuned dispersion model. The simulations conducted used the numerical velocity fields obtained in Chapter 7 and were validated against the experimental data collected in the gaseous concentration experiment, Chapter 5, refer to figure 1.1.

The generality of the method was assessed looking at the influence of factors such as mass flow rate and vehicle speed on dispersion character. In addition the passive technique of particle tracking was used to visualise the trajectory of mass-less particles demonstrating another way of visualising a predicted velocity and dispersion field. The technique was not used to model particle pollution but visualise the path of a mass-less particle using the existing velocity field to gain further insight into the dispersion character within the near wake recirculation region.

It should be understood that the study was not conducted to gain detailed information on general pollution dispersion but to assess the feasibility of a modelling technique and understand in a little more detail the near wake dispersion character of the model in question. The success of the study and further development of such an approach would allow the modelling of pollutant dispersal within the wake of a vehicle without the need for the limiting assumptions made in previous dispersion modelling approaches, chapter 2.

7.2 Problem definition

The commercial code STAR-CD (V3.05) was used for all the simulations to be discussed. A Silicon Graphics workstation with a 225Mhz R11000 chip and 512 MB of RAM was used (except where stated) which effectively put a constraint on the size of the numerical model.

7.2.1 Mesh definition

The following numerical simulations used the velocity field solutions of chapter 6 as their foundation therefore it was essential to use the same block-structured mesh as used in the near wake flow field simulations. Details of the mesh structure and density are therefore not given here but may be found in section 6.2.1 of chapter 6 and are illustrated in figure 6.1. The mesh did not include the geometry of the representative exhaust used in the experimental study (chapter 5). Its inclusion at this stage would have required additional velocity calculations and further validation; the representative exhaust was not present during the wake survey. However it was anticipated that the presence of the representative exhaust pipe would not have had a significant influence on the integrity of the near wake flow structure (section 5.2.1.1). The technique used to model the gaseous dispersion was chosen because it did not require the inclusion of the representative exhaust in order to introduce a pollutant source into the flow (chapter 5).

7.2 2 Problem set-up

As a consequence of using the velocity solutions of chapter 6 as the foundation for the gaseous dispersion simulations the boundary, initial conditions and free stream flow properties were the same as described in Sections 6.2.2.1 and 6.2.2.2, Chapter 6. The dispersion modelling technique applied did not require the definition of any additional boundaries therefore the modelled dispersion was forced to obey the conditions applied and in particular the assumption of centreline symmetry. The implications of this assumption are discussed where appropriate.

The tracer gas or scalar quantity was introduced into the flow field through existing computational cells, which were identified using a different cell index to that of the bulk flow field (Computational Dynamics, 1998b). Figure 7.1 shows the location of the chosen cells and the index definitions. The chosen cells were given a cell index 8 for which all the properties of the scalar to be released were associated i.e. density, fluid viscosity etc. The fluid properties related to each cell index were specified elsewhere i.e. the properties of the bulk fluid air and the properties of the additional scalar were defined via a separate property module (Computational Dynamics, 1998b).

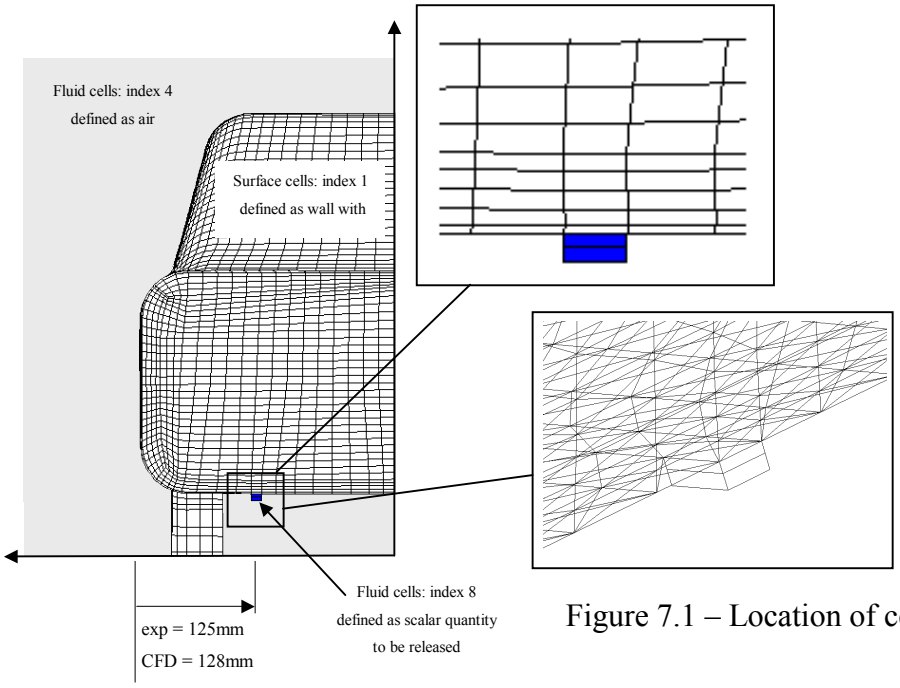

Figure 7.1 – Location of cells for scalar release

The nature of the block-structured mesh did not allow for the release of the scalar at the exact same location of the representative exhaust used in the experimental study, figure 7.1. The cells were selected based on the release height of the tracer gas the reasons for which are discussed in section 7.2.3. It was necessary to select two computational cells, to cover the appropriate release height, as opposed to a single cell at the release height. The consequence of selecting only one cell at the appropriate release height is shown in figure 7.2a. The calculated values of the velocity components in the cell above the release point would interfere with the release of scalar creating an unrealistic condition. The injection method used (section 7.2.3) sets a zero velocity field in the selected cells unless otherwise stated i.e. a specified release rate. The approach using two computational cells, figure 7.2b, was thus considered more appropriate.

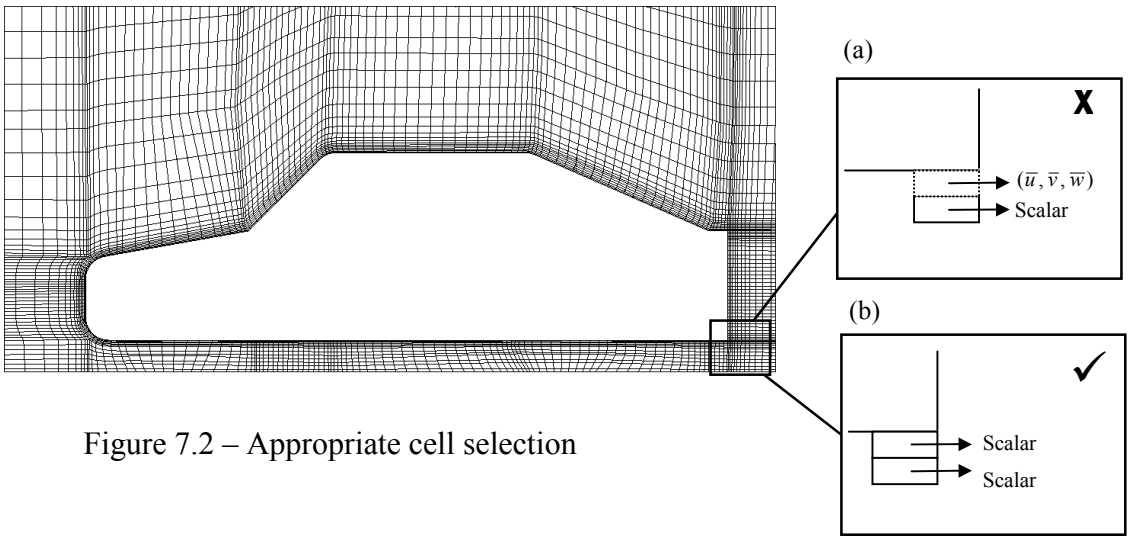

Figure 7.2 – Appropriate cell selection

The two cells selected were of approximately the same area as the representative exhaust (section 5.2.1.1). The scalar was released 6mm below the base of the model into the computational domain equivalent to the centre of the exhaust.

The calculated velocity fields (chapter 6) used as the basis for the dispersion simulations were,

1. Solution D - non-linear k-ε model/upwind differencing using non-refined mesh (section 6.3).
2. Solution H - non-linear k-ε model/linear upwind differencing using refined mesh (section 6.5).

Solution D was chosen because of its relatively short processing time in comparison with the higher order solutions and its good representation of the main near wake flow features particularly in the vicinity of the location of the representative exhaust. The higher order solution, solution E, was not chosen due the convergence difficulties encountered. The second solution, solution H using the refined mesh was used essentially to obtain increased flow detail in the simulation of the dispersion the scalar and not because it offered increased solution accuracy in terms of the predicted velocity field, refer to Chapter 6, Section 6.5. An additional velocity solution was calculated to assess the influence of vehicle speed on dispersion. More detail on the general modelling strategy is given in section (section 7.2.4).

7.2.3. Fluid (scalar) injection technique and dispersion simulation

The technique of fluid injection was applied, using the user subroutine 'fluinj', to release a scalar variable into the simulated near wake flow field. The method enables local fluid injection into specified cells (fluid cells only) at a prescribed flow rate ($kg/s/m^3$) and provides an alternative and convenient way of injecting a fluid into the solution domain without the need for complex mesh alterations. The effect is similar to that of an inlet or fixed flow outlet condition but without the need to declare an actual boundary adjacent to the cells concerned. The injection of fluid is then modelled as an additional source term s_ϕ in the finite volume equation for the cells in question (Computational Dynamics (1998a). The additional source term is of the form,

$$s_\phi = \dot{m}_f \phi \tag{7.1}$$

where $\dot{m}_f$ is the mass flow rate of the fluid being injected per unit volume and ϕ is the value of velocity, temperature etc. of the injected flow. In the current study ϕ was defined as the injection velocity in m/s. A source term is provided, via the user subroutine, to each of the cells selected. An example of the 'fluinj' subroutine and the relevance of each statement are given below.

```
C     Sample coding: Fluid injection and removal
C
1)     IF(ICTID.EQ.8) THEN              ⇒ Marked cells (fluid cell, index 8)
2)        FLUXI= 'mass flow rate'/VOLP  ⇒ Mass flux specified
3)     TI=293.0                         ⇒ Fluid temperature (K)
4)        UI=2                          ⇒ Injection velocity (m/s)
5)        SCINJ(1)=0.011                ⇒ Properties of injected fluid (see below)
6)     ENDIF

7)      RETURN
8)      END
C
```

SCINJ(1) =0.011 – this identifies the properties of the scalar variable being injected i.e. scalar variable no.1 which in this case was set-up to represent a propane source. The proportion of propane to air in each of the specified cells is 0.011 or 1.1%.

The mass flow rate was set equivalent to that used in the experimental study 0.00007018kg/s; a volume flow rate of 0.0000527m^3/s. An injection velocity 'UI' was required and calculated based on the area of injection i.e. the approximate cell face area.

The type of the fluid being injected is specified by line 5 of the subroutine. The properties of the scalar variable were specified elsewhere via the 'Properties Module' to include both the physical and material dependent properties (Computational Dynamics, 1998b). The physical properties of the scalar variable, propane, were defined using the chemical species database available within STAR-CD to include density, molecular weight and molecular viscosity and the variable was classified as passive in that it did not contribute in any way to the overall properties of the bulk flow. The material or stream dependent properties depend on the stream's background fluid as well as the scalar itself. These included

- Solution method – *transport* i.e. solve the standard scalar transport equation
- Initial concentration - set to zero as value is defined in sub-routine (line5)
- Diffusivity – a constant value of molecular diffusivity, 3.004E-5
- Constant turbulent Schmidt number, 0.9.

Line 5 of the subroutine effectively 'calls' on the properties defined for the scalar and specifies the proportion of the scalar to air to be injected into the marked cells i.e. 0.011 for a 1.1% propane/air mix. The user subroutine works with the main solution procedure providing an additional source term in the finite volume equations for each marked cell in order to model the injection of the scalar (Computational Dynamics, 1998a,b). Each chosen velocity solution, detail above in section 7.2.2, was restarted using the restart facility (section 6.3) with the user subroutine activated. The restarted velocity solutions retained all previously applied turbulence modelling parameters (section 3.4 and section 6.2.2). The scalar field was solved using a standard scalar transport equation for scalar quantity φ, of which a general form may be expressed as

$$\rho \frac{\partial \Phi}{\partial t} + \rho U_j \frac{\partial \Phi}{\partial x_j} = \frac{\partial}{\partial x_i}\left[\Gamma_\Phi \frac{\partial \Phi}{\partial x_j} - \rho u_i' \varphi' \right] \tag{7.2}$$

where u_j' is the fluctuating velocity component and φ' is the fluctuating component of the mean scalar quantity Φ. The solution of a standard transport equation for turbulence parameters and chemical species conservation takes place within the sequential operations performed during each iteration of the solution procedure for the rest of the flow field (figure 3.2) (Computational Dynamics, 1998a,b). For turbulent flow calculations using the *k*-ε model(s) the link between the flow and scalar fields is particularly strong with coupling occurring via the turbulent viscosity, μ_t,

$$-\overline{\rho u_i' \varphi'} = \frac{\mu_t}{\sigma_t} \frac{\partial \Phi}{\partial x_i} \tag{7.3}$$

where μ_t is the turbulent eddy viscosity, σ_t the turbulent Schmidt number[7.1] and, $\mu_t / \sigma_t = \Gamma_t$, turbulent diffusivity which is expected to have a value close to that of μ_t. Comparing equation (7.3) with equation (3.11) the similarities are clear. Equation (3.11), the Boussinesq equation shows that turbulent momentum transport may be assumed proportional to the mean gradients of velocity. Therefore by analogy the turbulent transport of a scalar is taken to be proportional to the gradient of the mean value of the quantity being transported and modelled via equation (7.3). STAR-CD uses the same principle using an equation similar to that of equation (7.3) to forge the link between the flow turbulent flow calculations and the scalar field via turbulent viscosity μ_t (Computational Dynamics, 1998a).

Numerical discretisation of the scalar transport equation was achieved using either upwind differencing (UD) or linear upwind differencing (LUD) (section 3.3).

[7.1] turbulent Schmidt number $\sigma_t = \mu_t / \Gamma_t$

It should be noted that while the second line of the subroutine detailed above shows the mass flux, FLUXI to be specified in terms of cell volume VOLP this was only required because STAR-CD immediately multiples by volume outside the subroutine. This is the reason why cells for fluid injection maybe selected based on release height alone.

7.2.4 Modelling strategy

The primary aim of the investigation to be discussed was to assess the feasibility of using STAR-CD in the simulation of pollution dispersion within the near wake of a model vehicle. The objective was to demonstrate the approach as an alternative technique to dispersion modelling behind a road vehicle without the need for the limiting assumptions applied in previous methods (chapter2, section 2.4). For example the current approach allowed the detailed near wake flow close behind the vehicle to be modelled as opposed to assuming a velocity deficit at some distance downstream to represent the wake flow field as a whole.

The strategy applied to meet this aim is detailed in figure 7.3

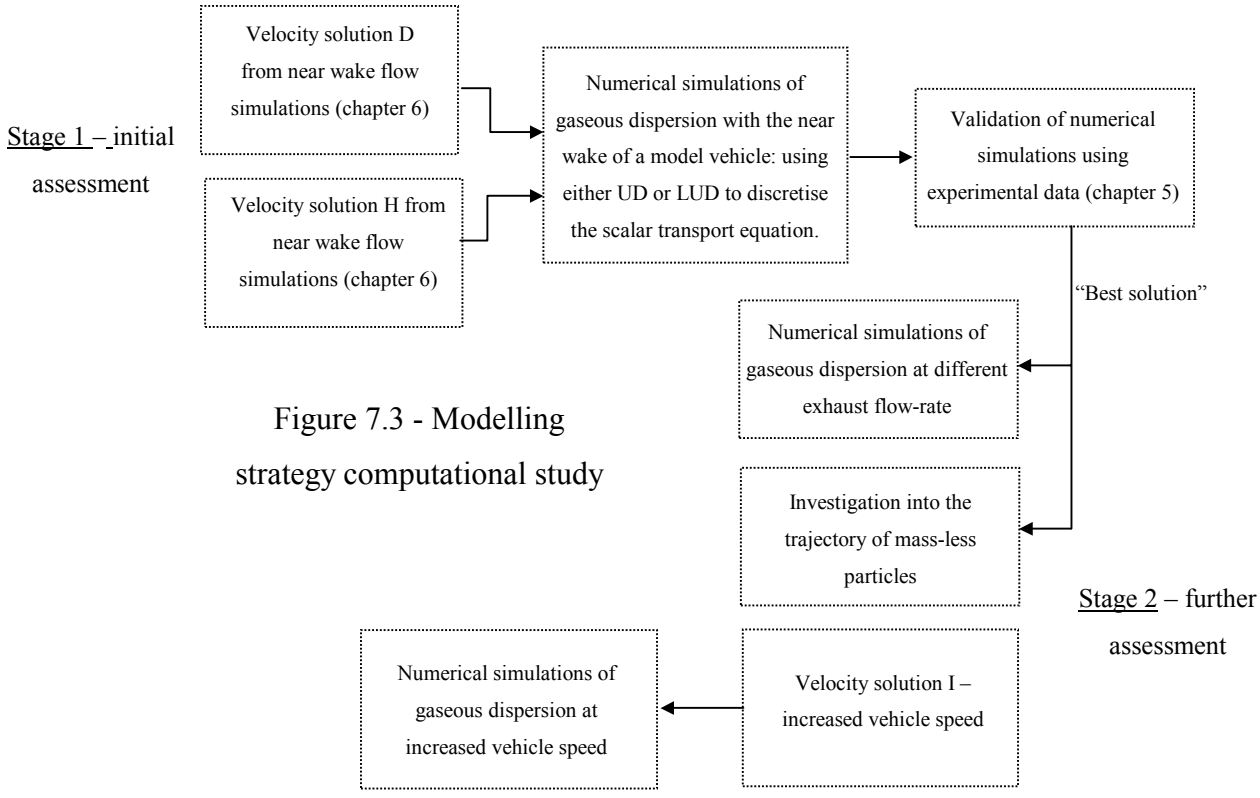

Figure 7.3 - Modelling strategy computational study

The use of STAR-CD to simulate the dispersion of a gaseous pollutant behind a model vehicle is novel and therefore the investigation was primarily a feasibility study as opposed to the development of a tuned model. The fluid injection technique used was a simple but effective method for simulating the dispersion of a passive scalar with the potential to produce agreeable solutions with the minimum of user input. The model strategy adopted first assesses the capability of STAR-CD in the simulation of a passive pollutant (stage 1) and then further shows the application of the technique in the investigation of other factors influencing dispersion. Data collected during the experiment to measure tracer gas dispersion (chapter 5) was used to validate the simulations performed in stage 1. The underlying velocity solutions were validated in good agreement with the measured near wake flow field in particular the flow field close to the exhaust location and therefore were used to aid in the discussion of the simulated dispersion field. The simulations conducted in stage 2, figure 7.3 were based on the success of those in stage 1 but there was no experimental data available for their validation. The study was not comprehensive but shows the general applicability of the technique at this initial stage. The scalar transport equation was discretised using either upwind or linear upwind differencing and an assessment made of each application (sections 3.3.1.1 and 3.3.1.2). The "best" solution from stage 1 was used as the foundation for the simulations in stage 2 using the solution restart facility (section 6.2.3). A new velocity solution was calculated to assess the influence of vehicle speed. All solutions obtained are listed in Table 7.1 and subsequently referred to by the given index in the following discussions.

Solution	Velocity solution	Reference	Free stream velocity	Scalar mass flow rate	Scalar transport discretisation
1	Non-linear k-ε/UD	Section 7.4	13m/s	7.018×10^{-5} kg/s	UD
2	Non-linear k-ε/UD	Section 7.4	13m/s	7.018×10^{-5} kg/s	LUD
3	Non-linear k-ε/LUD refined mesh	Section 7.5	13m/s	7.018×10^{-5} kg/s	LUD
4	Non-linear k-ε/UD	Section 7.4	13m/s	1.404×10^{-4} kg/s	LUD
5	Non-linear k-ε/UD	Section 7.4	13m/s	3.509×10^{-6} kg/s	LUD
6	Non-linear k-ε/UD	Section 7.4	17m/s	7.018×10^{-5} kg/s	LUD

Table 7.1 – Details of gaseous simulations.

Details of the underlying velocity solutions may be found in Appendix 4b. The scalar quantity injected i.e. propane, was treated as passive i.e. solely dependent on the flow field for its dispersion and had no influence on the bulk flow. The intention was to simulate the conditions from the tracer gas experiments (chapter 5) not the conditions of a real exhaust flow. The effects of heat and buoyancy were therefore neglected. The successes of the gaseous simulations were highly dependent on the accuracy of the velocity field calculations. The dependency of this final stage of the complete study is demonstrated in figure 1.3.

All the calculations conducted were steady state even though it was demonstrated in the experimental studies that the near wake flow field is inherently unsteady. The aim of the current work was to determine whether STAR-CD could be used to simulate the dispersion of a pollutant in the near wake of a model vehicle. Therefore it was more appropriate, and common place, to begin with the simulation and validation time-averaged flow and dispersion field. To begin such a study using transient calculation would be ambitious (section 6.2.3). The relative success of the current work could then be used as a foundation for further time-dependent studies.

A passive technique of particle tracking was used to visualise the trajectory of mass-less particles demonstrating an additional method of visualising a predicted velocity and dispersion field. This technique was not used to model the particle pollution but visualise the path of a mass-less particle using the existing velocity field to gain further insight into the dispersion character of the recirculation region. However particles emitted from vehicles are generally <2.5μm in size (Greenwood *et al*, 1996; Rickeard *et al*, 1996) and may be considered to behave like a gas. Such a technique could therefore be applied to understand the dispersion of a cloud of fine particle pollution, which are themselves a growing concern in terms of their health effects (chapter 1).

7.2.5 Solution control, monitoring and accuracy

Solution control was achieved using under relaxation factors applied to the flow variables *u, v, w, p, k* and ε to suppress any numerical instability in the solution

underlying velocity solution (section 3.3.2) and to assist in maintaining an adequate convergence level. The progress of each solution was monitored using the global residuals, equation (3.9), of each variable and a user specified monitoring cell giving absolute values of the flow variables at a specified point in the flow. The monitoring cell was placed in the near wake recirculation region to monitor any rapid changes in the absolute values of flow variables. For a satisfactory solution these absolute mean values of flow variables should remain consistent. The solution convergence criterion was set based on the value of the global residual for each flow variable. At least 10^{-3} was achieved for all flow variables, Appendix 4b.

Round-off error became a significant factor due to the small concentration values. The round-off error was dictated by the precision of the solution therefore it was necessary to apply double precision accuracy to each solution. Double precision accuracy works to 22 decimal places and demands extra computing resources increasing the run time per iteration.

7.3 Stage 1 – Initial assessment; numerical simulations of experimental pollutant dispersion – direct validation.

The following discussion details results from solutions 1-3 listed in Table 7.1. The velocity solutions D and H (Table 6.1) were used as the foundation for the numerical solutions to be discussed. Both velocity solutions used the non-linear k-ε model. Solution D used the upwind differencing scheme to discretise the momentum transport equations and solution H the linear upwind differencing (LUD) scheme. Both solutions used the upwind differencing (UD) to discretise the turbulent transport equations (Appendix 4b). Solution H used a refined mesh within the near wake (figure 6.2). Both the UD and LUD schemes were used to discretise the scalar transport equation and an assessment made of each. The simulations of tracer gas dispersion were validated directly against the experimental data using contour maps of concentration, velocity vector maps and concentration profiles from both predicted and measured data. The underlying velocity solutions were validated in good agreement with the measured near wake flow field in particular the flow field close to the exhaust location (Chapter 6) and therefore were used to aid in the discussion of

the simulated dispersion field. Statistical techniques, described in section 3.5 were also used to conduct a more global validation i.e. in terms of all predicted and measured points. It should be noted that due to practical difficulties during the tracer gas measurements concentration data was only obtained within the recirculation region therefore only this region could be validated. However as the recirculation region was the area of primary concern for initial dispersion of pollutant this was not considered to be a disadvantage at this initial stage.

Figure 7.4 compares the results of solution 1 and solution 2 with the experimental data using contour maps of mean concentration expressed as proportion of propane to air, $\overline{\varpi}_p$ i.e. 0.011 would indicate 1.1% propane to air in that cell, equivalent to maximum $\overline{\varpi}_{p_{max}}$ or source strength. It should be noted that the experimental measurements did not extend to the floor (figure 5.6) therefore to make fair comparisons the predicted data was displayed to the same height above the floor as the measured data.

The primary difference between the two solutions shown in figure 7.4 is the method of discretisation applied to the scalar transport equations. The upwind differencing (UD) scheme was used in solution 1 and the linear upwind differencing (LUD) scheme in solution 2. Both solutions applied the same exhaust mass flow rate 7.018×10^{-5} kg/s, the same as applied during the experimental study. The scalar was set as passive and did not have any influence on the bulk properties of the main flow field relying solely on the predicted velocity field to carry it. The predictions by both solutions of the measured concentration field were fair with the general size and shape of the dispersion field being reproduced for x/l = 0.036, 0.073 and 0.146. The predicted dispersion fields show, as in the experiment, a general upward dispersion of tracer gas as it is drawn up by the lower vortex of the recirculation region and cross-stream spread due to recirculation and internal cross-flow.

The differences between the dispersion fields at x/l = 0.036. 0.073 and x/l = 0.146 are represented by the numerical simulations, figure 7.4a-b(iii). From the experimental measurements ~x/l = 0.146 was identified as the primary pick-up region for tracer gas from the exhaust plume by the lower vortex.

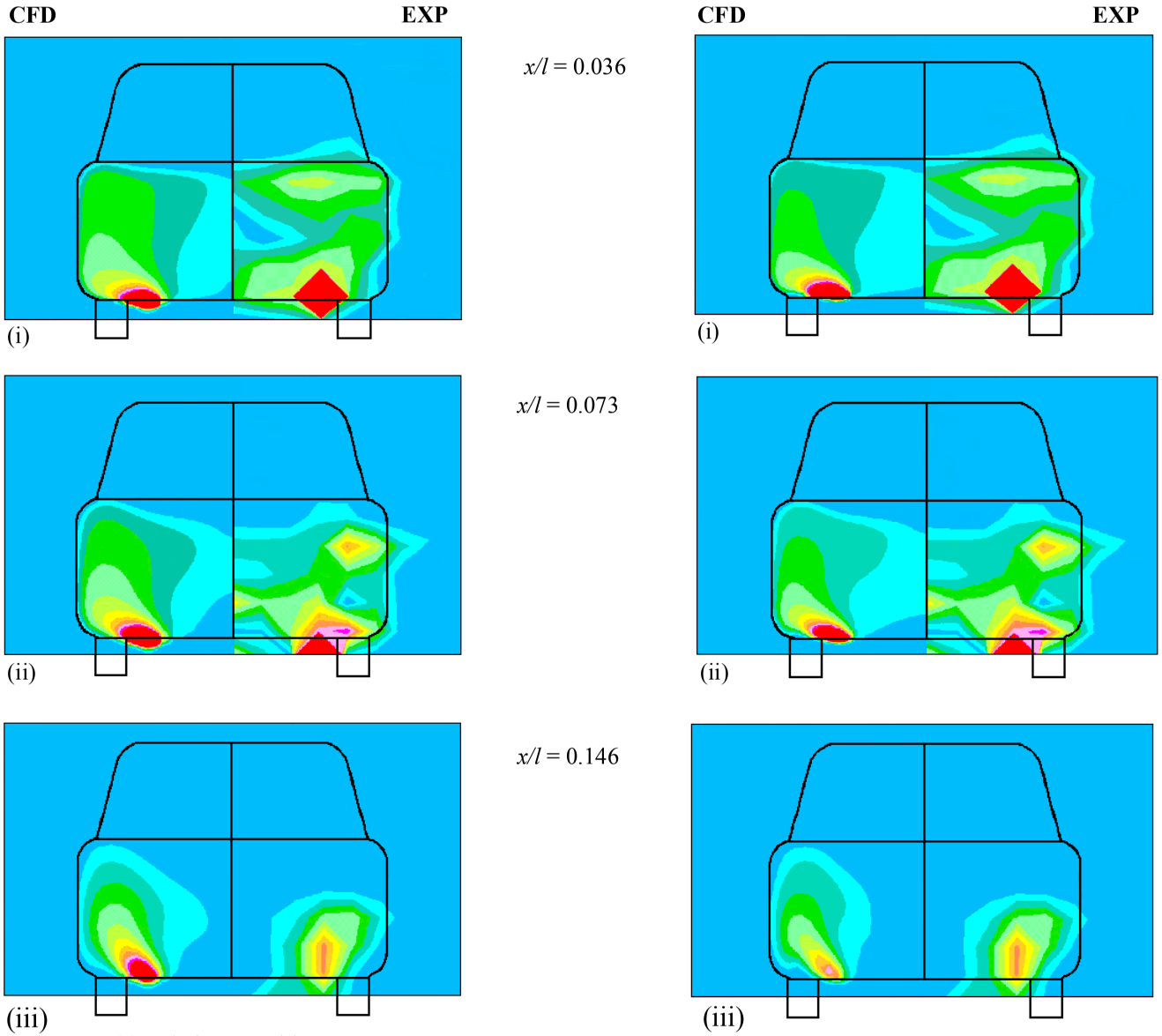

(a) Solution 1, Table 7.1.

(b) Solution 2, Table 7.1.

Figure 7.4 – Comparison of predicted and measured concentration fields for solutions 1 and 2.

The fair agreement of predicted and measured concentration fields at x/l = 0.146 would suggest that the pick-up region was predicted in good agreement. The underlying velocity solution, solution D showed good agreement with prediction of the pick-up region of the lower vortex and as the scalar was classified as passive theoretically it should follow the predicted velocity field, figure 6.10, Chapter 6. Figure 7.5 presents a contour map of mean concentration $\overline{\omega}_p$ at y/H = 0.256 for solution 1 and shows the point of high concentration to occur at x/l = 0.146 and further demonstrating good agreement with the measured pick up region.

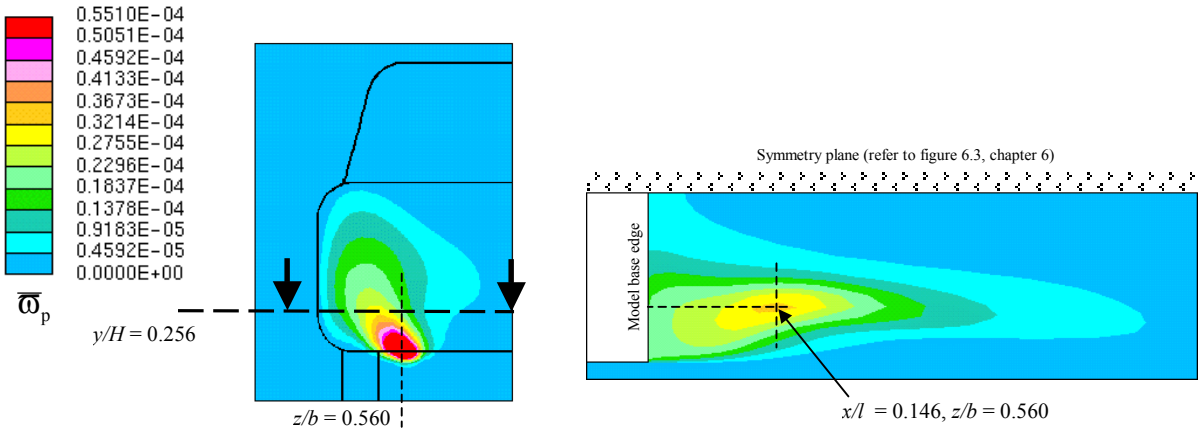

(a) Cross-stream contour map at x/l = 0.146 (b) Streamwise contour map at y/H = 0.256

Figure 7.5 – Prediction of pollutant pick-up region

In addition most significant difference between the actual predictions of solution 1 and solution 2 occurred at x/l = 0.146, figure 7.4 a/b(iii). Solution 2 which applied linear upwind differencing to the scalar transport equation made better prediction of both the dispersion and magnitude of $\overline{\omega}_p$ within the vicinity of the exhaust at x/l = 0.146. Figure 7.6 shows the measured and predicted values of concentration at z/b = 0.560 with solution 2 making a more realistic prediction of local maximum of $\overline{\omega}_p$, $\overline{\omega}_{p_{Lmax}}$ over predicting by only 17% whereas solution 1 over predicted by 70%.

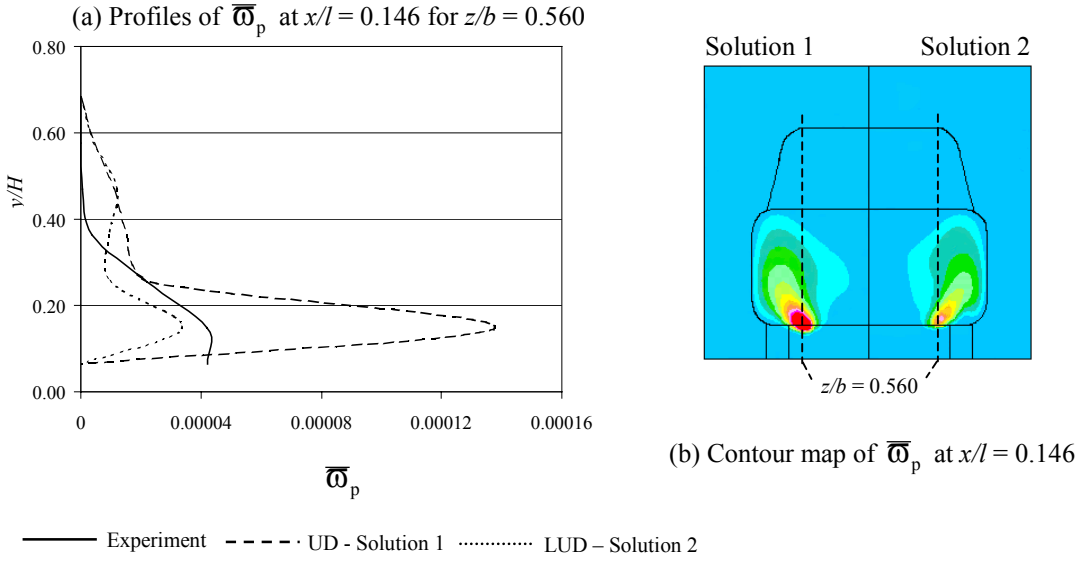

Figure 7.6 - Comparison of predicted $\overline{\omega}_p$ at $x/l = 0.146$ for $z/b = 0.560$ for solutions 1 and 2

However from figure 7.4a-b(i-ii) predictions by both solutions 1 and 2 did not show the distinct concentration pattern illustrated by the experimental results at $x/l = 0.036$ and 0.073. Figure 7.7 compares the predicted and measured profiles of concentration at $x/l = 0.036$ and 0.073 for $z/b = 0.560$ and 0.746 respectively. The general shape of the predicted concentration profiles at $x/l = 0.036$ and 0.073 are in fair agreement with the measured profiles but the magnitude of $\overline{\omega}_p$ was generally under predicted by both solutions 1 and 2. However while not shown in figure 7.4 the influence of the two-tier vortex structure was still evident by the marginal local increase in predicted $\overline{\omega}_p$ towards $y/H = 0.5$ at $x/l = 0.036$ and 0.073 figure 7.7b, the result of scalar being caught within the rotation of the upper vortex of the recirculation region. However only solution 2 predicted a local increase in $\overline{\omega}_p$ at $x/l = 0.073$ at approximately $y/H = 0.4$ albeit only 5% rise compared to the measured 18% rise. Solution 1 made a similar prediction of $\overline{\omega}_p$ around $y/H = 0.4$ but showed no increase in $\overline{\omega}_p$ up to that point only a steady decrease. The slight improvement in predictions by solution 2 may be due to the application of LUD to discretisation the scalar transport equations. The LUD scheme offers increased solution accuracy through the use of two upwind nodes in its approximation of convective fluxes (section 3.3.1.2).

In addition the under prediction of the increase in local $\overline{\omega}_p$ may result from under predictions in the velocity field compromising the flows ability to 'pick-up' tracer gas from the exhaust plume and draw it into the near wake recirculation region.

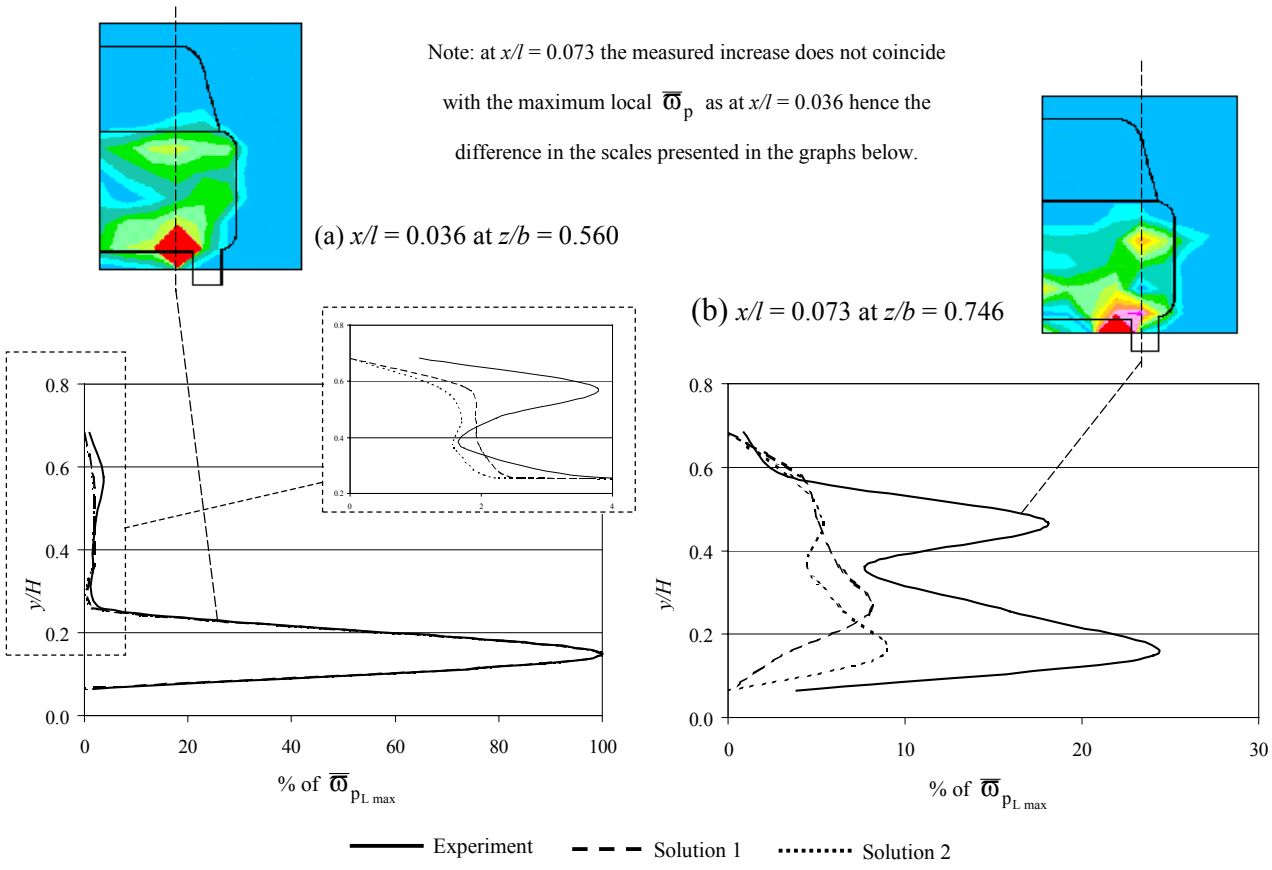

Figure 7.7 – Comparison of predicted and measured profiles of $\overline{\omega}_p$

Although it was more probable that the under predicted in concentration was a consequence of the difference in methods used to obtain the data being compared as solution showed good agreement with the measured velocity field at $x/l = 0.146$. The measured mean concentrations were established from an inherently unsteady and changing concentration field, which showed, through flow visualisation regular build up and purge of pollutant from the recirculation region, figure 5.5 chapter 5. The predicted concentration field however was established from an unchanging flow field obtained through a number of numerical iterations i.e. steady state. While the method applied to model the scalar dispersion does take account of turbulence through k-ε model and coupling with turbulent viscosity (equation 7.3) it does not account of the pollutant build observed in the highly unsteady concentration field

therefore predicted mean concentrations would undoubtedly be lower. Nevertheless the general profiles and distribution of concentration in figures 7.4 and 7.7 were in fair agreement with the measured concentration field.

With reference to figure 7.4 the predictions of cross-stream dispersion by both solutions 1 and 2 show fair agreement. Figure 7.8 compares predicted and measured distributions for both the cross-stream and vertical positions z/b = 0.560 and y/H = 0.149 respectively. Note the vertical dispersion of tracer gas at z/b = 0.560 for x/l = 0.036 was not included as it was illustrated in figure 7.7a. While generally both solutions made agreeable predictions of the concentration profiles at the illustrated locations however the position of the measured local maximum and predicted local maximum $\overline{\varpi}_{p_{Lmax}}$ at x/l = 0.073 were different. As a consequence there was a disagreement between the predicted and measured vertical and cross-stream distributions at this point, figure 7.8a(i) and b(ii). Through both measurement and observation (chapter 5) it was suggested, that at x/l = 0.073 the plume was drawn toward the floor due to fluctuations within the plume causing $\overline{\varpi}_{p_{Lmax}}$ to occur closer to the floor than at x/l = 0.036 and 0.146. This was not reflected in the predicted results which might be a consequence of the difference in the predicted and observed mean recirculation length resulting in different flow characteristics at that point compared with the same point measured during the wake survey. Although it is more likely to be a consequence of using steady-state methods to obtain the numerical concentration field i.e. the mean measured values captured the fluctuation in the exhaust plume and the numerical mean values did not. At x/l = 0.036 both solutions 1 and 2 over predicted the local maximum of $\overline{\varpi}_p$, $\overline{\varpi}_{p_{Lmax}}$ by 4%.

It might also be suggested that the difference in the position of $\overline{\varpi}_{p_{Lmax}}$ between x/l = 0.036 and 0.073 be due to applying a fixed floor condition i.e. the thickening boundary layer draws the plume towards the floor (section 5.3.2). Therefore the difference in the position of the predicted and measured local maximum at x/l= 0.073 might be due to inaccurate predictions of the developing floor boundary layer. However during the experimental study the floor boundary layer was believed to have no significant influence over the concentration field (Section 5.4.1).

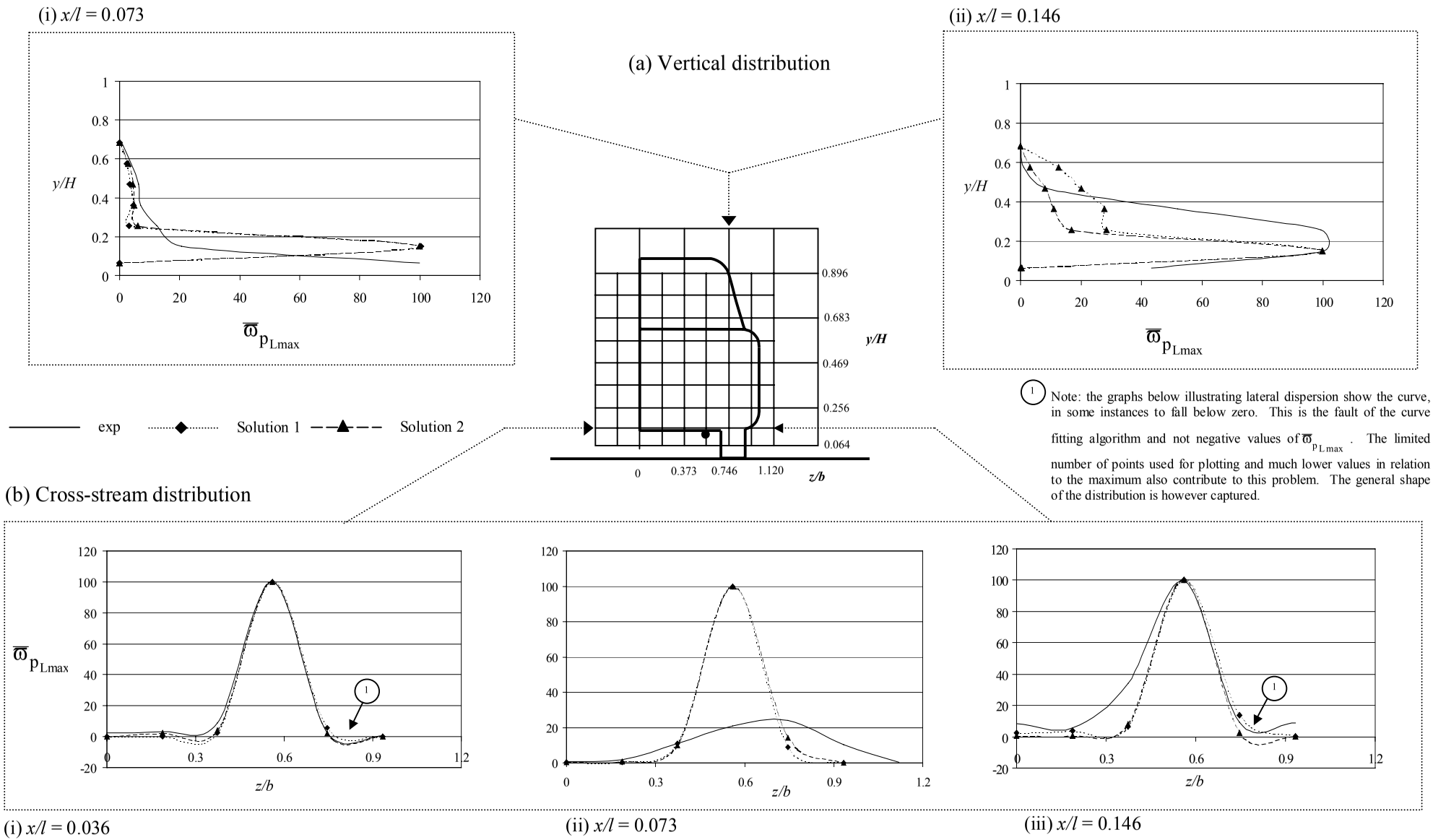

Figure 7.8 – Comparison of measured and predicted distributions of tracer gas within the vicinity of the exhaust

In addition there was a general disagreement in the cross-stream distribution of $\overline{\omega}_p$ towards the lower part of the concentration field at both at *x/l* = 0.036 and 0.073. Figure 7.9a shows the predicted concentration field at *x/l* = 0.036 with the corresponding predicted velocity field from solution D. Note for clarity of flow pattern the size of the vectors in each vector map magnified by a factor of 4. The disparity at the lower edge of the concentration field towards the model centreline was a consequence of no significant predictions of cross-flow at *x/l* = 0.036 towards the lower part of the recirculation region in comparison with a small measured cross-flow at *x/l* = 0.036 figure 7.9b. However despite the disagreement towards the lower part of the concentration field the agreement of predictions improved with height above the ground as illustrated by the concentration profiles shown in figure 7.9b (i-iii). While not represented in the contour map of concentration at *x/l* = 0.036 solution 2 predicts a similar drop then rise in concentration towards the centreline at *y/H* = 0.363. Both solutions predicted similar profiles of $\overline{\omega}_p$ at *y/H* = 0.432. The measured local maximum shown at x/l = 0.036 in figure 7.9b(iv) was predicted by both solutions albeit much lower than the measured value hence it was not shown on the contour map.

An assumption of centreline symmetry was enforced for the velocity calculations (section 6.2.2.1) and as a consequence of these velocity solutions being used as the foundation for the dispersion simulations the same symmetry boundary was enforced. The experimental results presented in figure 5.6 chapter 5 showed tracer gas to clearly spread across the model centreline, a similar pattern observed during the flow visualisation study, figure 5.5b. It is therefore probable that enforcing centreline symmetry suppressed any tendency for cross-stream dispersion of pollutant across the model centreline in the numerical simulations.

(a) Comparing predicted and measured the cross-stream dispersion patterns at $x/l = 0.036$

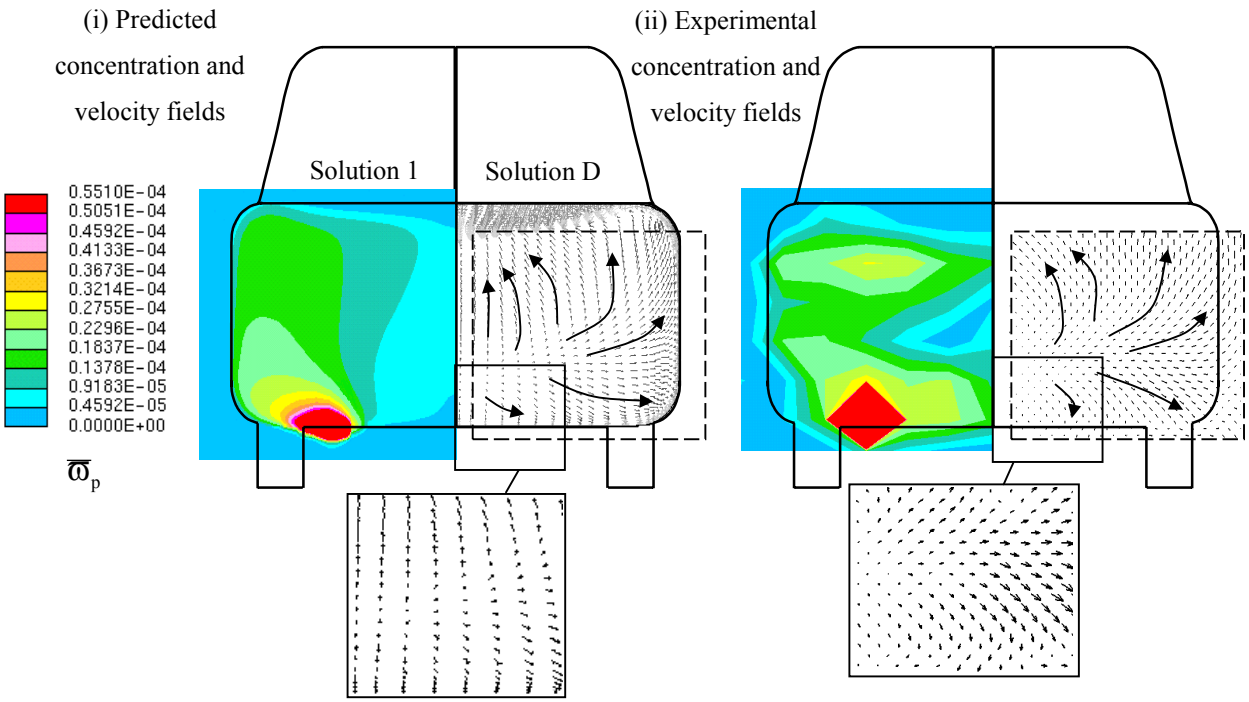

(b) Comparing predicted and measured profiles of $\overline{\omega}_p$ for various y/H at $x/l = 0.036$

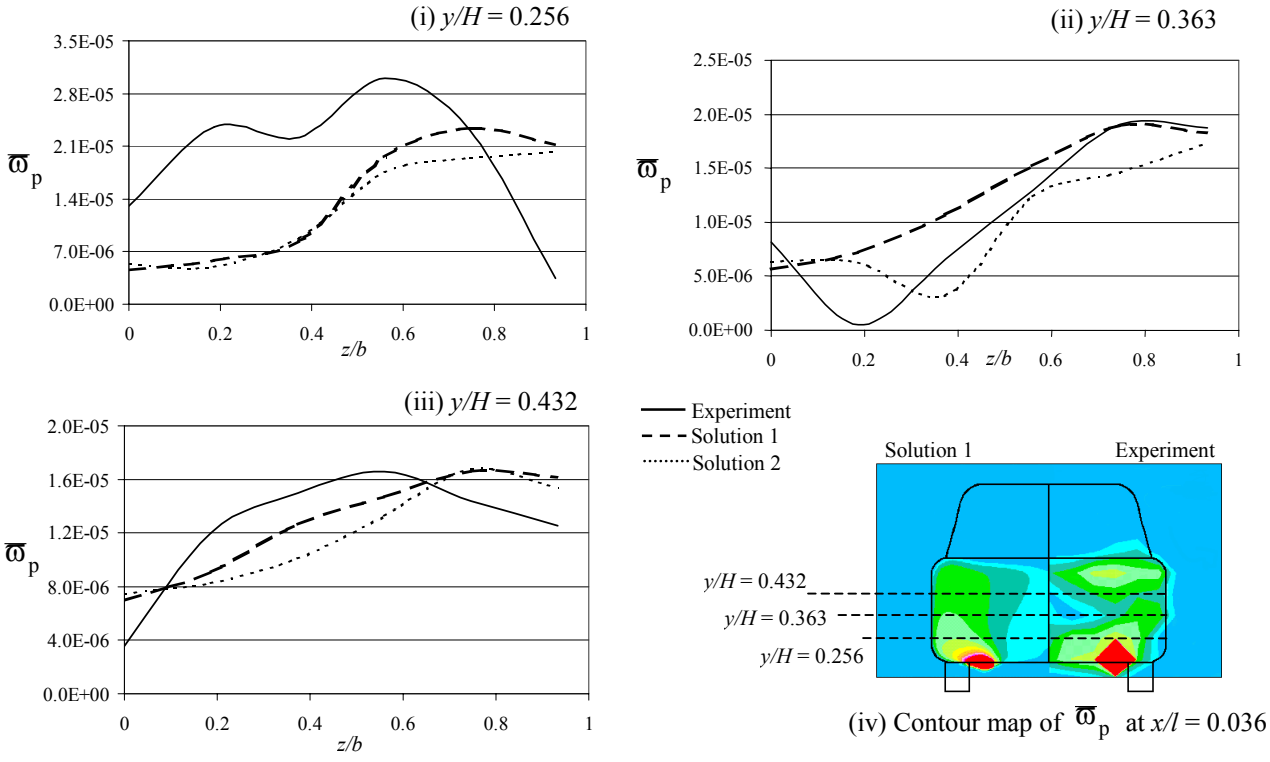

Figure 7.9 Comparing predicted and measured the cross-stream dispersion at $x/l = 0.036$

Solution 3 detailed in Table 7.1 was run but unfortunately with no success. The problem seemed to lie with the mesh and not the technique applied. Solution 3 used the velocity field of solution H as its foundation which when combined with the necessary application of double precision accuracy resulted in serious strain on computer resources. As a consequence assistance was sought from the support team at Computational Dynamics. However the mesh file became corrupted during transfer and the conversion for use with STAR-CD version 3.1b resulted in the misallocation of boundaries. Unfortunately it was not possible to re-run the solution before the completion of the project. Nevertheless the results already presented have shown a fair degree of success in the prediction of the measured concentration field. While both predicted and measured concentration fields are weak it must be remembered that the prime aim was to reproduce the test results and not to make any conclusions on levels of concentration.

7.3.1 Statistical validation – Stage 1

Two different techniques were used to make a more global validation of the numerical solutions discussed above. The first technique used the absolute percentage difference between the experimental and predicted data to assess the general ability of the CFD to predict the measured concentration field. The second used the uncertainty of the experimental data to determine the probability of predicted values falling within the uncertainty of an equivalent measured value. The second technique allowed any uncertainty in the experimental data to be accounted for when making comparisons with the numerical predictions. As a consequence of the scalar being defined as passive the scalar distribution were solely dependent on the underlying velocity field therefore the agreement of the predicted velocity field must also be considered. The comparison techniques are detailed in section 3.5.

7.3.1.1 Absolute percentage difference

The absolute percentage difference between the measured and predicted results were calculated according to the description given in section 3.5.1. The general performance of the CFD in reproducing the measured concentration field was

assessed in terms of the percentage of predicted values falling within 50% or 75% of their equivalent measured values. The analysis at x/l = 0.036 and 0.073 was dealt with separately to that at x/l = 0.146 because the number of points at which tracer gas was detected during the experimental study decreased with distance downstream. The points considered for the validation at x/l = 0.036, 0.073 and = 0.146 are shown in figure 7.10.

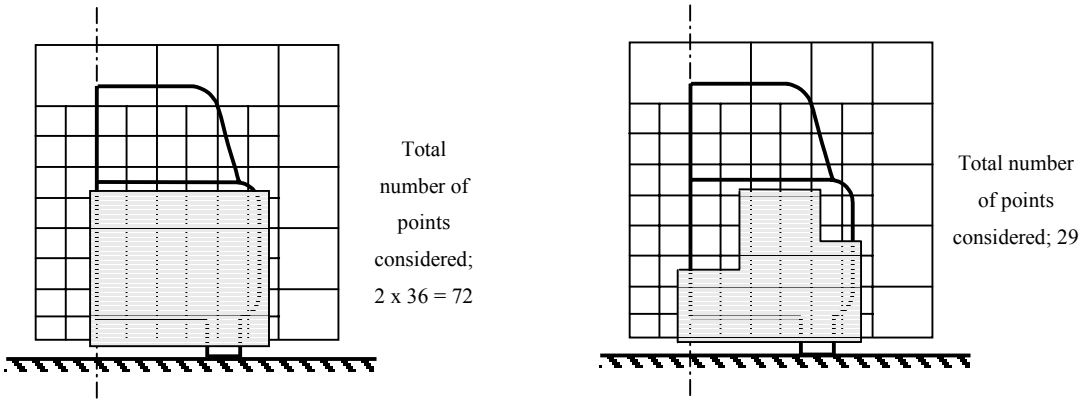

(a) Points used at x/l = 0.036 and 0.073. (b) Points used at x/l = 0.146

Figure 7.10 Points used in absolute percentage analysis

The limited number of points considered in the analysis could result in a misleadingly large percentage therefore the number of points used was made clear. The method provided a good overall indication of predictive performance.

All points at x/l = 0.036 and 0.073 were considered together. The results of the analysis for x/l = 0.146 also expressed in terms of the number of points were considered separately. Table 7.2 provides a summary of the analysis results.

	$x/l \leq 0.073$		$x/l = 0.146$	
	%≤50%	%≤75%	%≤50%	%≤75%
Solution 1	49 (35/72)	61 (44/72)	31 (9/29)	41 (12/29)
Solution 2	46 (33/72)	61 (44/72)	35 (10/29)	48 (14/29)

Table 7.2 - Results summary of absolute percentage difference comparisons for scalar solutions 1 and 2 (Table 7.1)

The numbers in brackets () denote the number of points

Figure 7.4 showed both solutions 1 and 2 to make similar predictions at x/l = 0.036 and 0.073. These results were reflected in the analysis with both solutions making comparable predictions at x/l = 0.036 and 0.073, Table 7.2. Both solutions generally under predicted values of $\overline{\varpi}_p$ implying an under-prediction in the general dispersion field. At x/l = 0.036 both solutions 1 and 2 over predicted the local maximum of $\overline{\varpi}_p$, $\overline{\varpi}_{p_{Lmax}}$ by 4%. Both solutions failed to predict the location of the local maximum $\overline{\varpi}_{p_{Lmax}}$ at x/l = 0.073 thus under predicted by 100% for the equivalent measurement point which was thought to be a consequence of using steady-state calculations the model what was essentially a highly unsteady flow field. Solution 2 made generally better predictions of $\overline{\varpi}_p$ at x/l = 0.146 (Table 7.2). Both solutions predicted the local maximum $\overline{\varpi}_{p_{Lmax}}$ but solution 2 made a significantly better prediction, figure 7.3a/b(iii) over predicting by 19% as opposed to 70% for solution 1.

The general over prediction of the local maximum $\overline{\varpi}_{p_{Lmax}}$ suggests scalar not to be dispersed adequately which might account for the under prediction of $\overline{\varpi}_p$ at most points away from the exhaust plume. The underlying velocity field used for solutions 1 and 2 was solution D, non-linear k-ε/upwind differencing, and showed good agreement with the measured flow field particularly within the vicinity of the exhaust at z/b = 0.560 (section 6.3.1). On average 82% of all predictions of the three velocity components $\overline{u}$, $\overline{v}$ and $\overline{w}$ being with 75% of the measured values at $x/l \leq$ 0.218 i.e. within recirculation. Under predictions of the concentration field are more likely a consequence of the method itself in that the steady-state calculations did not capture the true fluctuations in the mean concentration field thus resulting in lower predicted values particularly in areas of measured local increase. Nevertheless predictions by both solutions 1 and 2 of the concentration field at x/l = 0.036, 0.073 and 0.146 were considered to be in fair agreement under the criteria set in section 3.5.1, chapter 3 with 40% of predicted values falling within 50% of the measured values.

7.3.1.2 Prediction error in terms of experimental uncertainty

The uncertainty in $\bar{c}$ was, in section 5.2.4, expressed in terms of the maximum uncertainty at the location of highest uncertainty i.e. at *x/l* = 0.036. The maximum uncertainty expressed in $\overline{\omega}_p$ at *x/l* = 0.036 being $\overline{\omega}_p \pm 5.96 \times 10^{-6}$ for FID 1 and $\overline{\omega}_p \pm 4.02 \times 10^{-6}$ for FID 2 with a 95% confidence (dividing the uncertainty in $\bar{c}$ by 10^6 to give the uncertainty in $\overline{\omega}_p$). However when these maximum uncertainties were used to represent prediction error (equation 3.27) the results produced were unrealistic showing a good agreement when in reality the agreement was poor i.e. at points where there was strong disagreement with the measured values the actual uncertainty was much lower than even the maximum of $\overline{\omega}_p$ thus showing good agreement. Instead the uncertainty in $\overline{\omega}_p$, $E_{\overline{\omega}_p}$ calculated for each measurement point was used in the comparison of the equivalent predicted values. The uncertainties assigned to values of $\overline{\omega}_p$ measured by FID 1 and FID 2 are $E_{\overline{\omega}_{p1}}$ and $E_{\overline{\omega}_{p2}}$ respectively. Some points within the measurement field were measured twice by virtue of the experimental set-up (section 5.2.1). Thus the calculated values at these points were taken as the average of the two mean measured values (section 5.2.3). As a result there were two calculated uncertainties available for certain points, one related to the measurement made by FID 1 and the other to FID 2. For these measurement points the highest uncertainty between FID 1 and FID 2 was used for validation.

The method used to determine the uncertainty in $\bar{c}$ assumed the measured data to be normally distributed (section 3.5.2). Appendix 3b(i) shows the raw data to be normally distributed therefore it was assumed that the calculated concentration data and thus $\overline{\omega}_p$ was also normally distributed. However points, which coincided with the local maximum concentration, had a skewed distribution, Appendix 3b(ii). For this reason point 53 at *x/l* = 0.036 and 0.146 and point 54 at *x/l* = 0.073 were not considered in the following analysis.

The prediction error was calculated, using equation (3.30) for each individual data point and compared against the appropriate uncertainty in $\overline{\varpi}_p$ i.e. $E_{\overline{\varpi}p1}$ and $E_{\overline{\varpi}p2}$. The predicted results were considered in good agreement with the experimental data if at least 50% of the predicted results lie within $\pm 4E_{\overline{\varpi}p}$ (figure 3.5). The range of acceptability was wider than used in the comparison of predicted and measured velocity data because in general $E_{\overline{\varpi}p1}$ and $E_{\overline{\varpi}p2}$ were at least one order of magnitude smaller than the actual value of $\overline{\varpi}_p$, whereas for the velocity data the uncertainty, σ was generally the same order of magnitude. The CFD effectively had a smaller range of $\overline{\varpi}_p$ in which to make predictions and thus a wider range of acceptability was more practical, Appendix 5a.

The predicted data at x/l = 0.036 and x/l = 0.073 was dealt with separately to that at x/l = 0.146 for the reasons given in section 7.3.1.1. The actual data points considered were the same as those shown in figure 7.10 points containing the most significant concentration data.

The analysis in the previous section comparing absolute percentage difference showed that at x/l = 0.036 and 0.073 61% of the predicted values of $\overline{\varpi}_p$ fell within 75% of the experimental values with on average 48% lying within 50% however the current more stringent analysis showed a not so favourable agreement. Figure 7.11 shows the general agreement between the predicted and experimental data to be fair but marginally better at x/l = 0.073. While at both x/l = 0.036 and 0.073 both solutions 1 and 2 predicted on average 49% of $\overline{\varpi}_p$ to be $\leq 4E_{\overline{\varpi}_p}$ a higher percentage of predictions $> 8E_{\overline{\varpi}_p}$ occurred at x/l = 0.073. The comparisons shown in figure 7.11 were in terms of the number of points because the results at x/l = 0.036 and 0.073 were being compared against each other thus reducing the number of points for comparison. Comparing in terms of the percentage of points alone could have been misleading due to the smaller number of points considered. Solution 1 generally made better predictions at x/l = 0.036 than solution 2 and vice versa at x/l = 0.073.

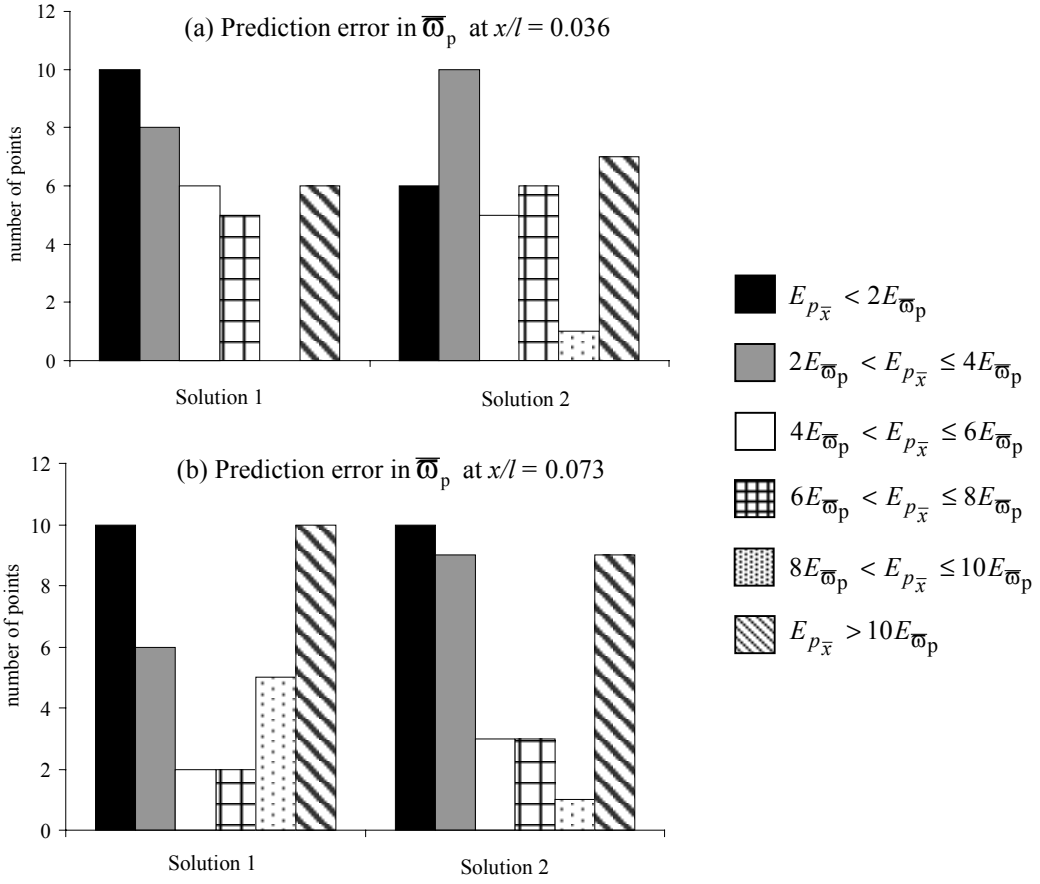

Figure 7.11– Prediction error for $\overline{\varpi}_p$ in terms of experimental uncertainty, $E_{\overline{\varpi}_p}$

At both x/l = 0.036 and 0.073 there were a significant number of predictions, for both solutions 1 and 2 where $E_{p_{\bar{x}}} > 10E_{\overline{\varpi}_p}$. These disagreements generally occurred in regions of low concentration i.e. where $\overline{\varpi}_p$ was very low thus exaggerating the difference; in particular close to the model centreline where cross-stream dispersion was not well predicted (section 7.3.1). This tendency to over exaggerate in regions of low concentration was considered a limitation of the comparison technique.

Solution 2 made significantly better predictions of $\overline{\varpi}_p$ at x/l = 0.146, figure 7.4. This is reflected in results presented in figure 7.12. Solution 2 predicted 48% or 14 out of 28 values of $\overline{\varpi}_p$ within $\pm 4E_{\overline{\varpi}_p}$ while solution 1 predicted only 41% (12) of the points within the same range. The general performance of solution 2 was better with more values of $\overline{\varpi}_p$ being predicted within the lower uncertainty ranges. Solution 2 predicted 58% of $\overline{\varpi}_p$ to within $\pm 6E_{\overline{\varpi}_p}$ as opposed to 48% for solution 1. Again

both solutions 1 and 2 made predictions within the range $E_{\overline{\omega}_p} \geq 10E_{\overline{\omega}_p}$, the result of very low concentrations exaggerating the difference between measured and predicted values.

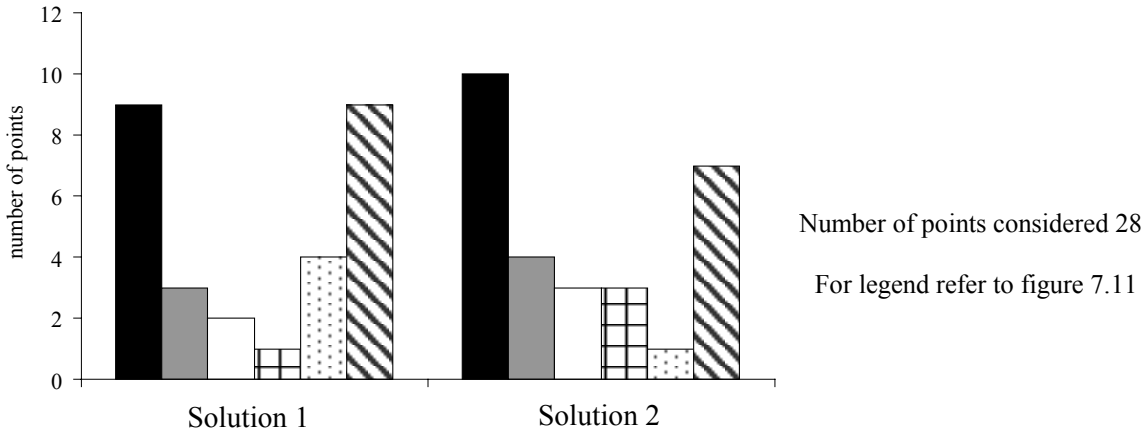

Figure 7.12 – Prediction error for $\overline{\omega}_p$ at x/l = 0.146 in terms of experimental uncertainty, $E_{\overline{\omega}_p}$

Based on the criteria set in section 3.5.1 and the consideration that there were a significant number of predictions $E_{p_{\bar{x}}} \geq 8E_{\overline{\omega}_p}$ the predictions by both solutions 1 and 2 at $x/l \leq 0.073$ were considered in fair agreement with on average on average 49% of predicted $\overline{\omega}_p$ falling to within $\leq 4E_{\overline{\omega}_p}$ of the measured values. Similarly predictions at x/l = 0.146 with on average 45% of $\overline{\omega}_p$ within $\pm 4E_{\overline{\omega}_p}$ but again with a number of predictions $E_{p_{\bar{x}}} \geq 8E_{\overline{\omega}_p}$.

7.3.1.3 Solution run times – stage 1

The scalar simulations were run as an addition to the underlying velocity solution, (refer back to section 7.2.2 and 7.2.3) but as double precision accuracy was required in the calculation of the scalar field the overall computational effort was increased. As a consequence run times for the scalar solutions could not be expressed using the same CPU index, as it would be unfair to express them relative to the velocity solutions. However each simulation took approximately 36 hours additional CPU time.

7.3.2 Stage 1: Initial assessment - Conclusions

It would not be realistic to make a definitive statement on the success of the method based on only the two solutions presented. A more comprehensive study at this stage would have been desirable, in particular simulations using the refined mesh but constraints on computing resources did not allow for this. However from the comparisons it was suggested that the use of steady state calculations might not be appropriate for the current application. The measured mean concentrations used in the validation were established from an inherently unsteady and constantly changing concentration field the result of an inherently unsteady and constantly changing velocity field (Section 5.6). The numerical results however were mean concentrations calculated using the steady-state modelling approach i.e. the unchanging flow pattern of under a given set of boundary conditions is obtained through a number of numerical iterations. Therefore peaks in concentration captured in the measured mean values would not be reflected in the numerical predictions i.e. the predictions mean concentrations are based only on calculations of constant recirculation not unsteadiness therefore resulting in under prediction particularly in areas of measured local maximum concentration. This was also the reason for no further solutions in this stage as it was felt no improvement would be made on the current predictions.

Nevertheless it has been shown that the simple method of fluid injection can be used to introduce a pollutant source for the investigation of pollutant dispersion behind a road vehicle although further development would be required to include effects of heat and buoyancy. The generally fair agreement between the measured and predicted data shows the potential of using STAR-CD for the numerical simulations of pollution dispersion behind a model vehicle and the results presented provide a good foundation for further simulations to include the unsteady effects of the flow field i.e. transient calculations.

7.4 Stage 2 – Further assessment

Stage 1 of the investigation showed the application of STAR-CD in the simulation of the measured dispersion field and while there was some doubt over the application of steady state calculations the results presented were still in fair agreement with the experiment. Changing key factors that influence the dispersion of a pollutant i.e. the exhaust flow rate and vehicle speed further assessed the application of the fluid injection technique. Increasing the exhaust mass flow rate one would expect a higher concentration field and increasing the vehicle speed but maintaining the same mass flow rate greater dispersion would be anticipated.

The "best" solution from the previous section, solution 2 was used as the foundation for the further assessment using the solution restart facility (section 6.2.3). The underlying velocity solution to both the simulations was solution D detailed in Table 6.1 and Appendix 4b. There was no experimental data to validate these further simulations instead the relative ability of the CFD code demonstrated in the previous simulations were used in the assessment. For example did the overall concentration level increased through increasing the exhaust mass flow rate in comparison with the previous solutions. Solutions 1 and 2 were shown to be in fair agreement with the experimental data but their shortfalls in predictions were kept in mind during the further assessment. The area and number of points considered in all comparison were the same as those used in the previous section (figure 7.10a).

7.4.1 The influence of exhaust flow rate on numerical predictions

In order to assess the ability of the method to investigate the influence of exhaust mass flow rate on dispersion, the flow rate was doubled and halved relative to solutions 1 and 2, to be known as solutions 4 and 5 respectively. Note this was not a detailed investigation into the effects of increased mass flow rate on dispersion character but more a feasibility of the use of the method in such an investigation.

Details of the simulation are given in Table 7.1. Solutions 1 and 2 used the exhaust mass flow rate applied during the experimental study (chapter 5), which due to restrictions in the supply of tracer gas was significantly reduced. The mass flow rates applied here were 1.404×10^{-4} kg/s and 3.509×10^{-6} kg/s for solutions 4 and 5 respectively as opposed to 7.018×10^{-5} kg/s for solutions 1 and 2, and the experimental study. For a 1.6 litre engine vehicle in a typical urban cycle the exhaust mass flow rate would be 1.825×10^{-4} kg/s implying that the flow rate applied for the further assessment, solution 5 was 77% of the "ideal rate". The vehicle speed at model scale (33%) was 13m/s. No changes were made to any other modelling parameters applied for the initial investigation during the current assessment (section 7.2).

Figure 7.13 compares the results from the solutions 4 and 5 with those from solution 2. The contour plots used the same scale as applied to the comparisons in figure 7.4 so that changes in concentration field were clearly visible in relation to previous predictions and the experimental data. Figure 7.13a(i-ii) shows that as a consequence of increasing and decreasing the mass flow rate the magnitude of the concentration field increased and decreased accordingly but the general distribution of the scalar field remained unchanged. These findings substantiates the decision made during the experimental study to use a less than ideal exhaust flow rate i.e. the overall distribution of concentration would remain the same regardless of flow rate.

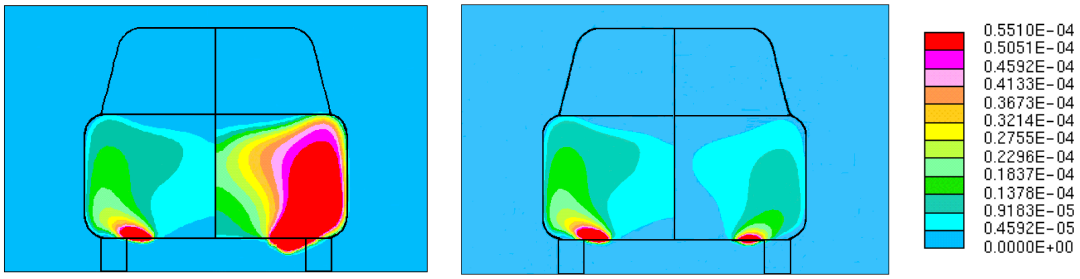

(i) Solution 2 vs Solution 4 (ii) Solution 2 vs Solution 5

Figure 7.13 - Comparing distributions of $\overline{\omega}_p$ for different exhaust flow rates at *x/l* 0.073

The results shown in figure 7.13 demonstrate that given a different exhaust mass flow rate STAR-CD was able to predict concentration field that reflected the conditions applied. For the same vehicle speed an increase and decrease in exhaust mass flow rate resulted in an increase and decrease in concentration field respectively. Figure 7.14 shows more quantitative comparisons between solutions 4 and 5 and solution 2 based on the difference in the magnitude of predicted concentration expressed as a factor difference $F_{\overline{\omega}_p}$ between values of $\overline{\omega}_p$. For double the exhaust mass flow rate figure 7.14a shows 60% and 57% of the predictions to be different by $3 < F_{\overline{\omega}_p} \leq 4$ at x/l = 0.036 and 0.073 respectively whereas at x/l = 0.146 the difference was more varied with only 23% with the aforementioned factor difference. Figure 7.14b shows that for half the exhaust mass flow rate 40-44% of predicted $\overline{\omega}_p$ were different by a factor of $0.6 < F_{\overline{\omega}_p} \leq 0.8$ at x/l = 0.036 and 0.146 with 40% different by $0.4 < F_{\overline{\omega}_p} \leq 0.6$ at x/l = 0.073. In comparison with solution 2 doubling the exhaust flow rate while maintaining the same vehicle speed one might anticipate double the magnitude in concentration field and similarly for half the exhaust mass flow rate, half the magnitude in concentration field.

The results in figures 7.13 and 7.14 show both solutions 4 and 5 to make predictions greater than those anticipated suggesting that the magnitude of distribution not to be proportional to the source strength i.e. half the source strength = half the concentration field. However it was not appropriate to draw any definite conclusions from these two solutions, as there was no experimental data to make direct comparisons. Nevertheless the results from solutions 4 and 5 demonstrate the potential in using the method for the investigation of such factors as exhaust mass flow rate on dispersion and concentration field.

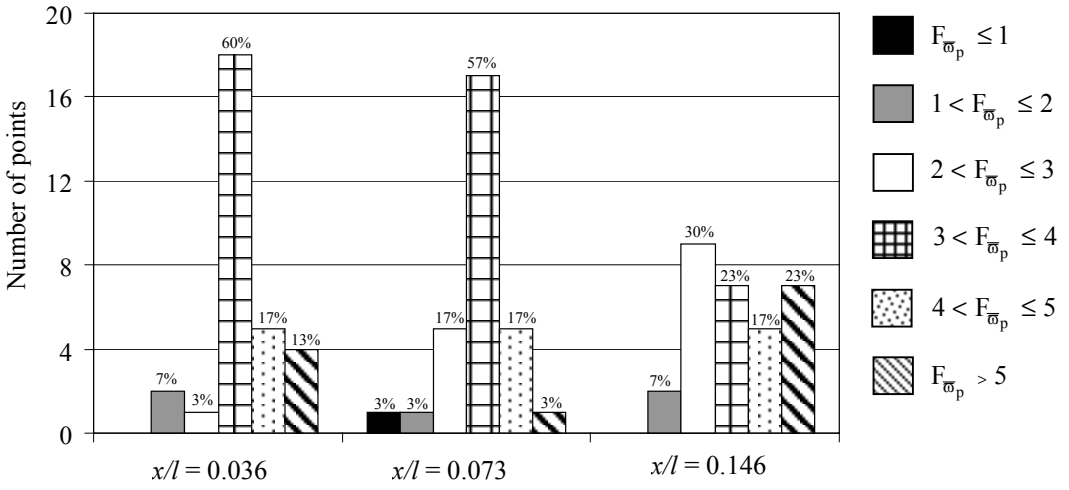

(a) Comparing predicted values of $\overline{\omega}_p$ for solution 2 and solution 4 i.e. at double exhaust mass flow rate

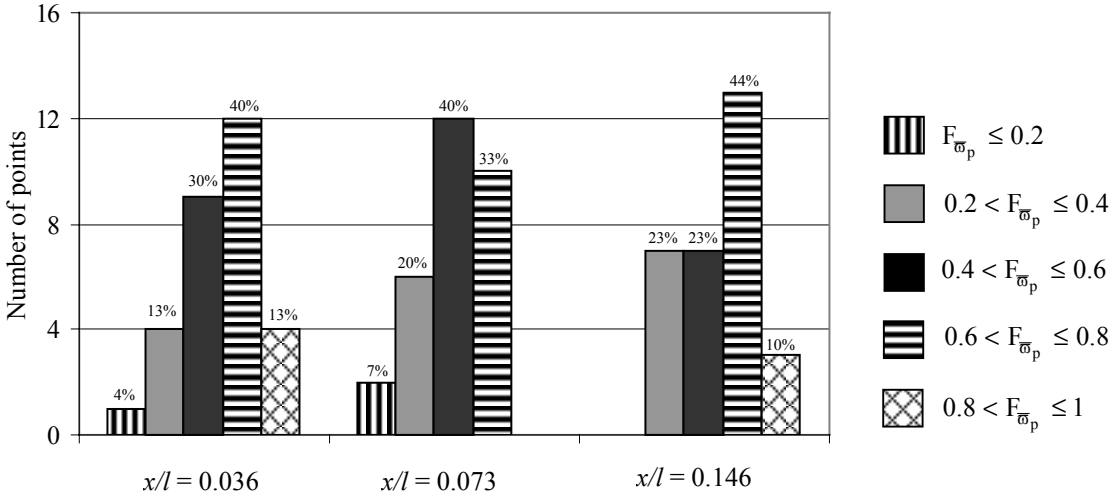

(b) Comparing predicted values of $\overline{\omega}_p$ for solution 2 and solution 5 i.e. at half exhaust mass flow rate

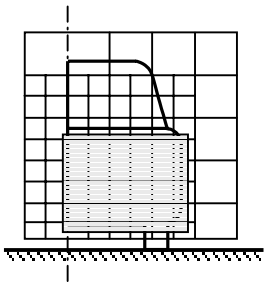

Points consider in the comparison; 30 points at each *x/l*

Figure 7.14 – Assessing the influence of different exhaust mass flow rates

Solution 4 applied an exhaust mass flow rate 77% of an ideal rate for a typical medium size vehicle and was used to look at the extent of the dispersion field downstream of the model vehicle demonstrating a further application of the method. The findings were based on observation alone, as no experimental data was available to make any validations. The results from solution 2, at less than ideal flow rate, showed the scalar to be dispersed by $x/l = 0.51$ or one half vehicle length. However solution 4, at increased flow rate, showed a small concentration field at $x/l = 1.02$. Figure 7.15a shows the changing concentration field from solution 4 with distance downstream of the model vehicle.

The predicted near wake mean recirculation length (mean stagnation point) for the underlying velocity solution, solution D was $x/l = 0.188$ and 0.230 at the model centreline and $z/b = 0.560$ respectively (section 6.3). Figure 7.15 shows a clear change in the concentration pattern upstream and downstream of the mean stagnation point. The concentration field becomes more circular suggesting the longitudinal vortices (section 2.2.1) to be more influential in the dispersion of a gaseous pollutant further downstream. In general the initial development of a longitudinal vortex is complicated by the presence of the recirculation region and it is only downstream of this region that the vortices are free to develop in all directions (section 2.2.1 and section 4.4.2).

Figure 7.15a(i-iv) shows velocity vector plots for one half of the model vehicle illustrating the growth of one of a pair of longitudinal vortices, which develop behind the model. The velocity vector plots show the longitudinal vortex to grow both in size and rotational strength with increasing distance downstream of the model with the potential to disperse pollution outside the bounds of the model base area. It is clear from figure 7.15 that the predicted concentration field extends further downstream than $x/l = 1.02$. However the closing proximity of the wind tunnel collector which was included into the simulated domain (figure 7.1) may have hinder full development of the longitudinal vortex and potentially any further cross-stream dispersion.

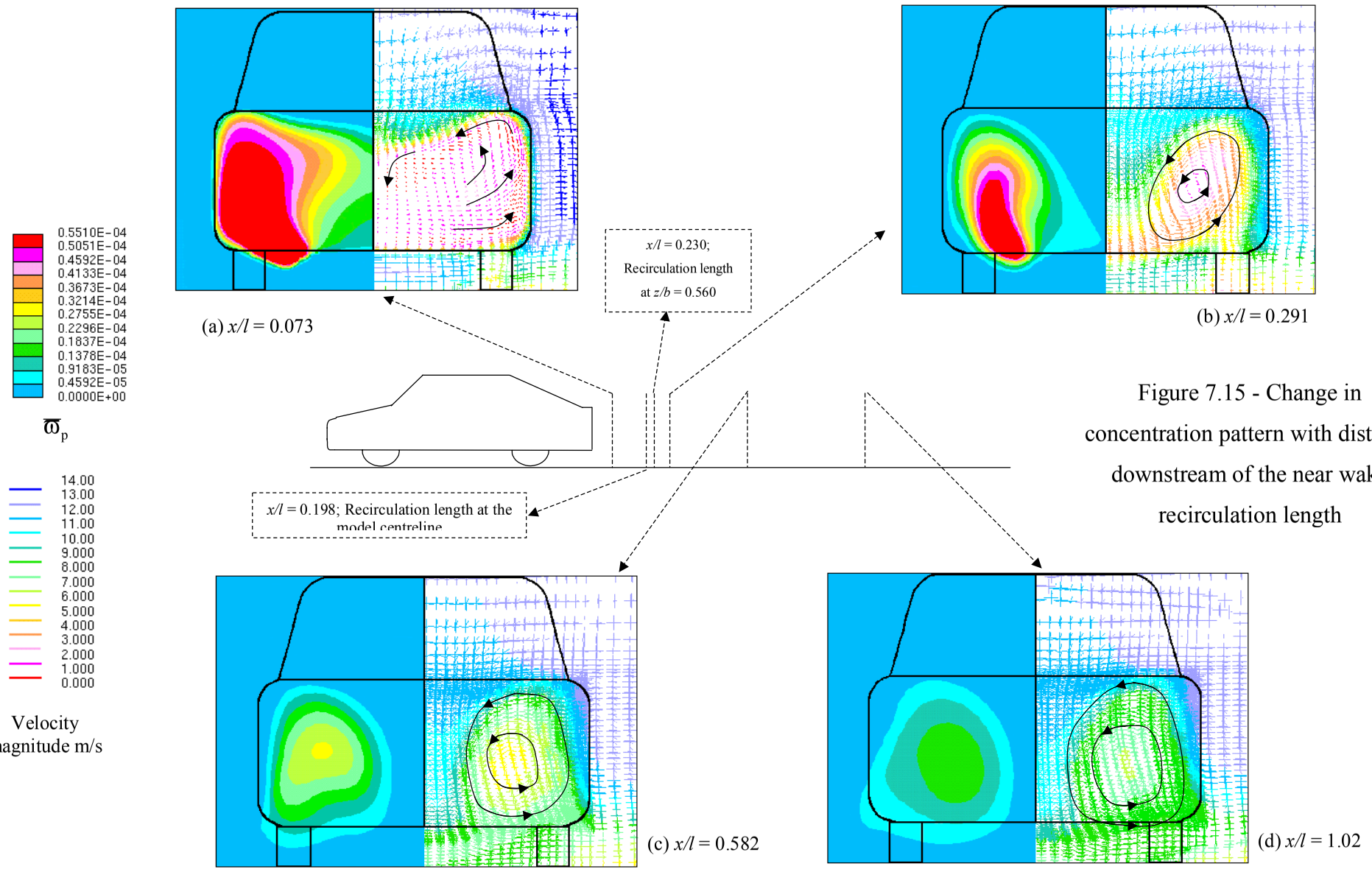

Figure 7.15 - Change in concentration pattern with distance downstream of the near wake recirculation length

Nevertheless based on the knowledge of the general vehicle flow it may be hypothesised that as the longitudinal vortex grows in size with distance downstream of the model the concentration field of a gaseous pollutant will widen despite its weaker strength. This wider dispersion has possible health implications for pedestrians on a roadside therefore the modelling technique demonstrated could be used to examine the levels of pollutant received by pedestrians at the roadside from passing vehicles.

It has been shown that an increase in exhaust mass flow rate changes only the magnitude of the mean concentration field and not the mean distribution. However the experimental study showed the near wake flow and subsequent dispersion field to be inherently unsteady with high-energy fluctuations of the order of 28-280Hz present within the vicinity of the exhaust plume (section 5.4.1). An increase in the exhaust flow rate may contribute to these higher frequency fluctuations thus increasing the energy within the vicinity of the exhaust plume. This in turn may influence the flow within the lower vortex thus increasing its dispersive capacity of the recirculation region. These effects were not observed in the simulations as only the steady state or mean concentration fields were calculated. The influence of the near wake unsteadiness on dispersion is an area for further study (chapter 8).

7.4.2 The influence of vehicle speed on numerical predictions

To assess the influence of vehicle speed on the numerical predictions of dispersion of the scalar and at the same time gaining a brief insight into the influence of vehicle speed on dispersion it was necessary to recalculate the underlying velocity field for an increased vehicle speed. The velocity field was re-calculated for a free stream velocity of 17m/s, which equates to approximately 40mph at model scale i.e. effectively increasing the vehicle speed. The solution restart facility was used with solution D in order to obtain the new solution, to be referred to as solution I. Appendix 4b gives details of solution I including the mean y^+ value and the solution run time in terms of CPU index. The initial, boundary conditions and problem set-up for the velocity and subsequent scalar calculations were the same as described in sections 6.2 and 7.2 respectively. The exhaust mass flow rate was kept the same as

used in solution 2 in order that comparisons with this lower vehicle speed solution could be made. The solution discussed in the following section is referred to as solution 6 details of which are given in Table 7.1.

Figure 7.16 illustrates the effect of increased vehicle speed on the predicted near wake flow structure. The results from velocity solution I are compared directly with solution D (table 6.1). Figure 7.16a(i-ii) shows the magnitude and distribution of the velocity components $\overline{v}$ and $\overline{w}$, at $x/l = 0.146$. While there are slight increases in the magnitude of these velocity components at an increased vehicle speed the overall flow pattern remains the same. The increase in magnitude of both components, $\overline{w}$ and $\overline{v}$, implies an increase in activity within the near wake recirculation region. The unchanging velocity distribution of $\overline{v}$ suggested that the two-tier internal vortex structure of the recirculation region to remain unchanged. Figure 7.16b compares the vortex structure at $z/b = 0.560$ for both vehicle speeds and shows the internal vortex structure to remain unchanged. The increase in internal wake velocity would however result in increased circulation within the recirculation region implying greater mixing and thus more efficient dispersion. The recirculation length at both the model centreline and at the exhaust location, $z/b = 0.560$ remained unchanged at an increased vehicle speed although this may just be a function of the k-ε model itself. However it was suggested by Lane and Stukel (1976) that once the boundary layer separates from the rear end of a vehicle the wake characteristics become insensitive to vehicle speed i.e. at Reynolds numbers typical of road vehicle little sensitivity to changing Reynolds number is expected.

The results of the dispersion simulations from solution 6 and solution 2 are compared in figure 7.17 to assess the influence of increased vehicle speed on the dispersion of the scalar. Figure 7.17a compares the distributions of $\overline{\varpi}_p$ at all x/l and shows the dispersion field predicted by solution 6 to be similar in shape but generally not quite as wide spread. This was thought to be the result of increased turbulent mixing and circulation within the recirculation due to an increase in vehicle speed i.e. increased dilution. For example figure 7.17b shows an increase of approximately 1-2 m/s within the centre of the recirculation region at $x/l = 0.073$ which would increase in the rate of dispersion and thus resulting in a less extensive concentration field.

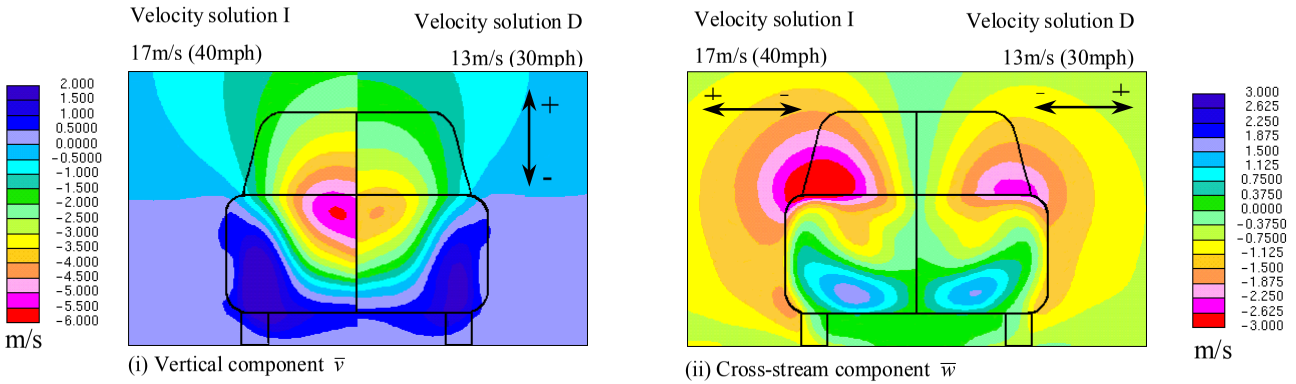

Figure 7.16 – The influence of vehicle speed the near wake flow field.

(a) Comparison of predicted velocity fields at $x/l = 0.146$

(b) Comparison of predicted near wake structure at $z/b = 0.560$

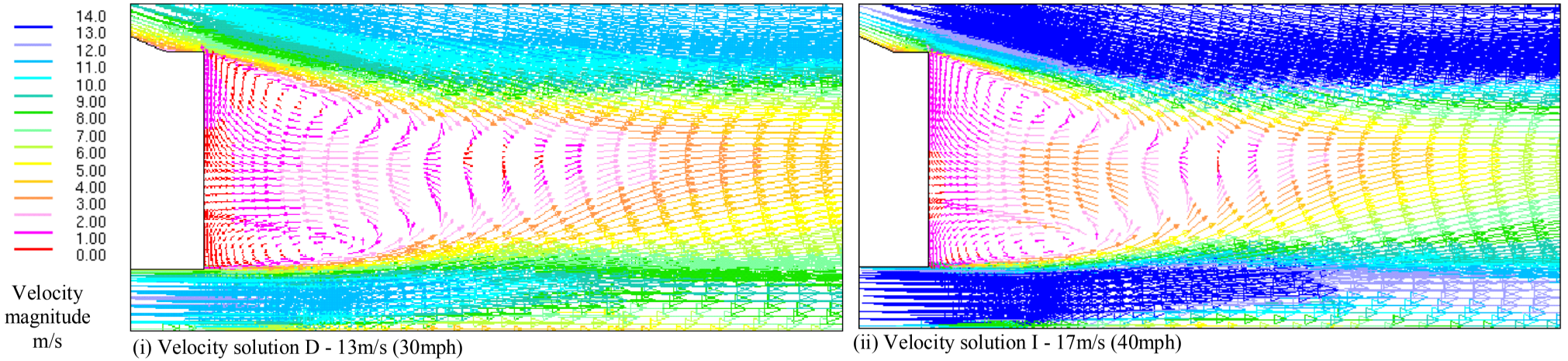

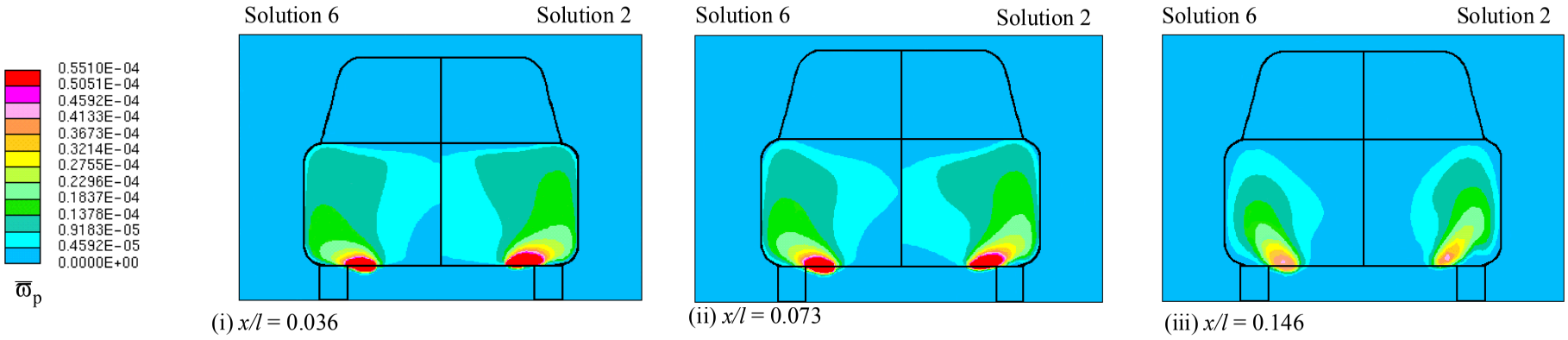

(i) $x/l = 0.036$ (ii) $x/l = 0.073$ (iii) $x/l = 0.146$

(a) Comparison of predicted distributions of $\overline{\omega}_p$

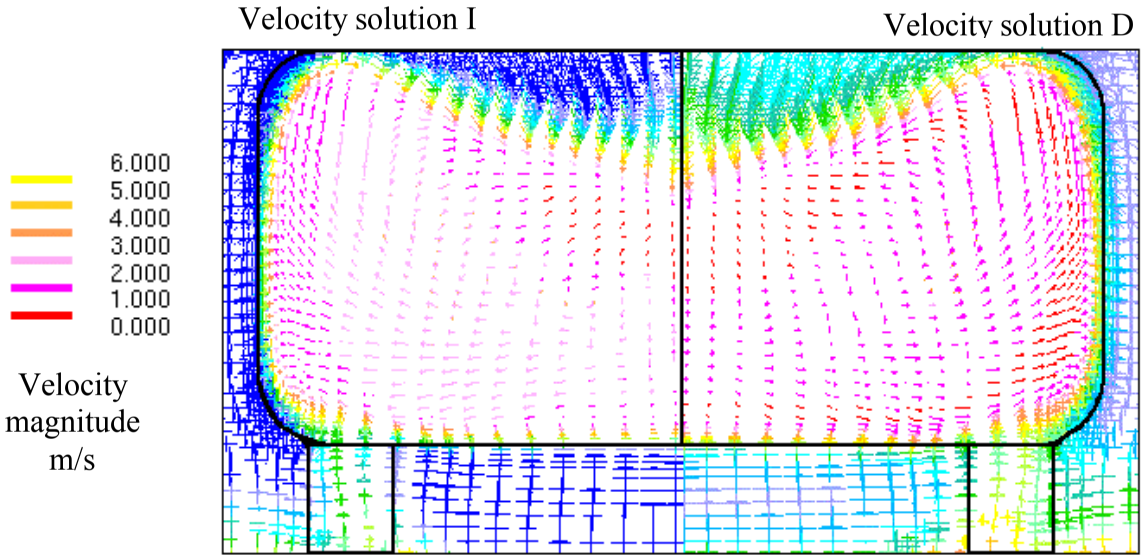

(b) Cross-stream velocity vectors at $x/l = 0.073$

Figure 7.17 – The influence of vehicle speed on the distribution of $\overline{\omega}_p$

Figure 7.18 compares the difference in magnitude of the two predicted concentration fields in terms of the factor difference $F_{\overline{\omega}_p}$ between the predictions.

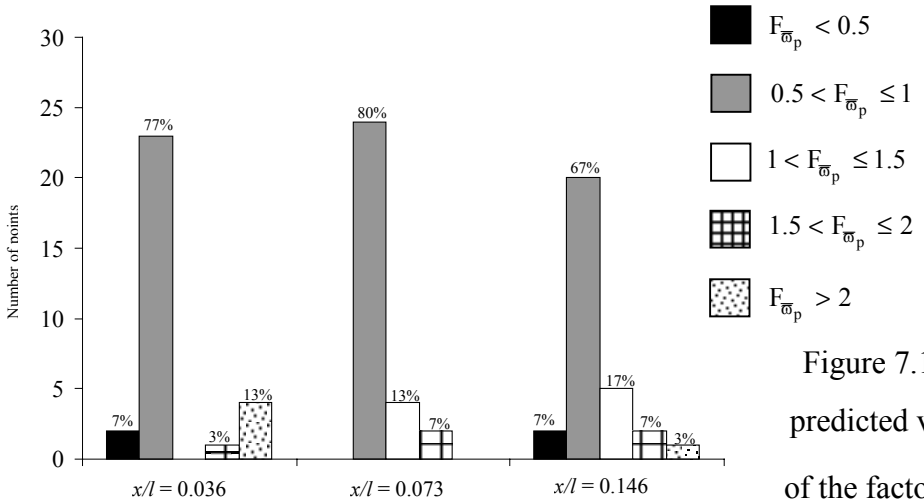

Figure 7.18 – Comparing the predicted value of $\overline{\omega}_p$ in terms of the factor difference between solution 2 and solution 6.

At the higher vehicle speed of 17m/s (40mph) the predicted values of $\overline{\omega}_p$ were generally one-half that predicted at a lower vehicle speed of 13m/s. This implies that at a vehicle speed of 17m/s, increase of 4m/s, the dispersion rate within the near wake recirculation region has approximately doubled. While the results shown in figures 7.16 to 7.18 illustrate the expected result of an increase in vehicle speed while maintaining mass flow rate i.e. increased dispersion, it was not possible to draw and definite conclusions from the one simulation alone. However was nevertheless demonstrated that the technique applied was capable of producing a plausible solution to the criteria given and thus could potentially be used to investigate the influence of vehicle speed on dispersion rate and possibly examine roadside levels of pollutant for different traffic speeds.

The criteria specified for solution 6 were not realistic, as an increase in vehicle speed would always be accompanied by an increase in exhaust mass flow rate thus negating any increased dilution due to increased dispersion. The situation was used purely to demonstrate the influence of increased vehicle speed. In addition the effects of heat and buoyancy in the exhaust flow have not been considered.

7.4.3 Further visualisation of dispersion character using "Particle Tracking"

The results discussed in following section demonstrate the use of a post-processing[7.3] technique known as "Particle Tracking" as an additional method of visualising the dispersion of a pollutant (Computational Dynamics, 1998a,b). The technique was not used to model the particle pollution but visualise the path of a mass-less particle using the existing velocity field to gain further insight into the dispersion character within the near wake recirculation. Fine particle pollution emitted from road vehicles is generally sub-micron in size (<1μm diameter) and therefore may be considered to behave like a gas or as mass-less particles and thus rely solely on the flow field for their dispersion. The objective of this short study was to show the potential of this application in further visualising the behaviour of a pollutant within (mass-less particles) in the near wake of a vehicle, and in particular the trajectory of a mass-less particle, as fine particle pollution is a major concern to health (chapter 1). Additional insight in the dispersion character of the recirculation region was also obtained.

The method of Particle tracking is a passive technique that uses a 'virtual particle', which has no influence on the bulk flow field and enables the user to calculate and visualise the track of this particle based on the existing flow data. The effects of body forces on the particle i.e. in gravitational or rotating fields may be accounted for by assigning a density and volume to each particle but were not considered here.

The velocity solution D (Appendix 4b and section 6.3.1) was used as the foundation for the investigation because of its good agreement and representation of the near wake flow field of the model considered. The release area of particles covered the equivalent as the representative exhaust used in the experimental study (chapter 5) and incorporated the cells used for fluid injection technique (section 7.2.3). The technique dictated that the particles be released from the node points of each selected cell (Computational Dynamics, 1998b). Figure 7.19 gives details of release points for the mass-less particles with each point labelled and referred to by letter in the discussion.

[7.3] Post-processing involves the manipulation and display of output data from a numerical simulations performed.

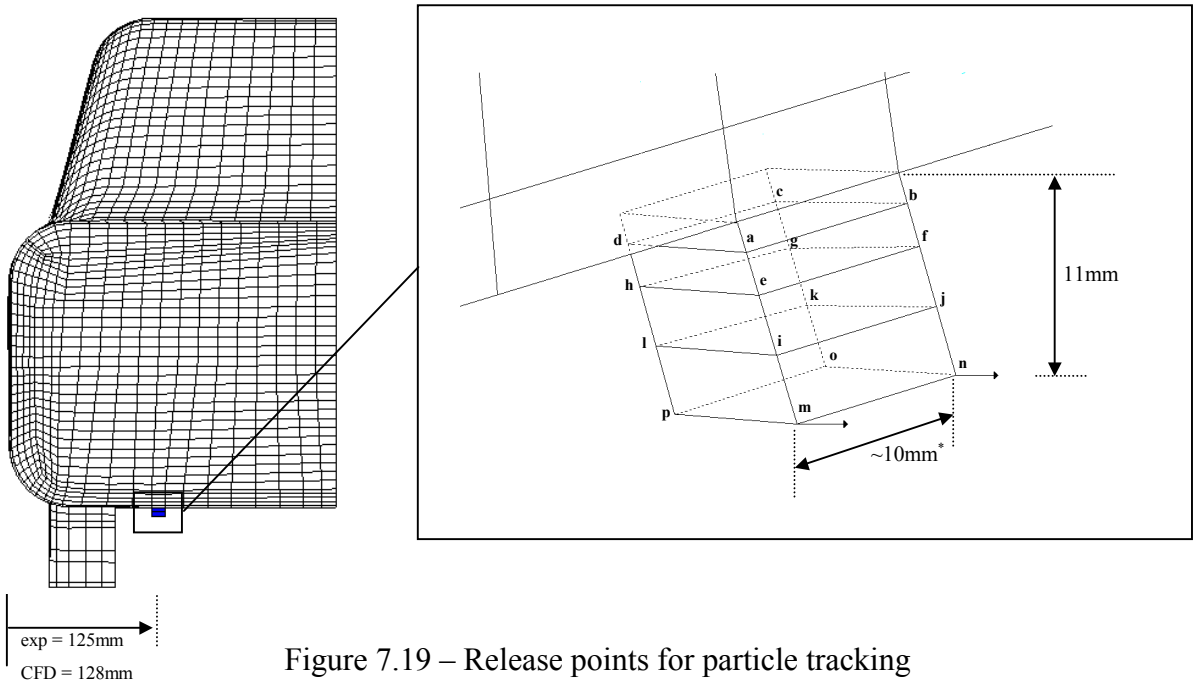

Figure 7.19 – Release points for particle tracking

* The cells were not square so the width varied slightly

Particles released from points a-h tended to be drawn up into the recirculation region and circulated before exiting towards the trailing edge of the region whereas particles released from point's g-p passed below the recirculation region following the flow within the shear layer. However the trajectories of particles within these groups tended to vary. Figure 7.20a (i-ii) shows the trajectory of particles released from point's b and e to be different. The particle released from point b was drawn into the recirculation region through the lower vortex, circulated within the lower and upper vortices twice before exiting the region via the lower vortex. The particle released from point e was also drawn in through the lower vortex but remained in the upper vortex where it was circulated twice before exiting from the top of the region via the upper vortex.

Particles released from the remaining upper points, a, c, d, f, g, h all varied in their trajectory and exit point from the recirculation region but were are all drawn into the recirculation via the lower vortex, the same dispersive mechanism shown during the experimental study (chapter 5). Figure 7.20b illustrates two examples of particle trajectories from the lower points i.e. points i-p where none of the particles released were drawn into the recirculation region but instead carried away by the shear layer

emanating from the lower edge of the model base. All the particles released from points i-p followed a similar path with the only difference being the distance the particle was swept upwards as the lower shear layer converged with the upper shear layer just past the free stagnation point (section 2.2.1 and 4.5).

The observations made from figure 7.20 and from the study in general suggest that the release height to be a significant influence on the trajectory of a particle. The current investigation showed a difference of just 4mm in release height (vertical difference between e and i) resulted in a particle either being drawn up into the recirculation region or passing it by. To investigate further the influence of release point on particle trajectory individual particles were released from different locations along the width of the model base. Figure 7.21a(i-iii) shows example trajectories from 3 different release points along the model base. All points were at the same distance below the model base only the distance from the model centreline was varied. Velocity vector plots (from solution D) were to compared against the particle trajectories where it was shown that the change in particle trajectory with distance from the model centreline was the result of the changing near wake structure with distance from the model centreline (figure 4.12 and 6.9). Figure 7.21b shows the trajectories of all particles released along the width of the model base further illustrating the variation in particle trajectory with release point and the significance of the near wake recirculation region as a dispersing mechanism.

After leaving the recirculation region, or passing beneath the particles trajectories tend to converge and take a similar path onward downstream, figure 7.22. None of the particles left the recirculation region through sides or top of the region but when considering they are mass-less this was not surprising as the faster flow within the shear layers surrounding the near wake would carry any escaping particle quickly away downstream.

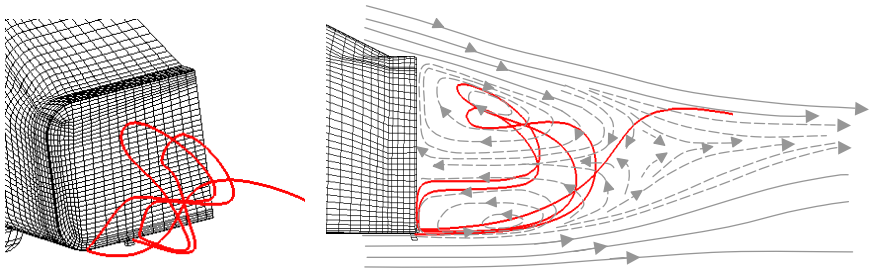

(i) Release point b

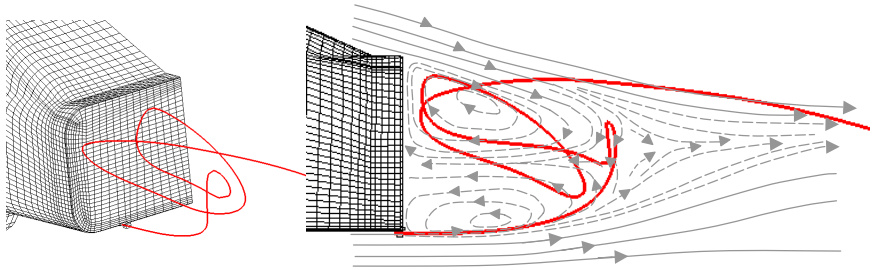

(ii) Release point e

(a) Example particle tracks from upper release points

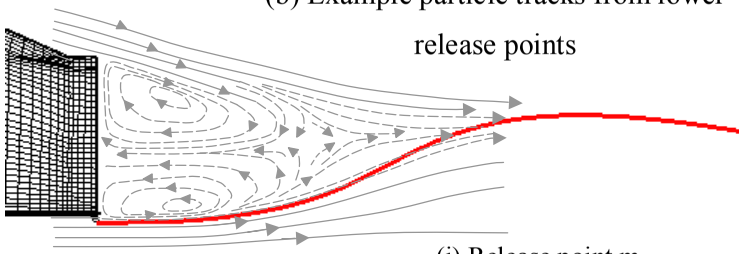

(i) Release point m

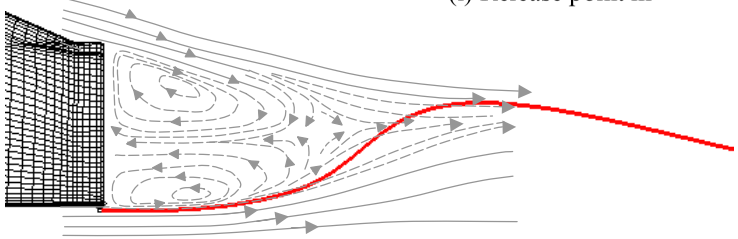

(ii) Release point j

(b) Example particle tracks from lower release points

Figure 7.20 – Particle trajectories at a vehicle speed 13m/s.

Refer to figure 7.19 for release points

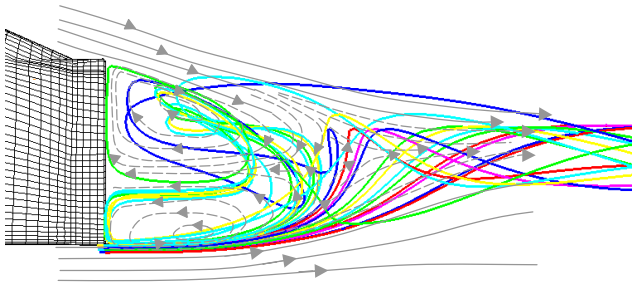

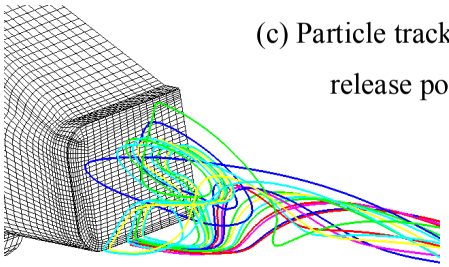

(c) Particle tracks from all release points

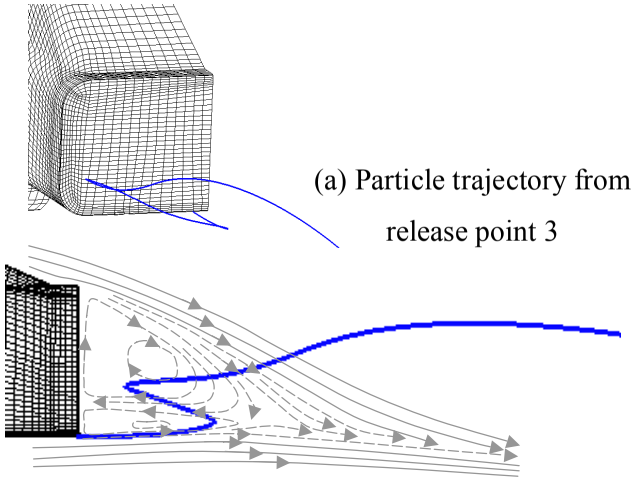

(a) Particle trajectory from release point 3

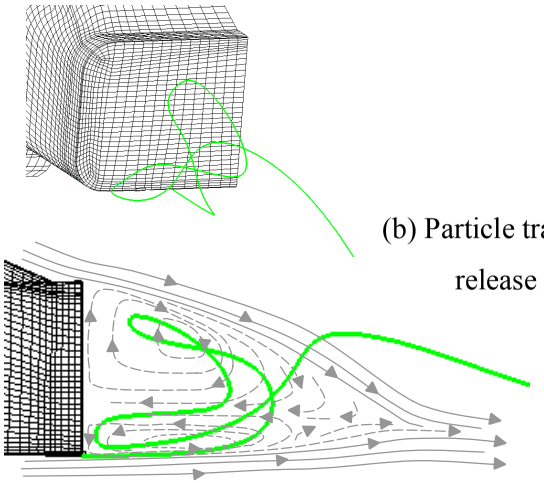

(b) Particle trajectory from release point 7

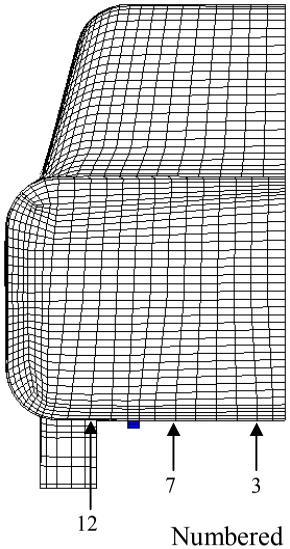

Numbered release points

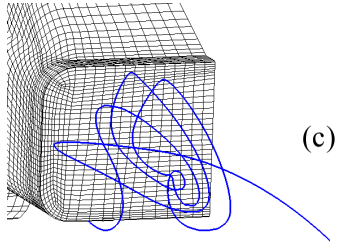

(c) Particle trajectory from release point 12

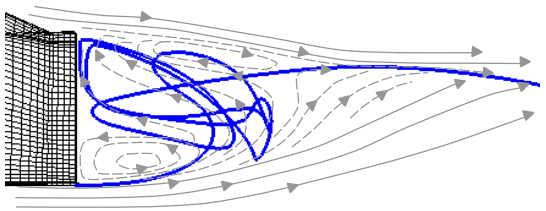

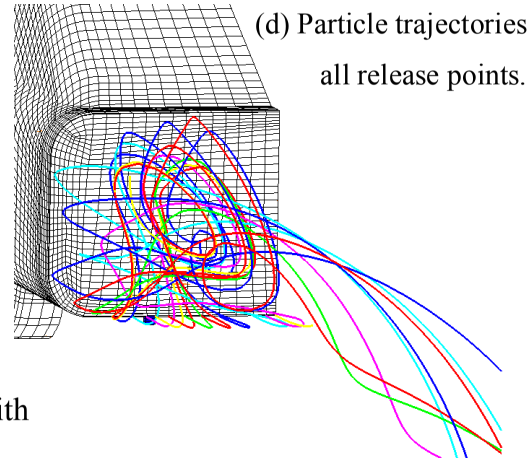

(d) Particle trajectories from all release points.

Figure 7.21 – Changing particle trajectory with distance from the model centreline.

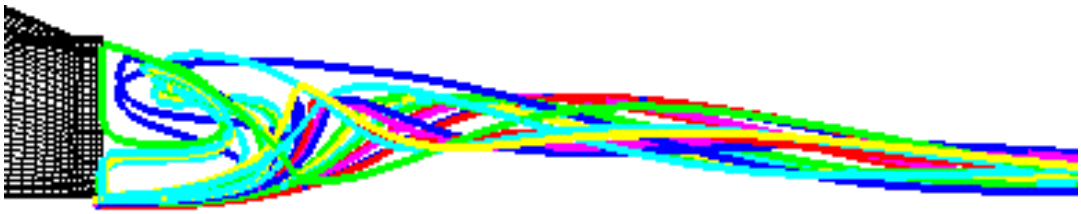

(a) Side view – all particle

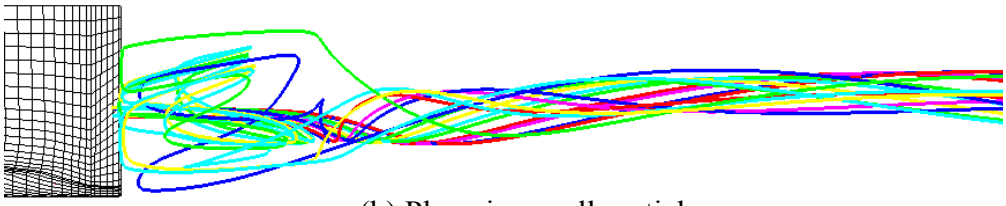

(b) Plan view – all particle

Figure 7.22 – Downstream particle trajectories

The current investigation did not show the stream longitudinal vortices to have any influence over the particles which may have been because the close proximity of the wind tunnel collector to the rear of the model vehicle, Appendix 2a, hindered the development of the longitudinal vortices further downstream. In addition the imposed centreline symmetry may have prevented any potential cross-stream spread of particles i.e. across the model centreline.

Observations made in section 7.4.2 showed vehicle speed to have no significant influence on near wake structure of the model vehicle in question and therefore the concentration distribution of the scalar to remain unchanged. The mass-less particles considered in the current investigation were also assumed to behave like a gas and therefore it was assumed that their trajectory would also remain unchanged regardless of vehicle speed. However increased vehicle speed might have an influence on particles, which do, have a small but significant mass. Hider (1998) showed particles of varying diameter and mass to travel different distances before coming to rest; maximum diameter of 20μm. It may be hypothesised that the trajectory of larger particles will be influenced by vehicle speed in that larger particles may not remain inside the recirculation region as shown but escape on a

different trajectory. Larger particles may also stay aloft longer at increased vehicle speed.

The observations discussed above were all based on a time-averaged near wake flow structure. However in reality the near wake region is inherently unstable and while the current investigation gave an insight into the anticipated path of a mass-less particle the investigation did not take account of near wake instability. Due to the small size and gaseous behaviour of the particles under consideration it is likely that the unsteadiness in the near wake would cause mass-less particles to be bounced around during the time they were recirculated within the recirculation region. The next stage in the study would therefore be to conduct time-dependent or transient simulations of the flow field. The most the desirable but most computationally expensive approach would be to use either Direct Numerical Simulations (DNS) or Large Eddy Simulations (LES). The effects of turbulence on the trajectories of particles may also be modelled via stochastic tracking techniques.

7.4.4 Stage 2: Further assessment – Conclusions

A further assessment was made into the application of STAR-CD and the fluid injection technique for simulating the dispersion of pollution behind a model vehicle. The influence of changing vehicle speed and exhaust mass flow rate were examined i.e. a greater exhaust mass flow rate would expect higher concentration fields and an increase in vehicle speed but maintaining the mass flow rate would result in greater dispersion. An increase of 10mph-model vehicle speed reduced the concentration levels within the recirculation region by a factor of 2 due to an increase in velocity magnitude thus increasing circulation and effective dispersion. A change in mass flow rate showed the magnitude of concentration to change accordingly but with the overall dispersion pattern remained essentially unchanged. Concentration predictions at double and half the original mass flow rate did not result in a magnitude difference of 2 and 0.5 as might have been anticipated but of approximately 3 and 0.6. Nevertheless the results presented demonstrate the potential in using the method for the investigation of such factors as exhaust mass flow rate on dispersion and concentration field but does require further and more detailed investigation and in particular the use of time-dependent calculations for the

underlying velocity field. In addition using the results of solution 5 to look at the extent of the concentration field downstream of the model demonstrates how CFD can be used as an investigative tool where experimental data is not available, providing that predictions where possible are successfully validated.

In addition the application of a particle tracking technique using mass-less particles demonstrated an alternative method to visualising the dispersion character of the recirculation region. The study showed how the positioning of the exhaust and the general release height could influence of dispersion patterns of a pollutant within the near wake. For the current study a difference in release height of 8mm dictated whether the mass-less particle was drawn into the near wake recirculation region. For a full size vehicle of 1.42m high (Rover 25) this equates to approximately 28mm. This could influence exhaust location if maximum dispersion were required. However it should be remembered that a fixed ground condition was applied in the current study and the flow under the vehicle may not be as realistic as it could be. Nevertheless it showed how sensitive exhaust location was to effective dispersion and how such a technique as particle tracking or even the fluid injection technique could be used to investigate the influence of exhaust size and location on dispersion i.e. undesirable effects due to bad location could be avoided. In addition the particle tracking technique could be used to examine the levels of fine mass-less particles reaching the roadside as a consequence of dispersion downstream of a road vehicle.

7.5 Chapter conclusions

The primary aim of the investigation discussed in the preceding chapter was to assess the feasibility of using CFD in the simulation of pollution dispersion within the near wake of a model vehicle. The objective was to demonstrate the approach as an alternative technique to dispersion modelling behind a road vehicle without the need for the limiting assumptions applied in previous methods i.e. the complete wake flow field could be simulated (chapter2, section 2.5). While it is not realistic to make a definitive statement on the success of the simulations based on the solutions presented it was nevertheless shown that CFD code STAR-CD could be applied to adequately model the measured mean dispersion field within the near wake of a

model vehicle. However from the results presented it was clear that the use of steady state calculations were not appropriate for the current application. The measured mean concentrations used in the validation were established from an inherently unsteady and constantly changing concentration field whereas the numerical results were mean concentrations calculated based on unchanging flow pattern under a given set of boundary conditions obtained through a number of numerical iterations i.e. steady-state. As a consequence peaks in concentration captured in the measured mean flow concentration field would not be reflected in the numerical predictions i.e. the predictions mean concentrations are based only on calculations of constant recirculation not unsteadiness therefore resulting in under prediction particularly in areas of measured local maximum concentration. It was clear therefore that the underlying velocity solution for such dispersion simulations should be calculated using time dependent techniques i.e. LES or DNS. This was the primary reason no further solutions for numerical dispersion were obtained as it was felt no significant improvement would be made on the current predictions. While it might be questioned why time-dependent techniques were not used from the outset the aim of the complete work was to determine whether CFD could be used to simulate the dispersion of a pollutant in the near wake of a model vehicle. It was therefore considered more appropriate, and common place, to begin with the simulation and validation time-averaged flow and dispersion field. The relative successes of the current work can now be used as a foundation for further time-dependent studies.

Taking into consideration the need for time dependent calculations it was further demonstrated that the CFD, in this case STAR-CD could be used to assess primary factors that influence dispersion i.e. exhaust flow rate and vehicle speed. Using simple examples the effectiveness of the technique was illustrated. With further assessment and the use of time dependent calculations for the underlying velocity solution such a technique could be applied to gain a more detailed understanding of local dispersion within the vicinity of a road vehicle and assess the concentration levels of various pollutants at the roadside. This information in turn could be used to help make clearer the associations between vehicle pollution and various health issues.

The additional investigation using mass-less particles showed further application of STAR-CD in obtaining information on pollutant dispersion from an existing velocity field calculation. The technique would be a useful and simple tool for investigating the influence of exhaust location, size and shape on the subsequent dispersion patterns. The release of many mass-less particles would approximate the release of a cloud of gaseous pollutant.

Chapter 8: Conclusions and further work

8.1 Introduction

The aim of the following chapter is to set out the main findings and conclusions of the study detailed in chapters 4-7. These are summarised in the form of a list, which is followed by recommendations for further work. The overall achievements of the project are also discussed commenting on the success in meeting the stated project aim and objective.

While the main aim of the complete study was to demonstrate the feasibility of using CFD to model the dispersion of a pollutant within the near wake of a model vehicle it is imperative to recognise the importance of the individual stages in the study that were necessary to achieve this aim, refer to figure 1.1. It was for this reason that care was taken in detailing and assessing each stage of the study in order to determine its relative success before continuing to the next stage.

8.2 Conclusions

8.2.1 Near wake velocity and tracer gas dispersion measurements

Wake velocity measurements were made using Particle Image Velocimetry (PIV) and hot-wire anemometry to obtain essential data for the validation of numerical simulations and to gain insight into the near wake flow of the MIRA reference vehicle, 33% scale, in the fastback configuration. The information gained on the character of the mean flow and its structure was useful in understanding the measured dispersion character of the region. PIV was used to obtained detailed flow information within the near wake recirculation region where hotwire measurements would otherwise be unreliable. A three component hot-wire anemometer was used to obtain flow information downstream of the recirculation region. The techniques

applied are commonplace for this type of measurement and produced good data that gave a clear representation of the mean flow field under investigation. Flame Ionisation detectors (FIDs) were used to measure the dispersion of a passive gaseous pollutant in the near wake of the MIRA reference vehicle. The tracer gas was released via a representative exhaust fixed to the underside of the model away from the centreline. The tracer gas measurements not only provided essentially data for validation of the numerical simulations of the same region but also gave insight into the dispersion character of the near wake recirculation region of the model considered. The use of FIDs 33% scale for detailed measurements in the near wake of a road vehicle is not common therefore the experiment showed the potential in using FIDs in the investigation of dispersion fields close behind a road vehicle. Flow visualisation using smoke allowed the unsteadiness in the near wake to be observed.

The main conclusions drawn from both the experimental studies are as follows:

Near wake velocity measurements of a model vehicle

1. The mean near recirculation of the MIRA reference vehicle (33%, fastback configuration) had a two-tier contra-rotating vortex structure.
2. At the model centreline the upper internal vortex was larger and more dominant than the lower vortex with a low velocity core occurring at $x/l \sim 0.079$ and $y/H \sim 0.298$. The lower vortex was smaller but extended further downstream with its core occurring at $x/l \sim 0.087$ and $y/H \sim 0.174$. Neither vortex extended upstream to the model base with the flow splitting into the two vortices occurring at $\sim x/l = 0.036$. As a consequence there was a region of positive streamwise velocity, $+\overline{u}$ very close to the model base albeit low in magnitude.
3. The relative size and dominance of the internal vortices changed with distance from the model centreline. At $z/b = 0.560$ the vortices were shown to become more equal in size and extend farther upstream towards the model base than observed at the model centreline.
4. The mean recirculation length at the model centreline, based on the location of minimum $\overline{u}/U_{\infty}$ was measured at $x/l = 0.166$. While no estimate could be

made of the recirculation length at distance from the model centreline i.e. z/b = 0.560 it was clear that its length was increased as a direct result of the change in vortex structure.

5. The change in recirculation region structure with distance from the model centreline was generally caused by three dimensional character of the flow away from the model centreline and influences from the flow around the sides and from underneath the model.
6. Flow visualisation using smoke showed the near wake recirculation region to be highly unsteady. Instantaneous velocity vector maps showed the "real" recirculation region structure to be more chaotic and consist of many smaller vortices demonstrating that the neat organised mean two-tier vortex structure does not to exist over short periods of time.
7. The unsteadiness was believed primarily due to the shedding of these smaller vortices from the free stagnation point further suggested by a peak in streamwise turbulence intensity at that same point.
8. While the use of a fixed floor condition in both experimental studies did not allow the simulation of the relative movement between the vehicle and the road it enabled the study, and thus subsequent numerical simulations to remain simple and controlled.

<u>Tracer gas dispersion measurements in the near wake of a model vehicle</u>

1. The use of FIDs and the novel approach of releasing tracer gas through a representative exhaust proved effective techniques in the measurement of the dispersion field in the near wake of a model vehicle.
2. While practical restrictions limited the sample time of measurement it was believed, from the results of spectral analysis, to be sufficient for the purposes of the study.
3. The two-tier vortex structure within the vicinity of z/b = 0.560 was shown to be the primary dispersion mechanism of tracer gas released from a representative exhaust at z/b = 0.560. Tracer gas from the exhaust plume was drawn up into the recirculation region by the lower vortex and recirculated via the upper vortex. The "pick-up" region of the lower vortex was estimated to be $\sim x/l$ = 0.146.

4. Dispersion within the recirculation was due to recirculation within the vortex structure and general flow field unsteadiness.
5. The distribution of the mean concentration field showed rapid dispersion away from the source with concentration values falling to 7% of the maximum source value within 50mm of the source. Low values of concentration within the recirculation region were thought to be the result of rapid dispersion and the fact that only a percentage of tracer gas was drawn up from the exhaust plume.
6. The time-dependent near wake flow field was shown to be highly unsteady thus also implying a highly unsteady and changing concentration field. Spectral analysis of the measured concentration data showed low to moderate energy frequency fluctuations within the range ~ 0.1 – 3**S** or ~3 – 83Hz within the recirculation region. A peak of ~ 1.5-1.7**S** or 42-47Hz within the vicinity of the mean recirculation length implied both the recirculation region and tracer gas concentration to fluctuate at these frequencies around x/l = 0.166.
7. Flow visualisation using smoke showed a build up and purge of pollutant at approximately 1-3 second intervals.
8. For the full-scale equivalent of the model tested the near wake and thus the concentration fluctuations would occur from 1-28Hz. While this range was wide due to general unsteadiness in the region the lower end of the frequency range was close to the breathing cycle of ~0.5Hz. The frequencies of fluctuations within the wake of a vehicle generally increase with change in base slant angle α from a fastback to squareback vehicle configuration. The results of the current study therefore suggest that for the squareback equivalent of the model under investigation the near wake recirculation region would fluctuate at frequencies even closer to or spanning the breathing cycle. This has implications on the health of pedestrians at the roadside.

8.2.2 Numerical simulations of near wake velocity and tracer gas dispersion

Two numerical studies were conducted to assess the feasibility of using CFD to model the dispersion of a passive pollutant within the near wake of a model vehicle. While CFD has been used on a number of occasions to simulate the wake flow of

road vehicles its application in the detailed simulation of the near wake recirculation region and the dispersion of a passive scalar within this region was new. A fluid injection technique was used to introduce the passive scalar into the flow field and the standard scalar transport equation solved to obtain the dispersion field.

The main conclusions drawn from both computational studies were as follows:

Numerical simulations of the near wake of a model vehicle

1. Using four variants of the k-ε turbulence model and both low and high order differencing schemes the ability of STAR-CD at simulating the near wake velocity field of a the MIRA reference vehicle was demonstrated.
2. All solutions predicted the structure and relative size of the vortices within the recirculation region at the model centreline but none of the solutions made accurate predictions of the upstream extent of the vortices close to the model base. As a consequence all solutions failed to predict the small region of positive streamwise velocity, $+\overline{u}$ very close to the model base observed in the measured flow field.
3. The vortex structure at z/b = 0.560, and in particular the lower vortex was shown through experiment to have a primary influence on the initial dispersion of tracer gas therefore prediction at this local was considered more critical for the purposes of this initial investigation. Predictions of the flow structure at z/b = 0.560 where in better agreement with the measured flow field compared with predictions at the model centreline. Nevertheless the general dispersing mechanisms of the flow close to the model centreline were still adequately represented.
4. All the numerical solutions obtained were considered to be in good agreement with the measured flow field with over 60% of all predicted velocities i.e. $\overline{u}$, $\overline{v}$ and $\overline{w}$ falling within σ of their equivalent experimental value with the region of recirculation i.e. $x/l \leq 0.218$.
5. An increase in mesh resolution within the recirculation region or improved numerical accuracy offered by higher-order differencing schemes did not necessarily result in improved predictions. Mesh dependency was believed to

be the reason for poorer predictions using a refined mesh and while mesh independency is desirable it was felt that no benefit would be gained by trying to achieve this as an adequate representation of the flow field had already been demonstrated. Moreover it was felt that given the limitations of a steady state solution applied to unsteady phenomenon using a more powerful computer would make no significant improvement on the solution already achieved.

6. Despite some disagreement with the measured flow field the results of the numerical study showed that even using the simplest turbulence model/differencing scheme combination it was possible to achieve good agreement with measured mean flow field and reproduce the main features within the near wake flow field without the need for detail changes to any modelling parameters. From a 'users' point of view this would enable a relatively inexperienced modeller to obtain a solution capturing the main features of the flow field under investigation with relative ease.
7. The solution used as the foundation of the numerical simulations of dispersion was the non-linear k-ε model with upwind differencing chosen not for its numerical accuracy i.e. upwind differencing is only first order accurate, but for its good representation of the flow field and relatively short run time in comparison with the higher order solutions.

Simulation of tracer gaseous dispersion in the near wake of a model vehicle

1. Predictions of the mean concentration field of a passive scalar within the recirculation region of a model vehicle were in fair agreement with the experimental results. However peaks in concentration captured in the measured mean flow field, the result of pollutant build-up due to unsteadiness were not reflected in the numerical predictions resulting in an overall under prediction of the mean concentration field. This was believed to be primarily due to the application of steady state calculations to an inherently unsteady flow field. The measured mean concentration field was established from an inherently unsteady and constantly changing concentration field whereas the numerical results were calculated mean concentrations based on an unchanging flow pattern obtained

over numerous numerical iterations i.e. steady-state therefore peaks in mean concentration due to build-up were not captured. It therefore became clear that the use of steady state calculations were inappropriate for the current application. As a consequence of these findings no further numerical solutions were obtained for comparison with the measured concentration field as it was felt no significant improvement would be made on the current predictions using steady state calculations. Real improvement could only be made through unsteady simulations, which were unfeasible in the scope of the current project.

2. In light of the inherent instabilities within the near wake concentration field it might be questioned why time-dependent techniques were not used from the outset. However the aim of the complete work was to determine whether CFD could be used to simulate the dispersion of a pollutant in the near wake of a model vehicle. Therefore it was considered more appropriate, and common place, to begin with the simulation and validation of the time-averaged flow field. The relative successes of the current work may now be used as a foundation for further time dependent studies.
3. With consideration of these shortfalls a further assessment of the method was conducted to demonstrate that CFD could be used to assess primary factors influencing dispersion, for example increased vehicle speed. Through simple examples the effectiveness of the technique was demonstrated and with further assessment using time-dependent velocity calculations has the potential to be used as a tool to understand local dispersion within the vicinity of vehicles.
4. Finally the application of particle tracking using mass less particles to further visualise dispersion character revealed the sensitivity of pollutant release position on its subsequent trajectory. A change in release height of just 12mmm model scale made the difference to whether the pollutant was drawn into the recirculation region or just passed it by through the surrounding shear layers.

8.3 Final comments and further work

The aim of the project was to assess the feasibility of using a commercial code such as STAR-CD to simulate the dispersion of pollutant in the near wake of a model vehicle. While the results of the study showed a fair degree of success in the representation of the mean concentration field the use of time dependent calculations for the underlying velocity is clearly required. With further investigation and numerical simulations it might be possible to obtain a more accurate mean concentration field however there would be no real gain in doing so as the true flow and concentration fields are inherently unsteady.

The objective was to demonstrate the use of CFD as an alternative approach to modelling dispersion behind a model road vehicle without the need for the limiting assumptions applied in previous methods and to demonstrate its potential as an investigative tool (chapter2, section 2.5). Despite the shortcomings described the potential of using STAR-CD as an investigative toll has been clearly demonstrated Unlike the theory of Eskridge and Hunt (1979), which is used as the basis for many wake and dispersion models, it was not necessary to assume a velocity deficit downstream of the model in order to represent the wake flow close to the model. The numerical techniques used in the current study allowed the complete wake flow, the near and far field to be modelled in some detail. However the assumption of centreline symmetry was applied which essentially enforces flow symmetry at model centreline thus suppressing any tendency for the simulated concentration field to spread to the other side of the wake as observed in the flow simulation study (Section 5.3.1). Nevertheless the results and validation show the main time-averaged features of the near wake structure to be adequately represented with little alteration to any of the modelling parameters. The technique used to introduce and simulate the dispersion of a passive gaseous pollutant was shown to be simple and effective and allowed a tracer to be release at a realistic exhaust location. While the results from the numerical dispersion fields showed the need for time dependent calculations the method was nevertheless shown to have the potential of being used to investigate and understand in more detail the dispersion of pollution close behind a road vehicle and possibly assess the concentration levels, at the road side of different pollutants

released. Using the approach of fluid injection in conjunction with time dependent techniques such as Direct Numerical Simulation (DNS) or Large Eddy Simulation (LES) has the potential for further investigation of the unsteady effects of pollutant dispersal in particular those observed in the frequency range close to that of the breathing cycle.

Further potential of the method was demonstrated through the simulation of primary factors that influence dispersion such as exhaust flow rate and vehicle speed. With further development the technique could be applied to gain a more detailed understanding of local dispersion within the vicinity of a road vehicle and assess the concentration levels of various pollutants at the roadside. This information in turn could be used to help make clearer the associations between vehicle pollution and various health issues. The additional investigation using mass less particles showed a further application of STAR-CD at obtaining information on pollutant dispersion from an existing velocity field calculation. The technique would be a useful and simple tool for investigating the influence of exhaust location, size and shape on the subsequent dispersion patterns. The release of many mass less particles would approximate the release of a cloud of gaseous pollutant.

8.3.1 Further work

The findings and achievements of the current study open up many opportunities for further work.

- The applications of time-dependent techniques are required to further assess the applicability of CFD in simulating the dispersion of a pollutant behind a model vehicle.
- To make simulations more realistic the effects of heat and buoyancy in the exhaust plume need to be included in addition to the simulation of a moving ground. This would require substantial new experimental work to obtain data for validation.
- A time-dependent study using Large Eddy Simulations (LES) to simulate and further investigate the unsteady character of the near wake of a road vehicle

and in particular at frequencies close to the breathing cycle. However this would require substantial computer resources.

- To compliment a numerical time-dependent study a more detailed experimental programme need be conducted to obtain more detailed spectral information of the flow field.

References

Abbott, M. B. and Basco, D. R. (1989), *'Computational Fluid Dynamics: an introduction for engineers',* Longman, ISBN 0470213167.

Ahmed, S.R. (1981), *'Wake structure of typical automobile shapes',* Transactions of ASME, Journal of Fluids Engineering, **103**, (162-169).

Ahmed, S. R. (1983), *'Influence of base slant on the wake structure and drag of road vehicles',* Transactions of ASME, Journal of Fluids Engineering, **105**, (429-434).

Ahmed, S. R. and Baumert, W. (1979), *'The structure of wake flow behind road vehicles',* Aerodynamics of Transportation, ASME-CSME Conference, Niagara Falls, June 18th-20th, (93-103).

Ahmed, S.R., Ramm, G. and Faltin, G. (1984), *'Some salient features of the time-averaged ground vehicle wake',* SAE International Congress and Exposition, Detroit, Michigan, 27th February – 2nd March (SAE 840300)

Amtec (2001), *'Tecplot Version 9.0-2-3',* Amtec Engineering Inc (1988-2001).

Anderson, J. D. (1991), '*Fundamentals of aerodynamics'*, McGraw Hill

Baker, C. J. (1996), *'Outline of a novel method for the prediction of atmospheric pollution dispersal from road vehicles',* Journal of wind Engineering and Industrial Aerodynamics, **65**, (395-404).

Baker, C. J. (2001), *'Flow and dispersion in ground vehicle wakes',* Journal of Fluids and Structures', **15**, (1031-1060).

Basara B., Plimon, A., Bachler, G. and Brandstatter, W. (1996), *'Calculation of the flow around a car body with various turbulence models',* MIRA International Vehicle Aerodynamics Conference, Birmingham, UK.

Bearman, P. W. (1984), *'Some observations on road vehicle wakes',* SAE paper 840301.

Bearman, P. W., Davis, J. P. and Harvey, J. K. (1983), *'Measurement of the structure of road vehicle wakes',* International Journal of Vehicle Design, Special Publications SP3, (493-499).

Bearman, P. W., De Beer, D., Hamidy, E. and Harvey, J. K. (1988), *'The effect of a moving floor on wind-tunnel simulations of road vehicles',* SAE paper 880245.

Bendat, J. S. and Piersol, A. G. (1980), *'Engineering applications of correlation and spectral analysis''* John Wiley and Sons, ISBN 0-47105887-4.

Bendat, J. S. and Piersol, A. G. (1986), *'Random data: analysis and measurement procedures'* 2nd Edition, John Wiley and Sons, ISBN 0-471-04000-2.

Benson, P. E. (1979), *'CALINE 3 – a versatile dispersion model for predicting air pollution levels near highways and arterial streets',* Report FHWA/CA/TL-79/23.

Berger, E., Scholz, D. and Schumm, M. (1990), *'Coherent vortex structures in the wake of a sphere and circular disc at rest and under forced vibrations',* Journal of Fluids and Structures, **4**, (231-257).

Boris, J. P. and Book, D. L. (1973), *'Flux corrected transport I: SHASTA, a fluid transport algorithm that works',* Journal of Computational Physics, **11**, (38-69).

Boussinesq, T. V. (1877): Mem. Pre. Acad. Sci., 3rd Edn., Paris XXIII (46).

Brown, M. A., Baxendale, A. J. and Hickman, D. (1998), *'Recent enhancements of the MIRA model wind-tunnel',* 2nd MIRA International Vehicle Aerodynamics Conference, 20-21st October, Coventry, UK.

Bruun H. H. (1995), *Hot-wire Anemometry: principles and signal analysis',* Oxford University Press Inc., ISBN 0 19 856342 6

Canuto, C., Hussaini, M. Y., Quarteroni, A. and Zang, T. A. (1988), *'Spectral methods in fluid dynamics',* Springer-Verlag, ISBN 0-387-52205-0.

Chandrsuda, C. and Bradshaw, P. (1981), *'Turbulence structure of a reattaching mixing layer',* Journal of Fluid Mechanics, **110**, (171-194).

Chen, Y. S. and Kim, S. W. (1987), *'Computation of turbulent flows using and extended k-ε closure model'*, NASA CR-179204.

Choudhury, D., Kim, S-E. and Flannery, W. S. (1993), *'Calculation of turbulent separated flows using a renormalisation group based k-ε turbulence model',* FED-vol. 149, Separated Flows, ASME, (177-187).

Colls, J. (1997), *'Air pollution - an introduction'*, E and F N Spon, ISBN 0-582-21884-5

Computational Dynamics (1998a), *'Methodology STAR-CD version 3.05',* Computational Dynamics Limited.

Computational Dynamics (1998b), *'User Guide STAR-CD version 3.05',* Computational Dynamics Limited.

COMEAP (1995a), *'Asthma and outdoor air pollution',* Department of Health, Committee on the Medical Effects of Air Pollutants, HMSO Publications, ISBN 0-11-321-958-X.

COMEAP (1995b), *'Non-biological particles and health',* Department of Health, Committee on the Medical Effects of Air Pollutants, HMSO Publications, ISBN 0-11-321952-0

COMEAP (1998), *'Quantification of the effects of air pollution on health in the United Kingdom',* Department of Health, Committee on the Medical Effects of Air Pollutants, HMSO Publications, ISBN 0-11-322102-9.

Craft, T.J., Launder, B.E. and Suga K. (1996), *'Development and application of a cubic eddy-viscosity model of turbulence',* International Journal of Heat and Mass Transfer, **17**, (108-115).

Dabberdt, W. F., Ludwig, F. L. and Johnson Jr, W. B. (1973), *'Validation and application of an urban diffusion model for vehicular pollutants',* Atmospheric Environment, **17**, (603-618).

Davis, J. P. (1982), *'Wind tunnel investigations of road vehicle wakes',* Ph.D. thesis, University of London.

Duell, E. G. and George, A. R. (1992), *'Unsteady wake flows of ground vehicle bodies',* AIAA-92-2641-CP.

Duell, E. G. and George, A. R. (1999), *'Experimental study of a ground vehicle body unsteady near wake',* SAE paper 1999-01-0812

Easom, G. (2000), *'Improved turbulence models for computational wind engineering',* Ph.D. Thesis, University of Nottingham.

Eskridge R. E. and Hunt J. C. R. (1979), *'Highway modelling part 1: Prediction of velocity and turbulence fields in the wake of vehicles'*, Journal of. Applied. Meteorology, **18**, (387-400).

Eskridge R. E., Hunt J.C. R., Binkowski F. S., Clark T. L., Demerjion K.L., (1979**),** *'Highway modelling part 2: Advection and diffusion of SF_6 tracer gas',* Journal of Applied Meteorology, **18**, (401-412).

Eskridge, R. E. and Rao, S. T (1983), *'Measurement and prediction of traffic-induced turbulence and velocity fields near roadways',* Journal of Climate and Applied Meteorology, **22**, (1431-1443).

Eskridge, R. E. and Rao, S. T (1986), *'Turbulent diffusion behind vehicles: Experimentally determined turbulence parameters',* Atmospheric Environment, **20**, 5, (851-860).

Eskridge R. E. and Thompson (1982), *'Experimental and theoretical study of the wake of a block-shaped vehicle in a shear-free boundary flow',* Atmospheric Environment, **16**, (2821-2836).

Fuchs, H. V., Mercker, E. and Michel, U. (1979), *'Large-scale coherent structure in the wake of axisymmetric bodies',* Journal of Fluid Mechanics, **93**, 1, (185-207).

Gaylard, A., Baxendale, and Howell, J. P (1998), *'The use of CFD to predict the aerodynamic characteristics of simple automotive shapes',* SAE paper 980036.

Greenwood, S. J., Coxon, J. E., Biddulph, T., and Bennett, J. (1996), *'An investigation to determine the particulate size distributions for diesel, petrol, and compressed natural gas fuels'*, SAE paper 961085.

Han, T. (1989), '*Computational analysis of three-dimensional turbulent flow around a bluff body on ground proximity'*, AIAA Journal, **27**, 9, (1213-1219).

Hargreaves, D. M. (1997), *'Analytical and experimental studies of vehicle pollution dispersion'*, Ph.D. Thesis, University of Nottingham.

Hargreaves, D. M. and Baker C. J. (1997), *'Gaussian puff model of an urban street canyon',* Journal of Wind Engineering and Industrial Aerodynamics, **69-71**, (927-939).

Hider, Z. E. (1998), *'Modelling solute and particulate pollution dispersal from road vehicles'*, Ph.D. Thesis, University of Nottingham.

Howell, J. P. (1975), *'Wake properties of typical road vehicles',* 2nd AIAA Symposium on Aerodynamics of Sports and Competition Automobiles, Los Angeles.

Hucho, W-H. (1987), *'Aerodynamics of road vehicles'*, Butterworth and Co. 1987, ISBN 0-408-01422-9.

Hucho, W-H. (1998), *'Aerodynamics of road vehicles'*, Society of Automotive Engineers, Inc., ISBN 0-7680-0029-7.

Hunt J. C. R., (1971*), 'A theory for the laminar wake of a two-dimensional body in a boundary layer'*, Journal of Fluid Mechanics. **49**, 1, (159-178).

Katz, J. (1995), *'Race car aerodynamics: designing for speed',* Robert Bentley Publishers, ISBN 0-8376-0142-8

Kim, S-E., Choudhury, D. and Duval, J-F (1994), *'Calculation of complex-three-dimensional turbulent flows using a renormalisation group based k-ε turbulence model',* FED-vol. 188 Turbulent Flows, ASME, (59-64)

Kreyzig, E. (1999), *'Advanced Engineering Mathematics',* Wiley, ISBN 0471154962

Lajos, T. and Hegel, I. (1996), *'Some experiences of ground simulation with moving belt',* MIRA International Conference on Vehicle Aerodynamics, UK.

Lane, D. D. and Stukel, J. J. (1976), *'Dispersion of pollutants in automobile wakes',* Journal of the Environmental Engineering Division, ASME, 102, No. EE3, (571-580).

Launder, B. E., Morse, A., Rodi, W. and Spalding, D. B. (1972), *'Prediction of free shear flows – A comparison of the performance of six turbulence models'*, NASA SP-321.

Launder, B. E. and Spalding , D. B. (1974), *'The numerical computation of turbulent flow'*, Comp. Methods in Applied Mechanics and Engineering, **3**, (269-289)

Morel, T (1978), *'The effect of base slant on the flow pattern and drag of three-dimensional bodies with blunt ends',* Proceedings of Symposium on Aerodynamic Drag Mechanisms of Bluff Bodies and Road Vehicles (editors G. Sovran *et al*) Plenum Press, NY, (191-226).

Morel, T (1980), *'effect of base slant on the flow in the near wake of an axisymmetric cylinder',* Aeronautical Quarterly, May, (132-147).

Namdeo, A. K. (1995), *'Modelling the emissions and dispersion of air pollution from motor vehicles',* Ph.D. Thesis, University of Nottingham.

Palin, R. (2001), Private Communication.

Patankar, S. V. and Spalding, D. B. (1972), *'A calculation procedure for heat, mass and momentum in three-dimensional parabolic flows',* International Journal of Heat and Mass Transfer, **15**, (1787-1806).

Pentz, M. and Shott, M. (1988), *'Handling experimental data',* Edited by Francis Aprahamian, Open University Press, ISBN 0-335-15897-8.

QUARG (1996), *'Airborne particulate matter in the United Kingdom'*, University of Birmingham Quality of Urban Air Review Group ISBN 09520771 3 2

Quinn, A. (1996), *'The ventilation of a chick transport vehicle',* Ph.D. Thesis, University of Nottingham.

Rabbitt, M. J. (1997), *'Some validation of standard, modified and non-linear k-ε turbulence models',* International Journal of Numerical Methods in Fluids, **24**, (965-986).

Rao, S. T. and Keenan, M. (1980), *'Suggestions for the improvement of the EPA-HIWAY model',* Journal of the Air Pollution Control Association, **30**, (247-256).

Richards, R. J. and Hoxey, R. P. (1993), *'Appropriate boundary conditions for computational wind engineering models using k-epsilon model',* Journal of Wind Engineering and Industrial Aerodynamics, **46-47**, (145-153)

Rickeard, D. J., Bateman, J. R., Yeong, K. K., McAughey, J. J., and Dickens, C. J. (1996), *'Exhaust particulate size distribution: vehicle and fuel influences in light duty vehicles'*, SAE paper 961980.

Rodi, W. (1979), *'Influence of buoyancy and rotation on equations for turbulence length scale'*, Proc. 2nd Symp. on Turbulent Shear Flows.

Sarkar, T., Sayer, P. G. and Fraser, S. M. (1997), *'Flow simulation past axisymmetric bodies using four different turbulence models',* Applied Mathematical Modelling, **21**, 12, (783-792).

Sciber-Rylski, A. J. (1984), *'Road Vehicle Aerodynamics'*, 2nd edition, Pentech Press Limited ISBN –0-7273-1805-5

Shaw, C. T. (1992), *'Using computational fluid dynamics',* Prentice Hall, New York. ISBN 0-13-928714-0.

Sims-Williams, D. B., Dominy, R. G. and Howell, J. P. (2001), *'An investigation into large scale unsteady structures in the wake of real and idealized hatchback car models,'* SAE paper – in press.

Shyy, W. (1994) *'Computational modelling of fluid flow and interfacial transport',* Elsevier Science Publishers B.V., ISBN 0-444-81760-3

Speziale, C. G. (1987), *'On non-linear k-l and k-ε models of turbulence'*, Journal of Fluid Mechanics, **178**, (459-475).

Speziale. C. G. and Ngo, T. (1988), *'Numerical solution of turbulent flow past a backward facing step using non-linear k-ε model',* International Journal of Engineering Science, **26**, 10, (1099-1112).

Speziale, C. G. and S. Thangam (1992), *'Analysis of an RNG based turbulence model for separated flow',* International Journal of Engineering Science, 30, 10. (1379-1388).

Thangam, S. and Hur, N. (1991), *'A highly-resolved numerical study of turbulent flow past a backward-facing step',* International Journal of Engineering Science, **29**, 5, (607-615).

United Nations, 1999, *'Statistical Yearbook'*, 43rd Issue. ISBN 92-1-061180-2

USEPA (1996), *'Air quality criteria for particulate matter',* Volumes I-III. Research Triangle Park, NC. United States Environmental Protection Agency.

Van Leer, B. (1977), *'Towards the ultimate conservative difference scheme, IV: A new approach to numerical convection',* Journal of Computational Physics, **23**, (276-299).

Verhoeff, A. P., Hoek, G., Schwartz, J. and van Wijnen, J. H. (1996), *'Air pollution and daily mortality in Amsterdam',* Epidemiology, 7, (225-230).

Versteeg, H. K. and Malalasekera, W. (1995), *'An introduction to computational fluid dynamics: the finite volume method'*, Longman Group Ltd. ISBN 0-582-21884-5

Wang, Q., Bearman, P. W. and Harvey, J. K. (1996), *'A study of instantaneous flow structure behind a car by particle image velocimetry',* Optical Methods and Data processing in Heat and Fluid Flows, IMechE, London.

Wilcox, D. C. (1994), *'Turbulence modelling for CFD'*, Griffin Printing California ISBN 0-9636051-0-0.

Wilkes, N. S. and Thompson, C. P. (1983), *'An evaluation of higher-order upwind differencing for elliptic flow problems',* AERE Harwell, CSS 137.

Williams, J., Quinian, W. J., Hackett, J. E., Thompson, S. A., Marinaccio, T. and Robertson, A. (1994), *'A calibration study of CFD for automotive shapes and CD',* SAE paper 940323.

Wright, N.G. and Easom, G. J. (1999), *'Comparison of several computational turbulence models with full-scale measurements of flow around a building',* Wind and Structures, An International Journal, **2**, 4, (305 – 323).

Wright, N.G.,Easom, G. J. and Hoxey, R. J. (2001), *'Development and validation of a non-linear k-epsilon model for flow over a full-scale building',,* Wind and Structures, An International Journal, **4**, 3, (177-196).

Xia, X. J. and Bearman, P.W. (1983), *'An experimental investigation of the wake of an axisymmetric body with a slanted base',* Aeronautical Quarterly, February, (24-45).

Yakhot, V. and Orszag (1986), *'Renormalisation group analysis of turbulence; I. Basic theory',* Journal of Scientific Computing, **1**, 1, (1-51).

Yakhot, V., Orszag, S. A., Thangham, S., Gatski, T. B. and Speziale, C. G. (1992), *'Development of turbulence models for shear flows by a double expansion technique'*, Phys. Fluids, **A4**, 7, (1510-1520).

Zalesak, S. T. (1979), *'Fully multidimensional flux-corrected transport algorithms for fluids',* Journal of Computational Physics, **31**, (355-362).

Appendix 1 - Turbulence model constitutive relation coefficients Computational Dynamics (1998a).

Table A1-1 – Values assigned to Standard k-ε turbulence model coefficients

C_μ	σ_k	σ_ε	$C_{\varepsilon 1}$	$C_{\varepsilon 2}$	$C_{\varepsilon 3}$	$C_{\varepsilon 4}$	κ	E
0.09	1.0	1.22	1.44	1.92	0.0	-0.33	0.42	9.0*

*For a smooth wall

Table A1-2 – Values assigned to Chen k-ε turbulence model coefficients

C_μ	σ_k	σ_ε	$C_{\varepsilon 1}$	$C_{\varepsilon 2}$	$C_{\varepsilon 3}$	$C_{\varepsilon 4}$	$C_{\varepsilon 5}$	κ	E
0.09	0.75	1.15	1.15	1.9	0.0	-0.33	0.25	0.4153	9.0*

*For a smooth wall

Table A1-3 – Values assigned to RNG k-ε turbulence model coefficients

C_μ	σ_k	σ_ε	$C_{\varepsilon 1}$	$C_{\varepsilon 2}$	$C_{\varepsilon 3}$	$C_{\varepsilon 4}$	κ	E	η_0	β
0.085	0.719	0.719	1.42	1.68	0.0	-0.387	0.42	9.0*	4.38	0.012

*For a smooth wall

Appendix 2 – Experimental study 1

Appendix 2a – Model wind tunnel dimensions and model position

(Brown *et al*, 1998)

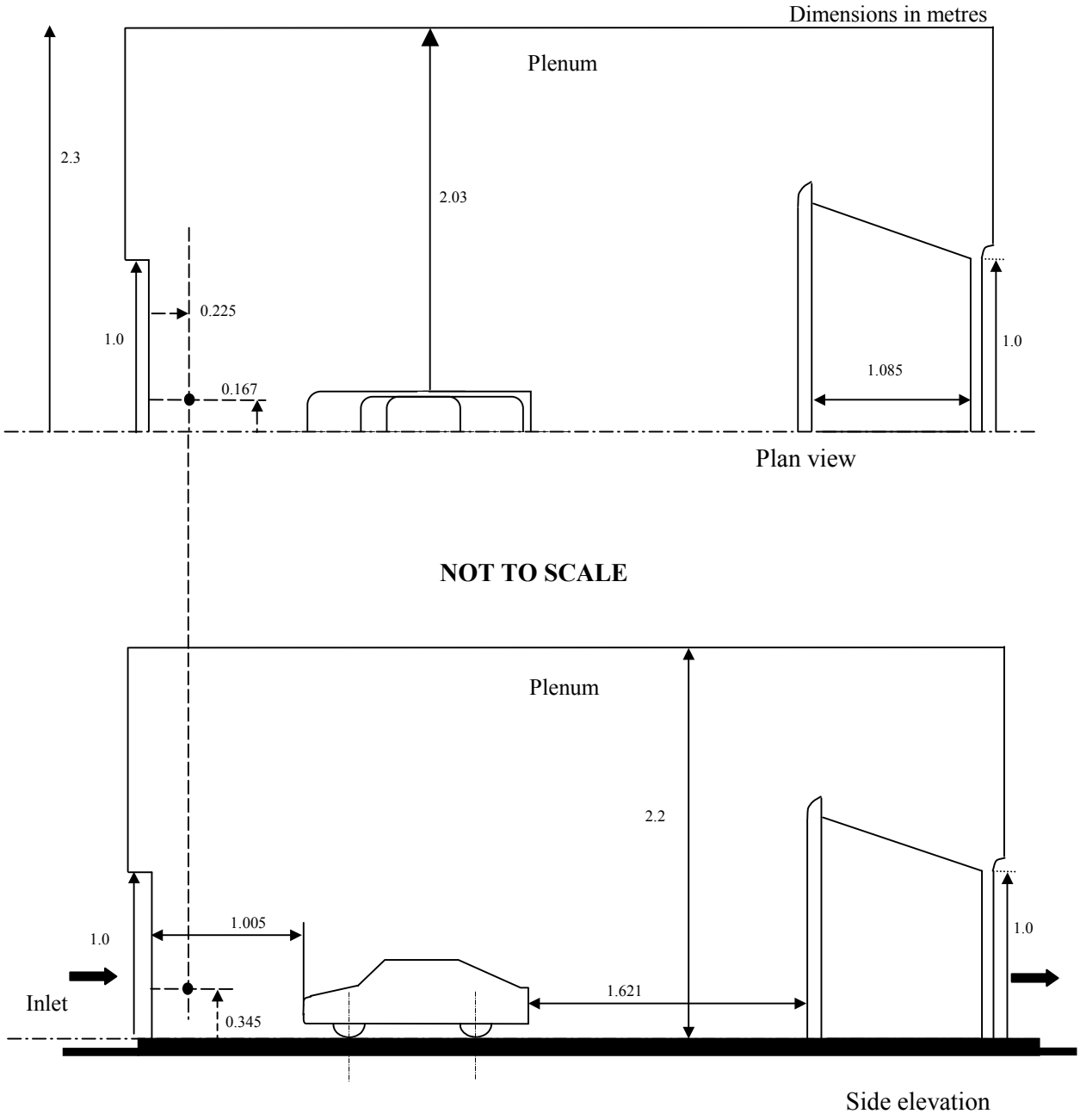

The dash lines indicate the position of the hot-wire during the calibration procedure (Section 4.2.2.2)

Appendix 2b – Boundary layer velocity profile without suction, with a fixed ground. (Palin, 2001)

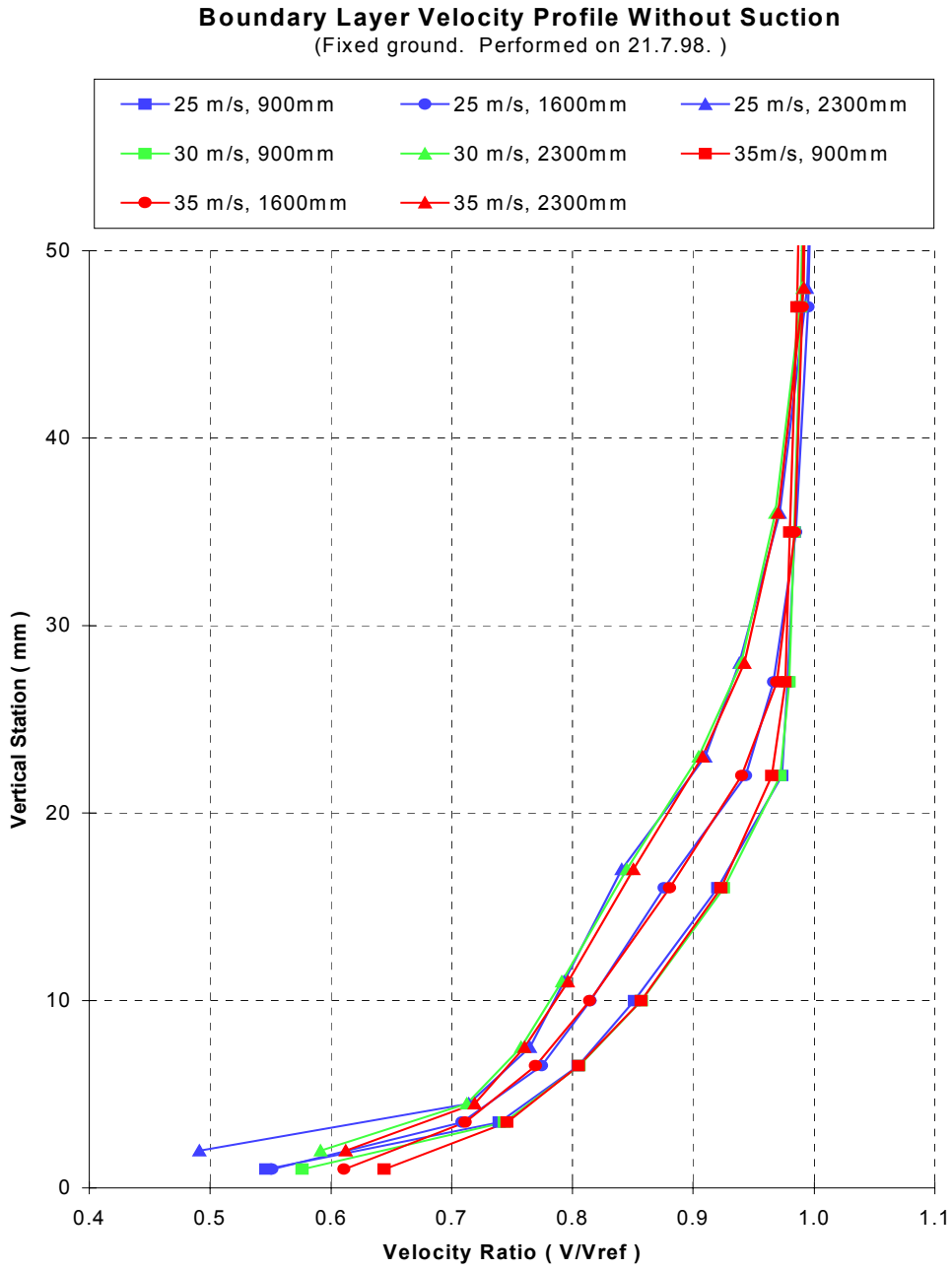

Velocity profiles measured at 900mm, 1600mm and 2300mm downstream of the model, correspond to the front middle and rear portion of the working section respectively.

Appendix 2c – Principles of Particle Image Velocimetry

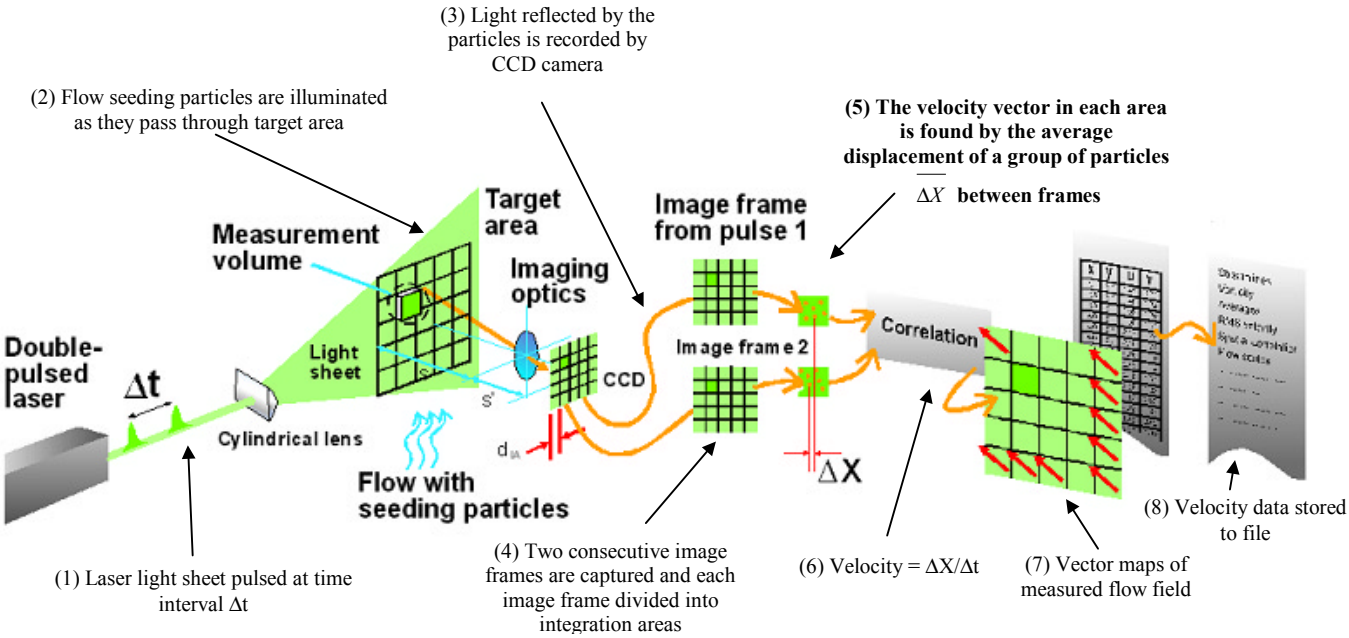

Appendix 2d – Surface pressure transducer location (in mm)

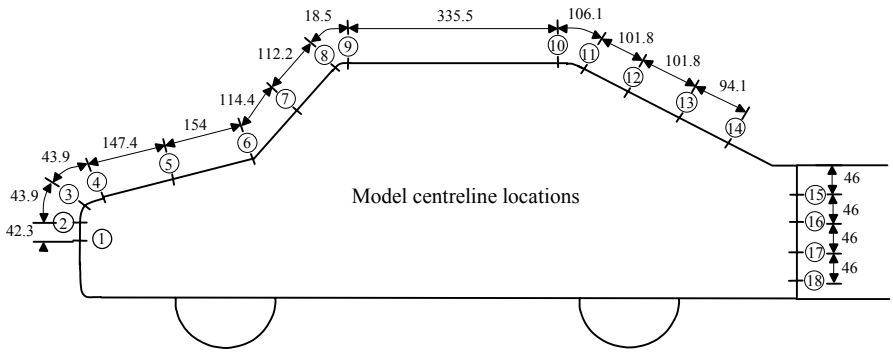

Appendix 2e – Example of normal distributed fluctuating velocity components for both PIV and hotwire data

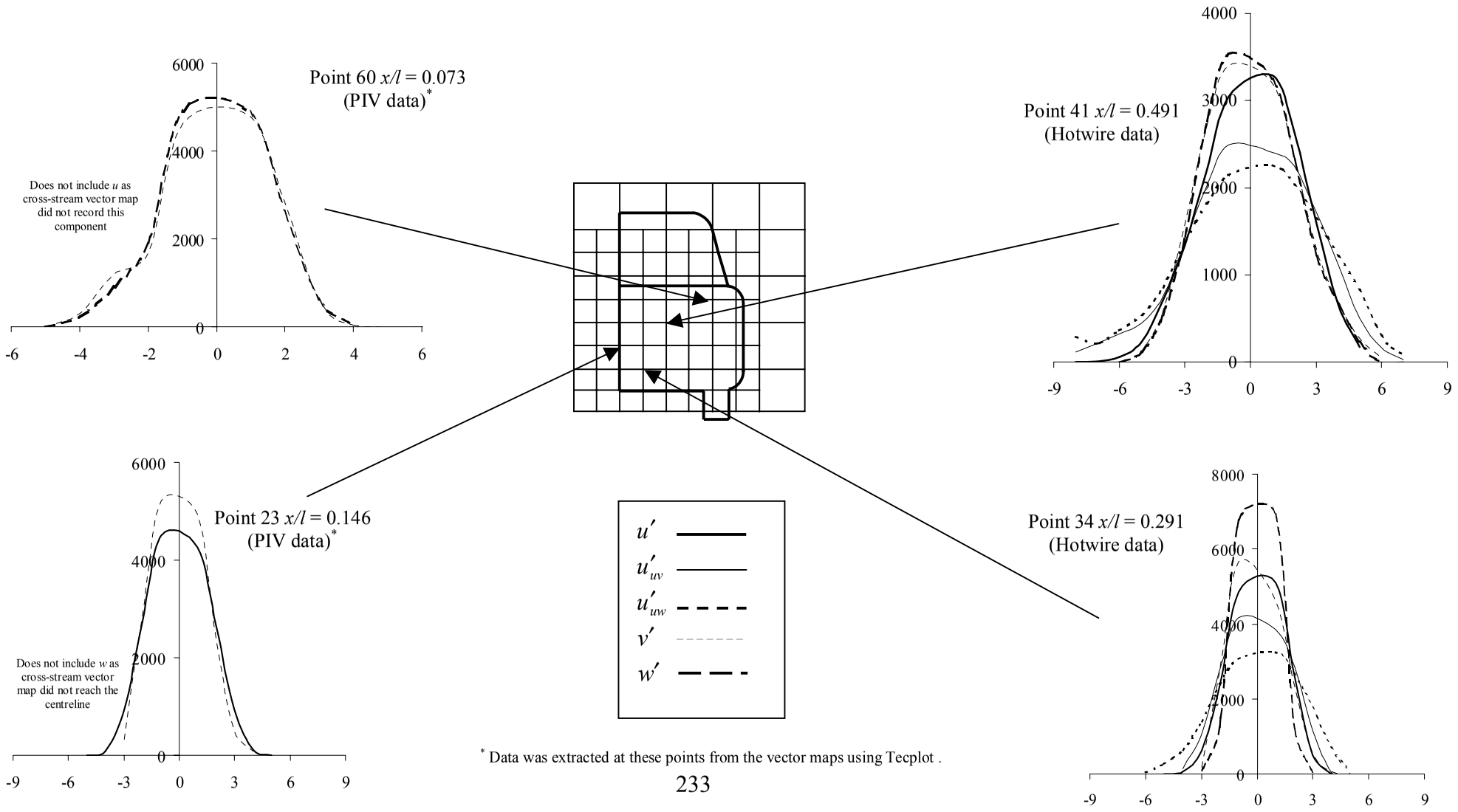

* Data was extracted at these points from the vector maps using Tecplot .

Appendix 2f – Summary of methods used in estimating the error in calculated quantities (Pentz & Shott, 1988)

If the independent measurements A and B, which have total errors ΔA and ΔB associated with them, are combined to give the result X, the error ΔX is,

$$\left.\begin{array}{ll}\text{if} & X = A + B \\ \text{or} & X = A - B\end{array}\right\} \text{ then } \quad \Delta X = \sqrt{(\Delta A)^2 + (\Delta B)^2} \qquad \text{(A2f-1)}$$

In the expression for ΔX only a plus sign appears. This is because errors in A and B increase by ΔX regardless of whether X is the sum or difference of A and B. Also,

$$\left.\begin{array}{ll}\text{if} & X = AB \\ \text{or} & X = A/B\end{array}\right\} \text{ then } \quad \frac{\Delta X}{X} = \sqrt{\left(\frac{\Delta A}{A}\right)^2 + \left(\frac{\Delta B}{B}\right)^2} \qquad \text{(A2f-2)}$$

$$\text{and} \quad X = A^n \quad \Rightarrow \quad \frac{\Delta X}{X} = n\frac{\Delta A}{A} \qquad \text{(A2f-3)}$$

If a constant k, which has no error associated with it, is involved, then,

$$X = kA \quad \Rightarrow \quad \Delta X = k\Delta A \qquad \text{(A2f-4)}$$

when there are more than two quantities involved equation (A2f-1) is simply extended,

$$\text{if} \quad X = A + B - C + D\ldots\ldots \quad \text{then,}$$

$$\Delta X = \sqrt{(\Delta A)^2 + (\Delta B)^2 + (\Delta C)^2 + (\Delta D)^2 \ldots\ldots} \qquad \text{(A2f-5)}$$

Appendix 2g – Workings to establish expressions for uncertainties in calculated values.

Mean streamwise velocity $\overline{u}$.

The value of $\overline{u}_{HW}$ was found by combining the values of u_{uv} and u_{uw}, equation (4.2). The uncertainty in $\overline{u}_{HW}$ was determined using the uncertainties associated with u_{uv} and u_{uw}, and equation (A2f-1). The maximum uncertainty in $\overline{u}$ may be expressed as

$$E_{\overline{u}_{HW(MAX)}} = \frac{1}{2}\sqrt{(S_{\overline{u}_{uv(MAX)}})^2 + (S_{\overline{u}_{uw(MAX)}})^2} \qquad \text{(A2g-1)}$$

where $S_{\overline{u}_{uv(MAX)}}$ and $S_{\overline{u}_{uw(MAX)}}$ are the maximum standard errors on the means of $\overline{u}_{uv}$ and $\overline{u}_{uw}$ respectively with 95% confidence (Table 4.1).

Streamwise vorticity ξ_x

To estimate the uncertainties in calculated vorticity the following example was considered,

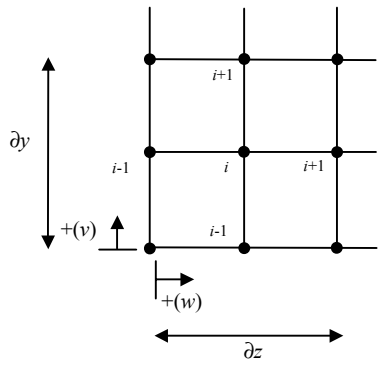

The streamwise vorticity at point *i*

$$\xi_{x(i)} = \frac{\partial \overline{w}}{\partial y} - \frac{\partial \overline{v}}{\partial z} = \left(\frac{\overline{w}_{i+1} - \overline{w}_{i-1}}{y_{i+1} - y_{i-1}}\right) - \left(\frac{\overline{v}_{i+1} - \overline{v}_{i-1}}{z_{i+1} - z_{i-1}}\right) \qquad \text{(A2g-2)}$$

The uncertainty in vorticity at point '*i*' $E_{\xi_{x(i)}}$ is estimated using the uncertainty in the mean velocity components at the surrounding points. There was no calculated error associated with the distances Δy and Δz. With reference to the example and using

equation (A2f-1) the uncertainty in ξ_s at point *p* in the flow, with 95% confidence, is estimated as,

$$E_{\xi_{s(i)}} = \sqrt{[(S_{\overline{w}_{i+1}})^2 + (S_{\overline{w}_{i-1}})^2] + [(S_{\overline{v}_{i+1}})^2 + (S_{\overline{v}_{i-1}})^2]} \qquad \text{(A2g-3)}$$

To calculate the maximum uncertainty in $E_{\xi_{x(MAX)}}$ the standard error on the mean at the individual points with 95% confidence $S_{\overline{w}_{i+1}}$, $S_{\overline{w}_{i-1}}$, $S_{\overline{v}_{i+1}}$ and $S_{\overline{v}_{i-1}}$, are replaced by the maximum standard errors on the means, $S_{\overline{v}_{HW(MAX)}}$ and $S_{\overline{w}_{HW(MAX)}}$ from Table 4.1;

$$E_{\xi_{sHW(MAX)}} = \sqrt{4S^2_{\overline{v}_{HW(MAX)}} + 4S^2_{\overline{w}_{HW(MAX)}}} \qquad \text{(A2g-4)}$$

Appendix 3 –Experimental study 2

Appendix 3a – System specification

HFR400 Fast FID Atmospheric Unit Features:

- Ultra-fast Response time (1-2ms typically)
- One or Two channel simultaneous operation
- Continuous real-time sampling
- Easy installation
- 10m flexible service cables as standard (custom lengths available)

Specification

Measurement principle	- Flame Ionisation Detector (FID)
Components measured	- Total Hydrocarbons (THC)
Number of channels	- 2
Measurement ranges	- 0-2,000 to 0-1,000,000 ppmC
Response Time ($T_{90-10\%}$)	- 1-2 milliseconds typically *(varies with sample tube dimensions)*
Drift	- < ± 2% FS*/hour
Linearity	- < ± 2% FS (@ 150,000* ppmC)**
Ambient sampling conditions	- 0-40°C
Sample gas flow	- ~80 cc/min
Output(analogue)	- 0 -10V, 47 Ohms
Power supply	- AC 50/60 Hz, 100-240V

(www.cambustion.co.uk)

*FS Full-scale

**ppmC parts per million concentration

***1.1% propane/air mix = 11000 ppmC.

For more information refer to HFR400 User manual, Cambustion Limted, Cherry Hinton, Cambridge, UK, or **www.cambustion.co.uk**

Appendix 3b – Distributions of raw data

(i) –Example of normally distributed data – raw concentration data

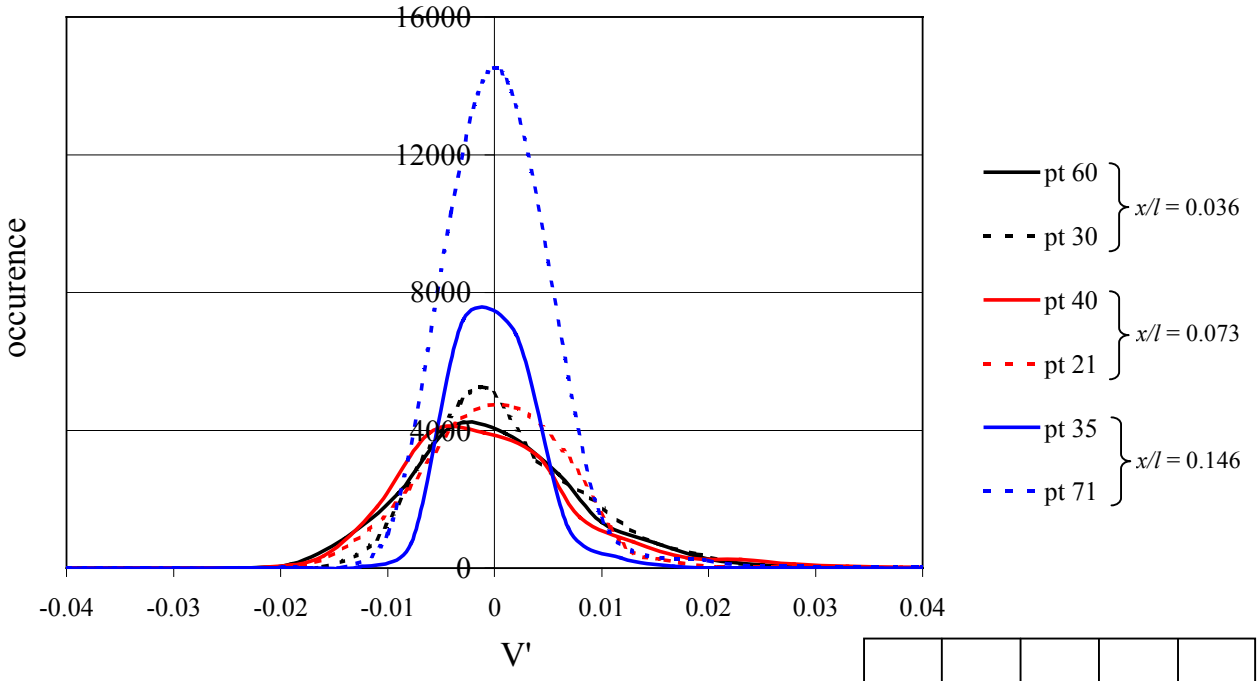

Distribution of V' at point 53 at x/l = 0.037

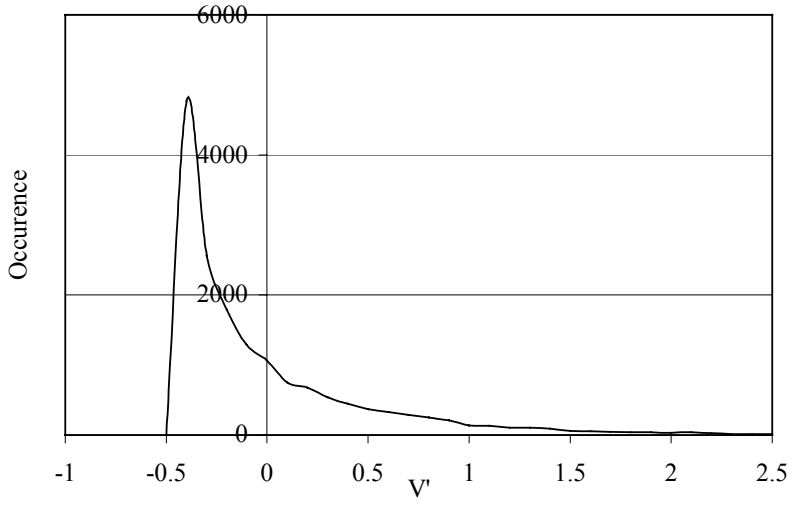

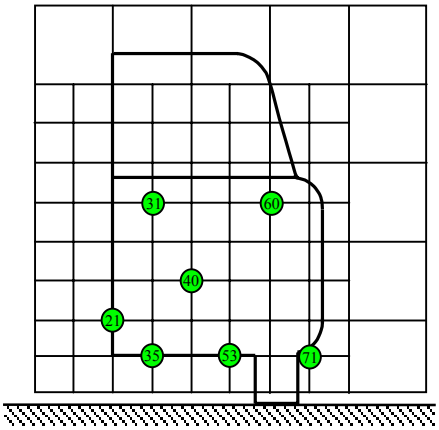

(ii) –Example raw data distribution at point of maximum concentration

Appendix 3c – Workings to establish uncertainty in $\bar{c}$

The uncertainty in $\bar{c}$ is obtained using the expressions detailed in Appendix 2f. Through substituting equations (5.1 and 5.3) into (5.4) the mean concentration maybe expressed as,

$$\bar{c} = SA \tag{A3c-1}$$

where S the maximum source strength is a constant and A is $\frac{\overline{\mathrm{V}}_{rd} - z_r}{z_{off}}$. $\overline{\mathrm{V}}_{rd}$ is the mean measured raw voltage data, z_r is the wind-on zero reading taken at the beginning of each row, z_{off} is the zero wind-off reading and S the maximum source strength in ppm. Using equation (A2f-4) the uncertainty in $\bar{c}$, $E_{\bar{c}}$ may thus be expressed as

$$E_{\bar{c}} = SE_A \tag{A3c-2}$$

where E_A is the uncertainty in A. To find E_A it is necessary to split A into its component parts i.e.

$$A = \frac{\overline{\mathrm{V}}_{rd} - z_r}{z_{off}} = \frac{B}{C} \tag{A3c-3}$$

B is also a combination of values and must also be dealt with separately. Let $B=D-E$ and using equation (A2f-1) the uncertainty in B is thus expressed as,

$$E_B = \sqrt{(E_{\overline{\mathrm{V}}_{rd}})^2 + (E_{z_r})^2} \tag{A3c-4}$$

$E_{\overline{\mathrm{V}}_{rd}} = S_{\overline{rd}}$ and $E_{z_r} = S_{z_r}$ therefore,

$$E_B = \sqrt{(S_{\overline{rd}})^2 + (S_{z_r})^2} \tag{A3c-5}$$

Now $A=B/C$ therefore the E_A may be expressed using equation (A2f-2),

$$\frac{E_A}{A}=\sqrt{\left(\frac{E_B}{B}\right)^2+\left(\frac{E_C}{C}\right)^2} \quad = \quad \sqrt{\frac{(S_{\overline{rd}})^2+(S_{z_r})^2}{(\overline{\mathrm{V}}_{rd}-z_r)^2}+\left(\frac{E_{z_{off}}}{z_{off}}\right)^2} \qquad \text{(A3c-6)}$$

Letting $E_{z_{off}}=S_{z_{off}}$ and substituting this expression into equation (A3c-3), the uncertainty in $\overline{c}$ is

$$E_{\overline{c}}=SA\sqrt{\frac{(S_{\overline{rd}})^2+(S_{z_r})^2}{\left(\overline{\mathrm{V}}_{rd}-z_r\right)^2}+\left(\frac{S_{z_{off}}}{z_{off}}\right)^2} \qquad \text{(A3c-7)}$$

Substituting the values for the values of $S_{\overline{rd}}$, S_{z_r} and $S_{z_{off}}$ from Table 5.1 $E_{\overline{c}}$ is expressed with a 95% confidence in accordance with Appendix 2g. The maximum uncertainty in $\overline{c}$ was established by calculating $E_{\overline{c}}$ at each measured point and then finding the maximum value for FID 1 and FID 2.

Appendix 4 –Numerical study 2

Appendix 4a – Simulated flow through the whole domain

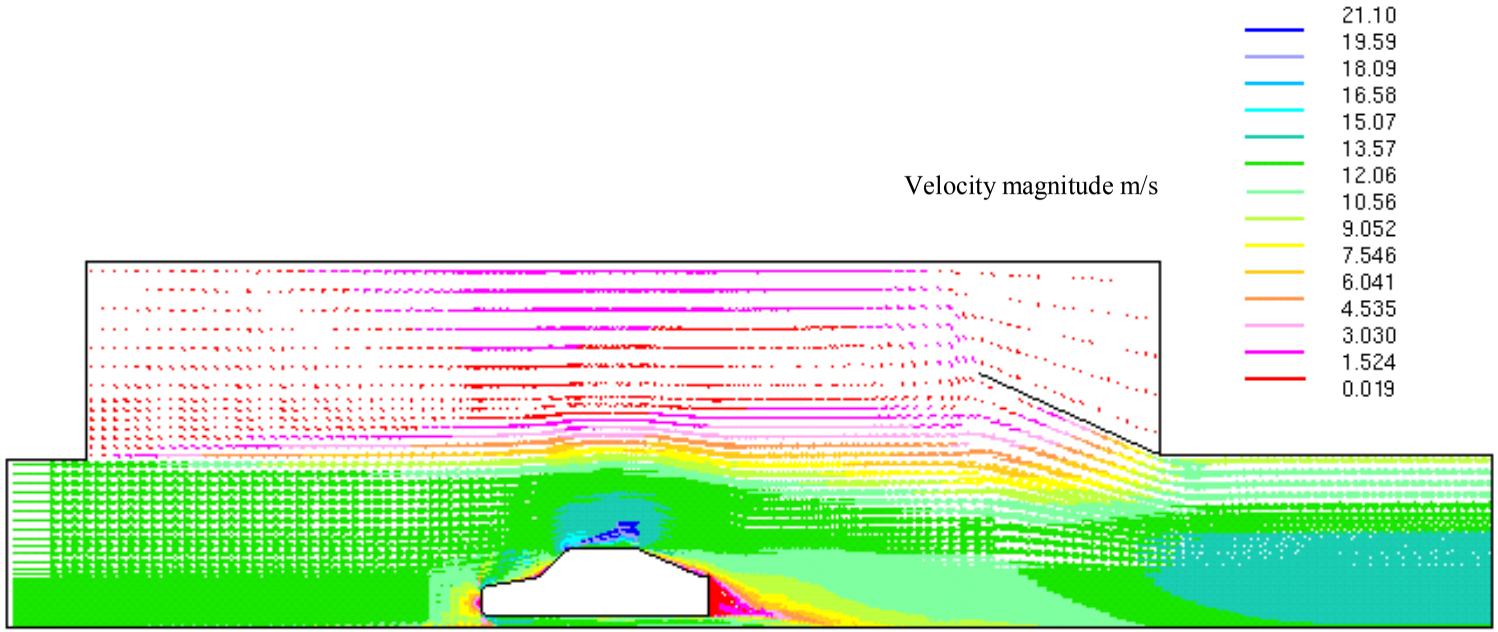

Taken from solution using non-linear k-ε using upwind differencing.(solution D) Inlet velocity = 13m/s

Appendix 4b – Summary of solution details

Solution	Turbulence model	mean y^{+} *	Normalised global residual for u **	Blending ***		CPU time index
				u,v,w	k, ε	
A	Standard k-ε	31.3	2.70E-03	UD 100%	UD 100%	1
B	Chen's k-ε	36.2	1.66E-03	UD 100%	UD 100%	3.7
C	RNG k-ε	31.99	3.34E-03	UD 100%	UD 100%	1.6
D	Non-linear k-ε	30.52	3.1E-03	UD 100%	UD 100%	2.7
E	Non-linear k-ε	32.2	5E-03	UD40%, 60%LUD	UD 100%	10.1
F	Non-linear k-ε	33.6	5.2E-03	MARS (0.5)Compression level	UD 100%	-****
G	Standard k-ε	37.56	2.11E-03	UD40%, 60%LUD	UD 100%	5.2
H	Non-linear k-ε (refined)	30.42	4.1E-03	UD40%, 60%LUD	UD 100%	-****
I	Non-linear k-ε (17m/s)	43.10	3.3E-03	UD 100%	UD 100%	2.9

* Mean y^{+} on the surface of the model vehicle.

** Absolute global residuals for each transport equation solved are recorded at each iteration to monitor solution progress. The final residual of the transport equation for u is given here to illustrate solution convergence, as it always was the largest of all the residuals at the last iteration. All other residuals were sub (E-04).

*** Different differencing schemes maybe applied to the various transport equations. It is also possible to blend LUD with UD to suppress dispersion (refer to section 4.2.4.5)

**** CPU time index not stated because run on a different machine and the comparison would be unfair

Appendix 5 –Computational Study 2

Appendix 5a – Acceptability range

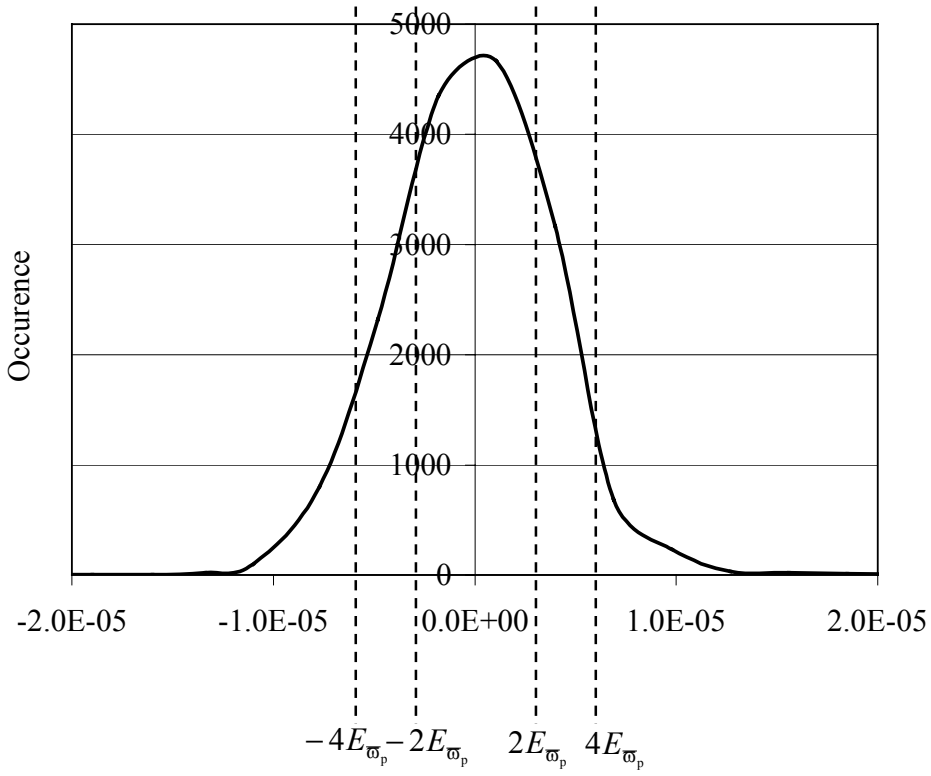

The graph above shows the distribution of $\overline{\varpi}_p$ at point 59 for x/l = 0.036 and illustrates how the range of acceptability for predictions of $\overline{\varpi}_p$ are wider. The uncertainty in the measured value of $\overline{\varpi}_p$ at point 59 is given as $E_{\overline{\varpi}_p}$ = 1.35E-6